

Spring 5-10-2017

Rhythmogenesis and Bifurcation Analysis of 3-Node Neural Network Kernels

Jarod Collens
Georgia State University

Follow this and additional works at: https://scholarworks.gsu.edu/neurosci_diss

Recommended Citation

Collens, Jarod, "Rhythmogenesis and Bifurcation Analysis of 3-Node Neural Network Kernels." Dissertation, Georgia State University, 2017.
https://scholarworks.gsu.edu/neurosci_diss/28

This Dissertation is brought to you for free and open access by the Neuroscience Institute at ScholarWorks @ Georgia State University. It has been accepted for inclusion in Neuroscience Institute Dissertations by an authorized administrator of ScholarWorks @ Georgia State University. For more information, please contact scholarworks@gsu.edu.

RHYTHMOGENESIS AND BIFURCATION ANALYSIS OF 3-NODE NEURAL NETWORK KERNELS

by

JAROD COLLENS

Under the Direction of Andrey L. Shilnikov, PhD

ABSTRACT

Central pattern generators (CPGs) are small neural circuits of coupled cells stably producing a range of multiphasic coordinated rhythmic activities like locomotion, heartbeat, and respiration. Rhythm generation resulting from synergistic interaction of CPG circuitry and intrinsic cellular properties remains deficiently understood and characterized. Pairing of experimental and computational studies has proven key in unlocking practical insights into operational and dynamical principles of CPGs, underlining growing consensus that the same fundamental circuitry may be shared by invertebrates and vertebrates.

We explore the robustness of synchronized oscillatory patterns in small local networks, revealing universal principles of rhythmogenesis and multi-functionality in systems capable of facilitating stability in rhythm formation. Understanding principles leading to functional neural network behavior benefits future study of abnormal neurological diseases that result from perturbations of mechanisms governing normal rhythmic states.

Qualitative and quantitative stability analysis of a family of reciprocally coupled neural circuits, constituted of generalized Fitzhugh–Nagumo neurons, explores symmetric and asymmetric connectivity within three-cell motifs, often forming constituent kernels within larger networks. Intrinsic mechanisms of synaptic release, escape, and post-inhibitory rebound lead to differing polyrhythmicity, where a single parameter or perturbation may trigger rhythm switching in otherwise robust networks. Bifurcation analysis and phase reduction methods elucidate qualitative changes in rhythm stability, permitting rapid identification and exploration of pivotal parameters describing biologically plausible network connectivity. Additional rhythm outcomes are elucidated, including phase-varying lags and broader cyclical behaviors, helping to characterize system capability and robustness reproducing experimentally observed outcomes.

This work further develops a suite of visualization approaches and computational tools, describing robustness of network rhythmogenesis and disclosing principles for neuroscience applicable to other systems beyond motor-control. A framework for modular organization is introduced, using inhibitory and electrical synapses to couple well-characterized 3-node motifs described in this research as building blocks within larger networks to describe underlying cooperative mechanisms.

INDEX WORDS: Network dynamics, Fitzhugh-Nagumo model, Dynamical systems,

Bifurcation analysis, 3-cell networks, Inhibitory coupling, Current stimulus, Phase return maps, Subcritical Andronov-Hopf, Supercritical Andronov-Hopf, Subcritical pitchfork, Supercritical pitchfork, Saddle-node bifurcation, Heteroclinic, Homoclinic, Asymmetric networks, Phase slip, Pattern stability, Jitter, Invariant circles, Modular networking, Visualization, Rhythmogenesis

RHYTHMOGENESIS AND BIFURCATION ANALYSIS
OF 3-NODE NEURAL NETWORK KERNELS

by

JAROD COLLENS

A Dissertation Submitted in Partial Fulfillment of the Requirements for the Degree of

Doctor of Neuroscience

in the College of Arts and Sciences

Georgia State University

2017

Copyright by
Jarod Collens
2017

RHYTHMOGENESIS AND BIFURCATION ANALYSIS
OF 3-NODE NEURAL NETWORK KERNELS

by

JAROD COLLENS

Committee Chair: Andrey Shilnikov

Committee: Igor Belykh

Remus Osan

Astrid Prinz

Electronic Version Approved:

Office of Graduate Studies

College of Arts and Sciences

Georgia State University

May 2017

DEDICATION

This work is dedicated to the many friends and family who have provided much needed support and sanity, not only during this latest academic venture but in the various outlets and pathways upon which my curious nature has taken me over the years. Foremost among all, I would like to thank David Elsea for his endless patience, unconditional love, and steady inner strength the past nine years. Without these I would not have made it this far, and surely have lost myself somewhere along this journey. Excellent role models and teachers helped set me on this path over the years, and I am forever grateful to Robert Stevenson and Ted Ashton, early scoutmasters and mentors who instilled in me the inner confidence and organizational skills I needed to pursue my many varied interests. Their belief not only that I could do anything I set my mind to, but that I needed to be challenged to push boundaries, lead me to believe in this myself. I can't begin to name the many other such teachers and leaders whose inspiration challenged me to keep doing more.

I have benefitted from the support of family in many ways over the years, both natural and adopted, and would be remiss not to thank in particular my sister Alexis for her unconditional love and undying spirit. Her extended struggle being born with hydrocephalus undoubtedly placed the first seed of my interest in the brain and in neural networks and control. My large and extended family has been a great font of love and support growing up, and adoptive families helped keep me strong over the years when I was far from my own. The Solaris kept me sane and safe through my chemical engineering and early economics studies, and the Elseas have been a constant source of love and support the past 9 years and through several degrees. Finally, many fantastic friends have helped define both my sanity and my character over the years, and particular thanks are due to my close friends Drake Knapper and Deniz Alaçam, who have been lab mates, classmates, coauthors, and best friends during this work. I will forever love and appreciate you all.

ACKNOWLEDGEMENTS

I would like to acknowledge Dr. Andrey Shilnikov, my committee chair and dissertation advisor. Little did I know that the first class I took with him would lead to many years of continued interest and collaboration. His tireless passion and youthful curiosity helped keep me excited and inspired over the years, and his deep loyalty and concern for his students makes him a true mentor and role model. I am especially grateful to have been adopted into his laboratory and the amazing lab family he has created over the years.

Special thanks are also due to Dr. Robert Clewley and Dr. Donald Edwards, whose enthusiasm for interdisciplinary and collaborative work facilitated my interest in the Neuroscience Institute and in applications of mathematics for modeling or robotics. In particular, Dr. Clewley's drive to interact and engage with students, making mathematics accessible to many more in the larger biological sciences community than would have otherwise, helped inspire and refine my own interest in applications for dynamic analysis.

I would like to acknowledge and thank the rest of my dissertation committee: Dr. Remus Osan, Dr. Igor Belykh, and Dr. Astrid Prinz for their time, insight, and recommendations. Dr. Osan offered valuable time and input over the years, even before this research, that has been appreciated and helped keep me going. Dr. Belykh was a big influence on my interest in nonlinear dynamics, and I'm grateful to have benefitted from his classroom instruction and his particular insight in driving motivation to interest the biological community in mathematical applications. Special thanks to Dr. Prinz for her tireless hours, detailed feedback and suggestions, and for the inspiration much of her own research provided for computational sweeping and analysis.

Much acknowledgment is due to the great people I have been inspired by, or collaborated with, in the Shilnikov lab: Dr. Jeremy Wojcik, Dr. Justus Schwabedal, Dr. Tingli Xing, Aaron Kelley,

Deniz Alaçam, Drake Knapper, and Krishna Pusulari. Jeremy's work with three-cell networks using Hodgkin-Huxley models was a big driver for preliminary research in this work, and his ability to push and to constantly question everything was an inspiration. Justus made this work possible by creating the tools necessary to broadly sweep the systems studied here. Tingli, Aaron, and Deniz were all part of the original team that inspired the beginning of this work and Aaron's constant feedback and ready edits have been invaluable over the years. Drake's energy and ability to quickly learn and implement coding skills from Justus were invaluable in helping create a framework to produce images and to sweep parameters. Krishna's help with coding and output for larger network configurations was an essential part of the work described in Chapter 6.

Special thanks are also due to both Dr. Laura Carruth and Dr. Anne Murphy, who not only were part of an amazing and supportive qualifying exam committee but have been a constant source of advice and strength over the years. They both have spontaneous smiles and a deep sense of caring that are impossible to miss, and immeasurably appreciated. Without their push and inspiration, this document would have never been possible. Finally, I would like to thank my undergraduate chemical engineering professor, Dr. Victor Vasquez, for being such a challenge and inspiration. His quirky grin every time he would say "You can rest when you are dead" has stuck with me over the years. While he did not mean this literally, it was his sincere desire to push us to succeed. Many times since then, when things became particularly challenging, thinking back to the amazing things he was able to inspire us to do gave me the strength to press forward.

Thank you all.

TABLE OF CONTENTS

ACKNOWLEDGEMENTS	v
LIST OF TABLES	xi
LIST OF FIGURES	xii
1 INTRODUCTION	1
1.1 Purpose of the Study	1
1.2 Research Design & General Methods.....	8
1.3 General Results.....	11
<i>1.3.1 Dynamical pattern characterization and bifurcation analysis.....</i>	<i>11</i>
<i>1.3.2 Verification of CPG motif models with Hodgkin-Huxley</i>	<i>13</i>
<i>1.3.3 Rhythm production in networks with embedded 3-cell motifs</i>	<i>16</i>
2 PATTERN GENERATION IN SYMMETRIC 3-NODE MOTIFS	21
2.1 Methods	23
2.2 Symmetric Motif Results	32
3 PATTERN GENERATION IN ASYMMETRIC 3-NODE MOTIFS	39
<i>3.1.1 Mono-Biased Motif.....</i>	<i>40</i>
<i>3.1.2 Pairwise-Biased Motif.....</i>	<i>47</i>
<i>3.1.3 King-of-the-Mountain Motif</i>	<i>52</i>
<i>3.1.4 Clockwise-Biased Motifs.....</i>	<i>57</i>
3.2 Discussion.....	61

4	KEY BIFURCATIONS AND DETAILED TRANSITIONS.....	65
4.1	Andronov-Hopf bifurcation	66
4.2	Pitchfork bifurcation.....	72
4.3	Saddle-node bifurcations	74
4.3.1	<i>Heteroclinic saddle-node bifurcation.....</i>	<i>76</i>
4.3.2	<i>Homoclinic saddle-node bifurcation.....</i>	<i>78</i>
4.4	Bifurcation transitions with increasing fast-slow separation.....	81
4.4.1	<i>Fast-slow transitions in symmetric motifs</i>	<i>81</i>
4.4.2	<i>Fast-slow transitions in mono-biased motifs</i>	<i>83</i>
4.5	Detailed bifurcation analysis and overlay	85
4.5.1	<i>Mono-biased bifurcation detail</i>	<i>86</i>
4.5.2	<i>King-of-the-mountain bifurcation detail</i>	<i>92</i>
4.6	Discussion and applications.....	99
5	FURTHER POLYRHYTHMICITY AND POST-INHIBITORY REBOUND	102
5.1	Additional asymmetric pattern generation.....	102
5.1.1	<i>Further rhythm switching in mono-biased motifs.....</i>	<i>103</i>
5.1.2	<i>Further rhythm switching in pairwise-biased motifs</i>	<i>110</i>
5.1.3	<i>Further rhythm switching in KOM motifs.....</i>	<i>113</i>
5.2	Additional fast-slow transition effects on trace patterns.....	116
5.3	Phase slipping across motifs.....	122

5.3.1	<i>Pacemaker-like phase-lock in slipping patterns</i>	122
5.3.2	<i>Mono-biased S-patterns within the escape mechanism.....</i>	123
5.3.3	<i>KOM S-patterns within the release mechanism.....</i>	124
5.4	Post-inhibitory rebound mechanism	126
5.4.1	<i>Post-inhibitory rebound methods</i>	128
5.4.2	<i>Symmetric PIR results</i>	131
5.4.3	<i>Asymmetric PIR results</i>	138
5.4.4	<i>Summary of PIR results.....</i>	143
5.5	Discussion and applications.....	144
6	TRANSITIONS IN 3-CELL MODULAR NETWORKING	147
6.1	Visualization of higher-dimension phase-lag return maps.....	148
6.1.1	<i>4-cell networks and 3-D visualization</i>	148
6.1.2	<i>Larger network visualization technique.....</i>	151
6.2	Inhibitory coupling of symmetric motifs.....	153
6.2.1	<i>Mono-biased single inhibitory-coupled symmetric networks</i>	154
6.2.2	<i>Pairwise-biased single inhibitory-coupled symmetric networks.....</i>	157
6.3	Electrical coupling of symmetric motifs.....	170
6.3.1	<i>Single electrically-coupled symmetric PM networks</i>	171
6.3.2	<i>Single electrically-coupled symmetric TW networks</i>	176
6.3.3	<i>Single electrically-coupled symmetric penta-rhythmic networks.....</i>	179

6.4	Electrical coupling of symmetric-clockwise hybrid networks.....	184
6.5	Very strong electrical coupling for node reduction.....	191
6.6	Discussion and applications.....	199
7	CONCLUSIONS.....	203
7.1	Polyrhythmicity in local 3-node networks	204
7.2	Modular networking and expansion techniques	212
7.3	Future extensions and applications	216
	REFERENCES.....	223
	APPENDICES	236
	Appendix A: Supplementary Methods.....	236
	<i>Appendix A.1: Rhythm Pattern Identification.....</i>	<i>236</i>
	<i>Appendix A.2: Sample Regime Identification in Release Bifurcation Diagrams</i>	<i>239</i>
	Appendix B: Supplementary Post-Inhibitory Rebound	241
	Appendix C: Supplementary Modular Networking	247
	<i>Appendix C.1: Doubly Electrically-Coupled Symmetric-Clock Hybrid</i>	<i>247</i>
	<i>Appendix C.2: Triply Electrically-Coupled Symmetric-Clock Hybrid</i>	<i>252</i>

LIST OF TABLES

Table 3.1 Polyrhythmicity and dynamic ranges in release network motifs	62
Table 3.2 Polyrhythmicity and dynamic ranges in escape network motifs	63
Table 4.1 Summary of key network motif bifurcations	101
Table 7.1 Summary of 3-node network polyrhythmicity and bifurcations.....	209
Table 7.2 Summary of coupled symmetric 3-node network outcomes	214
Table 7.3 Summary of coupled symmetric-clock 3-node network outcomes	215

LIST OF FIGURES

Figure 1.1 Generalized 3-cell circuit motif.....	2
Figure 1.2 Lobster pyloric system 3-cell CPG circuit	3
Figure 1.3 Trionia swimming 3-cell CPG circuit	4
Figure 1.4 Sample phase measurement using voltage traces	5
Figure 1.5 Hodgkin-Huxley model verification.....	15
Figure 1.6 Coupled 4-cell motif.....	17
Figure 1.7 Lobster gastric mill circuit.....	18
Figure 1.8 Natural circuits with embedded 3-cell local networks	20
Figure 2.1 3-cell network configuration and fast-slow separation	25
Figure 2.2 Trace convergence on a 2-D torus.....	26
Figure 2.3 Phase-lags and trace convergence	27
Figure 2.4 Phase-basin methodology for determining basins of attraction	28
Figure 2.5 Phase-basin methodology for determining basins of attraction	30
Figure 2.6 Release and escape mechanism state spaces	33
Figure 2.7 Symmetric release case near-knee.....	35
Figure 2.8 Symmetric release stereotypical case	36
Figure 2.9 Symmetric portraits for strong fast-slow separation	37
Figure 3.1 Key asymmetric network motifs	39
Figure 3.2 Mono-biased asymmetric release case	41
Figure 3.3 Mono-biased asymmetric bifurcation diagram.....	43
Figure 3.4 Mono-biased asymmetric escape case.....	44
Figure 3.5 Panel multiplicity for convergence determination	46

Figure 3.6 Pairwise-biased asymmetric release case	48
Figure 3.7 Pairwise-biased asymmetric escape case.....	50
Figure 3.8 Pairwise-biased asymmetric bifurcation diagram	51
Figure 3.9 King-of-the-mountain asymmetric release case	53
Figure 3.10 King-of-the-mountain asymmetric escape case.....	55
Figure 3.11 King-of-the-mountain bifurcation diagram	56
Figure 3.12 Clockwise asymmetric release case.....	58
Figure 3.13 Clockwise asymmetric escape case	59
Figure 3.14 Clockwise asymmetric bifurcation diagram.....	60
Figure 4.1 Subcritical Andronov-Hopf bifurcation	66
Figure 4.2 Supercritical Andronov-Hopf bifurcations.....	67
Figure 4.3 Torus bifurcation via changes in either I_{app} or g_{ij}	68
Figure 4.4 Full view of symmetric release Andronov-Hopf bifurcation	70
Figure 4.5 Example of symmetric escape Andronov-Hopf bifurcation.....	71
Figure 4.6 Pitchfork bifurcations	72
Figure 4.7 Pitchfork bifurcation via changes in either I_{app} or g_{ij}	73
Figure 4.8 Saddle node bifurcation	75
Figure 4.9 Simple saddle-node bifurcation in mono-biased network	76
Figure 4.10 Heteroclinic saddle-node bifurcation in pairwise-biased network	77
Figure 4.11 Homoclinic bifurcations of a saddle and saddle node	79
Figure 4.12 Homoclinic saddle-node bifurcation in mono-biased network	80
Figure 4.13 Increasing PM activity with decreased symmetric fast-slow separation.....	82
Figure 4.14 Increasing PM activity with decreased mono-biased fast-slow separation	84

Figure 4.15	Traveling wave formation within mono-biased networks	87
Figure 4.16	Pacemaker formation within mono-biased networks	88
Figure 4.17	Phase-slip within mono-biased networks	90
Figure 4.18	Detailed bifurcation transitions within mono-biased networks	91
Figure 4.19	Traveling wave formation within KOM networks	94
Figure 4.20	Pacemaker formation within KOM networks	95
Figure 4.21	Phase-slip within KOM networks	97
Figure 4.22	Detailed bifurcation transitions within KOM networks	98
Figure 5.1	Near-knee rhythm switching in mono-biased motifs	104
Figure 5.2	PM basin acquisition via fleeting jitter in a mono-biased network	105
Figure 5.3	TW basin acquisition via invariant circle in mono-biased network	106
Figure 5.4	Ergodic torus in a mono-biased escape case network	108
Figure 5.5	Basin-switching in a nearly mono-biased network	109
Figure 5.6	Invariant circle multiplicity in pairwise-biased systems	111
Figure 5.7	Heteroclinic SN bifurcation in pairwise-biased systems	112
Figure 5.8	Loss of TWs with heteroclinic loops in KOM systems	114
Figure 5.9	PM basin acquisition via heteroclinic SN bifurcations	115
Figure 5.10	Heteroclinic connection between SN separatrices	116
Figure 5.11	Increased fast-slow separation in symmetric release motif	118
Figure 5.12	Increased TW dominance with high fast-slow separation	119
Figure 5.13	Transitions in wave-form patterns with fast-slow separation	121
Figure 5.14	Vertical and horizontal phase-slip with quasi phase-lock	123
Figure 5.15	S-pattern phase-slip in mono-biased systems	124

Figure 5.16	S-pattern phase-slip in KOM systems	125
Figure 5.17	Minimum external perturbation required for PIR	127
Figure 5.18	Hard-locking effects in PIR systems	129
Figure 5.19	Coupling strength effects of on PIR behavior	130
Figure 5.20	Half-center oscillator reduction in PIR systems	132
Figure 5.21	Panel of return maps for symmetric ‘escape’ range PIR	133
Figure 5.22	Panel of return maps for oscillatory symmetric case PIR	134
Figure 5.23	Panel of return maps for symmetric ‘release’ range PIR	135
Figure 5.24	Pattern contribution with shifts in I_{app} for symmetric PIR	137
Figure 5.25	Initial symmetric states for asymmetric PIR examples	139
Figure 5.26	Asymmetry in moderately coupled right-knee PIR systems	140
Figure 5.27	Asymmetry in strongly coupled right-knee PIR systems	141
Figure 5.28	Strongly coupled clockwise right-knee PIR motifs.....	142
Figure 6.1	Sample 4-cell configuration and 3-D visualization	149
Figure 6.2	Anti-phase connectivity of mono-biased motifs with internal complexity	151
Figure 6.3	2-panel phase basin visualization for 6-cell networks.....	152
Figure 6.4	Trace convergence in mono-biased single-coupled symmetric networks	155
Figure 6.5	Basin visualization for mono-biased single-coupled symmetric networks	156
Figure 6.6	Weak inhibitory pairwise-biased symmetric mixed release	159
Figure 6.7	Weak inhibitory pairwise-biased symmetric release	160
Figure 6.8	Moderate inhibitory pairwise-biased symmetric mixed release	162
Figure 6.9	Moderate inhibitory pairwise-biased symmetric mixed release	164
Figure 6.10	Strong inhibitory pairwise-biased symmetric mixed system.....	166

Figure 6.11	Strong inhibitory pairwise-biased symmetric mixed release.....	167
Figure 6.12	Strong inhibitory pairwise-biased symmetric TW system	168
Figure 6.13	Strong inhibitory pairwise-biased symmetric TW networks.....	169
Figure 6.14	Single electrically-coupled symmetric PM systems.....	172
Figure 6.15	Single electrically-coupled symmetric PM systems, in-phase BPM.....	173
Figure 6.16	Single electrically-coupled symmetric PM systems, in-phase CTW	174
Figure 6.17	Single electrically-coupled symmetric PM systems, anti-phase CTW	175
Figure 6.18	Single electrically-coupled symmetric TW systems	176
Figure 6.19	Single electrically-coupled symmetric TW systems, in-phase CTW	177
Figure 6.20	Single electrically-coupled symmetric TW systems, anti-phase CCTW	178
Figure 6.21	Single electrically-coupled symmetric mixed rhythm.....	180
Figure 6.22	Single electrically-coupled symmetric mixed rhythm, in-phase BPM.....	181
Figure 6.23	Single electrically-coupled symmetric mixed rhythm, in-phase CTW	182
Figure 6.24	Single electrically-coupled symmetric mixed rhythm, anti-phase CTW	183
Figure 6.25	Single electrically-coupled symmetric-clock hybrid system.....	185
Figure 6.26	Single electrically-coupled symmetric-clock hybrid, in-phase BPM.....	186
Figure 6.27	Single electrically-coupled symmetric-clock hybrid, in-phase CTW	188
Figure 6.28	Single electrically-coupled symmetric-clock hybrid, anti-phase CTW	189
Figure 6.29	Very strong single electrically-coupled symmetric PM systems	192
Figure 6.30	Very strong single electrically-coupled symmetric TW systems	193
Figure 6.31	Very strong single electrically-coupled symmetric multi-rhythm systems	195
Figure 6.32	Very strong single electrically-coupled symmetric-clock hybrid system	198
Figure 6.33	Effective 5-node reduction of Sym-Sym and Sym-Clock networks	198

Figure 7.1	Symmetrically equivalent asymmetric 3-node motifs.....	207
Figure 7.2	Additional asymmetry within asymmetric 3-node motifs.....	210
Figure 7.3	Examples of alternate key motifs observed in nature.....	211
Figure 7.4	Hypothesized pyloric replication.....	217
Figure 7.5	3-cell motif identification within the gastric network.....	218
Figure 7.6	Effective 5-cell configuration with strong electrical coupling.....	219
Figure 7.7	Stepwise approach to analysis of 5-node gastric network.....	220
Figure 7.8	Sample boundary conditions in modular networking.....	221
Figure A.1	Identification of red pacemaker using traces and phase lag.....	236
Figure A.2	Identification of remaining pacemakers using traces and phase lag.....	237
Figure A.3	Identification of traveling wave patterns using traces and phase lag.....	238
Figure A.4	Pattern identification in symmetric release networks.....	239
Figure A.5	Pattern identification in mono-biased release networks.....	240
Figure A.6	PIR systems result in network silence for most conditions.....	241
Figure A.7	Pattern transitions within the post-inhibitory rebound mechanism.....	242
Figure A.8	Vertical traversal of PIR right walk case.....	243
Figure A.9	Horizontal traversal of PIR right walk case.....	244
Figure A.10	Traveling wave dominance in fully oscillatory symmetric case PIR.....	245
Figure A.11	Additional asymmetric motif results in PIR systems.....	246
Figure A.12	Doubly-coupled electrically connected Symmetric-Clock hybrid system.....	247
Figure A.13	Doubly-coupled electrically connected Sym-Clock, in-phase BPM.....	248
Figure A.14	Doubly-coupled electrically connected Sym-Clock, in-phase CTW.....	249
Figure A.15	Doubly-coupled electrically connected Sym-Clock, anti-phase CTW.....	250

Figure A.16	Very strong double electrically-coupled symmetric-clock hybrid system	251
Figure A.17	Triply-coupled electrically connected Symmetric-Clock hybrid system	252
Figure A.18	Triply-coupled electrically connected Sym-Clock, in-phase BPM	253
Figure A.19	Triply-coupled electrically connected Sym-Clock, in-phase CTW	254
Figure A.20	Triply-coupled electrically connected Sym-Clock, anti-phase CTW	255
Figure A.21	Very strong triple electrically-coupled symmetric-clock hybrid system	256

1 INTRODUCTION

Rhythm generation observed in nature as part of larger networks with central pattern generators (CPGs) is often poorly understood and characterized. This is of fundamental importance because CPGs formed from synergistic interactions of coupled interneurons produce bursting patterns underlying a broad range of vital rhythmic behaviors, including locomotion, heartbeat and respiration [1-9, 31, 86-89, 95-98]. Linking of well-known and extensively studied dynamics of half-center oscillators (HCOs) occurring between two cells, often forming the kernel of local CPG networks, to larger network dynamics and the robustness and stability of behavioral output observed in nature is still in its infancy [10-17, 25-27, 92-94]. Abnormal rhythmogenesis, or perturbations away from inherently produced rhythms, in local CPGs can lead to arrhythmias and other phenomena observed in dysfunctional neurological or locomotive states. Increasing collaboration between experimentalists and computational researchers underlines a growing consensus that the same basic structures and circuit elements are likely shared by both invertebrate and vertebrate animals, including mammals and people [20, 22, 26, 69-71]. It is important, therefore, to better understand the nature and robustness of these networks in a more general and qualitative manner to develop additional universal principles that can be applied across systems.

1.1 Purpose of the Study

The purpose of this work is two-fold: firstly, to identify and characterize rhythmogenesis in small local networks, with an eye both toward stability and robustness in natural systems and to modular network construction techniques, and secondly to develop and elaborate on visualization approaches and computational tools to reduce the problem and aid in future research. This will include building on, and adding to, the analysis of attractors in phase lag return maps between CPG building blocks. Pairing of experimental studies and mathematical and computational

modeling in this manner has already proven key in unlocking insights into operational and dynamical principles of CPGs, and continued work in this area will only continue to unlock more [18-21, 25, 57, 73, 104-107]. Emphasis is given on developing modular organization within larger network settings, and analysis of multi-functionality within local networks as a result of polyrhythmicity and the ability to readily switch rhythm with a single parameter stimulus or change [17-18, 29]. This is important for many behavioral outputs observed in nature, including storage or output of multi-phase rhythmic patterns that can underlie learning and repetitive tasks changes in locomotive gaits.

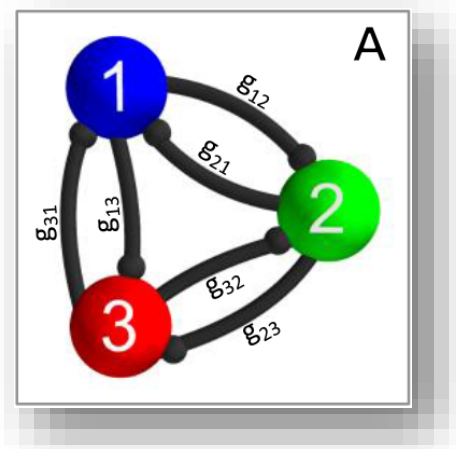


Figure 1.1 Generalized 3-cell circuit motif

Coupling strength, g_{ij} , of the inhibitory connections between cells may be manipulated, and are represented by the black connections with rounded connectors.

Modular organization explored in this work revolves around a 3-cell network of connected HCOs (Figure 1.1) as a basis to form the inner kernel of larger CPG networks. A Fitzhugh-Nagumo-type reduction is employed to simplify computation, while retaining the ability to manipulate biologically relevant parameters [39, 95]. Characterization and general rules derived from 3-node kernels can then be applied to experimental data and models where 3-cell circuits can be readily observed and manipulated, and then to hypothesize and test rhythm generation and switching in

larger settings in which the characterized local network will form a piece in either an expanded network (4+ cells) or in a multi-component networks built of 3-node modules (6, 9, etc. cells). The goal is to derive new approaches and universal rules for understanding CPGs of simple circuits, making these applicable to the study of governing principles of neurological phenomena in complex animals. CPGs responsible for locomotive and rhythmic behaviors in many animals are commonly tied to a component involving the coupling of neurons in half-center oscillators. Such half-center oscillator-based CPGs are implicated in behaviors ranging from respiration and circulation, to sleep and locomotion [1-9, 31, 86-89, 95-98]. While many insights into operational principles of CPGs have been obtained from mathematical studies, the robustness and stability of CPG systems observed in nature is still poorly understood [10-17, 79-84]. Many models exist for these, ranging from biologically relevant Hodgkin-Huxley type models in which individual parameters can be related to specific ionic currents or concentration gradients down to integrate-

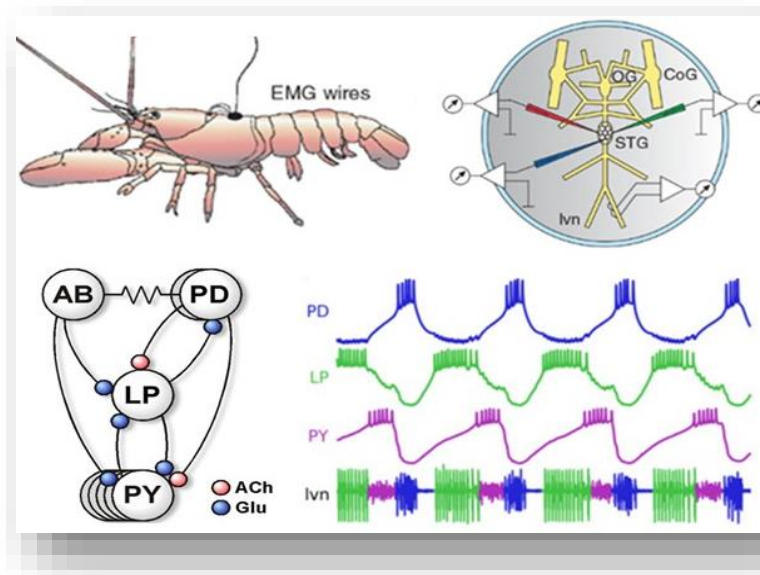


Figure 1.2 Lobster pyloric system 3-cell CPG circuit

Example of 3-cell circuit within the lobster pyloric system, a CPG driving movement of teeth used to digest food. This circuit may be considered an embedded 3-cell network with a 3+1 configuration, or as two overlaid 3-cell networks (LP-PD-PY and AB-PD-PY, for example) coupled to synchronize behavior of identical cells, as in Chapter 6 (modified from [24]).

and-fire type models in which parameters are not biologically relevant but remain reasonably effective in capturing general dynamical characteristics. Understanding the interplay of half-center oscillator components within larger network settings is of vital importance and one step in expanding this understanding is to explore a three-cell motif in which three neurons are interconnected by HCO circuits. Three-cell motifs are frequently observed in nature, often forming a constituent block or center for larger identified networks [2, 9, 22-27, 31-37, 64-68]. Examples of a couple of these can be seen in Figures 1.2 and 1.3, where three-cell kernels from CPG circuits driving either the movement of teeth aiding in digestion within the lobster stomatogastric system or swimming pattern output in the *Tritonia* sea slug.

Using known principles from two-neuron HCOs, exploration of the nature of symmetric and asymmetric connectivity between three such neurons on known mechanisms, such as synaptic

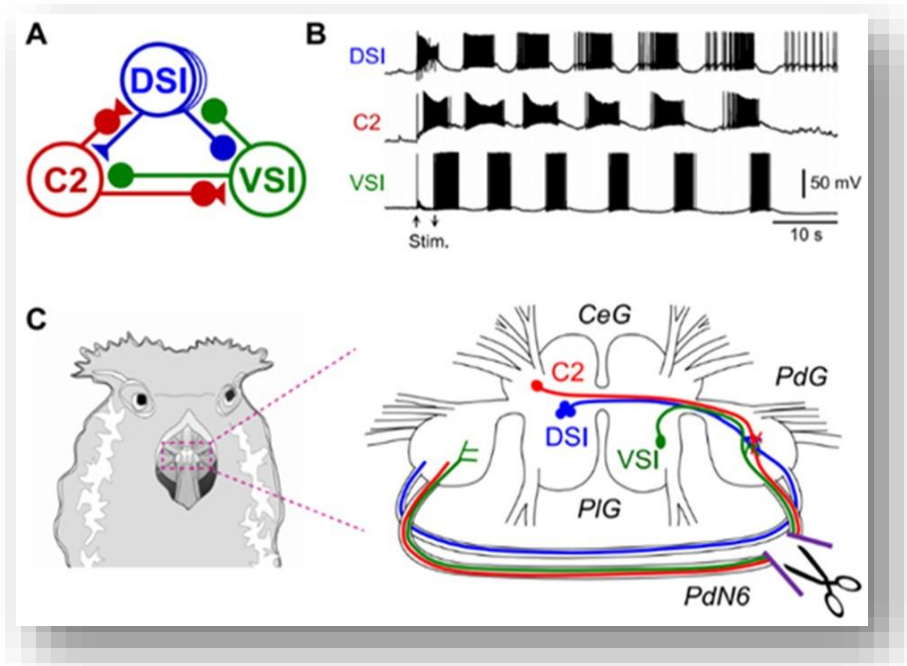


Figure 1.3 *Tritonia* swimming 3-cell CPG circuit

Example of a naturally observed 3-cell circuit within the *Tritonia* swim system, a CPG which drives rhythmic output driving different swimming behaviors (taken from [34]).

release, escape, and post-inhibitory rebound, exposes principles giving rise to anti-phase bursting in networks. An intermediate system based on generalized Fitzhugh-Nagumo (gFN) dynamics is used here to demonstrate replication of results previously obtained using Hodgkin-Huxley-type equations. Excellent work has been done in the characterization of similar two-cell systems, and some of this work will be reiterated in the context of three-cell networks. Extensive use of phase lags and Poincare return maps to characterize the state space of a given CPG motif [18, 39], with emphasis on novel use of gFN equations and brief comparison to prior results using Hodgkin-Huxley equations is therefore important in justifying generalization to universal principles throughout this work. The goal of this research is to present novel results describing multi-stability and parameter sweep results for three-cell gFN CPGs, and for larger networks of embedded or multiple 3-cell circuits, while also developing and providing a framework for others to duplicate this type of analysis using the tools outlined both through this work and in previous work. This

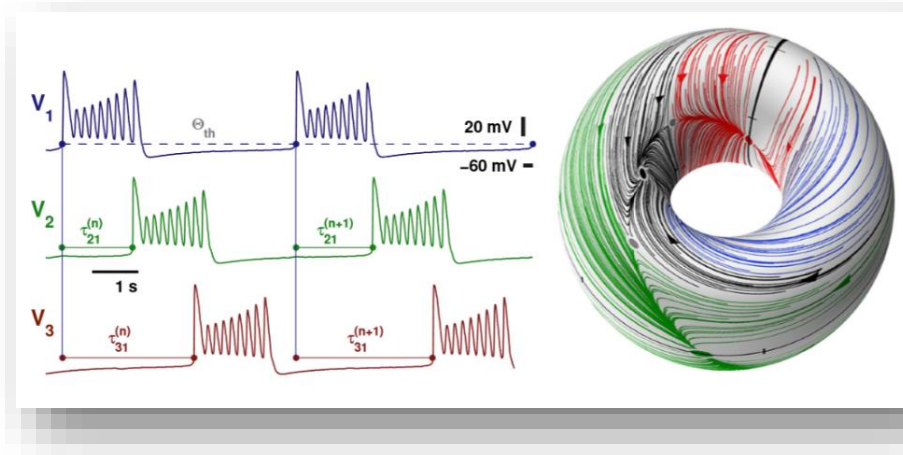


Figure 1.4 Sample phase measurement using voltage traces

Sample Hodgkin-Huxley modeled voltage traces for three-cell network, with phase lags defined by time delays, $\tau_{21}^{(n)}$ and $\tau_{31}^{(n)}$, between spike initiation with of cell 1 and that of cells 2 and 3. Return maps may be represented by two-dimensional tori in which periodic behavior oscillates in color-coded trajectories that converge to fixed points (image from [18]). Method described in more detail in Chapter 2.

work is therefore both an extensive characterization of the networks described, with emphasis on general principles and novel outcomes, and a guidebook for researchers who may benefit from results or approaches described.

This work is particularly important, as it remains unclear whether a single motor system may generate multiple rhythms using dedicated circuitry for each function or multi-functional circuitry that may govern several behaviors [17-18, 27-29, 76]. Using a Fitzhugh-Nagumo reduction (Figure 2.1 and Equations 2.1-4) with biologically plausible elements permits a useful and systematic exploration and quantification of CPG capacity in terms of both the number and robustness of its functional states. Both symmetric and asymmetric configurations are explored, with an increasing range of possible rhythm outcomes including peristaltic phase-varying lags or broader cyclical behaviors. Rhythm switching can result from perturbations or semi-periodic external stimuli will help clarify both the capability and robustness of these systems to produce outputs that can be validated against biological models derived experimentally. This will build on past work in which it has been demonstrated how the set of possible rhythmic outcomes in a CPG can be readily controlled by varying either the temporal characteristics of bursting or the structure of network coupling [15, 17-18]. Building on this research adds continued insight into the fundamental and universal rules governing pattern formation in complex networks of neurons.

Bi-parametric bifurcation diagrams created by classifying and categorizing these rhythm outputs, as well as the types of bifurcations that occur between different behavior regimes, will be used to derive general rules described in Chapters 2 and 3, and forming the core of a first part paper soon to be submitted, that can be used to hypothesize behaviors and mechanisms in experimentally derived circuits. Initial validation of this characterization was done using known network structures reflecting known physiological details of various CPG networks in real animals

involving three-cell motifs [2, 9, 22-27, 31-37, 64-68], with some general results described or shown in Chapters 5 and 6. Work focuses on integrating both known and observed principles for three-cell networks and applying them within the framework of larger networks, with exploration and characterization again being an underlying principle deriving general rules.

This characterization required the development of additional computational and visualization tools, which forms in part the basis for the novel work being proposed. Exploration includes four-cell motifs being viewed as a (3+1) dynamic in which we examined changes in three-cell outputs via introduction and increased connectivity of a fourth cell. Results can no longer be simplified to 2D maps (discussed in more detail in Chapter 2, as well as [18]) and require 3D or other creative frameworks for visualizing results. Some of these are demonstrated or alluded to in Chapter 6, the tools developed hopefully also being applicable to larger, or coupled networks of three-cell motifs in which 6, 9, or more cells could ultimately be explored. The general principles derived in explorations of these 4, 5, or even 6 cell configurations may then be used, as described in Chapter 7, to create a framework to hypothesize underlying mechanisms in known 4-cell or higher circuit motifs observed in nature. Some of these may include the swim CPGs of sea slugs such as *Melibe* and *Dendronotus* [7-8, 30-31, 36], or to expanded circuit networks for crustacean stomatogastric ganglion (STG) [9, 14, 32-33, 64-68]. Validation of the principles developed in Chapters 2-5 is therefore the goal of Chapters 6-7, introducing the concept of electrical coupling for node reduction and demonstrating potential extension toward a model for the gastric network.

Decades of study of CPG dynamics still underlines a deficiency in our understanding of their underlying principles, with the collected knowledge thus far not fully generalizable for other neural circuits. Using our computational toolkit to perform bifurcation analysis of attractors in the corresponding Poincaré phase lag return maps between oscillatory neurons, we can predict and

identify robust outcomes in CPGs with mixed, inhibitory and excitatory, slow and/or fast synapses, differentiated by phase-locked or periodically varying lags corresponding to stable fixed points (FPs) and invariant circles (ICs) of the return map. This powerful approach permits prediction of bifurcations and transformations of rhythmic outcomes before they occur in the network, while also revealing the capacity of the network and the dependence of its outcomes on coupling strength, wiring circuitry and synapses, and external stimuli, thereby letting one quantitatively and qualitatively identify necessary and sufficient conditions, for rhythmic outcomes to occur.

The purpose of this work is to use general principles and a suitable mathematical model, employing biologically plausible elements, to derive general and more broadly applicable rules for three-cell and larger network rhythmogenesis and pattern switching. This is aimed at not only advancing the current state of the theory but in the creation of additional tools that can be used in modular explorations of increasingly large and interconnected networks in the future, effectively beginning to build a bridge between the growing body of knowledge and expertise in two-cell and local network dynamics to the vast body of experimental data and behavioral outputs observed in the world around us.

1.2 Research Design & General Methods

A Fitzhugh-Nagumo reduction will be employed in exploring dynamic behavior between cells. This approach, along with the phase lag return analysis, and subsequent bifurcation analysis, will be the basis for all aims, with additional tools being developed, described, and implemented for 4-cell and larger networks in Chapters 6. As such, greater description of these methods is given in Chapter 2, as they will apply to the procedures for all following results. Examples of these methods will be described and reiterated more fully where they are employed. As described before, Fitzhugh-Nagumo equations are a simplification of the Hodgkin-Huxley formulas and provide a

useful intermediate system in which generic mechanisms can be more readily identified and manipulated generically in biological subsystems of bursting cells. Here a three-cell system of these cells is used, each forming HCOs with the other two (as seen in Figures 1.1 and 2.1). Coupling strength between cells, g_{ij} , and impulse current stimulus, I_{app} , will be most commonly explored in bi-parametric analysis, as these variables are most applicable to parameters that can be readily influenced in experimental studies and emphasize principles related to network connectivity and cellular capability. Three-cell configurations permit a broader range of phase difference patterns than simple two-cell systems and effectively mimic a spectrum of small local networks of cells across different systems and within different animal models. This research looks at the effects of manipulating these parameters, and spans systems of cells that are inherent bursters to cells that are inherently quiescent, and captures variations within the fast-slow system dynamic and briefly reiterates the effects of shifting from fast-slow to fast-fast systems on duty cycles and bursting behavior (discussed further in Chapters 2, 4, and 5).

The three-cell network of reciprocally inhibitory gFN cells can generate traveling waves, in which only one cell fires at a time and firing is in sequence, as well as pace-makers, in which one cell effectively inhibits the other two and fires in anti-phase with two in-phase cells. The phase lag of cells 2 and 3 are analyzed relative to cell 1 (Figures 1.4 and 2.3, Equations 2.5-2.6), and can converge to stable phase-locked states with fixed phase-lag differences. In a three-cell network such as this, a two-dimensional phase difference pairing is therefore described. Mapping the trajectories of many different initial condition combinations reveals basins of attraction, where different initial conditions converge to the same final phase difference fixed points. This visualization lends itself well to rapid identification of polyrhythmic stability. Sequences of these phase difference maps, varying across a selected parameter, can then be used to observe fixed point

movement and the emergence, or bifurcation, of fixed points dynamically changing the phase basins observed. We examine in fine detail the nature of some of these bifurcations, with the emergence or disappearance of different TWs or PMs, characterizing individual phase-lag return maps basin for given parameter sets as containing only pacemakers or traveling waves, or a mixture of both rhythm outcomes. This classification allows us to connect regions of varying intrinsic mechanisms by describing fixed point outcomes in summary in a bifurcation diagram. This approach can first be observed directly in Figure 2.5, discussing generally some symmetric systems results more thoroughly described in Chapter 2 and [39].

These bifurcation diagrams span the range of cellular capability between the release and escape mechanisms (Figure 2.6) [10, 27, 73], and therefore connect systems of endogenous bursting cells, periodicity set by inhibition, through to tonic spikers, which are induced to bursting behavior through inhibition. The post-inhibitory rebound mechanism, in which endogenously quiescent cells can be induced to bursting behavior via strong inhibitory coupling, will also be touched on in Chapter 5 for cases where its presence can be readily introduced by manipulating biologically relevant parameters and ranges. In addition, as parameters are varied, we can generalize findings in terms of increasing coupling strength for given parameter changes in other parts of the equations (ϵ demonstrated in Figures 4.13 and 4.14). This generalization is applied to fully symmetric (all connections of equal strength as in Figure 1.1) and key anti-symmetric systems described in detail in Chapter 3 (Figure 3.1), with specific examples of other asymmetric connectivity demonstrated when useful to demonstrate additional polyrhythmicity or stability. Bifurcation diagrams created in this manner can then be used to effectively analyze changes within the gFN network. By comparing bifurcation diagrams using another, varied, parameter we can gain a third dimension to

this bifurcation analysis and will show examples of this in Chapters 3-4, and some generalized effects on bifurcation diagrams resulting from fast-slow variation are discussed.

1.3 General Results

This research validates the ability of generalized Fitzhugh-Nagumo-type models to capture and characterize dynamic changes in rhythmogenesis of local and expanded 3-cell networks by exploring phase return maps and higher level visualizations. Analysis of universal rules, as well as more detailed exploration of biologically plausible parameter sets, are the guiding principles here. Further examples of the methods employed, and results obtained, are presented in extensive detail in Chapters 2 and 3, which form the key portion of a first-part paper to be submitted shortly, with the goal of making these methods and tools more readily available for use by both the mathematician and the experimentalist. In general, as mentioned before, bi-parametric exploration will be done varying coupling strength, g_{ij} , and impulse current, I_{app} , as these represent generic cellular capability and network connectivity and are the most readily manipulated in an experimental setting and therefore more readily testable for hypotheses in larger network setting and experimental results. Comparisons of other parameter shifts using these g_{ij} versus I_{app} bifurcation diagrams may be used to elicit further information.

1.3.1 *Dynamical pattern characterization and bifurcation analysis*

Clear transitions between regimes of fully pacemaker rhythms (with all three pacemakers), traveling wave rhythms (with both wave patterns present equally), and mixed rhythms (with all 5 stable rhythms present) are expected and observed in fully symmetrically connected networks. Since all connections are changed equally, no asymmetric behaviors or phase-varying lag was expected or observed. Exploration of the bifurcations between pacemaker, traveling wave, or mixed regimes results in the observation of two distinct bifurcation types are identified in these

transitions from pacemaker to mixed, or mixed to wave rhythm regions, as described in [39] and discussed further in Chapters 2 and 4 (Figures 4.3 and 4.7). These, or similar, bifurcation transitions were expected to exist in asymmetric settings, along with saddle-node bifurcations described in Chapter 4, the characterization of which is a first step toward classifying behaviors and mechanisms in local three-cell networks.

Additional bifurcations present themselves in exploration of asymmetric motifs where we change circuit connections within the three-cell motif unequally. In particular, results are described in detail four key asymmetric motifs: (1) Mono-biased: in which a single connection is changed, (2) Pairwise-biased: in which both connections between two cells are changed, (3) King-of-the-Mountain: in which both outgoing connections from one cell are affected, and (4) Clockwise-biased: in which clockwise connections are affected simultaneously, all while the remaining connections are held constant (Figure 3.1). More than the standard five stable rhythms described for symmetric networks in Chapter 2 were expected, and observed, for each of the key asymmetries explored. Increasing a single connection, for example, was expected to first result in some dominance by the uninhibited cell and then transition to situations where that cell has little influence on the others since it will be strongly inhibited by others. In pairwise-biased cases we expect some anti-phase locking between two cells with increasing strength, and in king-of-the-mountain increasing dominance of a single cell to the point is expected to lead to greater antiphase behavior between it and the others. In clockwise-biased networks we expect to see emphasis by one or the other traveling wave, depending on the strength of the directional connections. Many of these expectations are observed, as some are intuitive, with additional unexpected rhythms and behaviors were found. This underlines the ability of Fitzhugh-Nagumo models to maintain an ever broader and richer range of output behaviors and predictive power than originally anticipated.

As in the symmetric case, a somewhat reversed distribution of pacemaker behaviors versus coupling strength in the release and escape mechanism regions was observed in mono-biased systems, but much more dynamic transitory behavior and semi-phase locked phase-varying lags occurs only in the escape case for mono-biased systems. Pairwise-biased systems were hypothesized to be dominated by one PM, which is indeed observed, but a phase-varying lag pattern also emerges here, in which two cells may stay roughly in anti-phase (cells 1 and 3 in this case) while the third (cell 2) shifts continuously leftward. Doubly- and singly-dominant pacemaker states were expected within king-of-the-mountain motifs, as was the dominance of a PM regime in the bifurcation diagram, and this is observed (Figure 3.11). An unanticipated river behavior appeared here, however, with similar escape-case related effects leading to this behavior for higher values of I_{app} but with novel appearance of it in the otherwise purely oscillatory mid-range values of I_{app} . We again see additional peaks and transitions of behavior near full network connectivity symmetry, and a significantly reduced region of mixed rhythm generation. The clockwise-biased motif results are also as expected, but with much more interesting symmetry in behavior around fully-symmetric network transitions. Due to the overwhelming dominance of wave patterns in this motif, results are distinguished for this case in Chapter 2, between the 1- and 2- wave states, with additional color-coding in the bifurcation diagram in Figure 3.14. We again see effects of proximity of the nullclines within release and escape range values of I_{app} , and around system symmetry. Results for explorations of post-inhibitory rebound and further detail of new bifurcations observed in asymmetric release and escape systems are described in Chapter 5.

1.3.2 Verification of CPG motif models with Hodgkin-Huxley

This tested the ability of the characterized networks in Chapter 2 to both accurately duplicate qualitative features of widely accepted Hodgkin-Huxley models and predict or replicate results

obtained experimentally in known 3-cell networks in nature, like those for *Melibe*, *Dendronotus*, *Tritonia*, or the lobster pyloric or gastric sub-systems. This may be tested by direct duplication, replication, and comparison of both theoretical and natural models, results expected to effectively capture dynamics in both settings while introducing the ability to much more broadly sweep parameters and describe mechanisms than could be done solely by Hodgkin-Huxley prediction or experimental verification. Direct comparison was first made for results previously obtained in [18], for which bifurcation diagrams were not created, but using those created here to directly predict the effects of coupling strength ratios at varying values of I_{app} and observe replication of results previously obtained in that study. This was tested bi-directionally, both by qualitatively replicating parameters and connections shown in that work and verifying the outcome, or by identifying key transitions on bifurcation diagrams for motifs also explored in that paper and using the same model and framework used there to produce new figures and verify that the same bifurcations and transitions occur. Results validated duplication of phase-lag convergence observed using Hodgkin-Huxley model dynamics and are not shown here in detail, though some examples can be observed in Figure 1.5 and in Chapters 5 and 6.

Because the Fitzhugh-Nagumo reduction used here assumes that only bursting behavior is of interest, inter-spike intervals (ISIs) or other tapering effects observed in nature and captured by more complex models within bursting are not explored in this work. The benefit gained here, however, is the ability to much more broadly categorize macro-scale bursting behaviors and transitions that could then be used to identify areas of interest in which to introduce additional layers of complexity to the current gFN model to examine other effects of interest regarding subtler waveform variations in initiation and onset, or the effect of ISIs on additional cellular interactions not encompassed by the overall bursting pattern itself. It was expected that, neglecting any ISI

effects, general rhythm generation and bursting effects will be the same. Transitions from one rhythm regime to another, and the specific bifurcation types that occur are also duplicated and the breadth of the parameters explored in the work here actually elucidate new results within the Hodgkin-Huxley framework that were not apparent in the work already done in [18]. Results indicate that the gFN reduction employed successfully captures all the broad pattern generation and transition mechanics discovered previously, one simple preliminary verification done prior to the results shown in Chapter 3 (Figure 1.5) led originally to the hypothesis that verification of qualitative duplication between systems in a bi-directional manner as described above would produce these results. Work described in Chapters 2-3 may be used to accurately predict outcomes for 3-cell networks existing in nature, and this procedure can be bi-directional. Bifurcation analysis and diagrams could be used to direct experimental work by generating hypotheses for rhythmic outcomes not observed previously in laboratory settings but present in results here, or tested

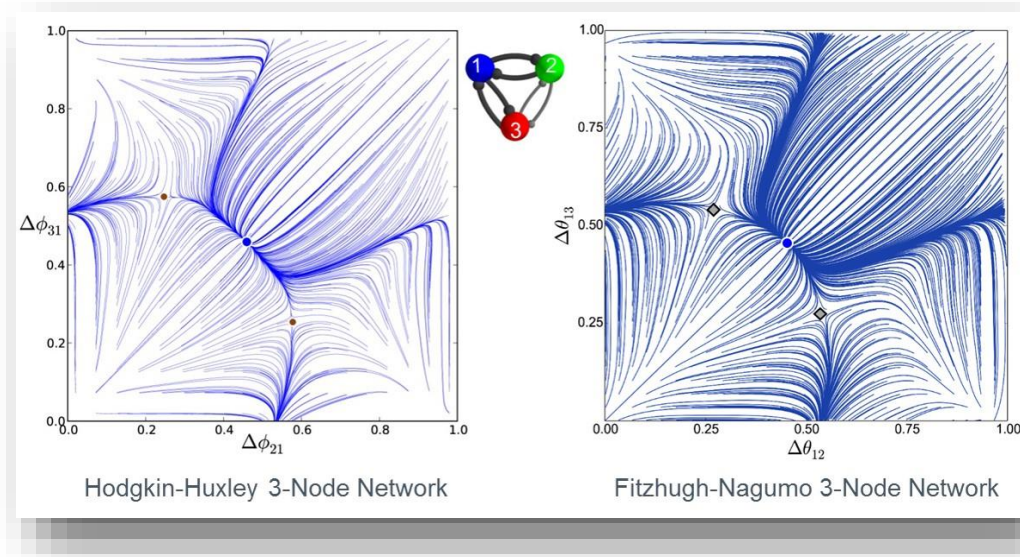


Figure 1.5 Hodgkin-Huxley model verification

Example of qualitative duplication of result from [18], w the connections between nodes 2 and 3 are half the strength of the rest. This motif is a pairwise-biased example, where the connections varied are g_{23} and g_{32} , rather than g_{13} and g_{31} as described in Chapter 3, but results are supported in bifurcation analysis demonstrated in Figure 3.8 and in outcomes in Chapters 3-5.

experimentally by direct manipulation in the lab. This work focuses, in part at least, on verifying the ability to qualitatively reproduce already derived experimental data using Fitzhugh-Nagumo equations. The goal for this being not only to reproduce but to verify universal principles derived and hypothesized in Chapters 2-3 to larger network settings and applications in specific examples observable in nature.

Some of these systems may require the introduction of excitatory connections or electrical coupling in order to fully replicate and anticipate behaviors, but both approaches have been implemented in other work in our lab and may be readily added to the bifurcation analysis performed. Chapter 6 will discuss more detailed results for the introduction of both inhibitory and preliminary electrical coupling in joining 3-cell motifs characterized in Chapters 2-5. Hypothesized outcomes using results of Chapter 2-3, and knowledge of other results pairing electrical coupling or excitatory connections [18, unpublished work by A Kelley] in three-cell networks, permit generalization of the transitions and bifurcations predicted to be observed in natural systems. One example of this, taken directly from [18] is shown in Figure 7.4. Results described in Chapters 2-3 and 5-6 show that gFN sweeping done in this work can effectively capture dynamics observed in experimental settings and may permit future hypothesis generation and testing to guide new experimental work using these and similarly derived results.

1.3.3 Rhythm production in networks with embedded 3-cell motifs

This portion of research is again primarily computational, with exploration of 4-cell configurations carried out in a manner like that described previously. All the same tools and procedures are used, with additional tools and visualization developed to readily identify and generalize behaviors and transitions as was done with the 2-D return maps for 3-cell systems. This approach is two-fold, looking at pairing coupled cells in various configurations and looking at the effect of gradually

introducing connections from a fourth cell into an already fully-characterized 3-cell network. For simplicity, most results of research described here focuses on purely symmetric networks, as shown in Chapter 2. This will result in base patterns and transitions that can then be added to future asymmetric research. Four cell visualization can be performed using a 3-D return map similar to the 2-D version described, in which the phase lag of the fourth cell is also displayed with reference to Cell 1, Δ_{14} . Or we can choose to display 2-D return maps for cells 1-3 as before, with another showing Δ_{42} versus Δ_{43} . This approach does not disentangle trajectories that will visually cross over one another in a 2-D reference frame, however, and some potential visualization concepts are described in Chapter 6. An example of this 3-D visualization approach is shown in Figure 1.6.

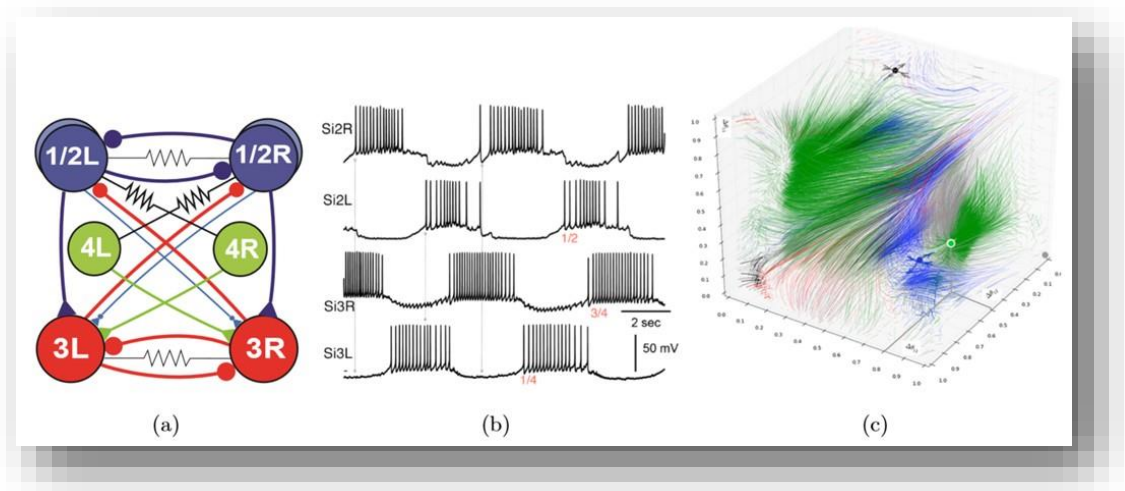


Figure 1.6 Coupled 4-cell motif

(a) Melibe swim CPG circuitry, including electrical synapses. (b) Robust network bursting, intracellular recording in-vitro of specified neurons. Characteristic $\frac{3}{4}$ -phase lag shift shown here [7,8]. (c) 3D phase lag return map example for swim CPG shown in (a). The stable green fixed point shown corresponds to network bursting in (b) with phase lags of ($\frac{1}{2}$, $\frac{3}{4}$, $\frac{1}{4}$) [31].

In a 3-D visualization of a 3+1 configuration, we observe a map matching the original 2-D return map for the 3-cell symmetric motif at given coupling strength when connections to cell 4 are unattached. Results in Chapter 6 first explore the effect of a single connection (which overlaps

with results of the other coupled 3-cell network shown in Chapters 2-3). While the intent of this is not direct application to animal experiments yet, lessons learned here apply to hypothesized circuit creation discussed in Chapter 7. These results are applied also to connected pairs of symmetric 3-cell motifs. It is expected that the addition of a fourth cell, or additional 3-cell motif, will add potential extra layers of rhythmicity, in which smaller sub-cycles may shift in an overall larger repeating rhythm. Identifying such rhythms in fully-symmetric systems in 3+1, or 3+3, configurations may be a first step at characterizing additional stable rhythm patterns and any new rhythm transitions that may exist. Results described in Chapters 6 indicate use of this approach in larger network settings may successfully capture rhythm dynamics observed experimentally, and uncover additional phase-varying lags that occur on a more macro level in which multiple intermediate ‘stable’ rhythms may be observed as part of a larger cycle. This work may be useful in future work modeling and describing longer term rhythms with repetitive features.

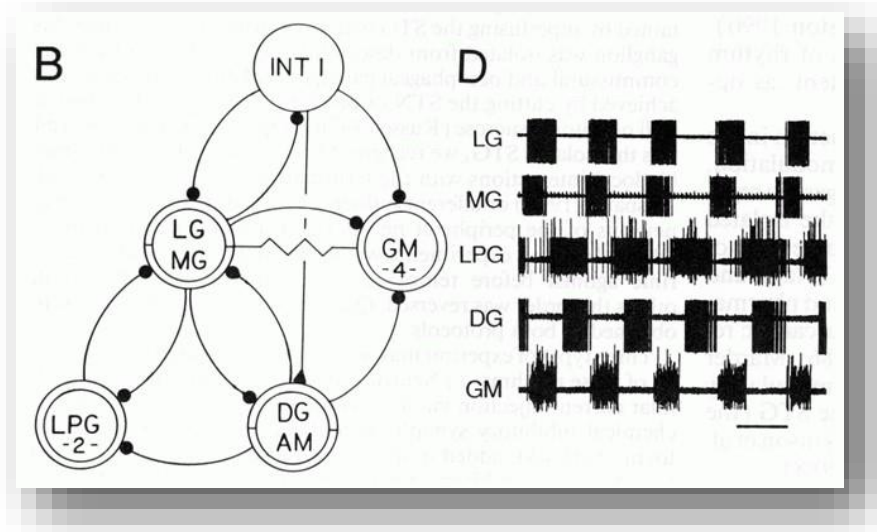


Figure 1.7 Lobster gastric mill circuit

Example of embedded 3-cell motifs within a larger circuit setting. The LPG-LG-DG network could be described as a mono-biased motif, with the LG-INT1-GM network appearing similar to a king-of-the-mountain motif. (B) Simplified circuit showing mostly inhibitory connections, a single electrical coupling, and one excitatory connection. (D) In vitro motor pattern with five phases, time bar ca 3 sec; taken from [37].

This tests the ability of the characterized networks in Chapters 2-5 to accurately predict or replicate results obtained experimentally in known larger networks with 3-cell kernels observed in nature, like that for the lobster pyloric or gastric systems. This can be tested by gradual replication, and comparison of experimentally derived natural models. Several specific potential examples are described and shown in Chapters 6-7 and in Figures 1.6 and 1.7. Specific application to and from experimental data in future research will however be the emphasis here, and the goal of this work is to begin the bridge to even larger networks, specifically the lobster gastric mill circuit shown in Figure 1.7 and described in Chapter 7. As seen, the gastric mill circuit could be decomposed as two 3-cell networks (DG-LG-LPG and LG-INT1-GM), which could be viewed as mono-biased and king-of-the-mountain motifs (as shown in Figure 2.5), respectively, in which the changed connections (g_{LPG-DG} , $g_{GM-INT1}$ and g_{GM-LG}) are simply set to zero. This allows for generation of preliminary hypotheses for rhythm outcomes based on results described in Chapters 2-6. These could be obtained incrementally using increasing electrical coupling between the LG cells of each 3-cell motif to effectively merge them into one cell for 5-cell dynamics, in a node-reduction technique described in Chapter 6. The two integrated motifs could then be enhanced by stepwise addition of the missing connections, a framework for this described in Chapter 7, describing a modular framework in which this work is set up to provide a toolkit from which further work and more complex systems can be built using characterized 3-cell motifs as building blocks. Additional examples of larger networks observed in natural circuits are shown in Figure 1.8, where we observe one or more potential embedded three-cell local networks.

General rules learned from broad characterization of inhibitory motifs, and then applied to mixed coupling networks in biologically relevant mathematical models, can be coupled with experimental data and understanding of specific ionic current effects of neuromodulators to

potentially deduce specific mechanisms for behavioral output changes. This underlines the vital importance of being able to more broadly classify and characterize full parameter ranges, as described and shown in Chapters 2-4, to streamline and generalize findings to a broader range of neuron types and biological systems. This will allow more adept pairing of modeling results with experimental work to better understand underlying mechanisms and more adeptly interact with them to modulate, control, or repair characterized circuits by introducing external stimulus via either electrical input or additional connectivity to restore pattern formation.

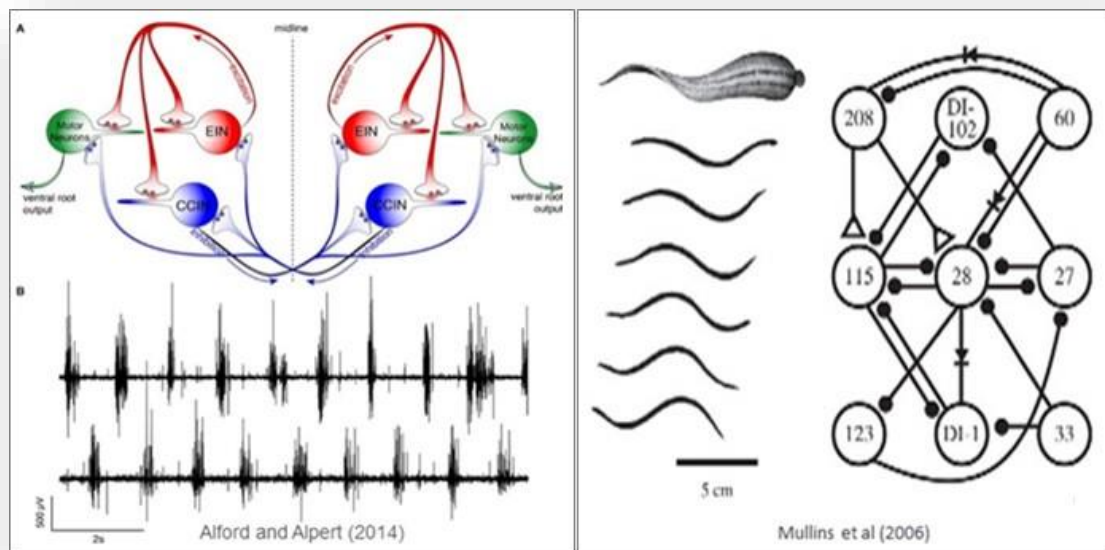


Figure 1.8 Natural circuits with embedded 3-cell local networks

Examples for two larger network settings in which one could describe the larger circuit as having one or more embedded 3-cell local networks. Left are two interconnected 3-cell circuits within the lamprey spinal network [58], and right a CPG which drives rhythmic output driving different swimming behaviors in the segmental movement of the leech.

2 PATTERN GENERATION IN SYMMETRIC 3-NODE MOTIFS

A central pattern generator (CPG) is a small network of coupled neurons that is often responsible for locomotive and rhythmic behaviors in animals [1, 6, 9]. The smallest building unit commonly tied to many of these CPGs is a component involving the coupling of neurons in half-center oscillators (HCO). Such half-center oscillator-based CPGs are implicated in behaviors ranging from respiration and circulation, to sleep and locomotion [2, 5, 7-8, 93-94]. While many insights into operational principles of CPGs have been obtained from mathematical studies, the robustness and stability of CPG systems observed in nature is still poorly understood and cannot be inferred a priori [10-17, 25-27, 75-77]. The cooperative dynamics of coupled cells is an area of ongoing research, with both biological and phenomenological approaches employed. Many models exist for these, including biologically relevant Hodgkin-Huxley (HH) type models in which individual parameters can be related to specific ionic currents or concentration gradients [18, 80-82]. The many interconnected dimensions of Hodgkin-Huxley models do not lend themselves to thorough dynamic analysis, making it difficult to effectively sweep parameters to broadly classify mechanisms and configurations of small networks. Integrate-and-fire equations, on the other end of the spectrum, can be overly simplistic and are inadequate to connect parameters to biological mechanisms that may be directly manipulated or affected, failing to capture nuances in dynamic behavior that intermediate systems can. Here research builds on previous work done using HH-type models for three-node networks, using a generalized Fitzhugh-Nagumo-like (gFN) model to simplify prior work and to facilitate broader parameter sweeping.

We are interested in the interplay of half-center oscillator components within larger network settings and explore a three-cell motif in which three neurons are interconnected by these HCO circuits. Three-cell motifs are observed in nature, often forming a constituent block or center for

larger identified networks [19-20]. Using known principles observed from the dynamics of two-neuron HCOs, exploration of the nature of symmetric and asymmetric connectivity [15, 17-18] between three such neurons, as well as fast, slow, and delayed effects is performed here. These effects on intrinsic dynamic properties, such as synaptic release, escape, and post-inhibitory rebound [73, 78-79] giving rise to anti-phase bursting in networks are discussed. Here we examine gFN dynamics, demonstrating and building upon replication of results obtained using HH-type equations. While maintaining generic behaviors, this reduction in complexity permits more extensive exploration of pivotal parameters and aids in the search for biologically relevant network connectivity that may insure the robustness of rhythmic patterns observed in nature. We examine the networks described with a particular eye for multi-stable rhythms, in which a single relevant parameter or perturbation can trigger a rhythm change in an otherwise robust network [28-29].

The goal of this work is to present novel results describing multi-stability and parameter sweep results for three-cell gFN CPGs and to provide a framework for others to easily and rapidly duplicate these methods using the novel systems outlined both here and in previous work. As one goal is to guide the reader, acting as a tutorial blueprint for network analysis, outlining of the computational technique employed is done in much greater detail than would otherwise be done, with the hope that this detail will facilitate and streamline understanding and duplication of similar work. Some results of this work will therefore be embedded within the description of methodology, as examples of the method in action will inherently involve some of the actual work done. We will nonetheless try to maintain a generality to our methodology within the methods section and keep most discussion of specific mechanisms and results for later.

Specific results are then be described in terms of the three primary mechanisms underlying network rhythmogenesis being explored here. Synaptic release and escape are discussed in detail in

Chapters 2-3, which form the core of a first-part paper to be submitted soon. Forming the second part, and outlined in Chapter 5, the post-inhibitory rebound mechanism will be highlighted along with further detail into specific additional bifurcations and detailed diagrams described in Chapter 4. Each of these are examined and described with special emphasis on how the circuitry of a neural network influences network capacitance on possible rhythms produced. As well as differences in rhythm transitions and resilience to multi-stability, we describe: (1) What patterns are possible, (2) How stable are these rhythms, (3) Existence of invariant circles, (4) Differences in phase locking and phase-slip (PS), and (5) Ranges of network parameters (synaptic coupling strength and external current amplitudes specifically) dictating these behaviors (Tables 3.1 and 3.2).

Within each mechanism we will contrast the behavior of symmetric, networks with all-to-all connections of equally inhibitory strength, and asymmetric motifs, where one or more of the connections within the network vary relative to the others, with analysis here of a representative subset of asymmetric configurations to be discussed later. We discuss the general results with specific examples within the subset chosen for both relevance and novelty, particularly to applications representative of locomotive or other rhythmic outputs like breathing or circulation in natural circuits. Additional asymmetric behaviors and mixed cases will be explored further in forthcoming papers. In the concluding part of this chapter we connect overarching mechanisms with observation of transitioning stages from release to escape in terms of sequences of bifurcations that fixed points undergo with changes in current amplitude, I_{app} .

2.1 Methods

Fitzhugh-Nagumo-like equations are a mathematical generalization of dynamical features often captured by Hodgkin-Huxley-like models [39, 95, 118]. In this paper, we use a generalized Fitzhugh-Nagumo system in which we introduce some features, providing a useful intermediate

system in which mechanisms can be more readily identified and manipulated generically for use in biological subsystems of bursting cells. Here we use a three-cell system of relaxation-like oscillator cells, each identical and coupled all-to-all forming HCOs with the other two in the following manner:

$$\dot{V}_i = m(V_i - V_i^3) - h_i + I_{app} + \sum G_{ij}(V_i, V_j), \quad \text{Equation 2.1}$$

$$\dot{h}_i = \varepsilon \left[\frac{1}{1+e^{-k(V_i-V_0)}} - h_i \right], \quad i, j = 1, 2, 3, \quad \text{Equation 2.2}$$

where ε represents a factor permitting fast-slow dynamics and the variables m and k influence the shape of the cubic and sigmoidal nullclines, respectively. Here, the state of the i th node is described by its activity variable V , representing membrane voltage, and a recovery variable h , as a way to reflect Hodgkin-Huxley formalism within this generalized model. By construction, active driving oscillators slow down or repress recovery dynamics of driven oscillators, with the inactive state ($V_i < 0$) induced or maintained by inhibitory coupling. This coupling of active and inactive nodes is captured by a sigmoidal coupling function using the following fast threshold modulation [57].

$$G_{ij}(V_i, V_j) = g_{ij}(V_i - V_{rev})\Gamma(V_j), \quad \text{Equation 2.3}$$

$$\Gamma(V_j) = \frac{1}{1+e^{-k(V_j-V_{th})}} \quad \text{Equation 2.4}$$

The G_{ij} term is used to indicate a shift to the fast nullcline (Figure 1(B)) induced by an active inhibitory connection, the magnitude dependent on the strength of that connection and the relative voltages of the pre- and post-synaptic cells in comparison to the threshold voltage of bursting for each. This choice of V_{th} guarantees that G is positively defined for the range of the V -variable being used, and is modulated by fast switching of Γ between 0 and 1.

Symmetric connectivity does not imply symmetric behavior, and duty cycles, or the time during each periodic cycle for which a cell is active, within a specific rhythm vary by cell but anything true for one cell may be applied generically to the others. Three-cell oscillatory networks permit a

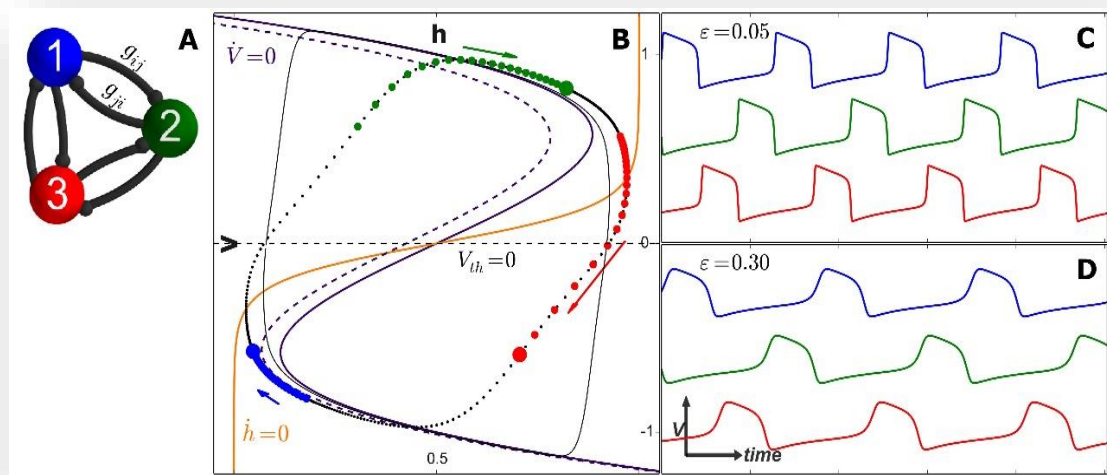


Figure 2.1 3-cell network configuration and fast-slow separation

(A) Network motif composed of 3-cells coupled by inhibitory connections with weights g_{ij} . (B) The (h, V) -phase portrait depicting a clock-wise periodic orbit (shown as a grey solid curve at $\varepsilon = 0.05$, and a dotted curve at $\varepsilon = 0.30$) with 3 strings of blue, green and red dots that represent snapshots of the time-evolution of the coupled cells - 1, 2 and 3, respectively. It is superimposed with a fast cubic nullcline labeled $\dot{V} = 0$, and shown as solid and dashed (purple) curves for pre- and post-synaptic cells, and a slow sigmoidal nullcline (orange), $\dot{h} = 0$. (C-D) Voltage traces generated by the 3-cell network at $\varepsilon = 0.05$ and $\varepsilon = 0.3$, respectively, corresponding to the periodic orbits in Panel B.

broader range of phase difference patterns and effectively mimic a spectrum of small local networks of cells across different systems and within different animal models. This research looks at the effects of manipulating these parameters, and spans systems of cells that are inherent bursters to cells that are inherently quiescent. This work also captures variations within the fast-slow system dynamic and briefly reiterates effects of shifting from fast-slow to fast-fast systems on duty cycles and bursting (Figure 1.1(C, D)) but focuses primarily on systems with less separation where more generalized ranges of behavior occur. In what follows, we show that 3-cell gFN networks produce multiple rhythms including traveling waves, in which only one cell fires at a time and firing is in sequence (dividing the period evenly in fully symmetric networks), as well as pace-makers, in which one cell effectively inhibits the other two and fires in anti-phase with two in-phase cells.

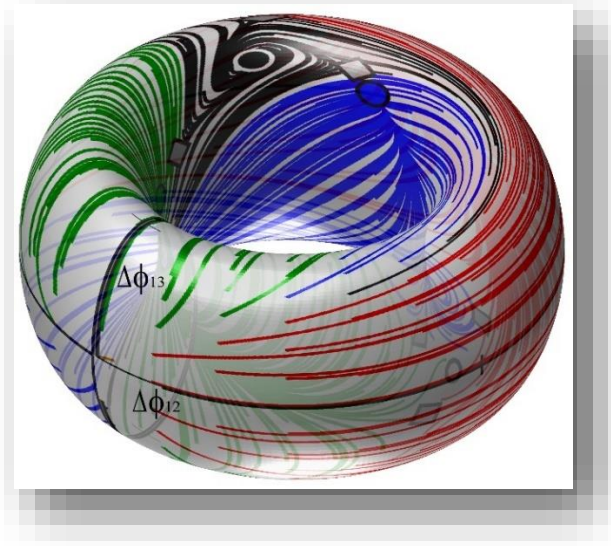


Figure 2.2 Trace convergence on a 2-D torus

A three-dimensional view of the 2-D Poincaré return map torus generated by multiple transients of the phase lags, Δ_{12} and Δ_{13} defined on mod 1, revealing stable fixed points (FPs) (represented by colored \bullet) with color-coded basins of attraction and separating saddles (represented by gray \blacklozenge). This representation can be unwrapped, as in Figure 2.3, by cutting the torus vertically and horizontally along the black axis displayed to better analyze dynamical convergence of $\Delta_{12}^{(n)}$ and $\Delta_{13}^{(n)}$ iterates in different systems.

As these phase lags are cyclical and repetitive in nature, visualization of the traces over time is inherently three-dimensional, as represented in Figure 2.2, in which we see rotation of the phase cycles through time with convergence to fixed points on a torus. This view is challenging to interpret without viewing from many directions and to analyze stability of the rhythms produced, we introduce the notion of phase lags between cells. Unwrapping this torus into a 2-D return map aids in visualization. Here we choose cell 1 as a reference to reduce dimensionality as follows. The phase lag of cells 2 (Δ_{12}) and 3 (Δ_{13}) relative to cell 1 (as shown in Figure 2.3(d)) are given by,

$$\Delta_{12}^{(n)} = \frac{\tau_{21}^{(n)}}{\text{Period}_1} = \frac{t_2^{(n)} - t_1^{(n)}}{t_1^{(n+1)} - t_1^{(n)}}, \quad (\text{mod } 1) \quad \text{Equation 2.5}$$

$$\Delta_{13}^{(n)} = \frac{\tau_{31}^{(n)}}{\text{Period}_1} = \frac{t_3^{(n)} - t_1^{(n)}}{t_1^{(n+1)} - t_1^{(n)}}, \quad (\text{mod } 1) \quad \text{Equation 2.6}$$

where t_l represents the time at which cell 1 is in upstroke through the threshold voltage, $V_{th}=0$. These phase lags can stabilize to fixed differences when stable phase difference fixed points exist in the system as n , or the number of cycles, increases. If phase lags continuously shift, there is no

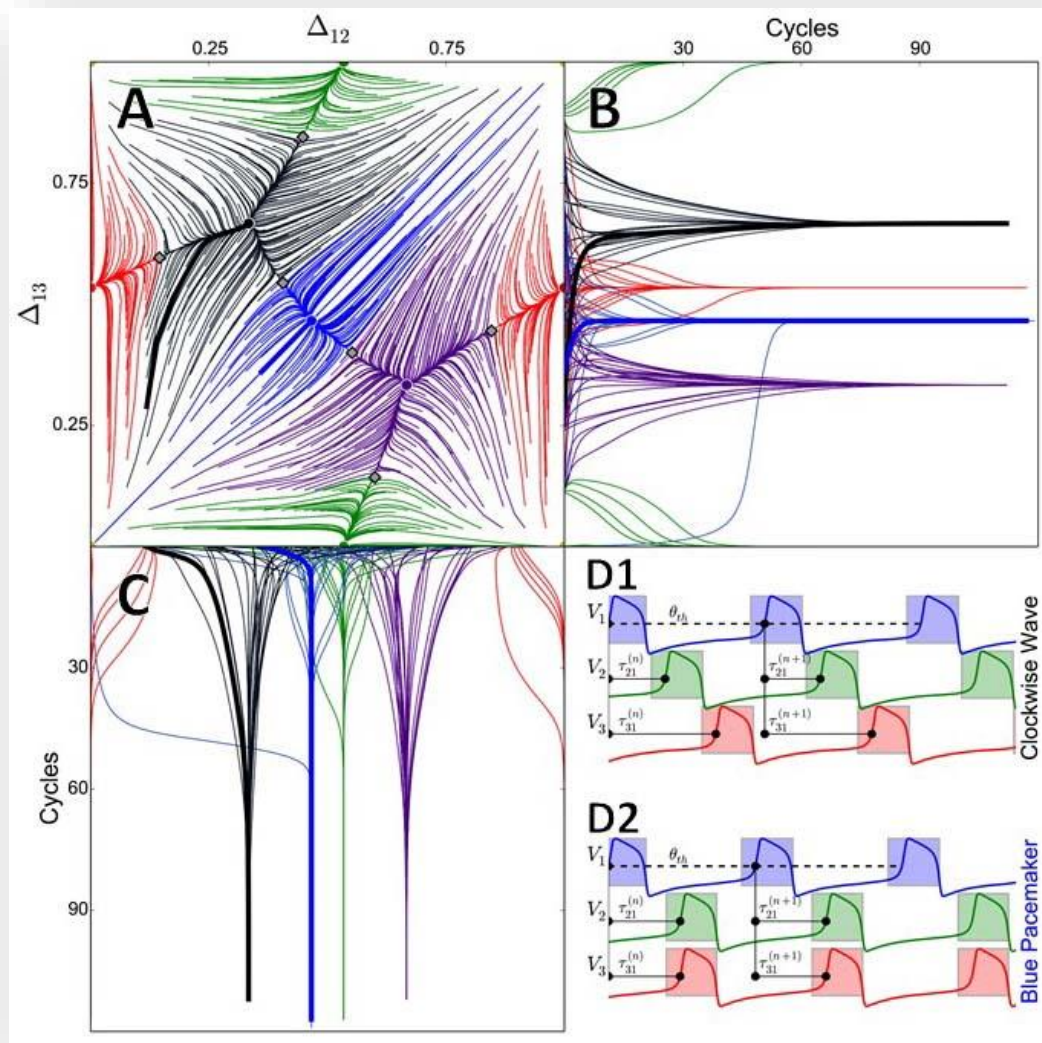


Figure 2.3 Phase-lags and trace convergence

(A) Poincaré return map for phase lags, Δ_{12} and Δ_{13} , revealing five stable fixed points (FPs) (represented by \bullet) with color-coded attraction basins, 6 separating saddles (represented by \blacklozenge), and a single repelling FP at the origin. (B, C) Transients of $\Delta_{12}^{(n)}$ and $\Delta_{13}^{(n)}$ converging to phase-locked states correspond to the color-coded FPs in Panel A. (D) Successive delays, $\tau_{21}^{(n)}$ and $\tau_{31}^{(n)}$, between voltage upstrokes in the reference blue cell 1 and in cells 2 (green) and 3 (red) at the n -th, characteristic for a clockwise traveling wave (D1) and pacemaker rhythm (D2) that are represented by the black and blue FPs, at $(1/3, 2/3)$ and $(1/2, 1/2)$ respectively, in Panel A.

local attractor. We can plot such trajectories from given initial phase lag combinations, phase differences revealing where phase lag combinations will converge to stable phase differences. In a three-cell network such as this, a two-dimensional phase difference pairing is therefore described. We examine multiple trajectories with differing initial conditions (Figure 2.3) to observe potential stability or poly-stability within the system, in which a single or multiple stable rhythm outcomes may be observed. Additional detail is provided in Appendix A1.

Mapping the trajectories of many initial condition combinations reveals basins of attraction for phase difference fixed points. Initial condition pairings within each basin converge to the same fixed phase lag attractor. Where appropriate, we examine systems under at least 900 initial conditions (1x30x30 grid of Δ_{12} versus Δ_{13}) for a given set of system parameters, obtaining phase basin diagrams which can be used to approximate attractive basins of initial conditions for each of the distinct rhythmic outputs observed. Color-coding of the traces within these diagrams matches

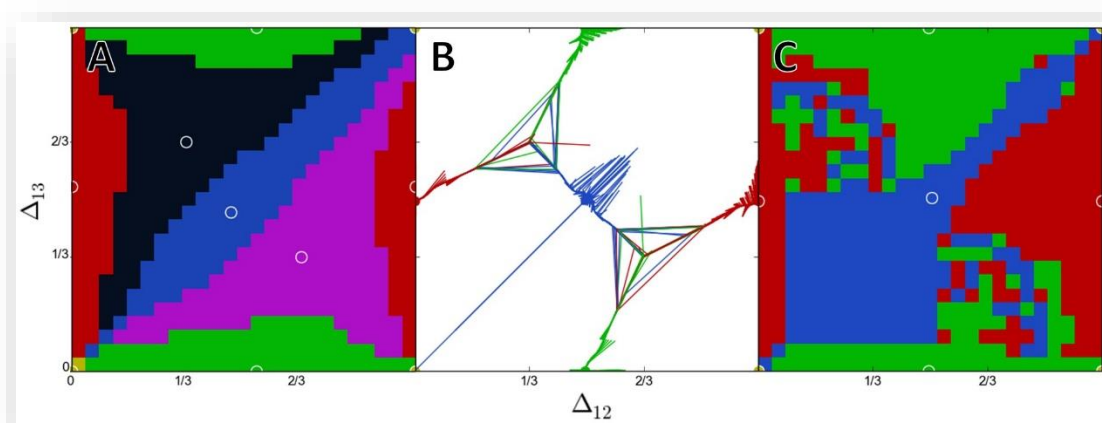


Figure 2.4 Phase-basin methodology for determining basins of attraction

(A) Compared with the $(\Delta_{12}, \Delta_{13})$ -Poincaré map in Figure 2.2A. $(\Delta_{12}, \Delta_{13})$ -Poincaré map of a stronger coupled network at $g_{ij} = 0.0554$ revealing the rapid and jagged convergence (B) to the three remaining phase-locked states corresponding to the red, green and blue FPs, represented as white circles \circ near $(\Delta_{12}, \Delta_{13}) = (0, 1/2)$, $(1/2, 0)$ and $(1/2, 1/2)$, respectively (A and C). Simplified attraction basin diagrams with mixed borders around two unstable fixed points near $(\Delta_{12}, \Delta_{13}) = (1/3, 2/3)$ and $(2/3, 1/3)$ to show network outputs clearly for smooth (A, representing Figure 2.2) and jagged Δ_{12} and Δ_{13} Poincaré maps (C).

the dominant cell for pace-maker regimes, as shown with the blue pacemaker in Figure 2.3, with separate colors chosen to represent traveling waves firing in (1–2–3)– (clockwise, in black) and (1–3–2)– (counter-clockwise, in purple) sequences, also shown in Figure 2.3. At times, particularly when nullclines intersect close to the knee, or when coupling strength is strong, a trace approach to visualize convergence is inadequate. For such cases, a phase basin approach in which initial conditions are color coded by where they ultimately converge can be used instead. This requires a higher mesh grid (50 x 50 or greater) and identifies basins of initial conditions which all converge to the same fixed point without visualization of the trajectory of any individual trace (Figure 2.4). This approach will be used most extensively in our exploration of the post-inhibitory rebound mechanism in Chapter 3, in which much higher coupling strengths are required.

This visualization lends itself well to rapid identification of poly-rhythmic stability. Sequences of these phase difference maps, varying across a selected parameter, can then be used to observe fixed point movement and the emergence, or bifurcation, of fixed points dynamically changing the phase basins observed. We examine in fine detail the nature of some of these bifurcations, with the emergence or disappearance of different traveling waves or pace makers. We also characterize individual phase basin diagrams for given parameter sets as containing only pacemakers (PM), a mixture of pacemakers and traveling waves, or only traveling waves (TW). When discussing detailed analysis of specific bifurcations, we will pay attention to the pacemakers or traveling waves involved. We classify any number of pacemakers generically as PM. We do not in general distinguish between specific pacemakers or pacemaker combinations in our broader examinations of dynamical characteristics, particularly in asymmetric systems. The same simplification will be made when identifying TW regimes and mixed regimes, without distinguishing between the total number of fixed points in a given phase basin. This classification allows us to connect regions of

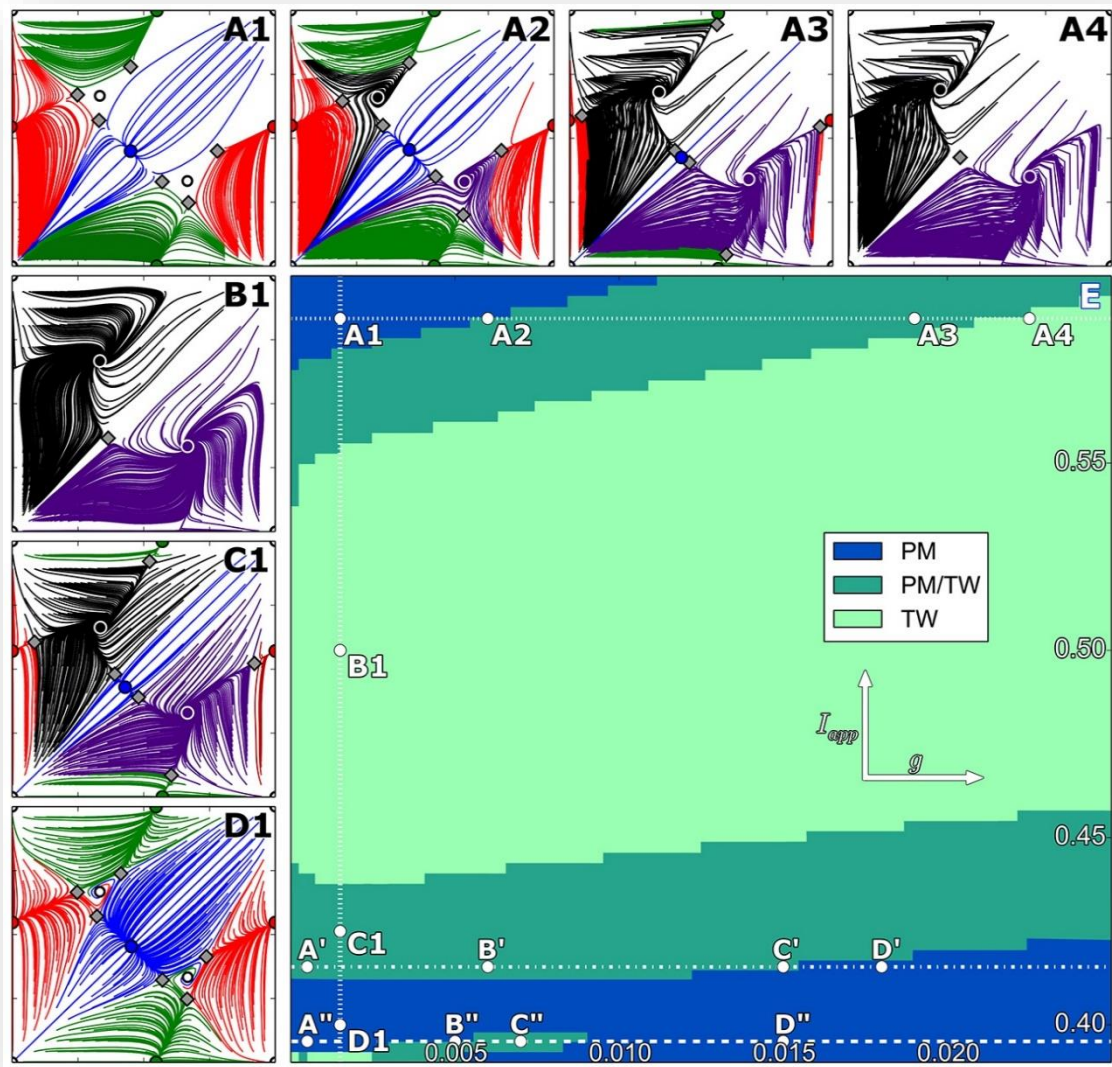


Figure 2.5 Phase-basin methodology for determining basins of attraction

Panel E represents the (g_{ij}, I_{app}) -bifurcation diagram with color-coded regions corresponding to rhythmic patterns of the fully symmetric motif: blue for PM, light green for TW and dark green for mixed PM and TW. Panels A1-A4 and A1-D1 are snapshots of the Poincaré return maps taken at the locations indicated by white dots along two parametric pathways in panel (E). (A1-A4) A series of the $(\Delta_{12}, \Delta_{13})$ -phase lag maps to reveal the capacity and bifurcations of rhythmic outcomes in the network due to the escape mechanism. As coupling g is increased (along the white barred pathway at the top of Panel E), (A1) both unstable TWs at $(1/3, 2/3)$ and $(2/3, 1/3)$ become stable (A2) through a torus bifurcation. All stable PMs, green at $(0, 1/2)$, red at $(1/2, 0)$ and blue at $(1/2, 1/2)$, becomes unstable through pitchfork bifurcations at larger values of g after merging with nearby saddles. Bifurcations in the network with the underlying release mechanism along two bottom pathways (labeled with either ' or ') are represented in Figures 2.7 and 2.8. Parameters for A1-A4: $I_{app} = 0.5886$, $g_{ij} = 0.0015, 0.006, 0.019$, and 0.0225 ; parameters for B1-D1: $g_{ij} = 0.0015$, $I_{app} = 0.493, 0.419$, and 0.393 .

varying intrinsic mechanisms by describing fixed point outcomes in summary in a bifurcation diagram, using classification as PM, TW, or PM/TW as described above. This approach can be observed directly in (Figures 2.5), where we first show samples of 4 different plots distributed either across g_{ij} (in panels A1-A4) or down I_{app} (in panels A1-D1). Observation of the rhythm patterns present in each of these 7 images makes clear the representation in E, in which we have overlaid those points on a bifurcation diagram and use a new coding scheme for the different rhythm combinations observed (additional example in Appendix A1).

Using bi-parametric sweeping, we examine this bifurcation which frames the release and escape mechanism neighborhoods in the (g_{ij}, I_{app}) -parameter plane, for our default parameter set with all-to-all equivalent inhibitory connections. The diagram reveals network rhythm groups about and between the two mechanistic regions of interest, which spans a range of network cells with highly varied duty cycles and firing frequencies. The range connects endogenous bursting cells whose periodicity is set by inhibition to tonic spikers that are induced to bursting behavior through inhibition. This analysis, performing bi-parametric sweeps of at least 50x50 of the previously described phase lag grids, is facilitated using Graphical Processing Units (GPUs) provided by NVIDIA (developed for garage science processing). This vastly reduces the computational time required to run the waveform traces we analyze, time required to produce each phase lag convergence plot for 900 traces typically taking 40-60 seconds instead of 5-10 minutes or more. Bifurcation diagrams created in this manner can then be used to effectively analyze changes within the gFN network.

We examined and verified outcomes observed in prior work, [39] for example, for the effect of shifts from fast-fast to fast-slow systems varying the parameter ϵ . We found in multiple cases that

small variations in ε did not change the network output qualitatively and this was not explored further. For the purposes of this research we have chosen not to significantly explore shifts in the slow-nullcline, as shifts to the fast nullcline directly represent applied currents that may be more readily manipulated in biological systems. In addition to nullcline shifting, via varying the I_{app} parameter, we also generalize our findings in terms of increasing coupling strength. This generalization applies to all-to-all equivalent networks of inhibitory connections networks (shown in previous figures) and to several key connection motifs that deviate from the all equivalent case which are described in detail in Chapter 3.

2.2 Symmetric Motif Results

Cells involved in the release mechanism are intrinsic bursters or spikers and will fire readily without external input. This mechanism involves intersection of the nullclines at or near the lower left portion of the cubic nullcline near the knee (Figure 2.6(A)), where a cell receiving inhibition can be effectively locked down in the hyperpolarized state until released from inhibition. Cells involved in escape are tonic spikers, bursting behavior only inducible via external input. This mechanism occurs when the nullclines intersect near the upper right knee of the cubic nullcline (Figure 2.6(B)). The position of the nullcline intersection in either case can make the system responsive to small magnitude inhibition between the cells, where a small perturbation can force the system to switch states, and we use small coupling strengths in most cases as a result.

The release mechanism occurs when neurons in the active state, or upper branch of the cubic nullcline, stop firing of their own accord and drop to the lower branch. This releases an inactive cell on the lower branch from inhibition, the effect of this being movement of the cubic or fast nullcline back to the right (solid purple line), restoring intrinsic activity by shifting the nullcline intersection from the a stable fixed point on the lower branch to an unstable oscillatory point on

the middle branch of the cubic nullcline (square symbol). As soon as this synaptic inhibition is removed, the inactive neuron passes the spiking or bursting voltage threshold and starts spiking or bursting (black dotted trajectory shows this limit cycle).

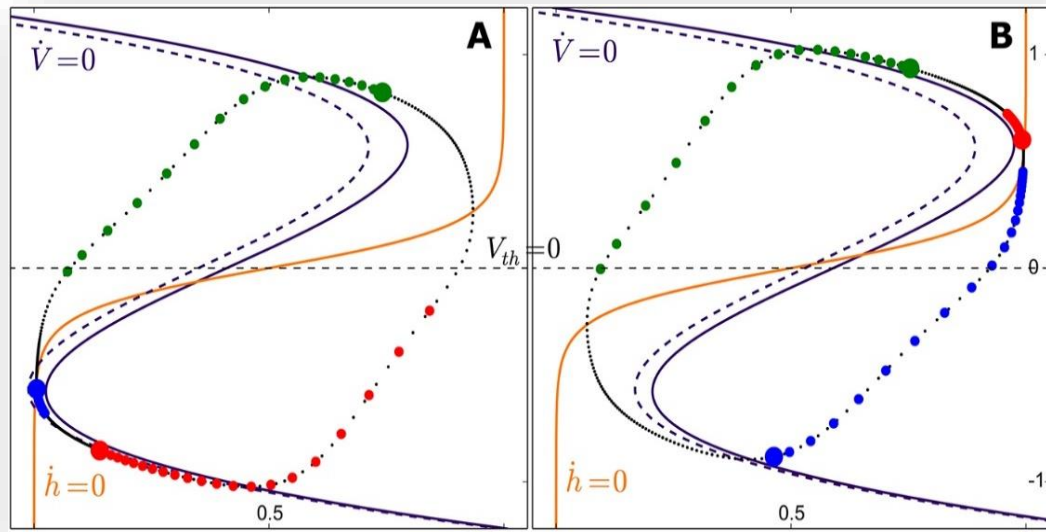


Figure 2.6 Release and escape mechanism state spaces

Phase portraits of the release (A) and escape (B) mechanisms of rhythmogenesis in the neural motif. Clusters of the dots, representing the phases of the coupled cells on the periodic orbit, at the lower-left and upper-right knees are indicative of stagnation due to bottlenecking near the tangency of the nullclines, fast cubic $\dot{V} = 0$, $V = 0$ (solid and dashed purple curves for pre- and post-synaptic cells), and slow sigmoidal $\dot{h} = 0$, (orange curve) (see also Figure 2.1(B)).

All three cells in the network act on this same cubic-sigmoidal intersection, with inhibition of one or more active cells shifting the respective cubic left (dashed purple line) and creating a stable inactive fixed point. Release from inhibition restores the bursting limit cycle (black orbit) for a given cell. Escape refers to the case where the slow nullcline intersects the upper branch, representing active voltage, of the fast nullcline and produces a stable equilibrium state. In this case, once a connected inactive cell passes threshold and begins firing it applies inhibition to the currently active cell. This allows the otherwise tonic firing cell to escape from the active state and

return to the lower branch of the cubic nullcline. The same color scheme is used to represent the nullcline shift and intersection points as in the release example. Manipulation of applied current stimulus allows us to connect the release and escape regimes as we transition from lower to higher values of I_{app} . Because of this, we discuss these two mechanisms together here and in Chapter 3 as we explore different connectivity motifs. This ability to span behavior between the two mechanisms can be represented through the bifurcation diagram approach outlined in methods, and we show here the similarity and differences in the bifurcations that occur and in the dominance of different rhythm outputs within each mechanism.

In fully symmetric 3-cell networks of Fitzhugh-Nagumo inhibitory cells, rhythm regimes follow a somewhat distinct pattern as either coupling strength, g_{ij} , or applied current shift, I_{app} , parameters are varied. Using bifurcation diagrams, as described in the methods section, we analyze these parameter variations. For stable and symmetric release cases furthest from the knee, or the minimum oscillatory intersection of the nullclines, we observe emergence of pacemaker patterns from traveling wave or mixed rhythm systems by either increasing coupling strength or decreasing the current shift. Close to the lower knee, spiking transitions are faster and we therefore see more traveling wave patterns at low coupling strengths, as well as an interesting gain and then loss of traveling waves as coupling increases (Figure 2.7). Shifting the cubic nullcline further from the lower knee, we observe a shift to hard-locking and can observe a similar bifurcation in which systems of traveling wave only patterns do not exist and we see the emergence of pacemaker-only patterns from mixed poly-rhythmic regimes (Figure 2.8).

This bifurcation occurs by increasing inhibitory synaptic strength, g_{ij} , or decreasing the current shift, I_{app} . It is important to note the effect of strong coupling strength, in which the system hard-locks and transitions to final fixed points occur much more quickly. If exploration of these strong

coupling regimes were of interest, we would use the phase basin representation discussed previously, but for this research we will primarily look at weak coupling within the release and escape mechanisms and visualization of trace convergence remains practical. An example within the escape mechanism for fully symmetric systems was already demonstrated within the methods

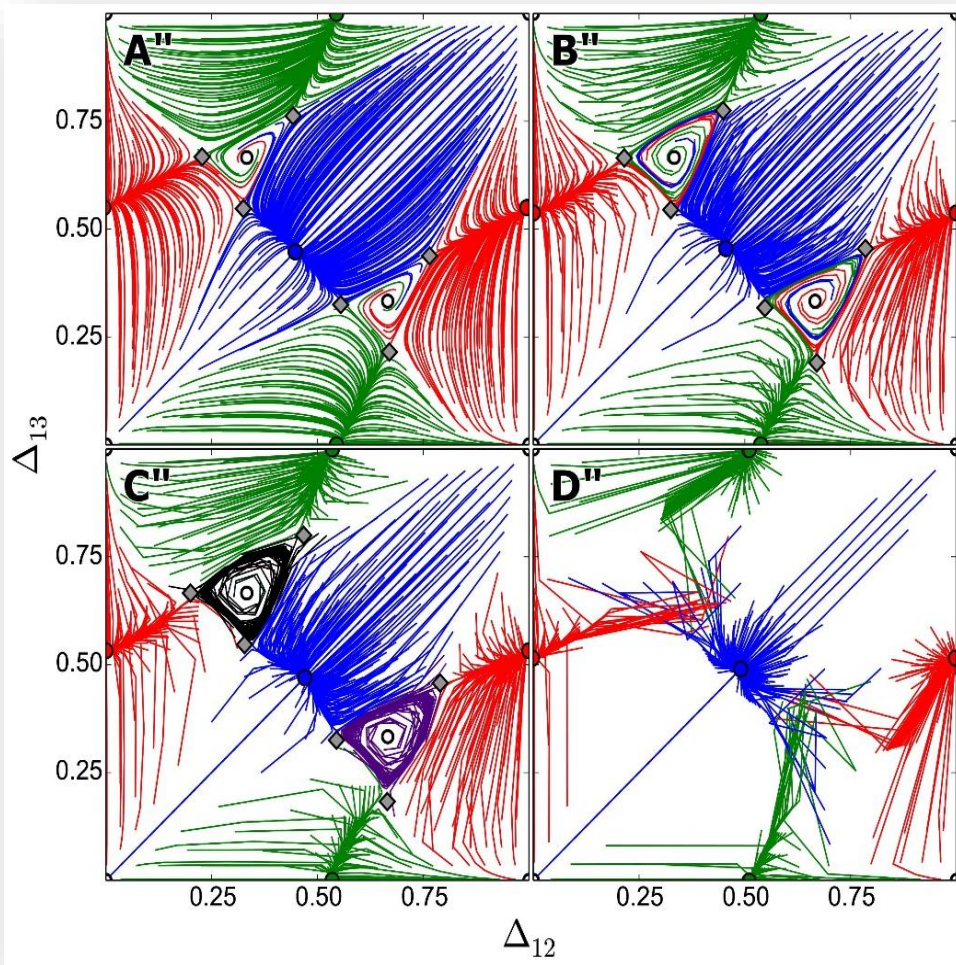


Figure 2.7 Symmetric release case near-knee

$(\Delta_{12}, \Delta_{13})$ -Poincaré return maps representing the symmetric release motifs as all connection strengths are increased. These maps are sampled along the horizontal pathway at $I_{app} = 0.3956$ in the (g_{ij}, I_{app}) -bifurcation diagram in Figure 2.4, and indicated there by labels with an “. The unstable TWs [near $(\Delta_{12}, \Delta_{13}) = (1/3, 2/3)$ and $(2/3, 1/3)$] in (A”-B”) panels, become stable through a secondary Andronov-Hopf/torus bifurcation in (C”), and back to unstable with a stronger synaptic strength resulting in the quick and jagged convergence to three PMs in the map (D”). Parameters: $g_{ij} = 0.0005, 0.005, 0.007$, and 0.015 .

section of this work, and we observe that transitions within this region move in the opposite direction. Where increasing coupling strength within the release mechanism cells tends to lead to less traveling wave, and more pacemaker, behaviors, the escape mechanism is characterized by transitions exhibiting less pacemaker and more traveling wave rhythms at higher coupling

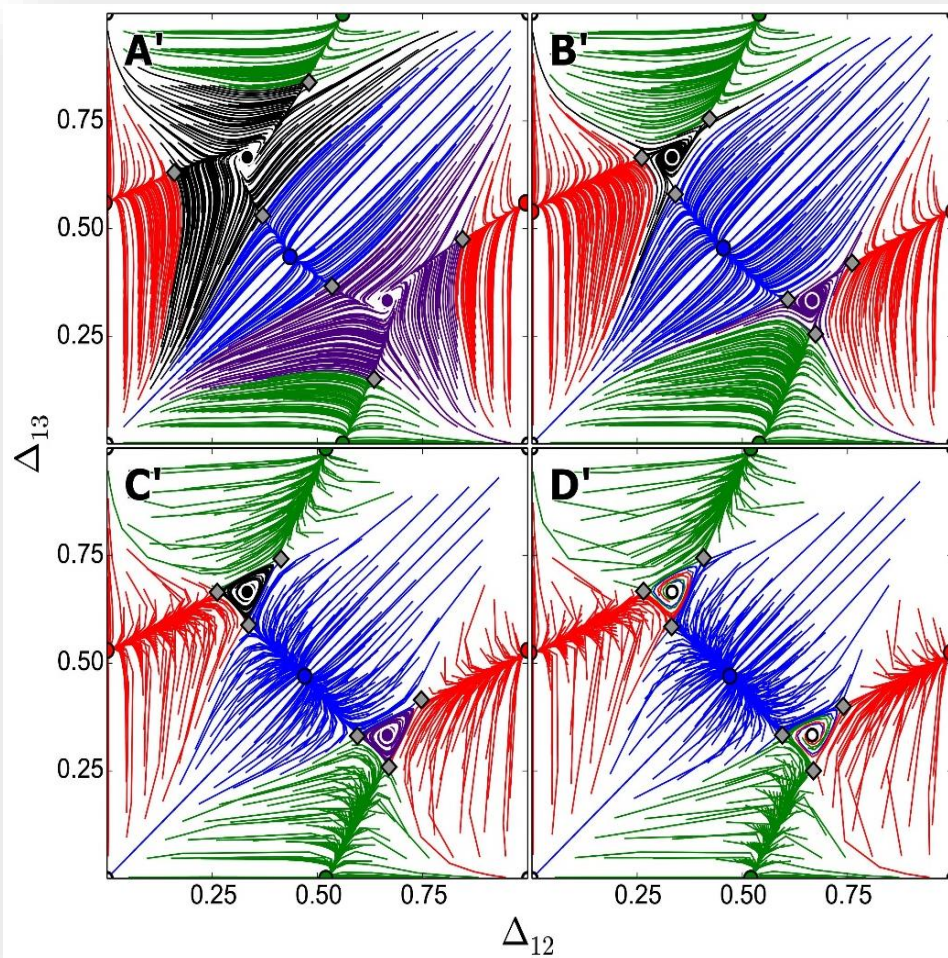


Figure 2.8 Symmetric release stereotypical case

$(\Delta_{12}, \Delta_{13})$ -Poincaré return maps to reveal the capacity and bifurcations of rhythmic outcomes in the symmetric, release-based motif as all connection strengths are increased [along the horizontal pathway at $I_{app} = 0.4155$ in the (g_{ij}, I_{app}) -bifurcation diagram in Figure 2.4. (A'-C') Increasing g_{ij} makes the separating saddle FPs move close to 2 stable TWs at $(1/3, 2/3)$ and $(2/3, 1/3)$, and away from 3 stable PMs thereby making the TW basins shrink and the PM basins widen. (D') With a further increase of coupling both TWs become unstable through a secondary Andronov-Hopf/torus bifurcation. Parameters: $g_{ij} = 0.0005, 0.006, 0.015, 0.018$.

strengths or lower applied currents. This underlies the importance of understanding within which mechanism a biological system behaves, to make hypotheses leading to practical experiments.

Another aspect explored is the effect of shifts in the fast-slow variable, ε , on possible rhythmic output and bifurcations between such. We have opted to focus primarily on less fast-slow separation using higher epsilon values (0.30 for most of the examples in this paper) but show an example of the effect of more fast-slow separation in Figure 2.9, when the same parameters are used as was done in the Figure 2.7. As can be clearly seen, shifts to more distinctly fast-slow systems with low epsilon values result in much more dominance of traveling wave rhythms. This happens because when depolarization occurs more rapidly, the period is more readily divided by all three cells and pace-making behaviors can only occur if induced by some initial conditions which already place it within this rhythm regime. We will mention more on such fast-slow systems

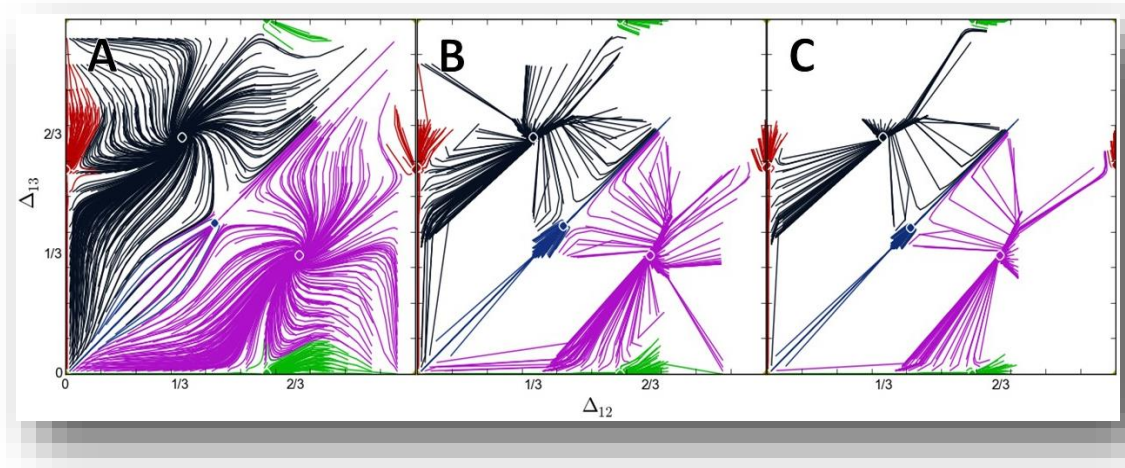


Figure 2.9 Symmetric portraits for strong fast-slow separation

$(\Delta_{12}, \Delta_{13})$ -Poincaré return maps representing the symmetric release motifs as all connection strengths are increased. These maps are sampled along the same horizontal pathway at $I_{app} = 0.3956$ as in Figure 2.8, but with $\varepsilon = 0.05$, and represent shifts from weaker to stronger coupling within the same range of values explored there. The basins of attraction for both TWs [near $(\Delta_{12}, \Delta_{13}) = (1/3, 2/3)$ and $(2/3, 1/3)$] are larger at all values of g_{ij} , and we see much more rapid transition to the fast convergence indicative by jagged traces. PM basins of attraction are significantly reduced, and disappear entirely for a much larger portion of the bifurcation diagram for this system. Parameters: $g_{ij} = 0.002, 0.008, \text{ and } 0.016$.

periodically throughout the paper, but will focus primarily on more mid-range epsilons where broader ranges of rhythms and rhythm transitions can be observed and described. Generalization of results here to more fast-slow systems will recognize the trend towards more travelling wave behaviors at lower values of ε . Varying coupling strength asymmetrically, however, results in a wide range of behaviors and bifurcation transitions otherwise unobserved in fully symmetrical systems. The nature of these bifurcations can be observed with variation of the system parameters, the focus in Chapter 3 being primarily on changes in coupling strength, changing g_{ij} , with comparison of different current shift strengths. These parameter variations remain biologically testable in labs.

3 PATTERN GENERATION IN ASYMMETRIC 3-NODE MOTIFS

As described within the methods in the previous chapter, an extension to the results described for the symmetric three-node motif explored involves examination of several key asymmetric motifs frequently observed in biological networks. Here four key asymmetric circuit structures are examined in detail: (1) Mono-biased, in which only a single connection, here g_{31} , is changed the rest are held constant, (2) Pairwise-biased, in which reciprocal connections between two cells are changed equally, here $g_{31} = g_{13}$, with the rest are held constant, (3) King-of-the-mountain, in which

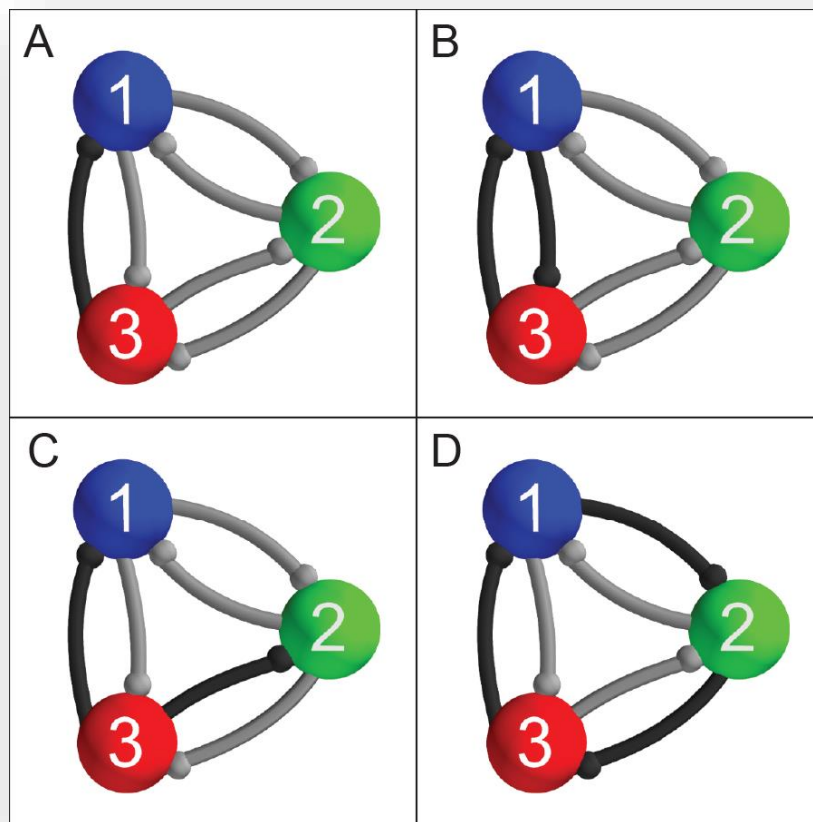


Figure 3.1 Key asymmetric network motifs

Principal configurations of network motifs explored in this paper. (A) Mono-biased motif with a single varying connection, here g_{31} . (B) Pairwise-biased motif with two reciprocally changing connections, here g_{31} and g_{13} . (C) King-of-the-mountain motif of a single cell with two outgoing varying connections, here g_{31} and g_{32} , and (D) Clockwise-biased motif with uni-directionally varying connections, here g_{12} , g_{23} , and g_{31} .

both outgoing connections from one cell are varied identically, here $g_{31} = g_{32}$, while the rest are held constant, and (4) Clockwise-biased, in which all clockwise connections are affected simultaneously, here $g_{12} = g_{23} = g_{31}$, holding the rest constant (Figure 3.1). The default connection strength for each unaffected connection shown is $g_{ij}=0.001$, unless otherwise specified.

3.1.1 *Mono-Biased Motif*

An initial examination of asymmetry compares the effect of increasing or decreasing only one connection (g_{31}) within an otherwise fully-symmetric, weakly-coupled system. As with the symmetric case, the effect of this when very close to the lower knee near intersection of the nullclines will be different from effects when further from the knee, effectively showing a transition from hard- to soft-locking, in which internal dynamics may rapidly drive the network to converge to its final outcomes. Here, and in each of the following asymmetric motifs discussed, we show first an example of transitions within the phase lag return maps as g_{31} is increased within the release mechanism regime of values for I_{app} (Figure 3.2). Following this, an example of transitions observed within the escape mechanism will be discussed, both placed upon a bi-parametric bifurcation diagram spanning g_{31} versus I_{app} . Unlike the fully symmetric case first discussed, here we observe asymmetric bifurcations in which only one or two pacemakers may appear or disappear rather than all pacemakers (or all traveling waves) simultaneously for a given bi-parametric set (g_{31}, I_{app}) .

For the release example shown, we initially start with a motif in which the g_{31} connection is turned off ($g_{31} = 0$) while all others are held constant at $g_{all} = 0.001$. With this connection off, we observe a case in which rhythm generation is dominated by the green PM rhythm for most initial phase lag condition combinations, a small region of blue PM pattern generation seen in the center of the return map (Figure 3.2(A')). Even at zero connectivity we can see the potential for formation of

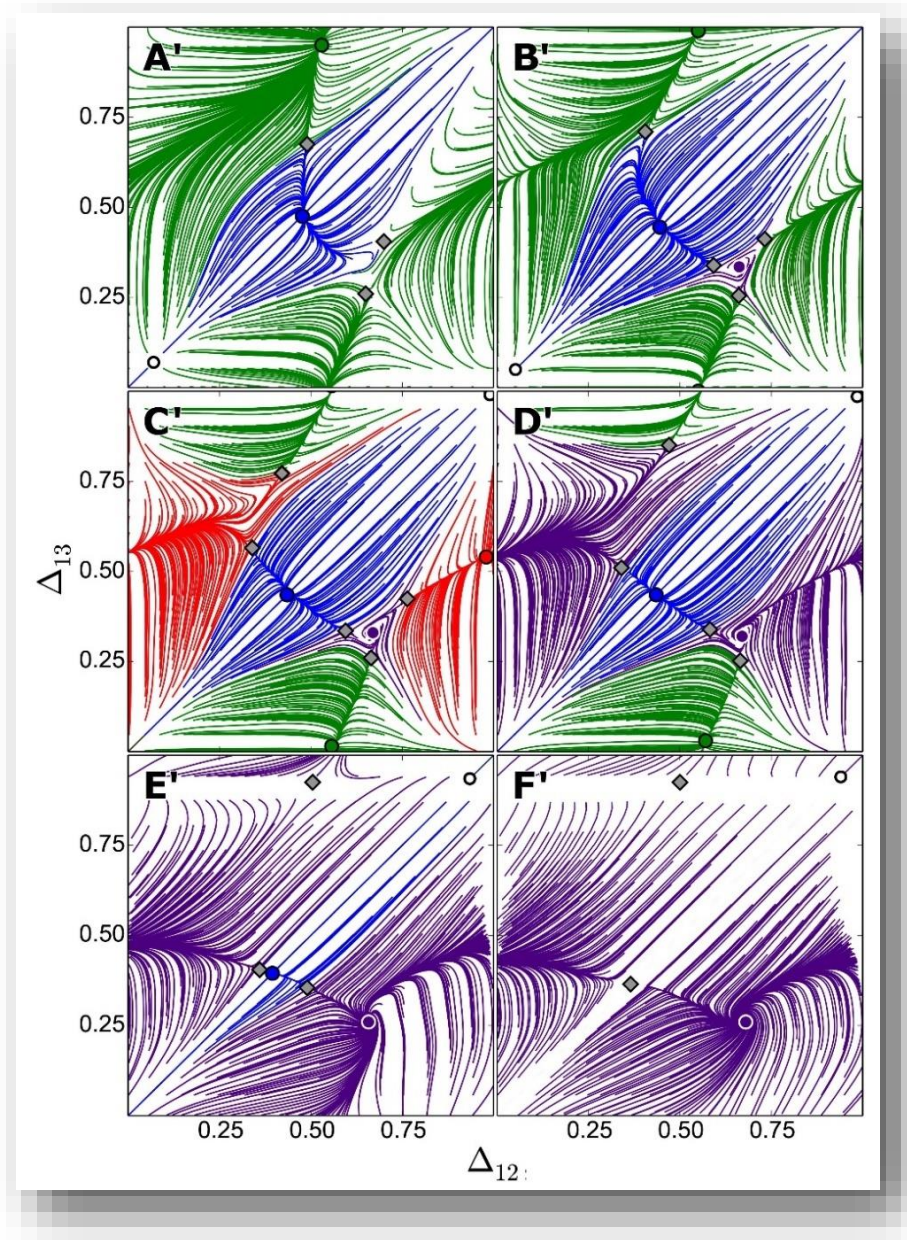


Figure 3.2 Mono-biased asymmetric release case

Evolution stages of the $(\Delta_{12}, \Delta_{13})$ -Poincaré return maps representing the mono-biased (shown in Figure 3.1A) release-based motifs as a single connection g_{31} is increased. These maps are sampled along the horizontal pathway at $I_{app} = 0.412$ in the (g_{31}, I_{app}) -bifurcation diagram in Figure 3.3. The green PM initially dominates, blue coexisting (A'). With increasing g_{31} , a sequence of five saddle-node bifurcations occur. The purple TW emerges [near $(\Delta_{12}, \Delta_{13}) = (2/3, 1/3)$] and the blue PM's basin increases in size (B'). The red PM [near $(0, 1/2)$] emerges (C') and then disappears as its FP collides with the red-to-purple saddle and is consumed within the purple TW's basin of attraction (D'). Increasing g_{31} further leads to winner-take-all by the purple TW, as first the green (E') and then the blue (F') FPs collide with the other saddles. Parameters: $g_{all} = 0.001$ except $g_{31} = 0, 0.00081, 0.00108, 0.00135, 0.004, 0.008$ in Panels A'-F', resp.

an additional pattern near the traditional (0.66, 0.33) location for the purple TW. This can be seen by the interesting whorl around this point with the two saddle nodes (gray diamonds) affecting trace behavior in this region. Connection of the g_{31} synapse leads almost instantly to the emergence of this TW (B'), as we see the appearance of an additional saddle node with the creation of the purple fixed point. A close examination shows additional shifting of the other saddle nodes from the locations observed in (A'). The emergence of the red PM point is much more dramatic, with the appearance of both a saddle node and fixed point that rapidly diverge (C') while consuming large portions of what had been in the green basin of attraction. The presence of this third PM regime is short-lived, however, as the newly created red PM basin is ultimately consumed by the purple TW regime with increasing g_{31} (here at only 1.35 times the magnitude of the rest of the connections). This occurs as the red PM FP collides with the saddle node between it and the purple TW FP (D'). Increasing the strength more significantly (first 4x at 0.004, and then 8x at 0.008, the symmetric connections) leads to the disappearance of first the green PM (E') and then the blue PM (F') as those fixed points collide with other saddle nodes and the purple TW dominates all initial conditions. These transitions can be seen within the context of the larger bifurcation diagram for mono-biased motifs in Figure 3.3.

As can be seen by the dashed line and points representing the transitions of Figure 3.2, these bifurcations are representative for many points along the diagram for different values of I_{app} but other transitions exist where some rhythm pattern combinations may not exist for certain values of I_{app} . We observe that PM behaviors (blue region) occur most at low coupling strengths for both g_{31} and I_{app} , with a brief increase in these rhythms as the nullclines first move further apart around $I_{app} = 0.40$ and then a decline as the system moves to purely TW patterns only for mid-range values of I_{app} between approximately 0.43 and 0.53 (the large light green expanse in the middle of the

bifurcation diagram). Moving further up, however, we observe the first appearance of an as yet unidentified rhythm (sky-blue region) within the escape mechanism for a mono-biased motif that will be discussed here in more detail. A more general shift in rhythm generation behavior is clearly

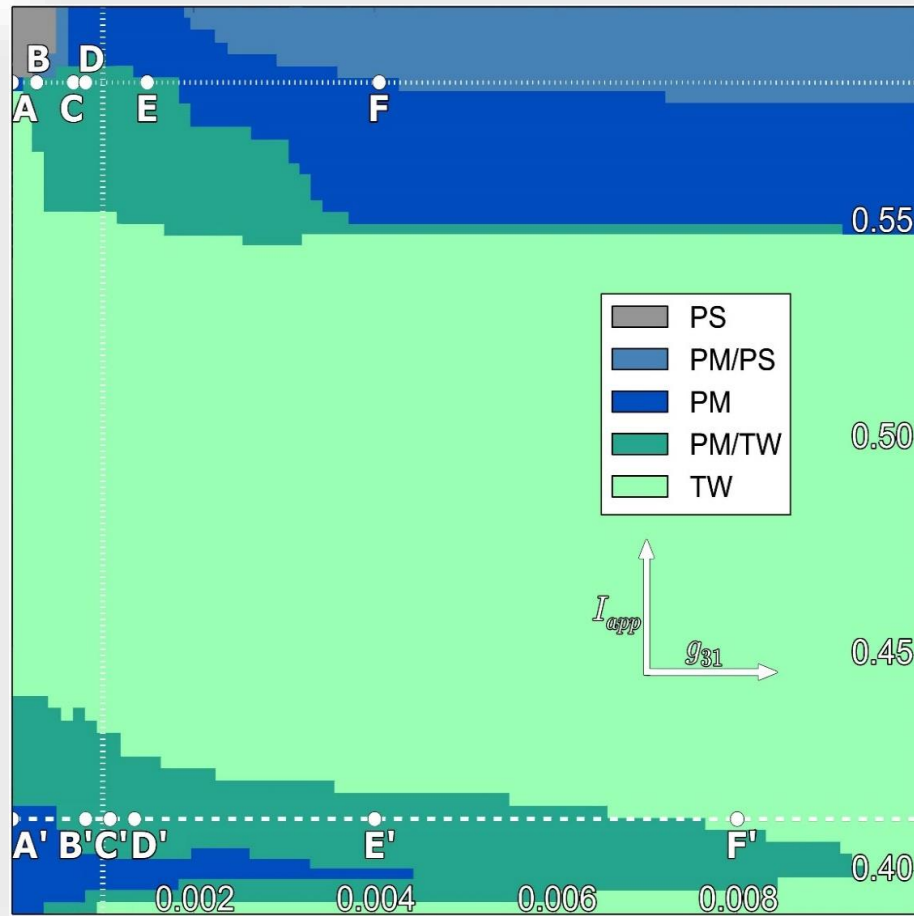


Figure 3.3 Mono-biased asymmetric bifurcation diagram

The (g_{31}, I_{app}) -bifurcation diagram with seven color coded regions corresponding to the various single and multi-stable rhythmic patterns of the mono-biased motif (Figure 3.1(A)): gray for phase-slip only, light-blue represents co-existence of phase-slip with PM, blue for PM only, dark-green for “mixed” PM and TW, and light-green for TW only patterns. Transitions between these regions are due to saddle-node (SN) bifurcations eliminating or restoring FPs to the map. The horizontal white-barred pathway near the top of the bifurcation diagram at large values of I_{app} corresponds to the $(\Delta_{12}, \Delta_{13})$ -return maps sampled for the escape case (Figure 3.4). The horizontal white-dashed pathways at the bottom corresponds to transitions due to the release case (Figure 3.2). The vertical line given by $g_{31} = 0.001$ corresponds to the fully symmetric network with all g_{ij} equal g_{31} .

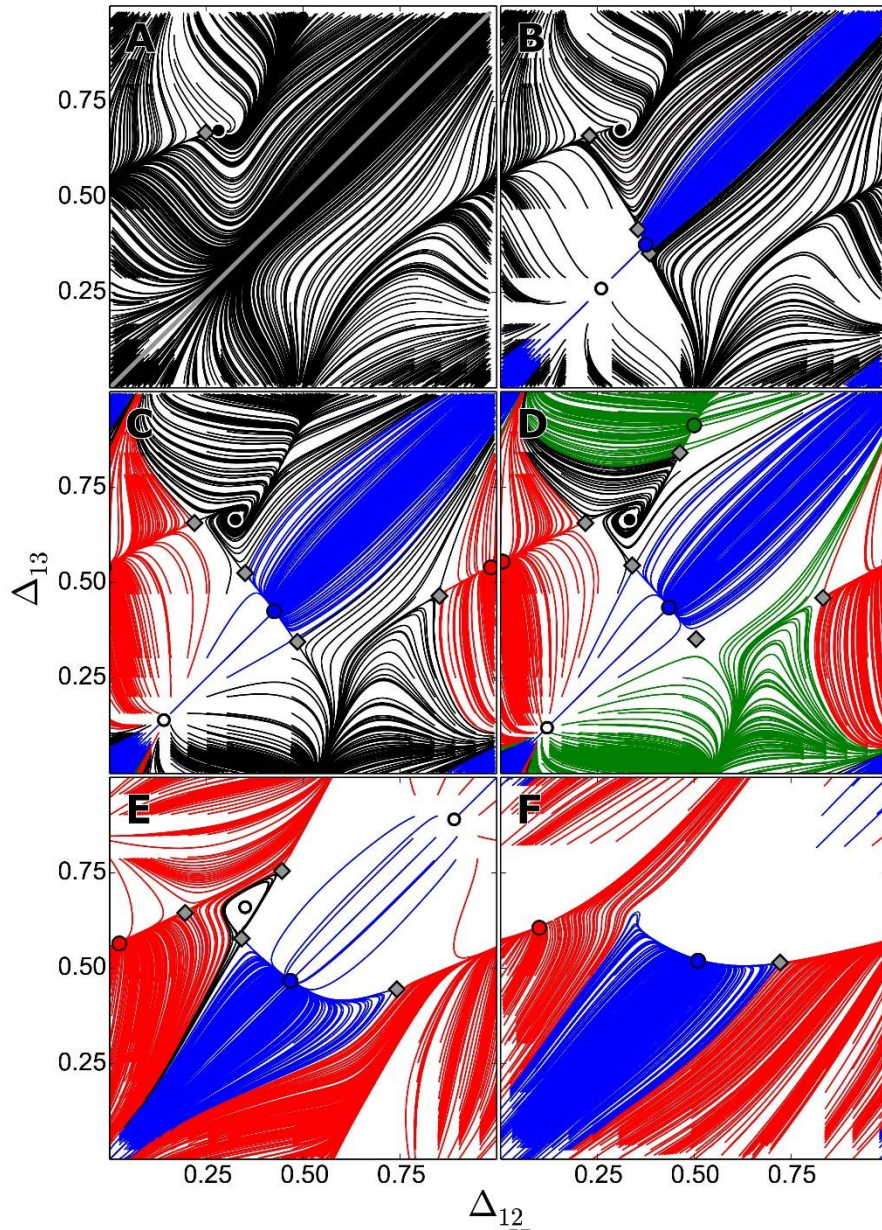


Figure 3.4 Mono-biased asymmetric escape case

Mono-biased escape motif evolving via increasing g_{31} explored by Δ_{21} and Δ_{31} Poincaré return maps. Only the black (clockwise) TW exists when $g_{31}=0$ (A). With increasing synaptic strength g_{31} pitchfork bifurcations occur with the appearance of the blue PM (B), red PM (C), and green PM (D). With even greater g_{31} synapse strength a torus bifurcation occurs while the size of the TW basin of attraction diminishes and the black TW fixed-point becomes a repeller (E), then disappears as the saddles converge with the black repeller (F). An invariant circle is seen near the wave region in Panel E. Parameters: $I_{app} = 0.5825$, $g_{ij} = 0.001$ except $g_{31} = 0, 0.00027, 0.000676, 0.00081, 0.00149, \text{ and } 0.00405$.

observed for the escape case, and shown in detail in the panels of Figure 3.4, in which we see the presence of TW patterns more at lower g_{31} coupling strength with the appearance of PM patterns at higher coupling, the opposite of what was observed in the release mechanism regions and example discussed above.

In the example in Figure 3.4, we observe the existence of a single dominant black clockwise TW regime when $g_{31} = 0$ with an interesting region where very close initial conditions can lead to fundamentally different trajectories but ultimately converge to the same fixed point. This occurs for initial conditions on either side of the saddle node point shown in (A) by the gray diamond. Points to the left will converge to, and traverse, the path shown by white arrows overlaying the black basin as they gradually converge to the final fixed point due to weak coupling for the other connections. Points to the right of the saddle node, however, will rapidly converge to the black FP as they are already close and are on the side of the saddle that will push them in this direction. The introduction of even weak g_{31} coupling in (B) leads to the appearance of a small basin of blue PM attraction in the center of the return map as both an FP and a repeller appear, along with two additional corresponding saddle nodes. Continuing to increase g_{31} strength leads not only to increased size of the blue PM basin of attraction, but to the formation of first a red PM (C) and then a green PM (D) as those fixed points and corresponding saddles appear within what had previously been the basin of attraction for the black TW. We therefore see a rapidly diminishing region of black TW attraction, which undergoes an additional torus bifurcation with increased g_{31} coupling, creating a brief range in which an invariant circle appears around a repeller where the black attractor had been (E) before the region is entirely consumed by the red basin of attraction (which first consumed the green PM basin as that saddle node and FP collided). This leads to systems in which only PM, in this case only red or blue, behavior can exist for any set of initial

conditions, with very rapid convergence for many initial conditions (exemplified by larger white regions on the return map, where convergence is so rapid that traces do not appear to traverse these areas). Although here we have emphasized the opposite formation or disappearance of rhythms as was observed within the release mechanism first discussed, we also see the appearance of a new pattern not previously observed. This pattern, and a close-up of the patterns leading up to and after the bifurcation can be seen in the detailed bifurcations in Chapter 4.

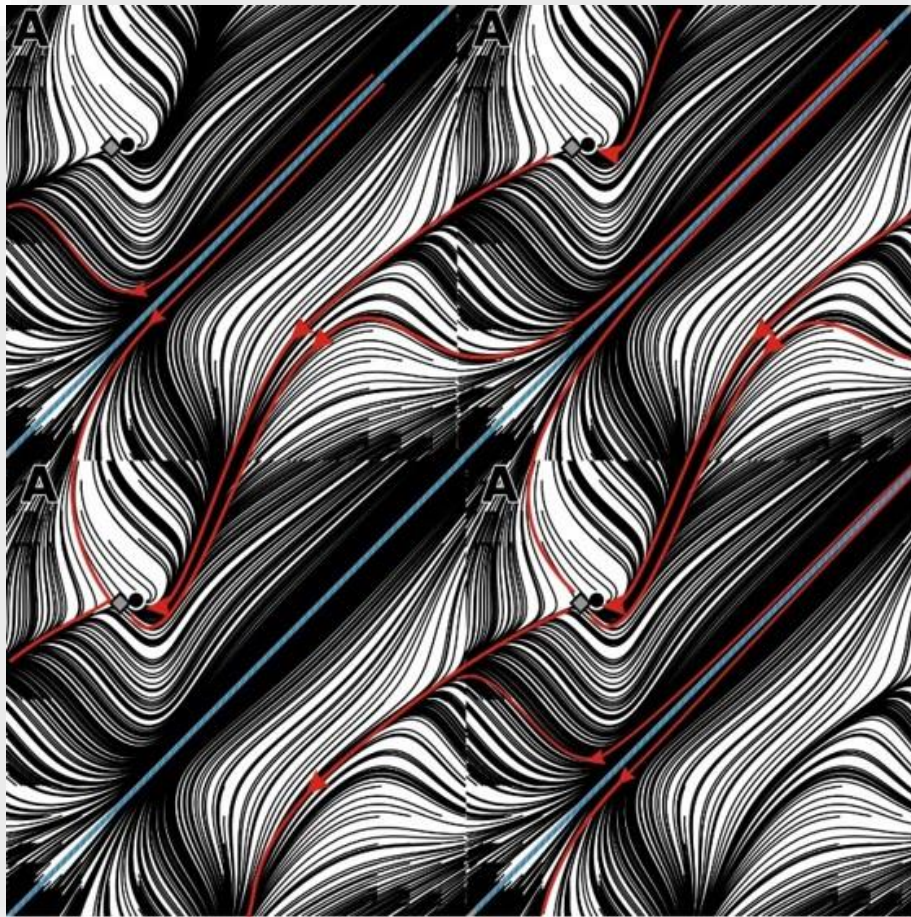


Figure 3.5 Panel multiplicity for convergence determination

Zoomed in view of Figure 3.4(A), with 4 identical panels placed adjacent to aid in visualization and determination of final convergence to the phase-locked black clockwise traveling wave (CTW) pattern. Overlay of arrows facilitates visualization of converging outcomes crossing boundaries of the 2-D return map. Parameters: $I_{app} = 0.5825$, $g_{ij} = 0.001$ except $g_{31} = 0$.

While we have chosen in this paper to specifically discuss the effects of changes to g_{31} , all results here have been examined and hold true for changes in g_{13} as well. The change in direction of the changing connectivity lead to opposite effects in which, for example, any regions in which the red PM (or Cell 3) dominated would now look symmetrically the same but with the blue PM (or Cell 1) dominating. This switch in context holds true for all changes in direction, and therefore all results for the g_{31} analysis are valid and transitive (with appropriate color and pattern perspective shifts) for changes in any other single clockwise or anti-clockwise connection, regardless which two cells the connection is between. We have therefore chosen to focus solely on connections involving cell 3 in this research.

3.1.2 *Pairwise-Biased Motif*

Asymmetry is accomplished in many ways, and while we have primarily focused thus far on an examination of single connection asymmetry within an otherwise symmetric 3-cell configuration, other interesting behaviors and trends can be seen when changing more connections. Other anti-symmetric cases are generated by changing both the g_{31} and g_{13} connections, either in harmony or separately. Changing both connections equally within the release mechanism region of values for I_{app} , we initially observe a system in which both connections are turned off and a single (green) PM dominates (Figure 3.6(A')). This makes sense intuitively since the green cell is the only one with outgoing inhibitory connections to both of the other cells. When we introduce weak coupling both ways between nodes 1 and 3, however, we see the emergence of the other two PMs (B'), as additional saddles appear with two repellers. These repellers are then consumed as they collide with saddles at increasing g_{31} and g_{13} strength, the basins of attraction becoming more distinct without the spiraling out regions from where the repellers had been previously. TW behavior is not seen within the release mechanism here, except for values of I_{app} that place the nullclines

extremely close at the lower knee (this can be observed at the very bottom of the bifurcation diagram in Figure 3.8). Additional increases in the coupling strength of the two synapses leads to the collision of the red and blue FPs with nearby saddles creating a so-called ‘river of fixed points’

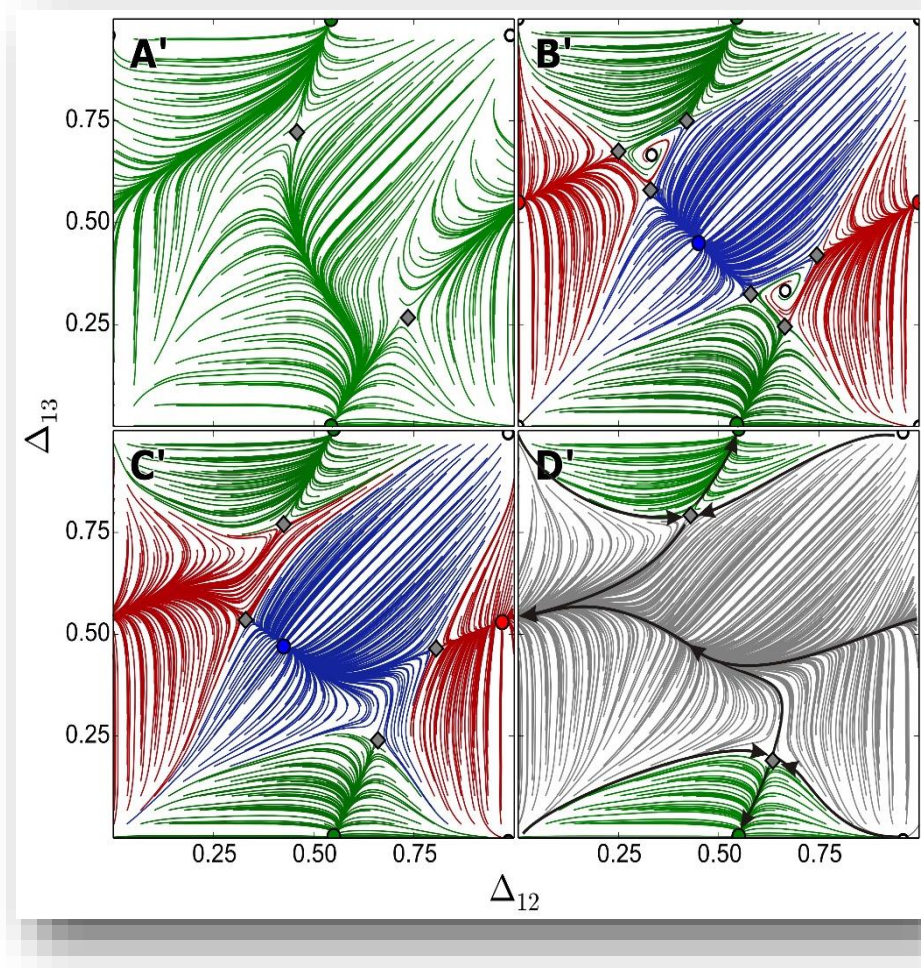


Figure 3.6 Pairwise-biased asymmetric release case

(A') When synapse strengths g_{31} and g_{13} equal zero only the green PM exists. (B') As coupling is increased, the blue and red PMs emerge with two saddles simultaneously, as well as the simultaneous emergence of two repelling FPs near $(\Delta_{12}, \Delta_{13}) = (1/3, 2/3)$ and $(2/3, 1/3)$, along with two saddles, all through SN bifurcations. (C') Further increasing g_{31} and g_{13} gives rise to a reverse SN bifurcation, eliminating these repelling FPs. Moreover, simultaneous loss of the blue and red PMs due to heteroclinic saddle-node bifurcation gives rise to the onset of a stable invariant circle, or gray “river” of slow Δ_{12} -phase slipping with $\Delta_{13} \approx 1/2$, that wraps around the torus. Hand-drawn lines in D' are sampled to illustrate the attraction basin bounded by the incoming separatrices of the saddles. Parameters: $I_{app} = 0.399$, $g_{ij} = 0.001$ except $g_{31} = g_{13} = 0.0005, 0.001, 0.0012, \text{ and } 0.0015$.

in which we observe peristaltic patterns with recurrently phase-varying lags (D'), or phase-slip (PS), with the green PM remaining. Not shown here, but observable on the bifurcation diagram, is the ultimate disappearance of this remaining green FP and the existence of a system of purely recurrent phase-varying lag in which Δ_{13} remains roughly constant with nodes 1 and 3 remaining locked in semi anti-phase, while Δ_{12} decreases constantly with phase slip in which cell 2 experiences a shorter period than the other two cells. As in the example of river behavior in mono-biased asymmetry, these are not true fixed points as we see phase-slipping in a consistent and recurring pattern.

When we change both connections equally within the escape mechanism region for I_{app} , we again initially observe a system in which both connections are turned off and a single (green) PM dominates (Figure 3.7(A)). When we introduce weak coupling both ways between nodes 1 and 3, however, we see the emergence of the other two PMs, followed by a brief period near full symmetry where TW patterns emerge and we see fully mixed regimes (C). Increasing coupling strength for both g_{31} and g_{13} leads to torus bifurcation as the TW patterns then disappear as their FPs collide with saddles. When coupling is strong (E), the green PM basin of attraction continues to shrink and ultimately disappears as its FP is consumed by a saddle and its basin of attraction joins the red one. At very strong coupling, both remaining FPs merge with their respective saddle nodes and we again see a 'river' in which we observe peristaltic patterns with recurrently phase-varying lags (F). In this escape case, however, this phase slip is characterized by increasing Δ_{12} separation in which cell 2 experiences a longer period than the other two cells.

Although we chose to show here examples in which no TW waves existed for the release mechanism, while they did for the escape mechanism, the trend we observed in both the fully symmetric and mono-biased asymmetric systems exhibiting the reverse appearance or loss of PM

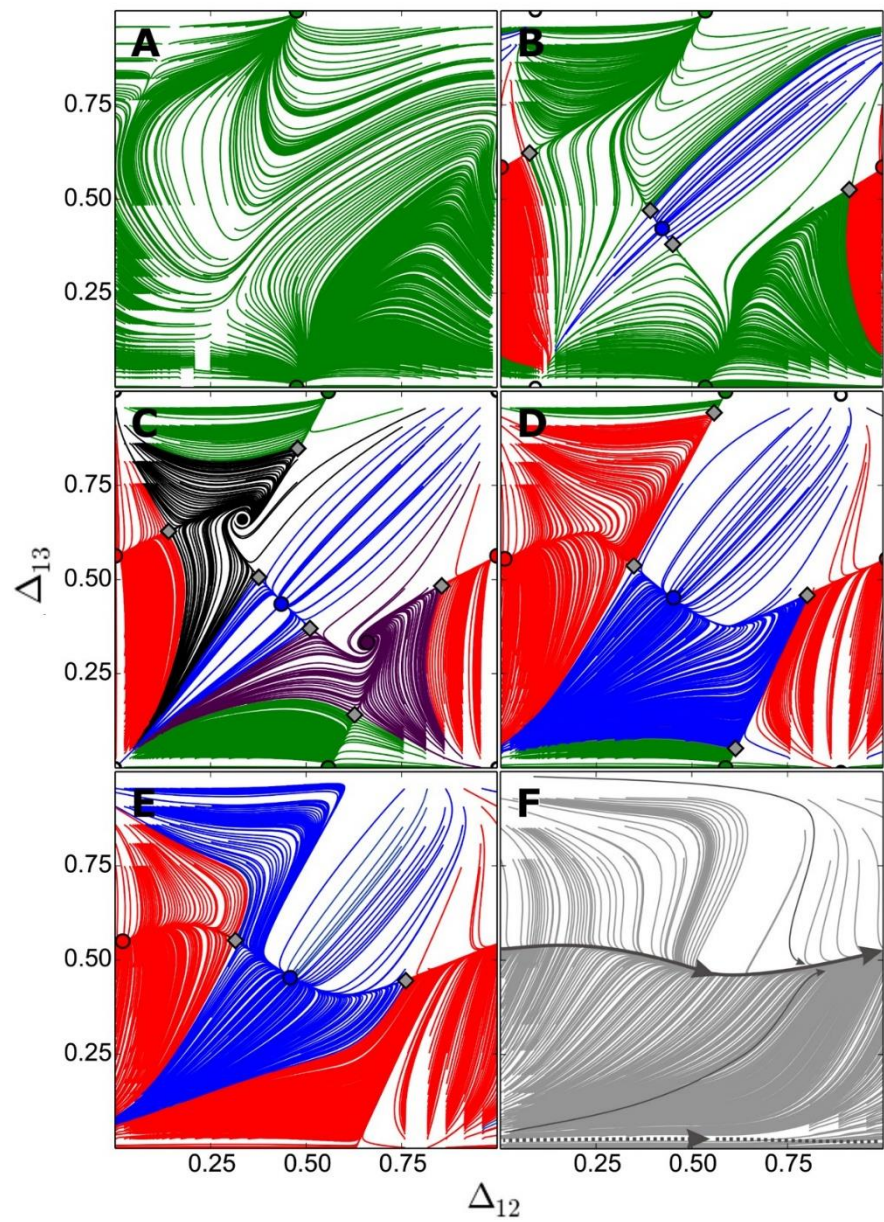


Figure 3.7 Pairwise-biased asymmetric escape case

When synapse strengths g_{31} and g_{13} equal zero only the green PM exists (A). As the pair of synapses g_{31} and g_{13} increase the blue and red PMs emerge through pitch fork bifurcations, (B). With further increases both TWs appear (C), and disappear (D) through SN bifurcations. Next the green PM disappears via additional SN bifurcation, (E). With the largest g_{31} and g_{13} values simulated, all PMs are gone and only a gray traveling river exists through a heteroclinic SN bifurcation. This gray 'river' shows that no stable rhythmic pattern remains, but a rhythm that is constantly changing in time. Parameters: $I_{app} = 0.5716$, $g_{ij} = 0.001$ except $g_{31} = g_{13} = 0, 0.000676, 0.001, 0.00128, 0.00155, \text{ and } 0.00331$.

or TW patterns does not hold for double-biased systems. As can be seen in Figure 3.8, PM patterns dominate low- or no- coupling of g_{31} and g_{13} for all values of I_{app} . Additionally, other than the unique behavior seen regularly very close to the lower knee, TW patterns only exist within the more oscillatory region of values for I_{app} that are not truly release or escape (I_{app} between 0.43 and

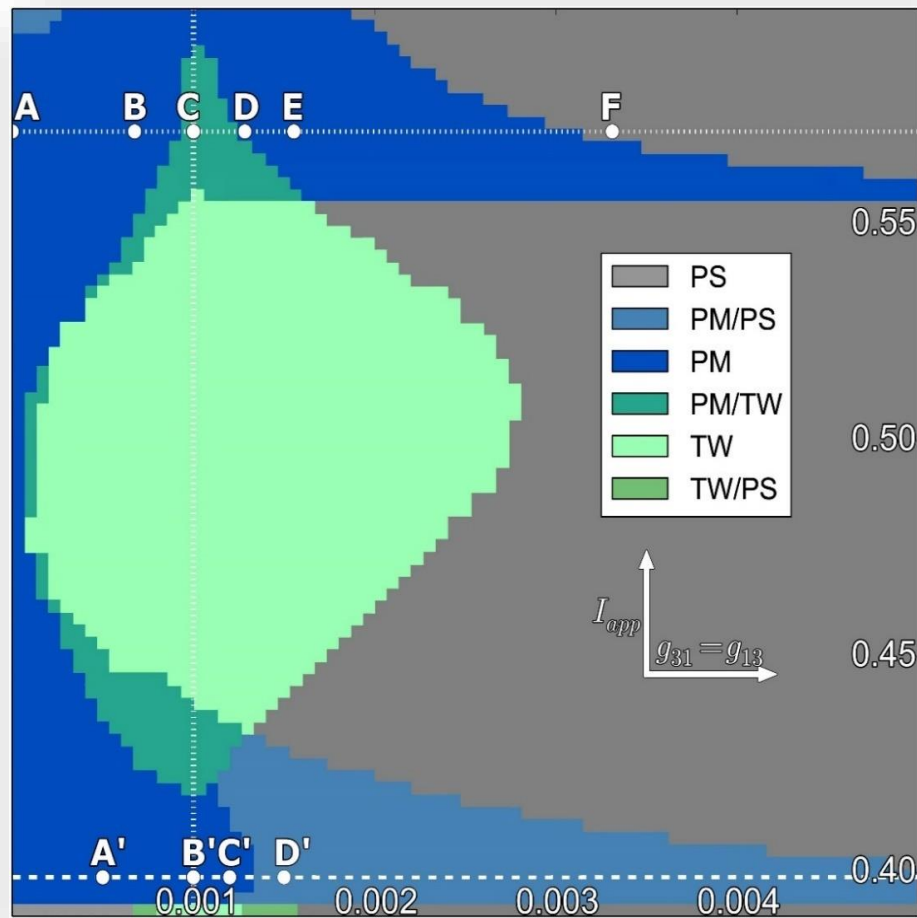


Figure 3.8 Pairwise-biased asymmetric bifurcation diagram

Bifurcations occur between differently colored regions in the bi-parametric space varying I_{app} and $g_{31} = g_{13}$. Light green represents purely TW, blue represents purely PM, dark green represents both types of rhythms, and gray represents purely phase-slip. Transitions between these regions indicate torus or pitchfork bifurcations. Specific examples are shown in Figures 3.6 and 3.7, these examples' values are represented by the points on the dashed and barred lines. The circles on the bottom horizontal line are the parameters sampled in the release case shown in 3.6 as phase difference portraits. And the top horizontal line points are the sampled escape cases in 3.7. The vertical line represents the line where network synapses are at full symmetry, with $g_{31} = g_{13} = g_{ij}$.

0.55). Mixed systems occur most frequently at the boundaries of release and escape mechanisms, and near full symmetry (vertical dashed line). PS behavior is observed at all values of I_{app} when coupling is strong for the asymmetric connections (large grey region on the bifurcation diagram). Double-biased motifs clearly exhibit all potential rhythm patterns identified so far, but do so in a manner that tends towards single pacemaker behavior at weak coupling and river behavior at strong coupling. Other rhythms are transitory and exist primarily within mid-ranges of values for I_{app} or near full symmetry for values of g . The abrupt transitions from TW or PM patterns to river behaviors represent interesting bifurcations in which fixed points and saddles collide to become consumed in different manners. We have shown first, in the mono-biased case, an example of this bifurcation with PMs colliding while one remains. In this double-biased case we have seen the complete elimination of all PM behaviors for a full ‘river’ pattern. In both cases, we have observed semi phase-lock between nodes 1 and 3 with phase slip by node 2. In the following king-of-mountain motif we will observe a different pattern for phase slip.

3.1.3 *King-of-the-Mountain Motif*

When asymmetry is achieved by changing the outgoing connections from one cell, however, we expect that increasing synaptic strength will result invariably in dominance of the cell being strengthened. This king-of-the-mountain case has results that are therefore intuitive at higher coupling strengths. We observe, however, interesting dynamics at weak coupling strengths, where we again see pacemaker dominance that can possibly transition through mixed or traveling wave regimes at higher current shifts. When closer to the lower knee, we see almost exclusive pacemaker behavior which merely transitions from two to three, and then to one, pacemakers. Further from the knee, as can be seen in the bifurcation diagram later in this paper (Figure 3.11), we observe transition through traveling wave regimes at intermediate coupling strengths near full symmetry.

This region of traveling wave dominance grows as I_{app} increases and we begin to span the gap between the release and escape mechanisms.

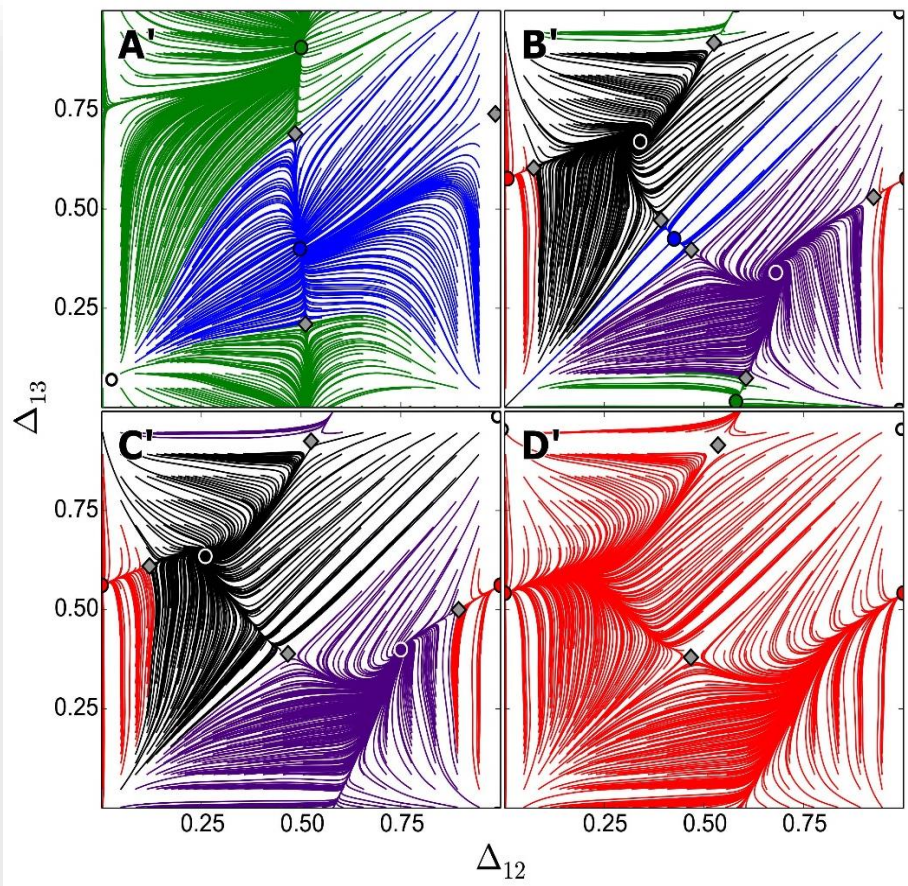


Figure 3.9 King-of-the-mountain asymmetric release case

When synapse strengths g_{31} and g_{32} are very small only the green and blue PMs exist (A'). As the synapse strengths g_{31} and g_{32} are increased the TWs and the red PM emerge. The TWs basins of attraction cover most the network phase difference space while the three PMs have small and relatively equal areas of basins of attractions (B'). With further increases of synapse strengths g_{31} and g_{32} the blue and green PMs begin to merge with saddles and the TWs begin to incorporate the PM basin areas (C'). With the strongest synapse strengths g_{31} and g_{32} modeled, both TWs disappear and the red PM takes all network state space (D'). Parameters: $I_{app} = 0.426$, $g_{ij} = 0.001$ except $g_{31} = g_{32} = 0.0001, 0.001, 0.00115, \text{ and } 0.0015$.

In the example shown here for the release mechanism (Figure 3.9), we observe the presence of both blue and green PMs at weak outgoing g_{31} and g_{32} connections from cell 3. With increased

coupling strength for these connections, we observe the simultaneous emergence of both TW patterns (B') near full symmetry as the basins of attraction for the PMs diminish. As the connections continue to strengthen, the green and blue PM basins continue to shrink and ultimately disappear as their FPs merge with saddle nodes. At strong coupling, the traveling waves also collapse as they merge with the saddle nodes being shared with the red PM. This leads to our king-of-the-mountain in which the red PM dominates rhythm output for all initial conditions.

Within the escape mechanism region, we again observe a new behavior in which 'river' like patterns exist now at low or no coupling connections leaving cell 3. When both g_{31} and g_{32} are at or near zero (Figure 3.10(A)), we observe recurring phase lag variance in which phase separation between cells 1 and 2 is now semi locked in anti-phase while cell 3 exhibits phase slip and undergoes shorter firing period than the other two cells. With even weak connection of these two connections, we observe the appearance of a small basin of attraction for the red PM. This continues to grow, as we also see both other PMs and the two TWs appear, again near full symmetry. With increasing coupling strength, the same loss of first the green and blue PMs and this time forming a temporary river, however, as a river of so called fixed points passes through the locations where the previous green, purple, blue, and black FPs had been (in that order, moving up the figure from the bottom in panel E). This behavior would appear to be random at first glance to an experimenter in a lab setting, and indicates the potential need for longer observation periods or other measures for pattern determination if one is not to miss the existence of larger macro patterns of recurrent behavior that would not be visible with a cursory examination of firing traces alone. Finally, at strong coupling, we again see the king of the mountain appear as the red PM basin of attraction dominates the entire initial condition set.

An examination of the entire bifurcation diagram (Figure 3.11) indicates consistency in this king

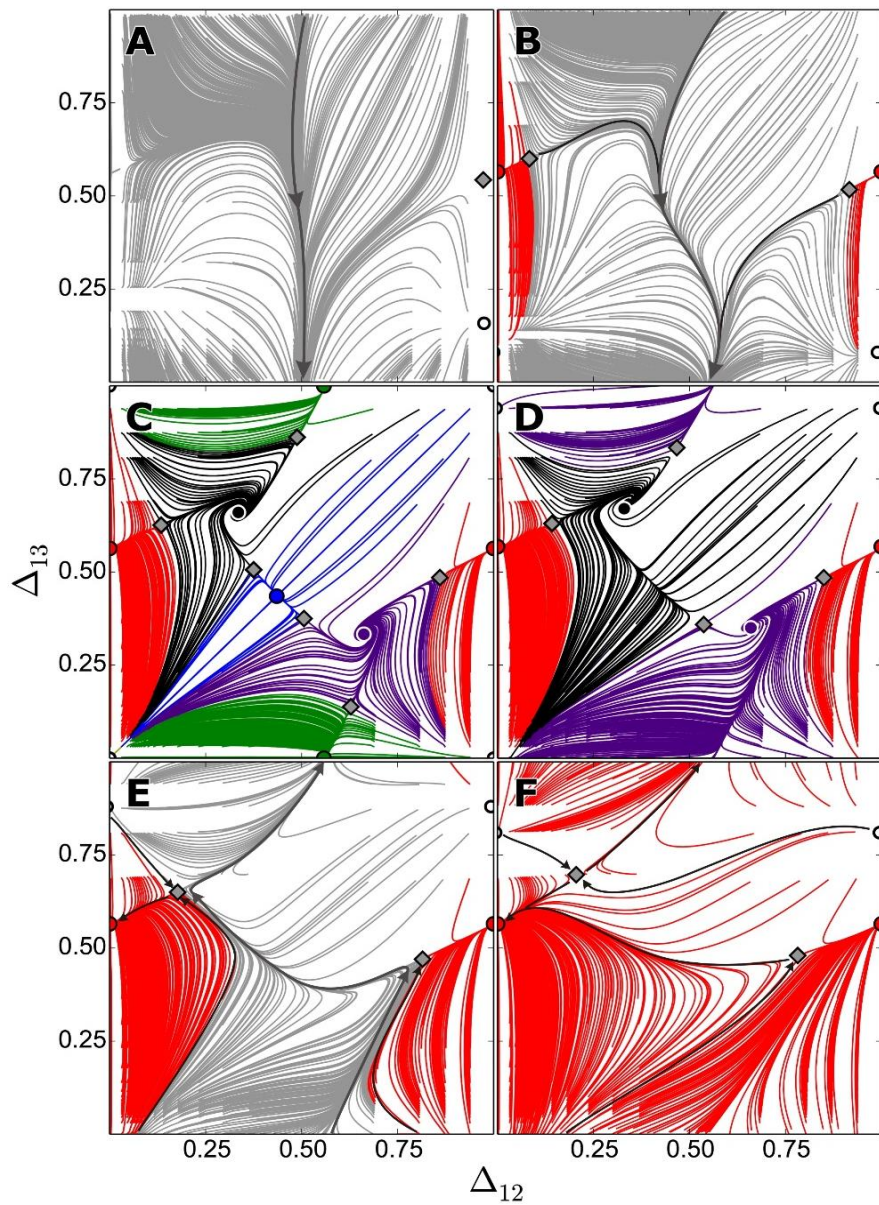


Figure 3.10 King-of-the-mountain asymmetric escape case

When synapse strengths g_{31} and g_{32} are very small only a grey river (slipping phase difference) exists (A). With increasing g_{31} and g_{32} synapse strengths the red PM emerges with a small basin of attraction area (B). With further increasing g_{31} and g_{32} synapse strengths a symmetric system with all TWs and PMs having nearly equal basins occurs (C). As the g_{31} and g_{32} synapse strengths continue to increase, the green and blue PMs disappear as they merge with saddle nodes (D). With further increase, the TWs bifurcate and disappear, replaced by a river, and only the red PM also remains (E). With the strongest coupling simulated, the river bifurcates and only the red PM remains (F). Parameters: $I_{app} = 0.57$, $g_{ij} = 0.001$ except $g_{31} = g_{32} = 0.00001, 0.00065, 0.001, 0.0011, 0.00136$, and 0.0025 .

of the mountain behavior and the ability of the red PM to fully dominate all ICs for nearly all values of I_{app} when the outgoing connections from cell 3 are sufficiently strongly inhibitory. At low connection strengths, we observe dominance of the other two PMs for low values of I_{app} within the release mechanism range, but an almost immediate shift to river behavior with semi phase-lock

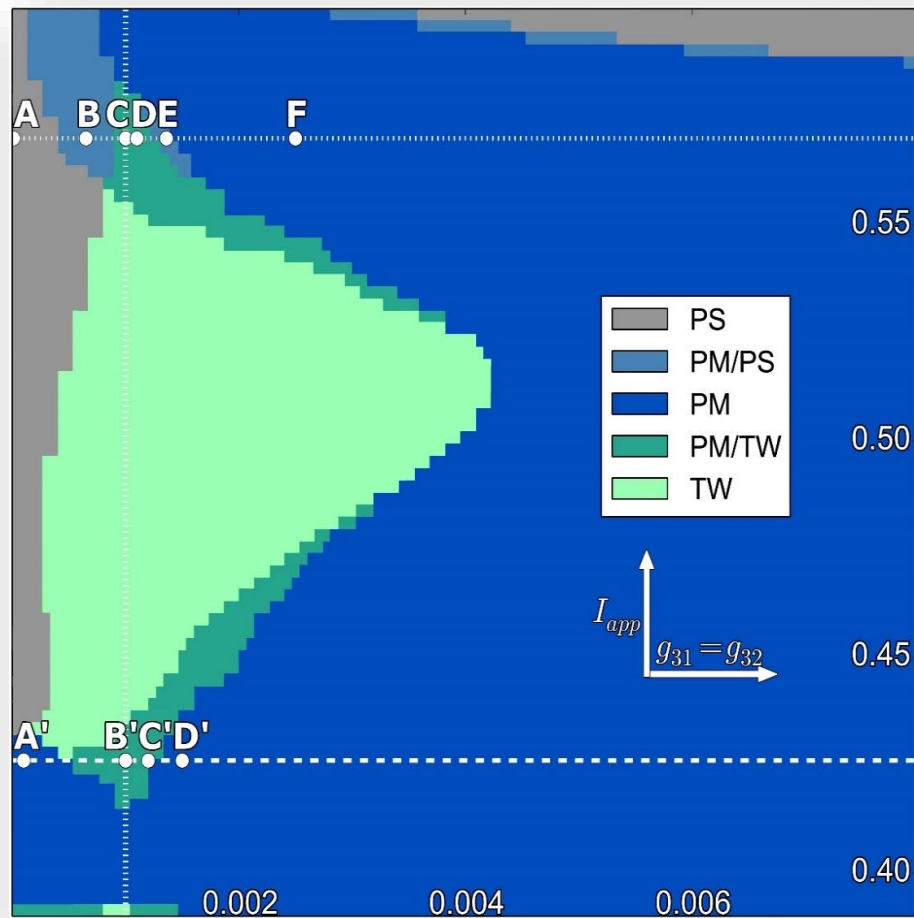


Figure 3.11 King-of-the-mountain bifurcation diagram

Bifurcations occurring in the bi-parametric space varying I_{app} and $g_{31} = g_{32}$. Light green represents purely TW, blue represents purely PM, dark green represents both PM and TW rhythms, gray represents purely phase-slip and grey blue is both phase-slip and PM. Transitions between these regions indicate torus or pitchfork bifurcations. Specific examples are shown in Figures 3.9 and 3.10, these examples' values are represented by the points on the dashed and barred lines. The circles on the bottom horizontal line are the release case samples shown in Figure 3.9 as phase difference portraits. And the top horizontal line circles are the sampled escape cases in 3.10. The vertical line represents the point where network synapses are fully symmetry, $g_{31} = g_{32} = g_{ij}$.

between nodes 1 and 2 for all other values of I_{app} . This river behavior is tempered somewhat with weak to symmetric coupling, in which we may observe the emergence of other PM or TW patterns as the system passes through full symmetry. These patterns are invariably lost, however, as the red basin of attraction gains dominance in most cases with strong g_{31} and g_{32} coupling. One interesting exception exists however, nearest the upper right knee of the cubic nullcline as high values of I_{app} position the nullclines in proximity to this region. We observe cases nearest the knee, for particularly high I_{app} values, in which river-like behavior may again occur even to the exclusion of the king-of-the-mountain red PM.

3.1.4 Clockwise-Biased Motifs

The final fixed asymmetric case examined is the clockwise case, in which we strengthen all clockwise connections (g_{12} , g_{23} , and g_{31}) simultaneously. The intuitive expectation, that this will result in traveling wave dominance at either end of the coupling strength spectrum explored, is precisely observed. Of note, however, is the way in which the transition from counterclockwise to clockwise traveling wave dominance occurs as it typically passes through a regime in which all five fixed points exist for both release and escape mechanisms (Figure 3.13). This can be seen in the release example shown (Figure 3.12), in which we first observe the simultaneous emergence of all three pacemakers (1 to 4 FP transition) at a critical coupling strength value (B'), followed quickly by the disappearance of the black clockwise TW pattern as its FP turns into a repellor. We then observe the mirror of this, in which there is a 3 to 4 fixed point transition (D'), as the counterclockwise TW disappears with increased clockwise coupling strengths, and then the simultaneous disappearance of all three pacemakers (E') and dominance of the counterclockwise traveling wave. At very strong coupling we see the return map approach showing trajectories begin

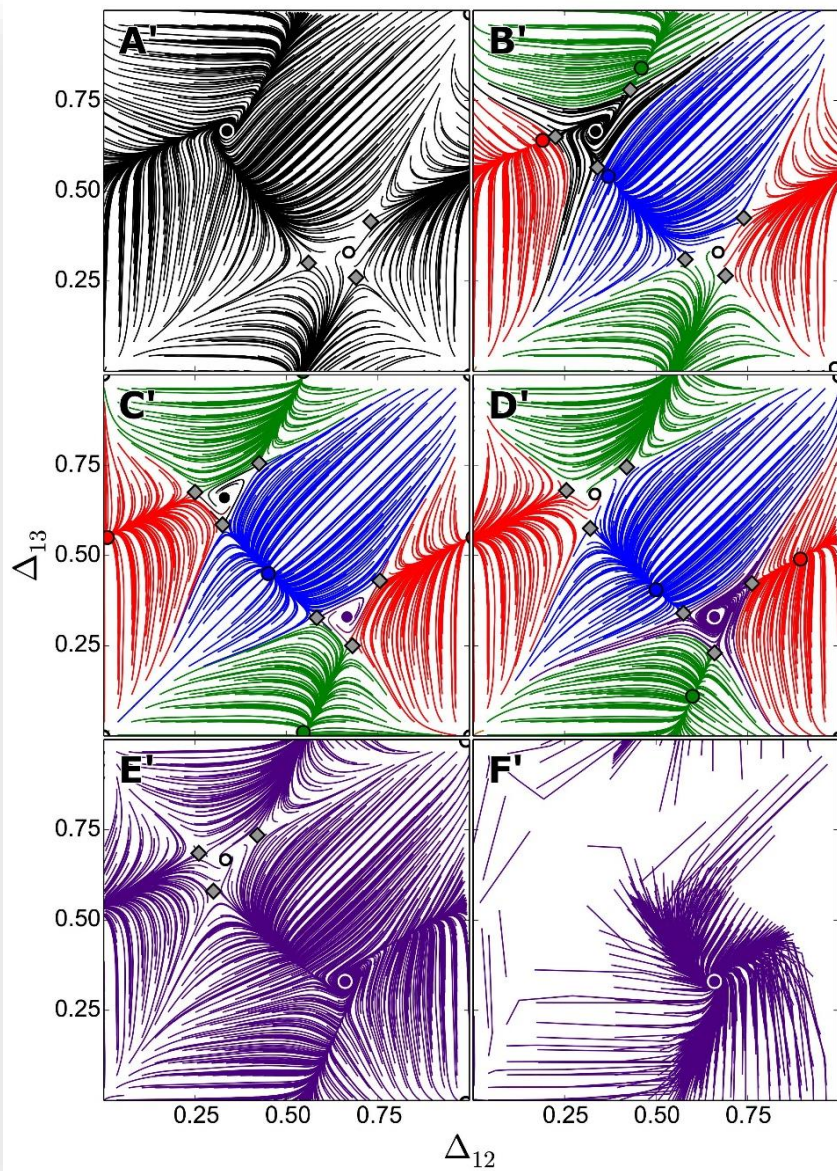


Figure 3.12 Clockwise asymmetric release case

When synapse strengths g_{12} , g_{23} and g_{31} are very small only the black TW exists (A). With increasing synapse strengths g_{12} , g_{23} and g_{31} the black TW basin of attraction shrinks to a relatively small area while the three PMs emerged and their basins of attraction are large and relatively equal in area to each other (B). As the g_{12} , g_{23} and g_{31} synapses are further increased the three PMs and their basins of attraction remain relatively constant while the black TW disappears (C) and then the purple TW emerges (D). With even greater strengths of g_{12} , g_{23} and g_{31} simulated the purple TW grows and takes all network phase difference space (E). With the strongest synapse strengths used the traces become jagged and cross paths do to hard locking (F). Parameters: $I_{app} = 0.4$, $g_{ij} = 0.001$ except $g_{12} = g_{23} = g_{31} = 0.0005, 0.00065, 0.001, 0.00135, 0.0016$, and 0.002 .

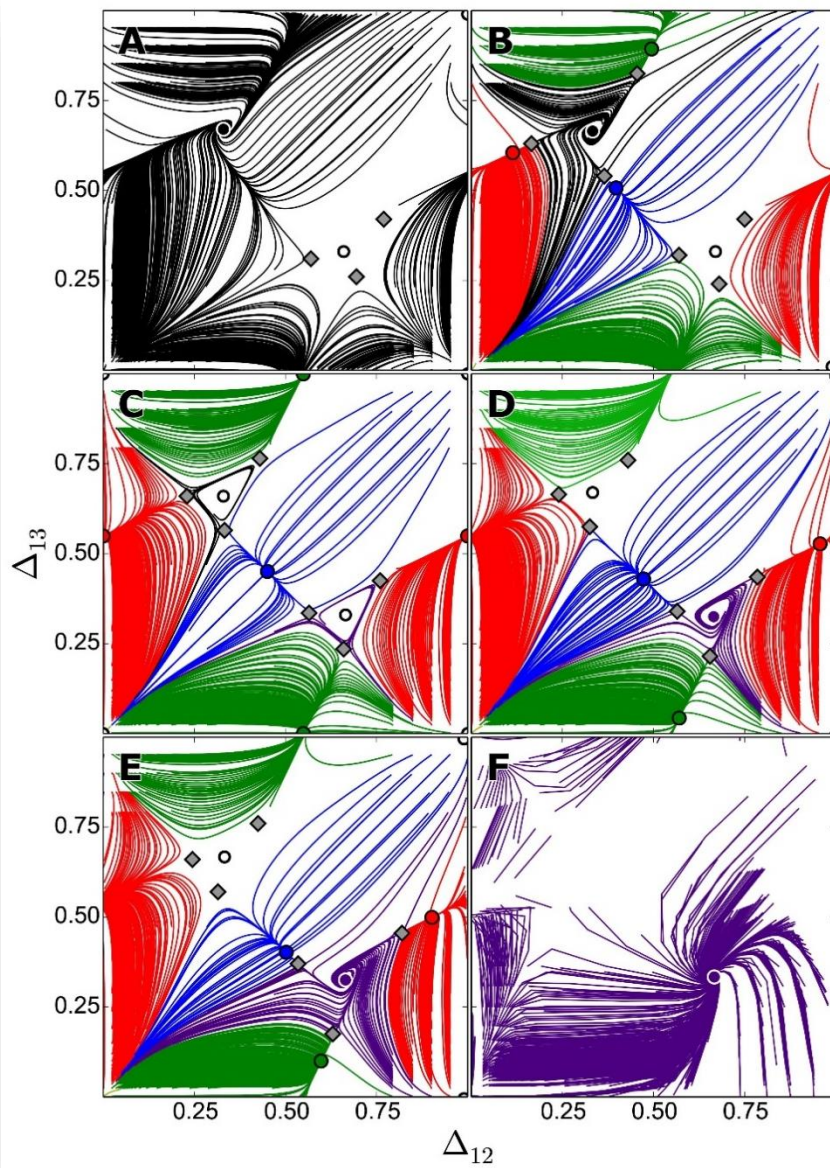


Figure 3.13 Clockwise asymmetric escape case

When synapse strengths g_{12} , g_{23} and g_{31} are very small only the black TW exists (A). With increasing synapse strengths g_{12} , g_{23} and g_{31} the black TW basin of attraction area shrinks while the three PMs emerged and their basins of attraction are relatively equal in area to each other (B). As the g_{12} , g_{23} and g_{31} synapses are further increased the three PMs basins of attraction remain relatively constant while the purple TW emerges and the black TW is contained within an invariant circle formed by three saddles (C). With greater synapse strengths, the black TW disappears and the purple TW's basin of attraction grows (D and E). With even greater strengths of g_{12} , g_{23} and g_{31} simulated the purple TW grows and takes all network phase difference space with the traces becoming a little jagged do to hard locking (F). Parameters: $I_{app} = 0.5886$, $g_{ij} = 0.001$ except $g_{12} = g_{23} = g_{31} = 0.0005, 0.000743, 0.001, 0.00116, 0.00132$, and 0.002 .

to break down, as was mentioned in the methods section. Rapid convergence makes the trajectory representation choppy and unclear, and the phase basin visualization might be more conducive if we didn't already know what was happening here from panel E'.

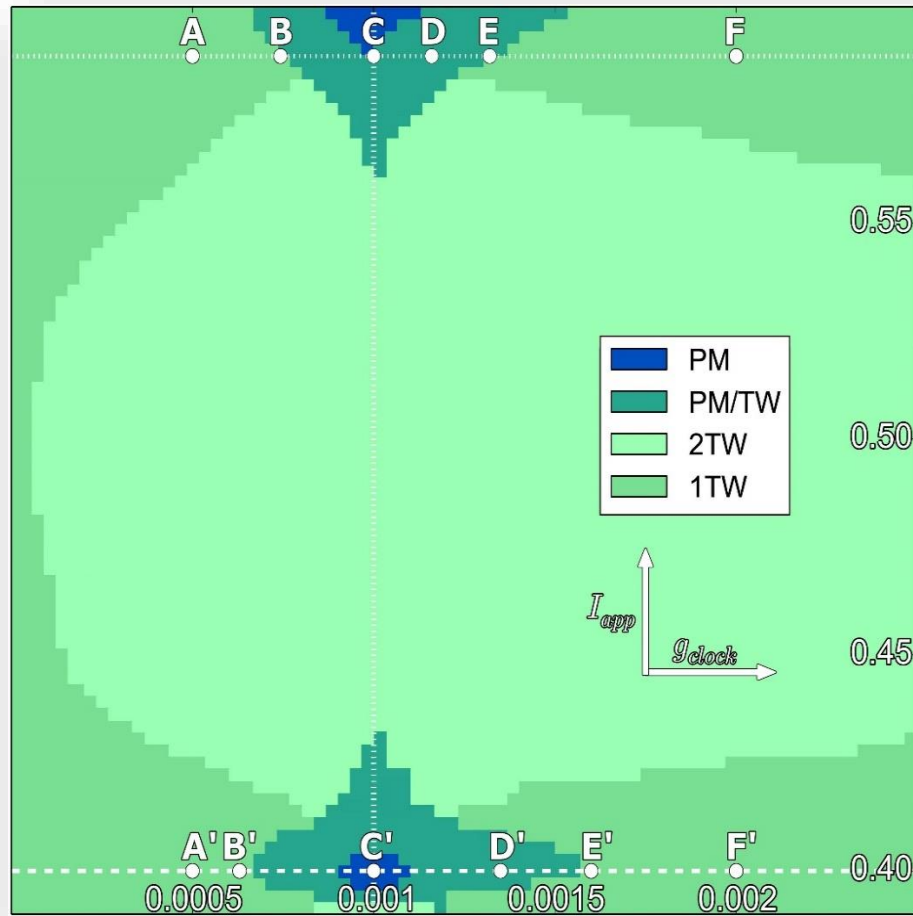


Figure 3.14 Clockwise asymmetric bifurcation diagram

Bifurcations occur between differently colored regions, in the bi-parametric space varying I_{app} and $g_{12} = g_{23} = g_{31}$. Very light green represents networks with only one TW, light green represents networks with both TWs, blue represents purely PM, dark green represents both types of rhythms. Transitions between these regions indicate torus or pitchfork bifurcations. Specific examples are shown in Figures 3.12 and 3.13, these values are represented by the points on the dashed and dotted lines. The points on the bottom horizontal line are the release case samples shown in Figure 3.12 as phase difference portraits. The points on the top horizontal line are the sampled escape cases in Figure 3.13. The vertical dashed line represents the point where network synapses are fully symmetry, $g_{12} = g_{23} = g_{31} = g_{ij}$.

The escape mechanism panels look nearly identical (Figure 3.13) as the same transitions are observed. A transition from the black clockwise TW to the purple counterclockwise TW occurs again via the formation of the 3 PMs, disappearance of the black TW, appearance of the purple TW, and disappearance of the 3 PMs. In this figure, some of these transitions are discernable in finer detail, as the escape mechanism is more conducive to permitting transitory limit cycle behavior previously observed as TWs appear or disappear (C). We are also able to more clearly see the respective PM FPs approaching the purple TW FP (and the saddle nodes between them moving further from the purple TW FP) just prior to merging with its basin of attraction.

A broader examination of the bifurcation diagram (Figure 3.14) indicates the universality of this trend at both ends of the I_{app} spectrum in which both release and escape mechanism behaviors are observed. In the intermediate region of more oscillatory behavior, we observe a lack of PM pattern generation entirely, with transitions occurring in which we see the black clockwise TW pattern transition to a purple counterclockwise TW through a region in which both TWs exist and the basin of attraction for each is gradually consumed by the other. This is less apparent using our traditional all-or-nothing color coding for PM, Mixed, or TW regimes, so here we have chosen to color code the differences between 1- or 2-TW regimes even though this has not been done in the previous figures.

3.2 Discussion

In previous work, as well as an examination of the symmetric motif within this research, we observe that differing affects are frequently observed within release and escape mechanism regimes as coupling strength between affected cells is increased. PM behaviors are prevalent in release regimes at lower I_{app} values (here we roughly approximate ranges below 0.44) while TW behaviors increase in dominance with increasing I_{app} , almost entirely dominating escape regimes

(approximately 0.55 and above) except at very low coupling strengths. The exact transition into, or out of, each of these mechanisms is only approximate and depends on the nature of the system and also upon the nature of hard-locking behavior. For simplicity, results observed are summarized in terms of these thresholds. Intermediate I_{app} ranges represent more standard oscillatory systems in which the dynamics are largely unaffected by proximity of the nullclines to one another.

Table 3.1 Polyrhythmicity and dynamic ranges in release network motifs

Release Motif	PM	TW	Mix	PS	Coupling Ranges	Stereotypical Transitions
Symmetric	X All	X >0.43*	X >0.44*	None	TW: 0–0.018 Mix: 0–0.060	TW → Mix → PM PM Dominates
Mono-Biased	X <0.42	X All	X All	None	PM: 0–0.0043 Mix: 0–0.0095	PM → Mix → TW TW Dominates
Pairwise-Biased	X >0.39	X >0.43*	X >0.41*	X All	PM: 0–0.0013 Mix: 0.0003–0.0012 TW: 0.0005–0.0015	PM → Mix ** → PM/PS PM & PS Dominate
King-of-the-Mountain	X All	X >0.42*	X >0.41*	X >0.43	TW: 0.0001–0.0015 Mix: 0.0005–0.0015 PS: <0.0004	PM → Mix → PM PM Dominates
Clockwise	X 0.4±0.05	X All	X <0.43	None	PM: 0.0009–0.0011 Mix: 0.0005–0.0016	TW → Mix → TW TW Dominates
*Except for exceptions observable in the bifurcation diagrams at very weak coupling or near the nullcline tangencies.						

Comparison of symmetric motif dynamic transitions and ranges of behavior between the release case (Table 3.1) and the escape case (Table 3.2), show not only differences in the dominant rhythms generated (PM for release, and TW for escape) but also orders of transition which are essentially opposite one another. In these two tables, an X is used to indicate that a particular rhythm or rhythm combination exists, with the value listed below it representing the I_{app} ranges for which they are observed. For example, we see that PM-only behaviors do exist for all I_{app} values within the release mechanism but that TW-only behaviors only exist for $I_{app} > 0.43$. It is important to note that both rhythms are observed in the mixed PM/TW regions as well, but not independently.

For patterns not present at all I_{app} values, the coupling ranges for which they are observed are also included, and we see for example that TW-only patterns within the release mechanism are observed below the I_{app} release threshold (0.44) mentioned for g_{ij} below 0.018. The asterisks indicate that the given value holds except for the small regions of exception observed in the bifurcation diagrams at very weak coupling, or cases in which the nullclines are nearly tangent. Comparisons between the two tables in this manner elucidates some of the very different behaviors already observed and described in previous sections. This differences are most opposite in the symmetric and mono-biased motifs, though phase-slipping behavior tends to occur most frequently within escape mechanism ranges of I_{app} . Phase-slipping behavior is prolific within the pairwise-biased motif and additional examples can be found in Chapter 5.

Table 3.2 Polyhythmicity and dynamic ranges in escape network motifs

Escape Motifs	PM	TW	Mix	PS	Coupling Ranges	Stereotypical Transitions
Symmetric	X >0.53	X All	X >0.57	None	PM: 0–0.011 Mix: 0–0.028 TW: >0.0004	PM → Mix → TW TW Dominates
Mono-Biased	X All	X <0.57	X <0.58	X >0.57	TW: 0–0.011 Mix: 0–0.0091 PS: >0.0015*	TW → Mix → PM PM & PS Dominate
Pairwise-Biased	X All	X <0.56*	X <0.59	X All	PM: 0–0.006 Mix: 0.0006–0.0014 TW: 0.0008–0.0015	PM → Mix → PM/PS PM & PS Dominate
King-of-the-Mountain	X All	X <0.56	X <0.58	X All	PM: >0.0002 Mix: 0.0007–0.0018 TW: 0.0007–0.0018	PS → Mix → PM/PS PM & PS Dominate
Clockwise	X >0.58	X All	X >0.56	None	PM: 0.0008–0.0012 Mix: 0.0006–0.0015	TW → Mix → TW TW Dominates
*Except for exceptions observable in the bifurcation diagrams at very weak coupling or near the nullcline tangencies.						

In nearly all motifs explored, unique behavior occurs around full symmetry where the strength of the connection being manipulated is close to those being held fixed at 0.0010. This is most apparent in the clockwise-biased motif in which the bifurcation looks nearly symmetrical around the vertical

line representing this equipotent connectivity, but is also clear in the extended ‘peaks’ and ‘troughs’ of PM/TW mixed behavior observed for the pairwise-biased and king-of-the-mountain motifs. Pacemaker behavior is least likely to occur in clockwise-biased motifs, as the nature of this connectivity induces traveling wave behavior at both weak and strong coupling, and we see PM-only behavior only near symmetry for very small ranges of $g_{12}=g_{23}=g_{31}$, and only at the extremes of both release and escape I_{app} .

Traveling waves and pacemakers are obtained in both the inherently bursting release and quiescent escape mechanisms; each is dominated more by one (PM and TW respectively) for most motifs and the other occurs mostly at low or asymmetric coupling. Post-inhibitory rebound described in Chapter 5 is characterized by a small growing traveling wave regime as coupling increases, and no pacemaker behavior observed with stereotypical dynamics. The unexpected regularity with which different phase-slipping behaviors can be observed in the mono-biased or the two double-connection motifs lends itself to analysis of macro-scale rhythmic behaviors in which we may see periods of apparently stable patterns interspersed by fast rhythm switching to another apparently stable rhythm without the need for external stimuli. These may present novel applications to experimental research of small local networks in which multi-stable rhythm production can be observed with the same connectivity. Rhythm switching for non-phase-slip systems can also be readily obtained in both release and escape cases, either by external stimulus in the form of a current pulse (abrupt temporary shift up or down in effective I_{app} value seen in the bifurcation diagrams) or by either natural or artificial connection plasticity (abrupt temporary shift up or down in effective g_{ij} value seen in the bifurcation diagrams). This has many potential applications for both the mathematician and the experimentalist, and some of these will be discussed in further detail in the following chapters.

4 KEY BIFURCATIONS AND DETAILED TRANSITIONS

A primary focus of this work has been the identification of key bifurcations in rhythm transition and rhythmogenesis within single or modular 3-node inhibitory networks. Many of these transitions have been described in the previous two chapters in the larger context of the release and escape mechanisms within both symmetric and several asymmetric circuit connectivity frameworks. Bifurcations represent qualitative changes in the dynamics of a system produced by varying parameters, in this research the primary focus being the connectivity strength, g_{ij} , and the current or pulse stimulus, I_{app} , parameters with some additional discussion of manipulation of the fast-slow separation variable, ε . Use of the autonomous ordinary differential equations (ODEs) described in Chapter 2, represented for generality as

$$\dot{x} = f(x, \alpha), \quad x \in \mathbb{R}^n, \quad \alpha \in \mathbb{R}^p, \quad \text{Equation 4.1}$$

where f is a smooth function and α represents the parameter changed, permits numerical determination of the occurrence of a bifurcation. Bifurcations occur at parameter $\alpha = \alpha_0$ if there is parameter value α_1 close enough to α_0 with topologically inequivalent dynamics from those at α_0 . The number and type of stable equilibria or periodic orbits can change with shifts from α_0 to α . The production of bifurcation diagrams dividing the α parameter space into topologically equivalent systems, as demonstrated in the previous chapters, is a primary goal of bifurcation theory, with bifurcations occurring at transitions between these regions.

Identification of ubiquitous bifurcation patterns has resulted in the naming of key types of transition dynamics, each with associated defining equations that locate them within a family with normal forms (where they exist) exemplifying them. Bifurcations may be viewed as structural stability failure within a family type, and here we discuss key families identified in this work. These include those previously identified in symmetric 3-node networks, Andronov-Hopf or torus

bifurcation and pitchfork bifurcation, and additional bifurcations identified in this work for asymmetric systems, three types of saddle-node bifurcation representing simple, homoclinic, and heteroclinic bifurcations. An example of the generic family type and behavior, as well as specific examples of these within the framework of this work varying parameters g_{ij} and I_{app} , is described here. As previous descriptions of Andronov-Hopf and pitchfork bifurcation were discussed in terms of changing parameter I_{app} , [Chapter 1 and 39], focus here will be on changes in g_{ij} .

4.1 Andronov-Hopf bifurcation

An Andronov-Hopf bifurcation occurs with the formation of a limit cycle from equilibrium in ODE dynamical systems, with equilibrium stability changing through a pair of imaginary eigenvalues. This transition can be either subcritical or supercritical, resulting in an unstable or stable limit cycle, respectively, within an invariant two-dimensional manifold [43-45]. For this

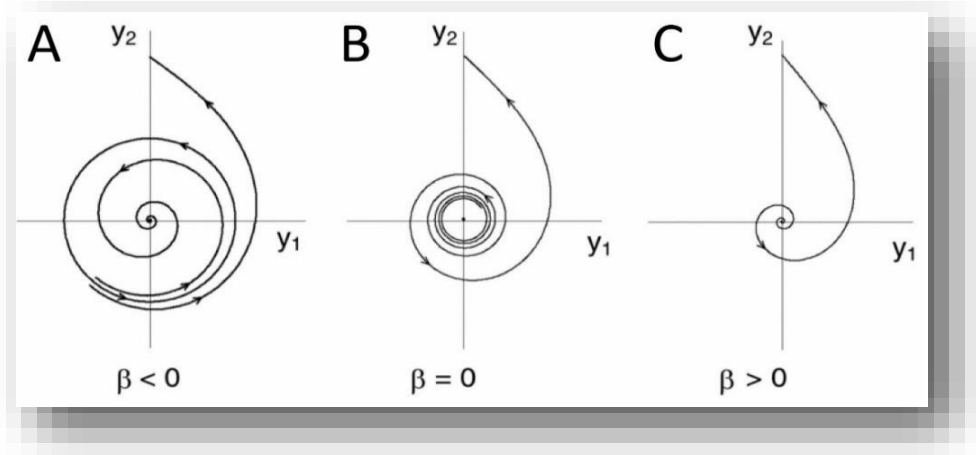


Figure 4.1 Subcritical Andronov-Hopf bifurcation

Subcritical Andronov-Hopf bifurcation resulting in an unstable limit cycle within an invariant two-dimensional manifold. The origin is a stable limit cycle bounding the basin of attraction of the stable focus for $\beta < 0$ (A) and unstable for $\beta \geq 0$ (C), weakly at $\beta = 0$ (B), while a unique unstable limit cycle exists for $\beta < 0$ (from [43]).

system, we assume a Jacobian matrix $A(\alpha) = f_x(x^0(\alpha), \alpha)$ with a pair of complex eigenvalues

$$\lambda_{1,2}(\alpha) = \mu(\alpha) \pm i\omega(\alpha) \quad \text{Equation 4.2}$$

where $\mu(0) = 0$ and $\omega(0) = \omega_0 > 0$ represents the case it becomes purely imaginary. If non-degeneracy conditions hold, the normal form for an Andronov-Hopf system is topologically equivalent locally near the equilibrium and is given by

$$\dot{y}_1 = \beta \cdot y_1 - y_2 + \sigma \cdot y_1(y_1^2 + y_2^2), \quad \text{Equation 4.3}$$

$$\dot{y}_2 = y_2 + \beta \cdot y_1 + \sigma \cdot y_2(y_1^2 + y_2^2), \quad \text{Equation 4.4}$$

where $y = (y_1, y_2)^T \in \mathbb{R}^2$, $\beta \in \mathbb{R}$, and $\sigma = \text{sign } l_1(0) = \pm 1$. And $l_1(\lambda)$ is the first Lyapunov coefficient. In the subcritical Andronov-Hopf bifurcation (Figure 4.1), $\sigma = +1$ and the origin in the normal form is asymptotically stable for $\beta < 0$ and unstable for $\beta \geq 0$ (weakly at $\beta = 0$), while a

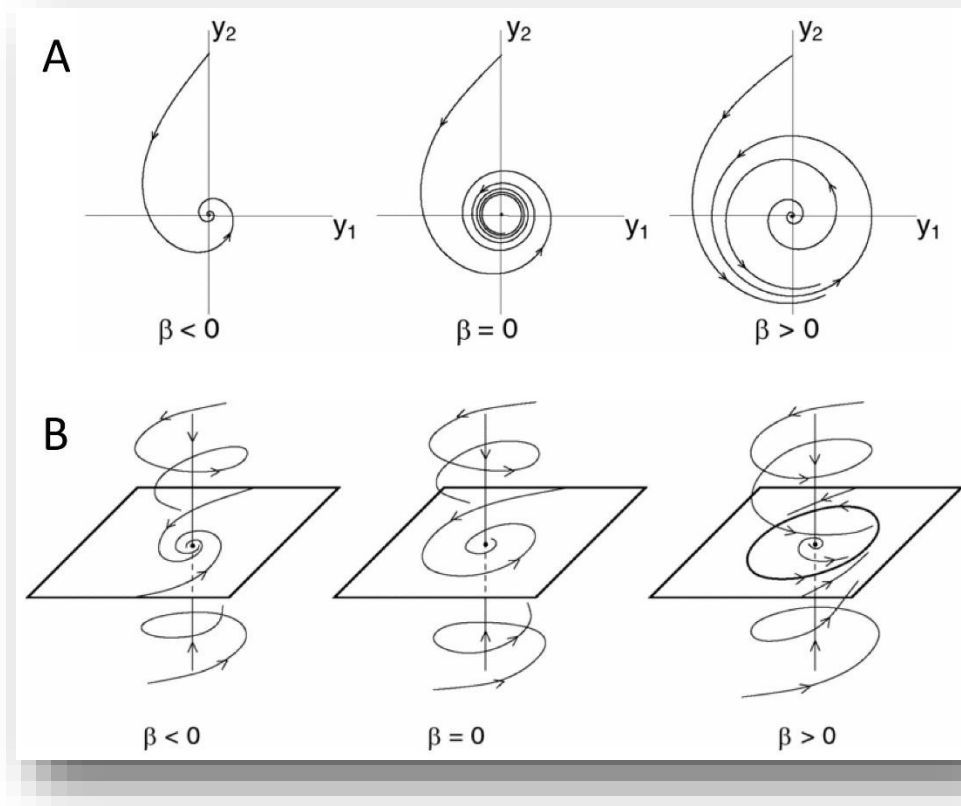


Figure 4.2 Supercritical Andronov-Hopf bifurcations

(A) 2-D supercritical Andronov-Hopf bifurcation resulting in a stable limit cycle within an invariant two-dimensional manifold. The origin has an equilibrium which is asymptotically stable for $\beta \leq 0$ (weakly at $\beta = 0$) and unstable for $\beta > 0$, while a unique and unstable limit cycle exists for $\beta < 0$ (from [43]). (B) 3-D supercritical Andronov-Hopf bifurcation with similar evolution of stability (from [44]).

unique and unstable limit cycle exists for $\beta < 0$. In the supercritical Andronov-Hopf bifurcation (Figure 4.2), $\sigma = -1$ and the origin in the normal form has an equilibrium which is asymptotically stable for $\beta \leq 0$ (weakly at $\beta = 0$) and unstable for $\beta > 0$, while a unique and unstable limit cycle exists for $\beta < 0$. There is a unique and stable circular limit cycle that exists for $\beta > 0$ with has radius $\sqrt{\beta}$. This logic can be extended to multi-dimensional cases where $n \geq 3$, the supercritical Andronov-Hopf bifurcation in this case also visualized in Figure 4.2. This type of bifurcation occurs primarily within the symmetric motif explored in this research, with the appearance, or disappearance, of both traveling waves simultaneously.

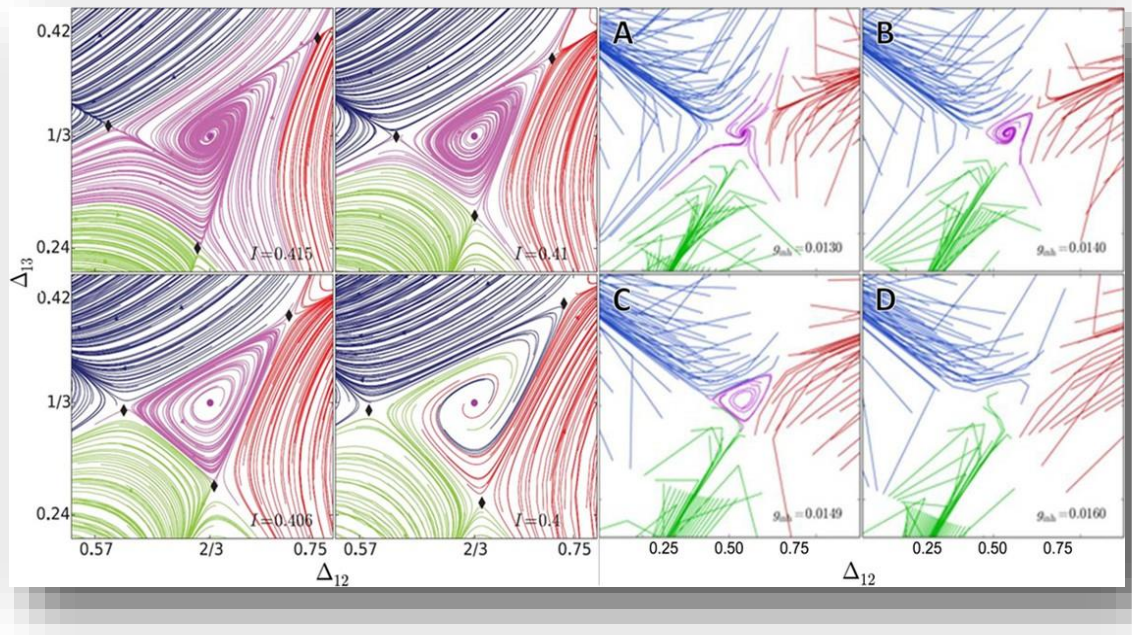


Figure 4.3 Torus bifurcation via changes in either I_{app} or g_{ij}

Changes in either I_{app} or g_{ij} can lead to a torus bifurcation, here resulting in the disappearance of the CCTW pattern (purple traces near $(\Delta_{12}, \Delta_{13}) = (2/3, 1/3)$). The left quad of panels is taken from [39], where this type of bifurcation was discussed in the context of transitions in I_{app} . The right quad of panels represents this same transition at approximately the same I_{app} range as in [39] but by increasing coupling strength, g_{ij} . The transition occurs more rapidly due to the nearly horizontal bifurcation transition (as observed in Figure 2.5(E) where the dark green region meets the blue PM region). The size of the basin of attraction diminishes (A-B) before briefly forming an unstable limit cycle (C), which is the lost as the point becomes unstable (D). Parameters: $I_{app} = 0.41$, $g_{ij} = 0.0130, 0.0140, 0.0149$, and 0.0160 .

As previous work [39] focused primarily on these transitions changing the parameter I_{app} , we focus here and in the remaining bifurcations discussed on transitions in parameter g_{ij} . Side-by-side zoomed in views of a torus bifurcation involving disappearance of the counter-clockwise traveling wave (CCTW) are shown in Figure 4.3, one from [39] in which the bifurcation was induced by changing I_{app} and the other showing the same bifurcation via increasing g_{ij} . We clearly observe the size of the basin of attraction decreasing until the brief formation of a brief unstable limit cycle near the critical value of g_{ij} , after which stability is lost and trajectories diverge, rather than converge, from this fixed point in a subcritical bifurcation. In Figure 4.4, we observe this same transition but in a view in which the full system and both traveling waves can be observed. This is a more focused view of the symmetric release case described in Figure 2.8, and follows the same evolution of pattern transitions as in Figure 4.3, but with changes in g_{ij} much closer placed to the bifurcation point.

Another example of a subcritical Andronov-Hopf bifurcation, for the escape case that was described first in Figure 2.5, can be seen in Figure 4.5. Here, however, we observe a reverse order in the transitions, with the formation of traveling waves with increasing g_{ij} . This is one key finding of Chapter 2, in which we identified reverse pattern formation between the release and escape mechanisms and can be readily observed in the bifurcation diagram there. This is due to the nature of the two mechanisms. The release mechanism, involving inherently bursting cells, occurs when neurons in the active state stop firing of their own accord, thereby releasing an inactive cell from inhibition, the effect of this being movement of the cubic or fast nullcline back to the right (Figure 2.6), restoring the bursting limit cycle for a given cell. This mechanism therefore promotes pacemaker behavior at lower values of g_{ij} due to limited inhibitory effects that would otherwise drive the cells to split the cycle. The escape mechanism, involving cells that typically fire tonically,

occurs when an inactive cell passes threshold and begins firing, thereby applying inhibition to any currently active cell. This allows the otherwise tonic firing cell to escape from the active state and therefore promotes traveling wave behavior at lower values of g_{ij} due to limited inhibitory effects that allow the cells to continue driving toward tonic activity until coupling is strong enough to cause one cell to dominate dynamics. While only symmetric examples have been shown here,

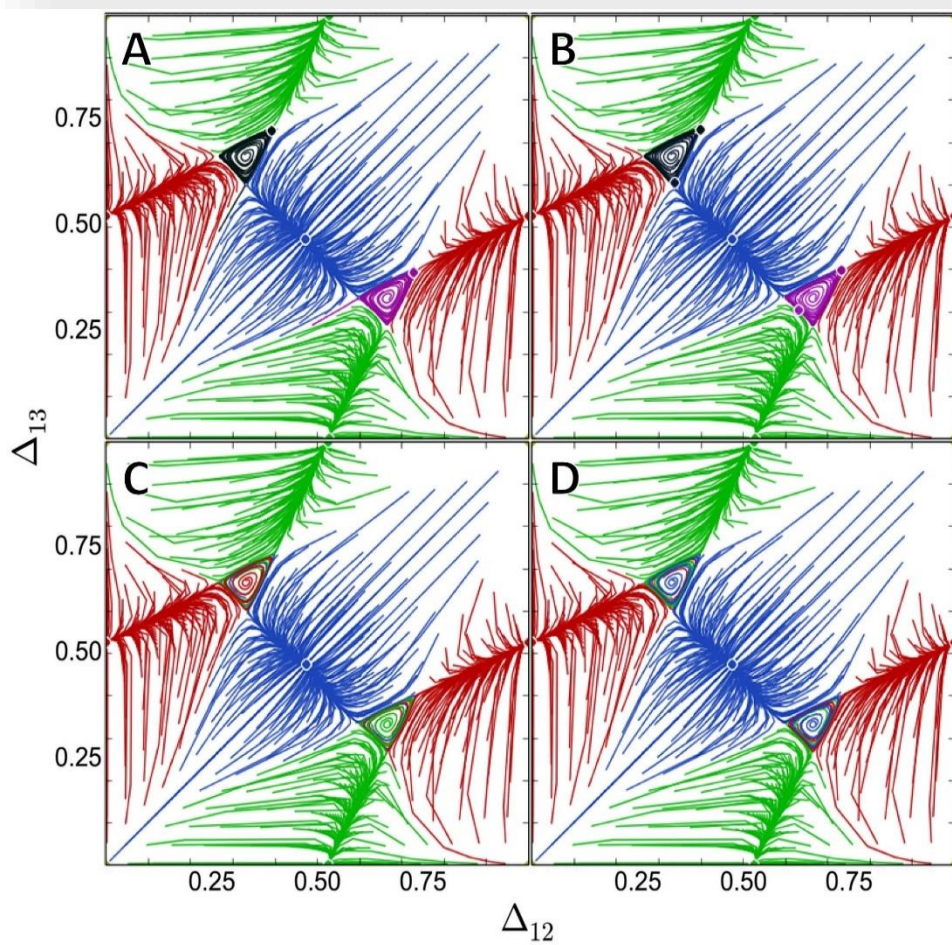


Figure 4.4 Full view of symmetric release Andronov-Hopf bifurcation

Increasing coupling strength of the network causes an Andronov-Hopf, or torus, bifurcation, resulting in the disappearance of both traveling waves (black and purple traces near $(\Delta_{12}, \Delta_{13}) = (1/3, 2/3)$ and $(2/3, 1/3)$). The size of the basins of attraction have diminished (A) to the point of briefly forming unstable invariant curves emerging from one-way heteroclinic connections (triangles) between 3 close saddles (B), which is the lost as the point increasingly unstable (C-D). Parameters: $I_{app} = 0.4155$, $g_{ij} = 0.015099, 0.015347, 0.015594$, and 0.015842 .

some cases of this may be observed in asymmetric motifs briefly transitioning at full network symmetry (near $g_{ij}=0.01$, unless otherwise indicated, and represented by the vertical line in bifurcation diagrams in Chapter 3) and is most readily observed via transitions in I_{app} and is therefore not explored in detail here.

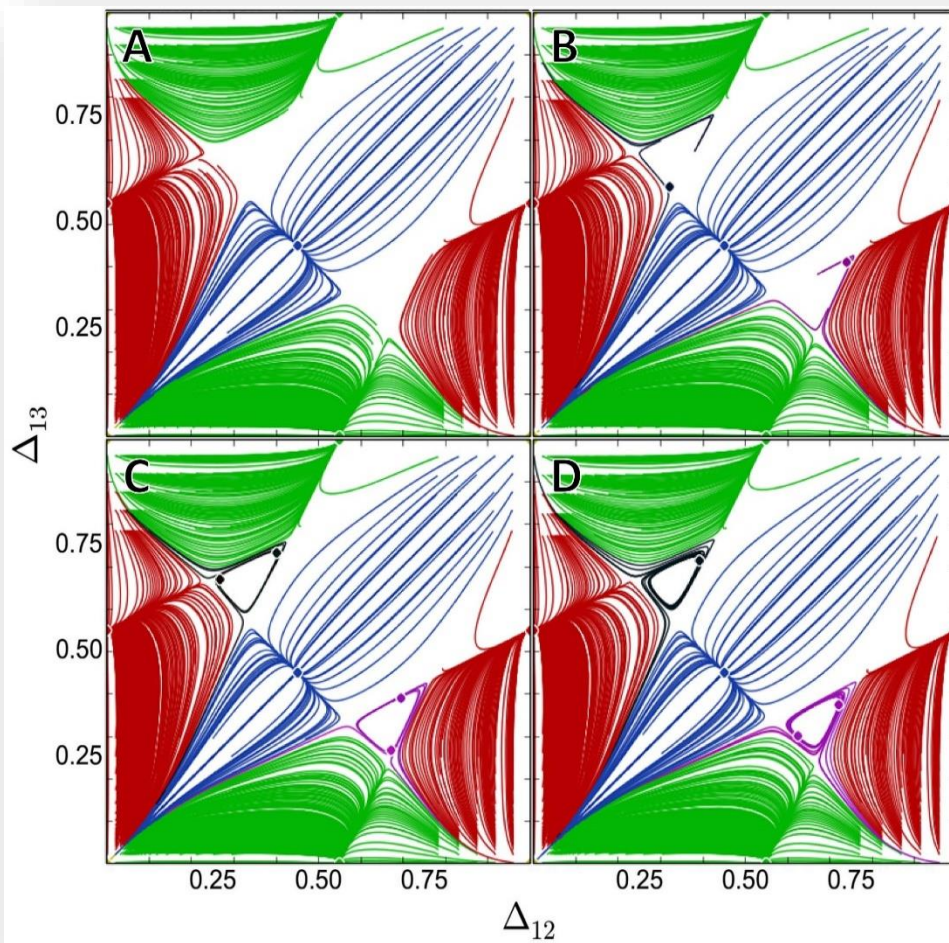


Figure 4.5 Example of symmetric escape Andronov-Hopf bifurcation

Increasing coupling strength of the network causes stable invariant curves and super-critical Andronov-Hopf bifurcations of traveling waves, resulting in the appearance of both TW patterns (black and purple traces near $(\Delta_{12}, \Delta_{13}) = (1/3, 2/3)$ and $(2/3, 1/3)$). A purely pacemaker system (A) evolves to the point of briefly forming unstable limit cycles (B-C), which are then lost as the point increasingly stable and acquire increasingly large basins of attraction (D, and Figure 2.5). Parameters: $I_{app} = 0.5886$, $g_{ij} = 0.000248, 0.000495, 0.00099$, and 0.001733 .

4.2 Pitchfork bifurcation

A pitchfork bifurcation is a local bifurcation that occurs when a system transitions from one to three fixed points, visualization of which looks much like a pitchfork. Much like the Andronov-Hopf bifurcation just discussed, pitchfork bifurcations can be either subcritical or supercritical. As in the Andronov-Hopf case, a normal form exists for pitchfork bifurcations and is given by the general relationship

$$\frac{dx}{dt} = \alpha \cdot x \pm x^3 \quad \text{Equation 4.5}$$

for the subcritical (+) and supercritical (-) forms, respectively. This version of $\dot{x} = f(x, \alpha)$ is described by a one-parameter function $f(x, \alpha)$ with $\alpha \in \mathbb{R}$ where f is an odd function in which the first and second order derivatives of $f(0, \alpha_0)$ equal zero while the third order derivative does not. This system has a pitchfork bifurcation at $(x, \alpha) = (0, \alpha_0)$, with the form given by the third derivative as follows.

$$\frac{\partial^3 f}{\partial f^3}(0, \alpha_0) \begin{cases} > 0, \text{ subcritical} \\ < 0, \text{ supercritical} \end{cases} \quad \text{Equation 4.6}$$

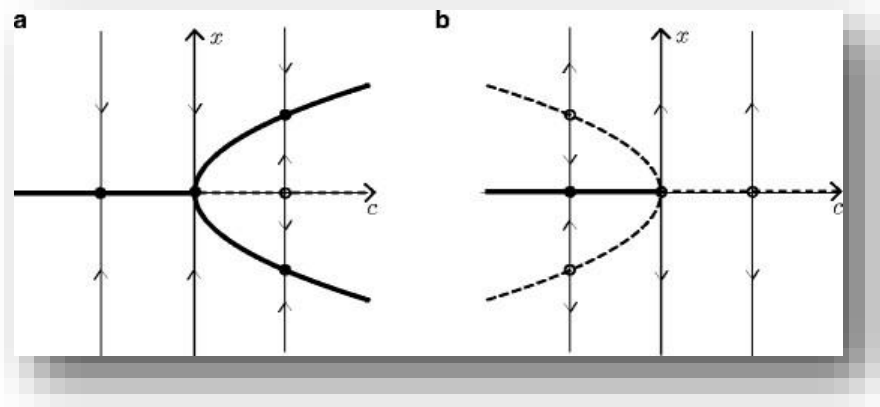


Figure 4.6 Pitchfork bifurcations

Supercritical (A) and subcritical (B) pitchfork bifurcations. Solid lines represent stable points, while dotted lines represent unstable ones. Arrows indicated direction of convergence or divergence, stable points occurring wherever both lines are incoming (modified from [41]). It is not the direction of the pitchfork shape that makes the bifurcation sub- or super-critical, but only the stability (solid) or instability (dashed) of the outer lines [41, 46].

In the subcritical case, one stable equilibrium exists at $x = 0$ while two unstable equilibria exist at $x = \pm\sqrt{-\alpha}$ for $\alpha < 0$. Bifurcation occurs at $\alpha = 0$, after which the equilibrium that existed at $x = 0$ becomes unstable. In the supercritical case for $\alpha < 0$ there is only a single stable equilibrium appear at $x = \pm\sqrt{\alpha}$. It is important to note that the direction of the occurrence of this pitchfork is not

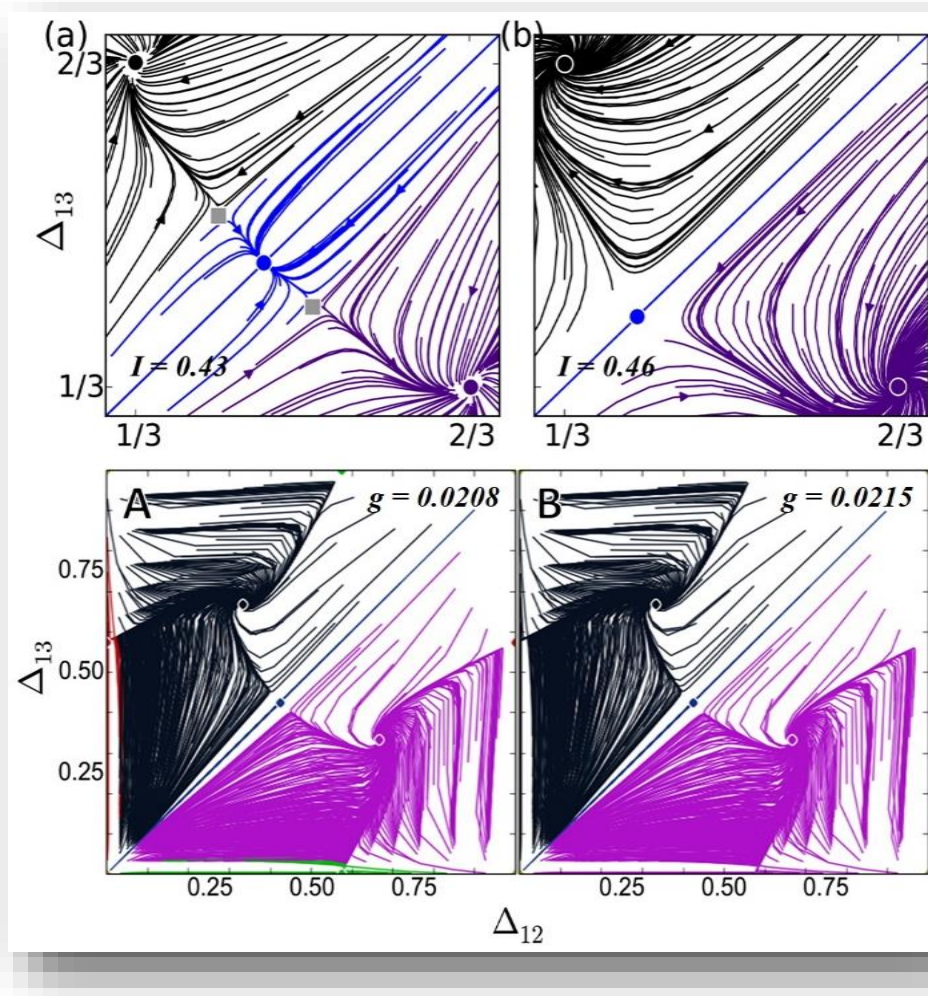


Figure 4.7 Pitchfork bifurcation via changes in either I_{app} or g_{ij}

Changes in either I_{app} or g_{ij} can lead to a pitchfork bifurcation resulting in the disappearance of the PM patterns. The top two panels are taken from [39], with a zoomed in view of the collapse and disappearance of the blue PM pattern (near $(\Delta_{12}, \Delta_{13}) = (1/2, 1/2)$), where this type of bifurcation was discussed in the context of transitions in I_{app} . The bottom two panels represent a full view of this same type of transition for all three PMs, (near $(\Delta_{12}, \Delta_{13}) = (0, 1/2), (1/2, 1/2)$ and $(1/2, 0)$), but by increasing coupling strength, g_{ij} . The basins of attraction have already diminished in size (A) and continuing to decrease until all three FPs becomes unstable and drive all initial conditions away (B). Parameters: $I_{app} = 0.5886$, $g_{ij} = 0.020792$ and 0.021535 .

what matters, but the stability or instability of the outer branches of the pitchfork in each case. Pitchfork bifurcations typically occur in flows for systems with symmetry, and this is also the case in research in this work in which we observe pitchfork bifurcations occurring only with the appearance or disappearance of all three pacemaker rhythms at once. Cases where only one or two pacemakers are generated will typically fall into one of the saddle-node bifurcations next. In Figure 4.7, we observe one such example of subcritical pitchfork bifurcation in which the basins of attraction for the three pacemaker rhythms have already diminished significantly in size with increased g_{ij} . As connectivity continues to increase, these basins diminish even further until all three fixed points collide with a nearby saddle and are obliterated, becoming unstable and now driving all trajectories away toward one of the traveling wave basins.

4.3 Saddle-node bifurcations

Saddle-node bifurcations occur when two fixed points, or equilibria, within a continuous dynamical system collide, annihilating one another in the process. This type of bifurcation is sometimes also called a tangential, limit point, or fold (for discrete dynamical systems) bifurcation and occurs when there is only one zero eigenvalue for the critical equilibrium [41-45]. For this system, we assume that $\alpha = 0$ and that the system has an equilibrium $x_0 = 0$ with a Jacobian matrix $A(\alpha) = f_x(0,0)$ with simple eigenvalue, $\lambda_1 = 0$. As α traverses $\alpha = 0$, a critical saddle-node equilibrium occurs when the two equilibria collide before then disappearing. If non-degeneracy conditions hold, the normal form for a one-dimensional saddle-node system is topologically equivalent locally near the origin to

$$\dot{y} = \beta + \sigma(y^2), \quad \text{Equation 4.7}$$

where $y \in \mathbb{R}$, $\beta \in \mathbb{R}$, and $\sigma = \text{sign } a(0) = \pm 1$. This form has one stable and one unstable equilibria at $y^{1,2} = \pm\sqrt{-\sigma \cdot \beta}$ when $\sigma \cdot \beta < 0$, one critical equilibrium at $y_0 = 0$, and no equilibria

for $\sigma \cdot \beta > 0$. For asymmetric motifs, the appearance or disappearance of traveling wave patterns occurs primarily through this bifurcation, as opposed to the exclusively Andronov-Hopf bifurcation observed within symmetric systems. Two additional types of special saddle-node bifurcations, heteroclinic and homoclinic, will also be discussed here, as they make frequent appearance within most of the asymmetric motifs explored in this research.

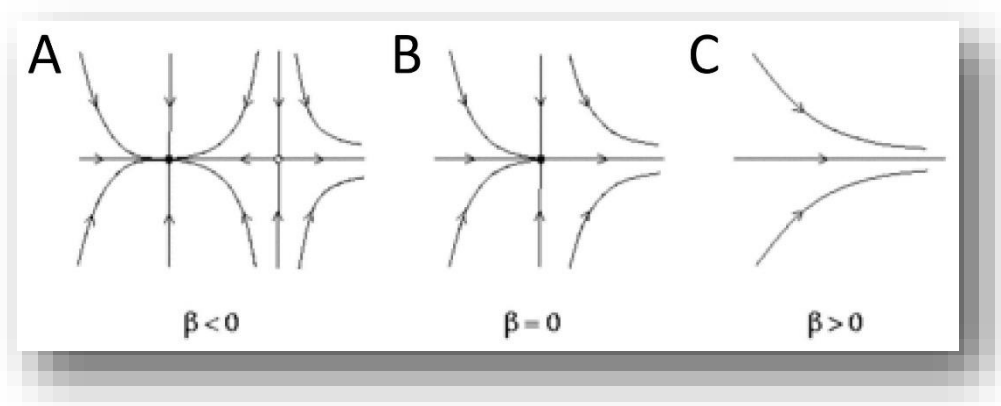


Figure 4.8 Saddle node bifurcation

A saddle-node bifurcation in which there exist one stable and one unstable equilibria at $\beta < 0$ (A), one critical equilibrium at $\beta = 0$ (B), and no equilibria for $\beta > 0$ (C) (taken from [42]).

In Figure 2.9, an example of this transition can be observed in reverse order for the release case within a mono-biased motif network. Here the counter-clockwise traveling wave forms with the appearance of both the node where this fixed point occurs, near $(\Delta_{12}, \Delta_{13}) = (2/3, 1/3)$, in addition to another saddle between the basin of attraction of the blue pacemaker and the newly formed traveling wave. Both the stable node and unstable saddle appear as the system passes through a critical value of g_{31} , formation of the traveling wave occurring via saddle-node rather than Andronov-Hopf bifurcation. Similar transitions can be observed in the formation or disappearance of pacemaker patterns, and have been shown in the results of Chapter 3 and will be described in greater detail within the detailed bifurcation diagrams for the mono-biased and king-of-the-mountain (KOM) motifs shown later in this chapter.

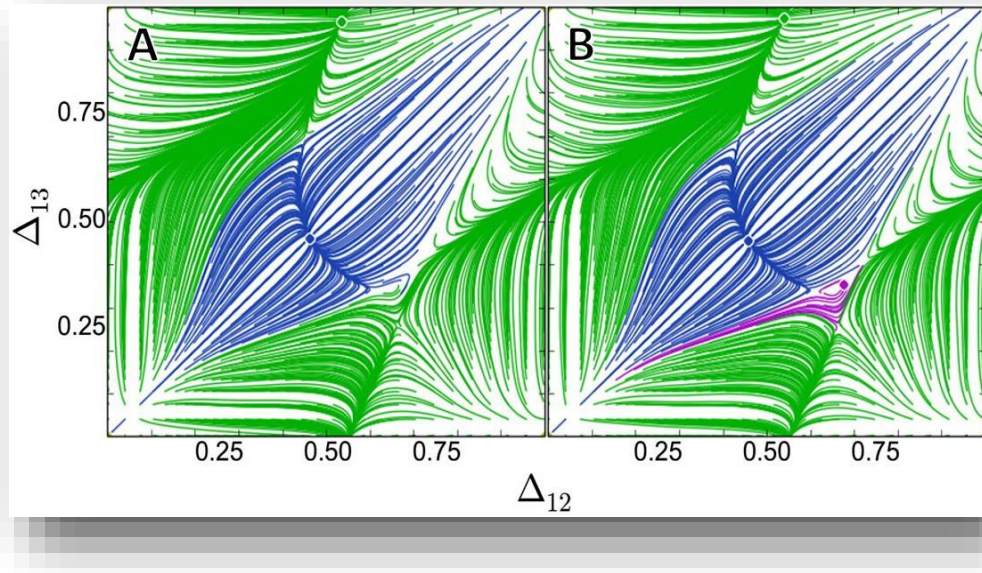


Figure 4.9 Simple saddle-node bifurcation in mono-biased network

Reverse order of saddle-node bifurcation, in which a single unstable point exists (A), the whorl around the instability increasing before passing the critical g_{31} value at which point a single attractor equilibrium (not observed) briefly occurs. Passing through this critical point, the formation of a stable counter-clockwise wave (node) appears along with an additional saddle between the blue and purple basins of attraction (B). The CCTW basin (near $(\Delta_{12}, \Delta_{13}) = (2/3, 1/3)$) continues to grow thereafter. Parameters: $I_{app} = 0.4125$, $g_{ij} = 0.001$ except $g_{31} = 0.00040541$ and 0.00067568 .

4.3.1 Heteroclinic saddle-node bifurcation

A heteroclinic saddle-node bifurcation is global, rather than local, and involves a heteroclinic cycle. These can be either resonance bifurcations, in which stability of the heteroclinic cycle changes when an algebraic eigenvalue condition for the equilibria is satisfied and accompanied by the creation or destruction of a periodic orbit, or transverse bifurcations, in which the stability of the heteroclinic cycle also changes when the real part of a transverse eigenvalue of an equilibrium passes through zero [40, 47]. One example of this can be observed in Figure 4.10 for the double-biased release mechanism, in which we observe red and blue basins of attraction that have already shifted from their usual positions (near $(\Delta_{12}, \Delta_{13}) = (1/2, 1/2)$ and $(1, 1/2)$) as the saddles between

the two basins each move closer to one of the two FPs. This transition is symmetric and basin lost in one is gained by the other, and vice versa, as they move closer together. The saddles and nodes ultimately collide and obliterate one another, leaving only the repeller near the origin, the green FP, and the two remaining saddles that had resided between the green PM and the other two. These

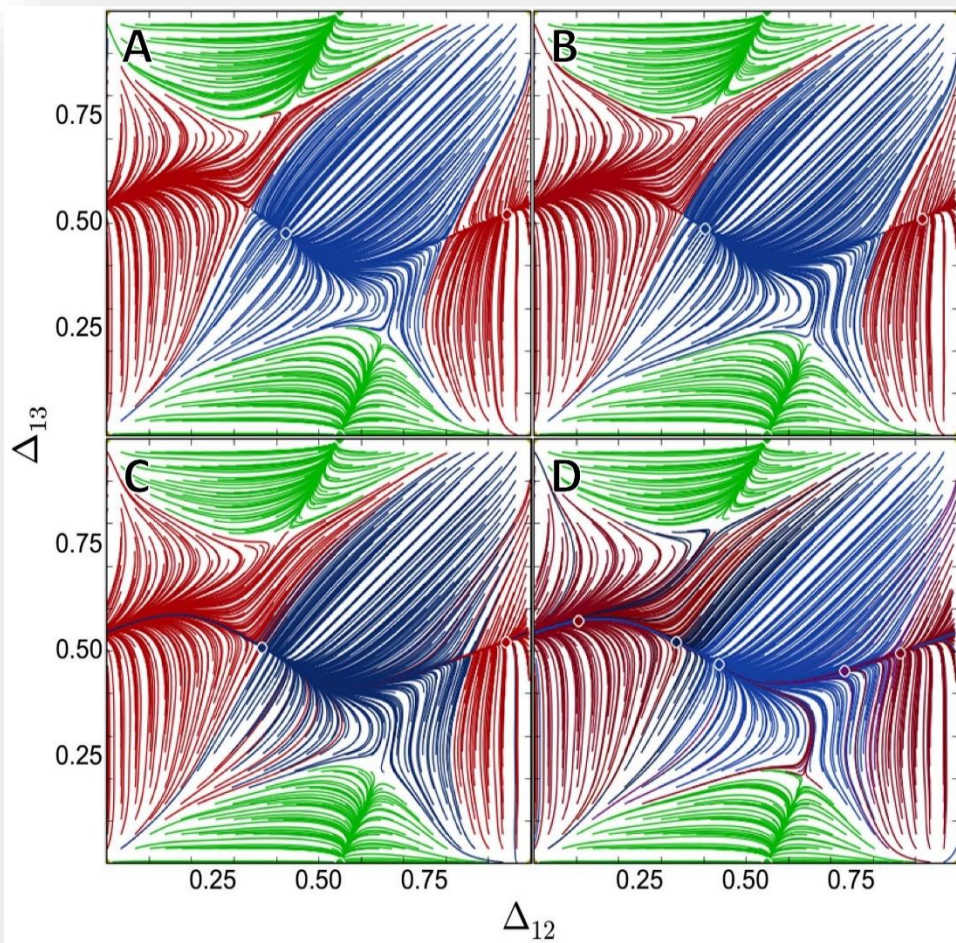


Figure 4.10 Heteroclinic saddle-node bifurcation in pairwise-biased network

Example of heteroclinic saddle-node bifurcation in which the red and blue PM FPs (usually near $(\Delta_{12}, \Delta_{13}) = (1/2, 1/2)$ and $(1, 1/2)$) can be observed to shift. The saddles between both basins also shift closer to one or the other of these FPs (A-B) until colliding and annihilating saddles and nodes pairwise to form a heteroclinic connection and giving rise to an invariant curve wrapping around the torus located between the remaining two saddles bounding the green basin of attraction. Parameters: $I_{app} = 0.3985$, $g_{ij} = 0.001$ except $g_{31} = g_{13} = 0.0012162, 0.0012838, 0.0013514$, and 0.0014865 .

two saddles continue to function as normal, and trajectories caught within what used to once belong to the red and blue basins of attraction now are continuously repelled from the one remaining stable fixed point. This results in a heteroclinic loop residing between the two remaining saddles and in an apparently semi-stable phase slip with the red and blue cells appearing to fire essentially in anti-phase while slipping leftward (at a quicker pace) in relation to the green cell. Similar rivers of phase-slip behavior occur in many of the asymmetric motifs because of this heteroclinic saddle-node bifurcation and some additional examples, not already shown in Chapter 3, will be described in Chapter 5 where other unique cases or regular periodic slip with differing patterns can be observed in greater detail.

4.3.2 Homoclinic saddle-node bifurcation

Homoclinic bifurcations are also global ones which may occur through collision of a saddle point with a periodic orbit. When this occurs, the periodic orbit grows until collision, resulting in the birth of a limit cycle when the saddle-node disappears. The period of this cycle tends to infinity as the parameter approaches its bifurcation value, becoming a homoclinic orbit after which no periodic orbit exists any longer [42]. This system is most commonly observed in systems where only one parameter is changing asymmetrically, and is therefore most dominant in mono-biased networks.

An example of a homoclinic saddle-node bifurcation occurring within this research can be seen in Figure 4.12, in which we see this within the framework of an escape case mono-biased network changing only the parameter g_{31} . Here we observe a network already pushed to the limits of both I_{app} and g_{31} , in which trajectories already show significantly abnormal behavior with only two stable fixed points converging all initial conditions to either the blue or red PM patterns. Some initial conditions are forced to very rapidly converge (significant white space in the figure) as

parameters are strong enough to drive them to regimes of behavior less abnormal to the dynamics of this system. The red PM dominates in a unique fashion, having acquired what was once the green PMs basin as well as significant portions of both wave basins. A whorl of unique behavior remains as a residual effect of the loss of stability of the CTW much earlier, when it previously collided with the saddle between it and the blue PM in a standard saddle-node bifurcation. Those residual traces now converge to the blue PM. As g_{31} increases, we again observe its node or FP

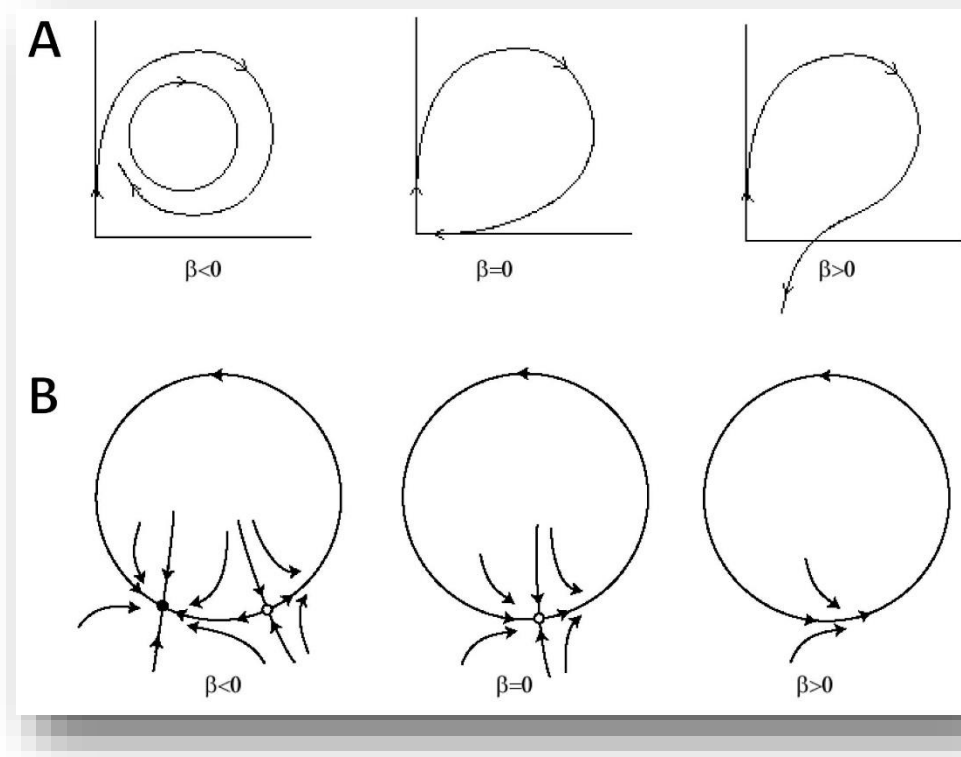


Figure 4.11 Homoclinic bifurcations of a saddle and saddle node

(A) A “small” or “type I” homoclinic bifurcation occurs when a periodic orbit collides with a saddle point. For small parameter values (left), there is a saddle point at the origin and a limit cycle in the first quadrant. As the bifurcation parameter increases (middle), the limit cycle grows until it becomes a homoclinic loop of the saddle point of infinite duration. When the bifurcation parameter increases further (right), the limit cycle disappears (taken from [https://en.wikipedia.org/wiki/Homoclinic_bifurcation]). (B) A saddle-node homoclinic bifurcation on an invariant circle in a plane: a 1-D unstable separatrix, Γ^u , comes back to the saddle-node with the characteristic exponents $\lambda_1 < 0$ and $\lambda_2 = 0$, as time approaches infinity. After the saddle-node has vanished, a single, stable periodic orbit emerges from its homoclinic loop $\bar{\Gamma}$ (from [42]).

and the saddle separating its traces (near $((\Delta_{12}, \Delta_{13}) = (1/5, 3/5))$) moving closer together. These ultimately collide in a homoclinic saddle-node bifurcation, obliterating one another and resulting in a homoclinic loop trapped between the two remaining saddles on either side of the blue basin of attraction.

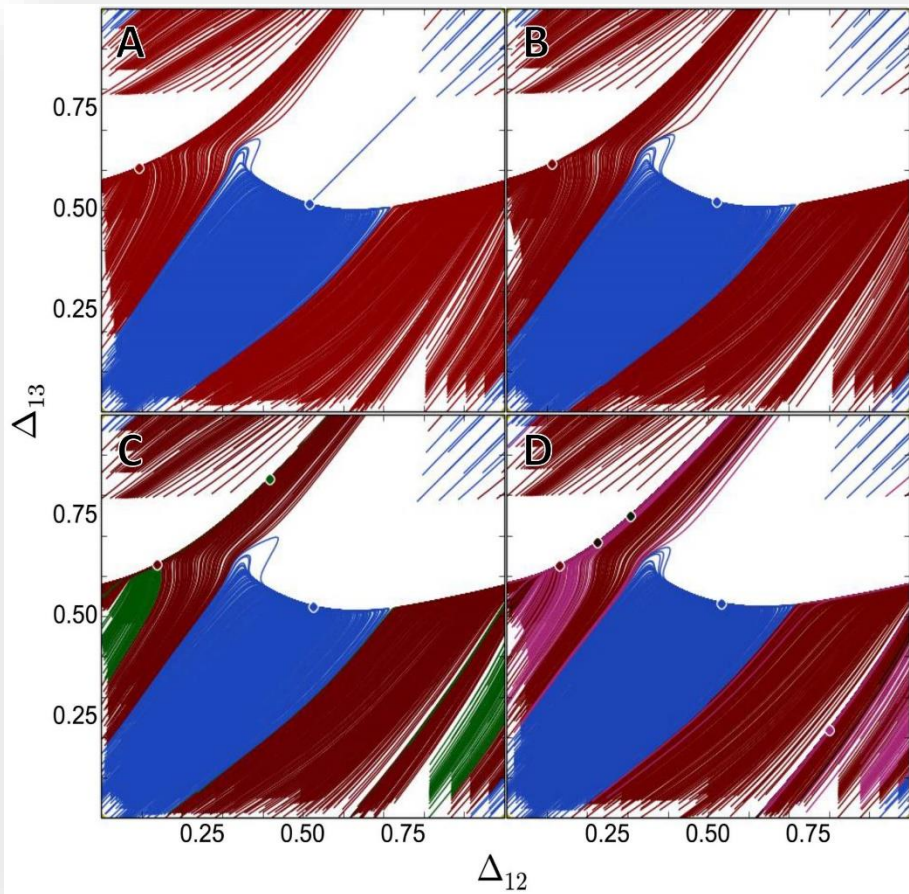


Figure 4.12 Homoclinic saddle-node bifurcation in mono-biased network

The red basin of attraction has already acquired that of the green PM, its FP having shifted left and up (A). The remaining red node and saddle between what used to be the red and green FPS (now near $((\Delta_{12}, \Delta_{13}) = (1/5, 3/5))$) continue to move toward one another (B), eventually colliding and obliterating one another (C) to form a homoclinic loop between the remaining Blue FP saddles. With increasing g_{31} strength, this homoclinic loop becomes more emphatic (D). Parameters: $I_{app} = 0.582$, $g_{ij} = 0.001$ except $g_{31} = 0.0036486, 0.0040541, 0.0044595$, and 0.0052703 .

4.4 Bifurcation transitions with increasing fast-slow separation

Although the focus of this research has been primarily on shifts within the (g_{ij}, I_{app}) bi-parametric space, shifts in the fast-slow separation variable, ε , have also been noted and it is important to return briefly to the effects of these again. This work has focused primarily on systems with only moderate fast-slow separation, with $\varepsilon=0.30$, due to the presence of a broader range of rhythms and rhythm transitions which can then be generally applied backward to other parameter shifts by examining how these transitions shift with changes in each. Previous work [39] touched on the shift to or from pacemaker behavior by manipulating this variable, and this is verified and extended upon here. In the sections below, work done on symmetric motifs is reiterated upon with additional results from this research, followed by similar comparisons for the mono-biased motif. Other network connectivity has not been examined in this detail but similar transitions and behaviors are expected to exist within these as well.

4.4.1 *Fast-slow transitions in symmetric motifs*

For symmetric inhibitory 3-node networks, fast-slow separation has the effect of controlling the appearance or disappearance of purely pacemaker regimes within the bifurcation diagrams. At small values of ε , which correlate with high fast-slow separation, transitions between the upper and lower branches of the cubic nullcline occur too fast to permit gathering of the cells near either knee. This clustering near the knees is what permits pacemaker rhythms to occur in either release or escape mechanisms, as it permits one cell to get released and become clearly inhibitory on the other two (or to be escape activity prior to the other two, depending upon the case). At high-fast slow separation the system dynamics are too fast to permit this clustering, and pacemaker rhythms are discouraged. In Figure 4.13, we observe this effect in action, where no purely pacemaker behaviors are observed at high fast-slow separation (seen in panel A) and only appear in mixed

PM/TW regimes at ranges where nullclines become proximal near either cubic knee. These mixed patterns occur universally for release case ranges ($I_{app} < 0.45$) in this panel, but for higher fast-slow separation (typically $\varepsilon \leq 0.05$) can completely disappear. Otherwise they first make appearance at system extremes in the upper left quadrant, representing very weakly coupled escape cases ($I_{app} > 0.55$), and in the mid-lower right quadrant, representing strongly coupled oscillatory

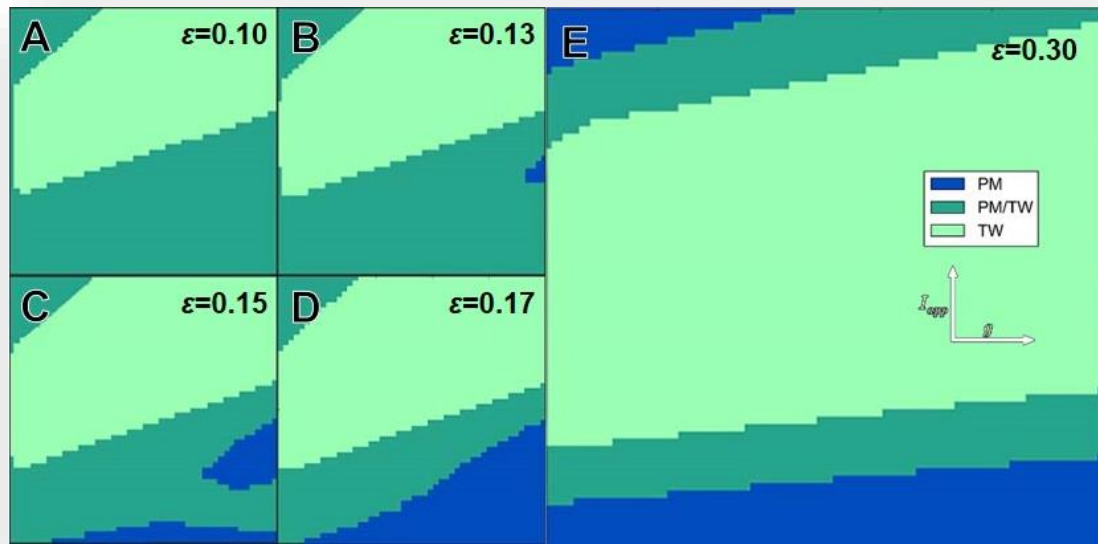


Figure 4.13 Increasing PM activity with decreased symmetric fast-slow separation

At high fast-slow separation (A) no purely pacemaker behaviors are observed in symmetric 3-node systems, mixed PM/TW behavior does exist universally within the release ranges for I_{app} , typically below 0.45, and at system extremes (upper left and lower right quadrants representing very weakly coupled escape cases and strongly coupled oscillatory cases approaching release-like behavior). With decreasing fast-slow separation we see minimal initial effect on the purely TW regimes but observe the gradual appearance of purely PM regimes, first at very strongly coupled oscillatory ranges approaching release-type behavior (B) and then at near-knee low values of I_{app} within the release case (C). These continue to grow and merge (D) to occupy the entire lower right quadrant. With only moderate fast-slow separation (E), we see the appearance of a purely PM regime within the escape case in the upper left quadrant with seemingly even bifurcation transitions between all regimes (note that this panel is zoomed in to the one-fourth the g_{ij} range as the others). Andronov-Hopf bifurcations occurring with the appearance or disappearance of TW patterns (blue to dark green), and pitchfork bifurcations occurring with the appearance or disappearance of PM patterns (light green to dark green). Parameters: $I_{app} = [0.39, 0.6]$, $\varepsilon = 0.1, 0.13, 0.15, 0.17$, and 0.30 , $g_{ij} = [0, 0.1]$ for panels A-D, and $g_{ij} = [0, 0.025]$ for panel E. Some results modified from [39] for lower values of ε .

cases ($0.45 < I_{app} < 0.55$) approaching release-like behavior. With decreasing fast-slow separation, via increasing values of ε , the purely TW regime appears to be minimally effected initially but purely PM regimes gradually appear. This emergence occurs first at very strongly coupled oscillatory ranges approaching release-type behavior, continuing to grow, and then at values of I_{app} approaching the lower-left knee of the cubic and residing well within the release case. These regions of purely PM behavior expand and merge to occupy the entire lower right quadrant. With only moderate fast-slow separation, in panel E we see the appearance of a purely PM regime within the escape case in the upper left quadrant (shown here at 4x magnitude, with g_{ij} only extending to 0.025 rather than 0.1 as in the other panels) with clear, and seemingly highly linear, bifurcation transitions between all regimes. Only pitchfork bifurcations are observed at high fast-slow separation, with the appearance or disappearance of pacemaker patterns. Andronov-Hopf bifurcations begin to occur at higher values of ε , as it becomes possible for the system to exhibit purely PM behavior and gain or lose traveling wave patterns.

4.4.2 Fast-slow transitions in mono-biased motifs

Similar analysis of the effect of fast-slow separation on mono-biased inhibitory 3-node networks also appears to primarily control the appearance or disappearance of purely pacemaker regimes within the bifurcation diagrams. Unlike within the symmetric network, purely PM patterns appear to be able to exist at all values of ε explored (see Figure 4.14), but appear exclusively within weakly coupled release case systems at low values of ε . This is a result both greater propensity for release mechanisms to promote pacemaker-like behaviors and of the effect of a single connection that is much more weakly coupled than the rest. This results in one cell (here cell 3) have little or no inhibitory effect on another (here cell 1) and leads to systems in which blue and green pacemakers exist for low values of g_{31} release case examples (like in Figures 3.2, 4.9, and 5.6). High fast-slow

separation is not adequate to overcome this effect for this case. TW-only regimes have much greater dominance than previous, though, which is in part promoted by the single-connection effects by pushing systems within oscillatory and escape case ranges of I_{app} to drive more to clockwise- or counter-clockwise-only traveling wave (CTW or CCTW) patterns for weak or strong values of g_{31} , respectively. This asymmetry couples with the same effects discussed within the symmetric case, leading to much more prolific growth in general in pacemaker activity, leading to

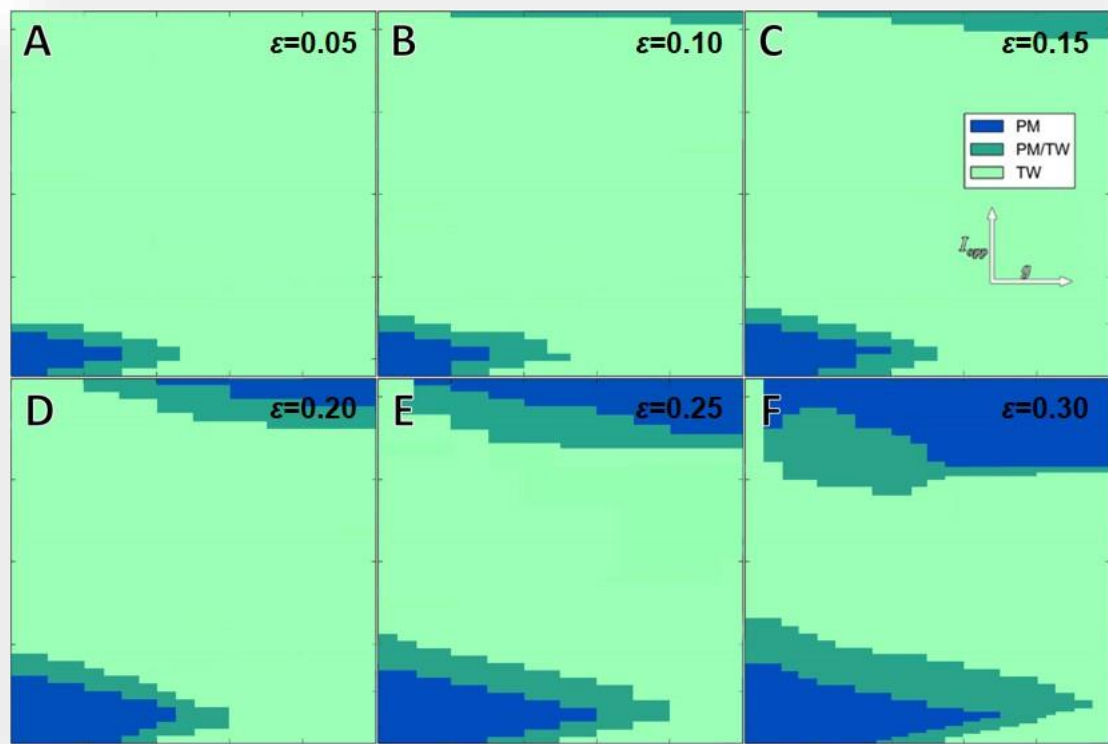


Figure 4.14 Increasing PM activity with decreased mono-biased fast-slow separation
Unlike in purely symmetric systems, we observe the formation of purely-PM regimes at high fast-slow separation (A) due to both asymmetric coupling and the propensity of the release mechanism to drive toward such rhythmic activity. Purely-TW regimes dominated at low values of ϵ , but are rapidly forced to share both escape and release ranges of I_{app} ($I_{app} < 0.45$ and $I_{app} > 0.55$, respectively), and then give up almost entirely any formation the escape case. Cases of phase-slip are not shown here, for simplicity, but grow to occupy broad stretches of the escape case and all low values of g_{31} with decreasing fast-slow separation. Parameters: $I_{app} = [0.39, 0.6]$, $\epsilon = 0.05, 0.1, 0.15, 0.2, 0.25$ and 0.30 , and $g_{ij} = 0.01$ except $g_{31} = [0, 0.025]$.

the appearance in Figure 4.14 of larger regions of both mixed PM/TW and purely PM behavior with decreasing fast-slow separation. This asymmetry also leads to phase-slip behavior not seen in symmetric systems that was discussed in Chapter 3 and is continued with discussion of a more detailed bifurcation diagram in the next sections. For simplicity, as a comparison to the symmetric transitions in TW and PM behaviors just discussed, phase-slip is not shown in Figure 4.14 and only the three different colored regimes are displayed. For more detail for the $\varepsilon = 0.30$ case, see either Figure 3.3 or Figures 4.15-19.

4.5 Detailed bifurcation analysis and overlay

In the pattern generation and bifurcation analysis performed in Chapters 2-3, difference was not made in the number of each type of pattern present and regimes with either 1 or 2 TWs were simply classified as TW generically (other than in the clockwise case in Figure 3.14), as were 1, 2, or 3 PMs as PM generically, etc. This permitted broad parameter sweeping for characteristic behaviors and transitions but did not tease out some additional specific bifurcation behavior existing within each of the PM, PM/TW, or TW regimes identified. Some of these specific transitions and bifurcations have been discussed within the context of specific examples in Chapter 3, where asymmetric motifs lead to additional bifurcation types, as well as earlier in this chapter in examples of each of the key bifurcations observed. More examples of unique rhythms and pattern-switching can be found in Chapter 5 as well, but here additional research has been made on the specific transitions and bifurcations within two of the key asymmetric motifs: the mono-biased and king-of-the-mountain (KOM) asymmetric motifs. In the following sections, specific examination of each key rhythm type (1- or 2-TW, 1-, 2-, or 3-PM, and PS) is performed and transitions are described in terms of each of the types of bifurcations outlined earlier in this chapter. This permits much more comprehensive detail than in the previous bifurcation diagrams in Chapters 2 and 3

and is done with these two specific motifs with an eye toward coupling of networks and potential future steps described in Chapters 6 and 7.

4.5.1 *Mono-biased bifurcation detail*

Previously, examination of the mono-biased system revealed broad regions of purely traveling wave behavior within oscillatory I_{app} ranges. This did not distinguish, however, between differences in clockwise and counter-clockwise traveling wave (CCT and CCTW, respectively) behaviors which are expected to dominate in one direction or the other with changes in a single connection, g_{31} . Although regions of purely TW behavior were minimal within the release and escape cases, mixed PM/TW patterns were prolific within the release case and at lower coupling strengths within escape cases approaching more oscillatory ranges, distinguishing between rhythms remains relevant here as well. Only standard saddle-node bifurcations are observed in this system with the appearance or disappearance of traveling waves, as opposed to the purely Andronov-Hopf bifurcations observed for these patterns in the symmetric motif.

Detailed examination in Figure 4.15 of traveling wave pattern formation separately from all other patterns reiterates the reverse dominance of these patterns, as seen in Figure 3.3, from that observed in symmetric systems, with TWs occurring primarily with weaker connectivity at lower g_{31} values for escape ranges of $I_{app} > 0.55$ and for stronger coupling at higher g_{31} values for release ranges of $I_{app} < 0.45$. A very restricted range of the bi-parametric (g_{31}, I_{app}) -space exists for which both traveling waves exist (lighter green region in the bifurcation diagram). This region extends upward and downward along I_{app} near full symmetry ($g_{31} = g_{ij} = 0.01$). System symmetry also dictates the transition point at which the clockwise traveling wave (CTW) to counter-clockwise traveling wave (CCTW) rhythm switch occurs with increasing g_{31} in regions with only one traveling wave (darker green region in the bifurcation diagram). Arrows in the figure indicate presence of saddle-node

bifurcations in which TW patterns are created or destroyed, via either the creation of both a FP-node and a saddle from an unstable point or collision of an FP-node and a saddle eliminating a rhythm and forming a repelling unstable point, and occur at every line in the system in this figure. Although emphasis here is primarily on changes due to g_{31} , Andronov-Hopf bifurcation may occur through vertical transitions in I_{app} at system symmetry in asymmetric systems and would be

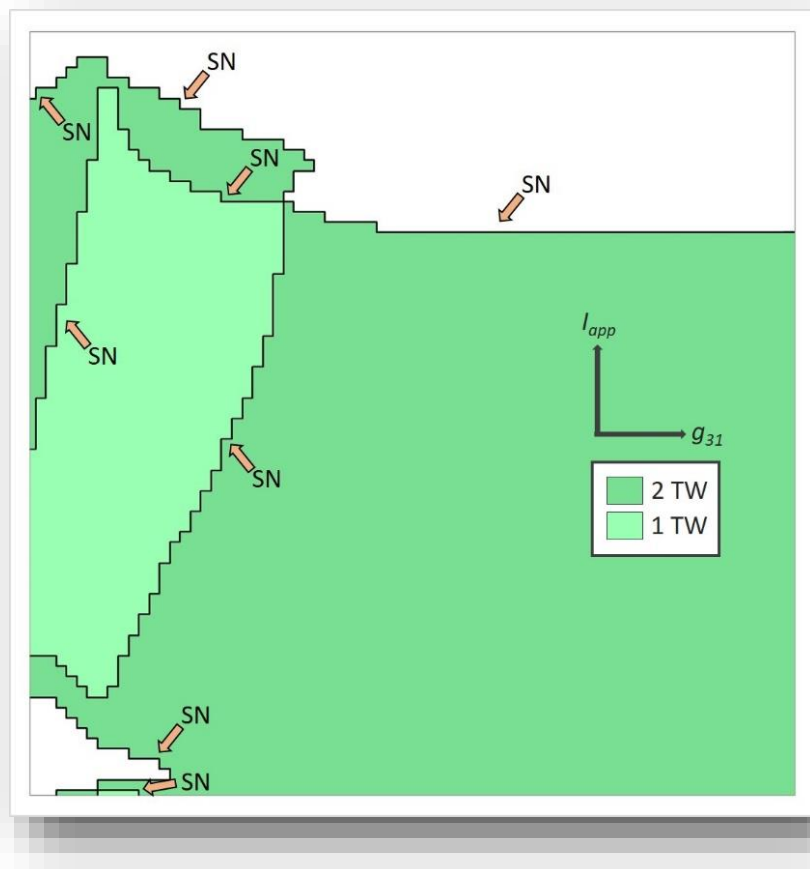


Figure 4.15 Traveling wave formation within mono-biased networks

Detailed examination of TW pattern formation separately from all other behavior reiterates reverse dominance of these patterns from that observed in symmetric systems (TW occurring typically at lower g_{31} for escape and higher g_{31} for release). Also observed is a very narrow range of bi-parametric (g_{31} , I_{app})-space in which both traveling waves exist (lighter green). This region extends upward and downward along I_{app} near full symmetry ($g_{31} = g_{ij} = 0.01$), line not shown here but visible in Figure 3.3. This vertical line also indicates the transition point at which CTW to CCTW rhythm switch occurs in regions with only one traveling wave (darker green), with CTW at $g_{31} < 0.01$ and CCTW at $g_{31} > 0.01$. All TW-related bifurcations occurring in the mono-biased motif are standard saddle-node bifurcations (indicated by arrows), with birth or destruction of both an FP-node and a saddle. Axes: $I_{app} = [0.39, 0.60]$, $g_{31} = [0, 0.01]$.

observed here as a direct vertical transition from two traveling waves to none. As can be seen, this type of bifurcation does not occur at all in the mono-biased motif.

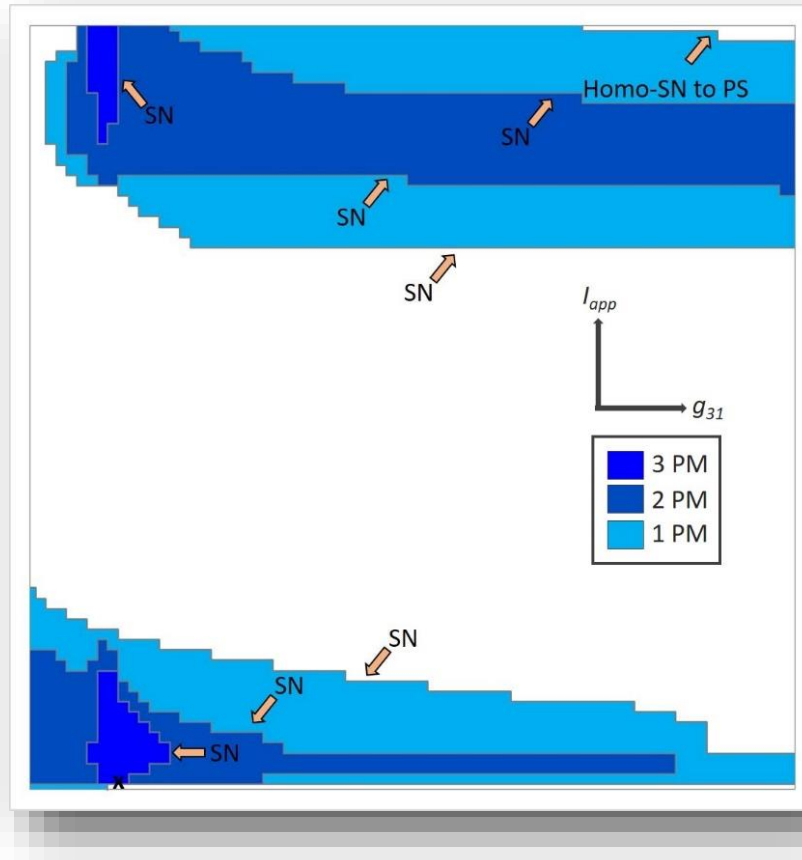


Figure 4.16 Pacemaker formation within mono-biased networks

Detailed examination of PM pattern formation separately from all other behavior also reiterates reverse dominance of these patterns from that observed in symmetric systems (occurring higher g_{31} for escape and lower g_{31} for release). Also observed is a very narrow range of bi-parametric (g_{31} , I_{app})-space in which all three PMs exist (bright blue). This region extends upward and downward along I_{app} near full symmetry ($g_{31} = g_{ij} = 0.01$), line not shown here but visible in Figure 3.3. This vertical line also indicates the transition point at which 1- and 2-PM rhythms (light and dark blue, respectively) gain or lose either the red PM, at values of $g_{31} < 0.01$, or blue PM, at values of $g_{31} > 0.01$, where these transitions occur. All PM-related bifurcations occurring in the mono-biased motif for 1-2, 2-3 PMs are standard SN bifurcations. Bifurcations gaining or losing the single blue or red PM are purely SN for release but may be either SN or homoclinic SN for escape, not all shown here with arrows but discussed in the body of text. A singular case of pitchfork bifurcation occurs with vertical transition of I_{app} at symmetry, marked by an x. Axes: $I_{app} = [0.39, 0.60]$, $g_{31} = [0, 0.01]$.

Detailed examination in Figure 4.16 of pacemaker formation separately from other patterns reiterates the reverse dominance of these patterns, as seen in Figure 3.3, from that observed in symmetric systems, with TWs occurring primarily with stronger connectivity at higher g_{31} values for escape ranges of $I_{app} > 0.55$ and for weaker coupling at lower g_{31} values for release ranges of $I_{app} < 0.45$. A very restricted range of the bi-parametric (g_{31}, I_{app}) -space exists for which all three pacemaker rhythms exist (bright blue region in the bifurcation diagram). This region extends upward and downward along I_{app} near full symmetry ($g_{31} = g_{ij} = 0.01$). System symmetry also dictates the transition point at which 1- and 2-pacemaker rhythms (light and dark blue, respectively) gain or lose either the red pacemaker, at values of $g_{31} < 0.01$, or blue pacemaker, at values of $g_{31} > 0.01$, where these transitions occur with increasing g_{31} in regions with only one or two pacemakers (light and dark blue regions in the bifurcation diagram, respectively). Arrows in the figure indicate presence of saddle-node bifurcations in which PM patterns are created or destroyed, via either the creation of both a FP- node and a saddle from an unstable point or collision of an FP-node and a saddle eliminating a rhythm and forming a repelling unstable point, and occur at every line in the system in this figure. For the release case, these are all standard saddle-node bifurcations. For the escape case, these may be either standard SN or homoclinic saddle-node bifurcations. Homoclinic cases only occur at or near transitions involving the formation of phase-slip, discussed next, with one example shown in the figure for the loss of a single red PM to phase-slip activity. Transition from phase-slip to generate a single blue PM, or both the blue and green PMs (not shown in figure), occurs below the line of symmetry at $g_{31} = g_{ij} = 0.01$ and only within escape values of $I_{app} > 0.55$. Although emphasis here is primarily on changes due to g_{31} , pitchfork bifurcation may occur through vertical transitions in I_{app} at system symmetry in asymmetric systems and would be observed here as a direct vertical transition from all three pacemaker

rhythms to none. An example of this bifurcation, denoted by an x in this figure, and in Figure 4.18, occurs only within the release case at near-knee proximity of the nullclines.

Detailed examination in Figure 4.17 of phase-slip formation separately from other patterns indicates that this transition occurs only within the escape ranges of $I_{app} > 0.55$ and for ranges of g_{31} coupling away from system symmetry. The gray regions within the figure indicate the presence

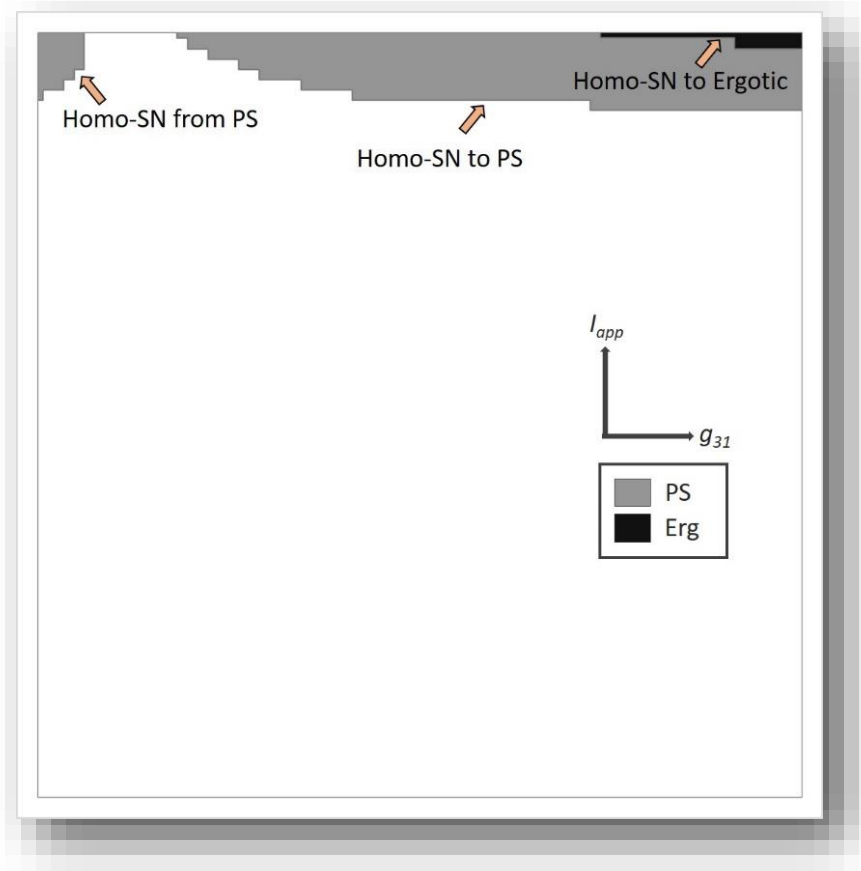


Figure 4.17 Phase-slip within mono-biased networks

Detailed examination of PS pattern formation separately from other behaviors indicates escape-case-only phase-slip away from full symmetry ($g_{31} = g_{ij} = 0.01$), line not shown here but visible in Figure 3.3. This vertical line also indicates the transition point at which the blue, or both blue and green, PMs appear, at values of $g_{31} < 0.01$, or either the red or blue PM disappear, at values of $g_{31} > 0.01$, where these transitions occur. The red PM is lost on the left side of the gray region, where $g_{31} > 0.01$, while the blue PM is lost on the right side in a unique case leading to an ergodic system in which no FPs or periodic behavior of any kind exists (see Figure 5.5) All PS-related bifurcations occurring in the mono-biased motif are homoclinic SN bifurcations, indicated by arrows. Axes: $I_{app} = [0.39, 0.60]$, $g_{31} = [0, 0.01]$.

of phase-slip, with the left region, where $g_{31} < 0.01$, exhibiting transition from phase-slip to blue, or blue and green PM, behavior through formation of a FP-node and a saddle (or two of each) where these align with those transitions in Figure 4.16. Collision of an FP-node and saddle results

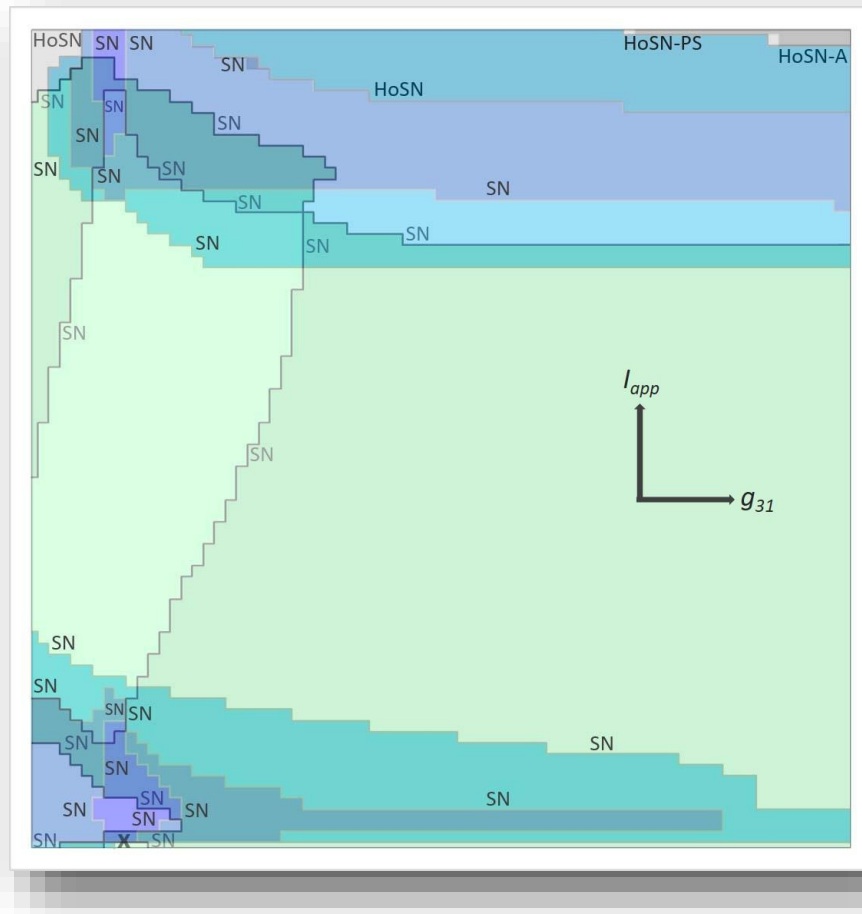


Figure 4.18 Detailed bifurcation transitions within mono-biased networks

Detailed overlay of bifurcations within the mono-biased asymmetric motif indicates a preponderance of standard SN bifurcation behavior, with several key cases of homoclinic SN bifurcation within the escape range of values for $I_{app} > 0.55$. It is important to note that two homoclinic SN bifurcations occur in sequence in a small number of cases where PM behavior appears within a system still exhibiting PS behavior, and can be observed by the light gray-blue region at the top left corner. Additionally, two homoclinic bifurcations also occur at the top right, where we observe two small light grey areas in which phase slip exists independently before being lost to ergodic behavior. A singular case of pitchfork bifurcation occurs with vertical transition of I_{app} at symmetry, marked by an x. Where possible, all transitions are clearly denoted but for complex cases near full symmetry, $g_{31} = g_{ij} = 0.01$, within release or escape cases refer to Figures 4.15-17. Axes: $I_{app} = [0.39, 0.60]$, $g_{31} = [0, 0.01]$.

in obliteration of a pacemaker rhythm and creation of phase-slip or ergotic behavior in mono-biased asymmetric systems. In the right region, where $g_{31} > 0.01$, This vertical line also indicates the transition point at which the blue, or both blue and green, PMs appear, at values of $g_{31} < 0.01$, or either the red or blue PM disappear, at values of $g_{31} > 0.01$, with the red PM disappearing on the left side of the gray region (see Figure 5.4) and the blue PM being lost on the right side to the formation of ergotic behavior in which no fixed points or periodic activity of any kind exists (see Figure 5.5 for example) All PS-related bifurcations occurring in the mono-biased motif are homoclinic saddle-node bifurcations, indicated by arrows in the figure.

Combining all three detailed analyses of the three key rhythm types, seen in Figure 4.18, provides a comprehensive view of the occurrence of the bifurcations described. Within the mono-biased asymmetric motif, only standard saddle-node and homoclinic saddle-node bifurcations occur, except for the singular case of pitchfork bifurcation at full symmetry for the release case system with near-knee proximity of the nullclines (shown with an x in Figure 4.16 but not here). Detailed analysis of bifurcations in this manner is expected to lead to better hypothesis development when coupling motifs within the framework of larger network circuitry, and will be demonstrated or alluded to for several cases in Chapters 6 and 7.

4.5.2 King-of-the-mountain bifurcation detail

Previously, examination of the king-of-the-mountain system revealed broad regions of purely pacemaker behavior within all I_{app} ranges. This did not distinguish, however, between differences in 1, 2, or 3 PM behaviors which are expected to dominate in one direction or the other with changes in two connections, $g_{31} = g_{32}$. Regions of purely TW behavior were observed primarily within oscillatory ranges between the release and escape cases, $0.45 < I_{app} < 0.55$, being largest at mid-range values where nullclines lead to the most generic oscillatory behavior. Mixed PM/TW

patterns most often occurred briefly for connectivity above symmetry, with a small region of such behavior around symmetry at near-knee proximity of the nullcline within the release case. Additional phase-slip behavior was observed for I_{app} below full symmetry, and additional in extreme escape cases in the upper right quadrant with strong g_{31} - g_{32} coupling. This connectivity framework is again dominated by the various saddle-node bifurcation, with Andronov-Hopf and pitchfork bifurcations only occurring at symmetry in some cases with vertical transitions in I_{app} . Detailed examination in Figure 4.19 of traveling wave pattern formation separately from other patterns emphasizes a narrow range of dominance of these patterns, as seen in Figure 3.11, with TWs occurring primarily around full system symmetry, $g_{31} = g_{32} = g_{ij} = 0.01$, and in or near fully-oscillatory systems with $0.45 < I_{app} < 0.55$. Most of the bi-parametric ($g_{31}=g_{32}, I_{app}$)-space for which these patterns exist is dominated exclusively by both traveling waves coexisting (lighter green region in the bifurcation diagram). This region extends upward and downward along I_{app} near full symmetry. A few singular cases of mono-TW behavior exist (darker green region in the bifurcation diagram), with such cases being dominated by clockwise patterns, for $g_{31} = g_{32} < 0.01$, and counter-clockwise patterns, for $g_{31} = g_{32} > 0.01$. Arrows in the figure indicate presence of saddle-node bifurcations in which TW patterns are created or destroyed, via either the creation of both a FP-node and a saddle from an unstable point or collision of an FP-node and a saddle eliminating a rhythm and forming a repelling unstable point, and occur at every line in the system in this figure. Heteroclinic saddle-node bifurcations occur with the appearance of both traveling waves from purely phase-slip behavior, discussed later, on the right side of the light green region where $g_{31} = g_{32} < 0.01$. Andronov-Hopf bifurcation may occur through vertical transitions in I_{app} at system symmetry in asymmetric systems and would be observed here as a direct vertical transition from two traveling waves to none. As can be seen, this type of bifurcation occurs only at symmetry for

the lower or upper bounds of the escape and release case values of I_{app} , respectively, or at near-knee proximity of the nullclines for the release case, and are indicated by o marks.

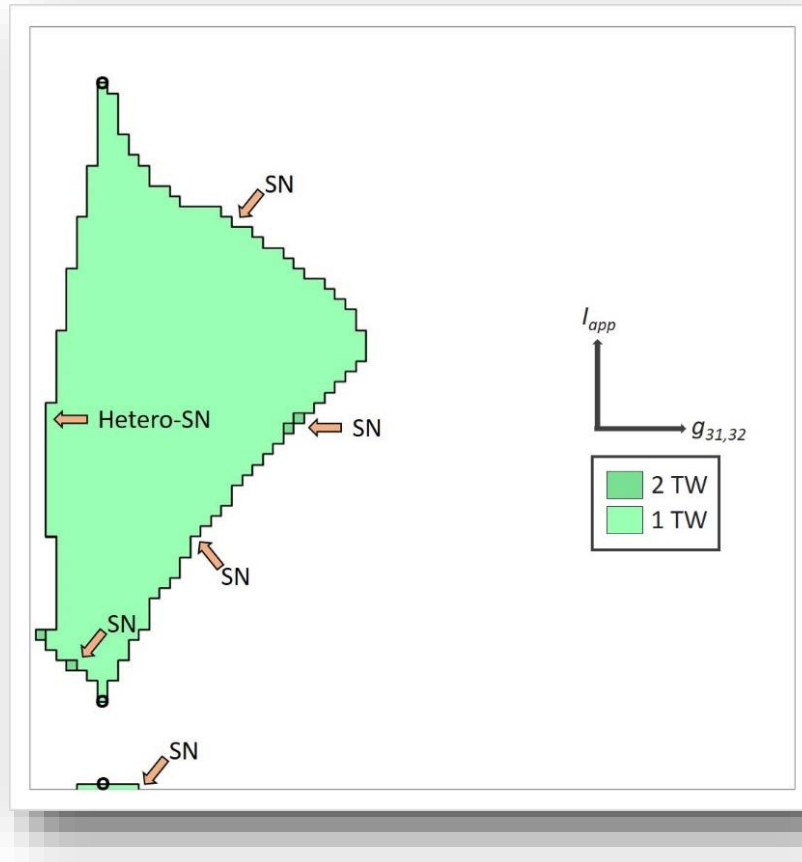


Figure 4.19 Traveling wave formation within KOM networks

Detailed examination of TW pattern formation separately from all other behavior emphasizes dominance of these patterns around full system symmetry, $g_{31} = g_{32} = g_{ij} = 0.01$, and in or near fully-oscillatory systems, with $0.45 < I_{app} < 0.55$. A singular exception exists in a small region of symmetry at near-knee proximity of the nullcline within the release case. Most bi-parametric ($g_{31}=g_{32}, I_{app}$)-space for which these exist is dominated by both TWs (lighter green region), extending upward and downward along I_{app} near full symmetry. Singular cases of mono-TW behavior exist (darker green regions), with such cases being dominated by either CTW, for $g_{31} = g_{32} < 0.01$, or CCTW, for $g_{31} = g_{32} > 0.01$. Most TW-related bifurcations in the KOM motif are standard SN bifurcations (indicated by arrows), with birth or destruction of both an FP-node and a saddle, a singular line of heteroclinic SN bifurcations occurring along the left edge where $g_{31} = g_{32} < 0.01$. AH bifurcation occurs through vertical transitions at symmetry at the bounds of 2-TW behavior, indicated by o marks. Axes: $I_{app} = [0.39, 0.60]$, $g_{31} = g_{32} = [0, 0.008]$.

Detailed examination in Figure 4.20 of pacemaker formation separately emphasizes dominance of these patterns across the bi-parametric ($g_{31}=g_{32}, I_{app}$)-space, with a narrow range extending upward and downward along I_{app} near full symmetry ($g_{31} = g_{32} = g_{ij} = 0.01$), line not shown here but visible in Figure 3.11, in which all three pacemakers exist (bright blue region in the bifurcation diagram).

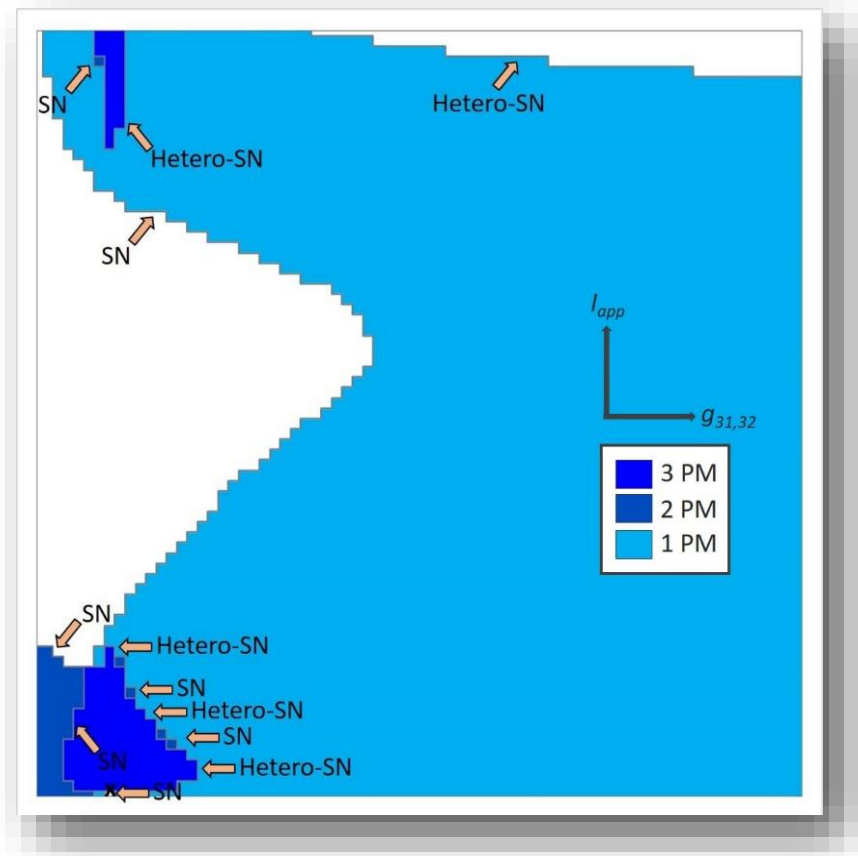


Figure 4.20 Pacemaker formation within KOM networks

Detailed examination of PM formation separately emphasizes dominance of these patterns across the bi-parametric ($g_{31}=g_{32}, I_{app}$)-space, with a narrow range extending upward and downward along I_{app} near full symmetry ($g_{31} = g_{32} = g_{ij} = 0.01$), line not shown here but visible in Figure 3.11, in which all three PMs exist (bright blue). This vertical line also indicates the transition point at which 1-PM rhythms (light blue) gain or lose the red PM, at values of $g_{31} = g_{32} < 0.01$ or $g_{31} = g_{32} > 0.01$, respectively, at the outer limits. A small region of 2-PM behavior, in which only the blue and green PMs occur, exists within the release case for $g_{31} = g_{32} < 0.01$. PM-related bifurcations (key areas noted by arrows) occurring in the KOM motif are evenly split between standard and heteroclinic SN for both release and escape, and exclusively standard SN for oscillatory ranges between. Transitions from 1-3, 3-1, or 1-none are all heteroclinic. Heteroclinic SN bifurcation from a single red PM to phase-slip is discussed in Figure 5.17. Axes: $I_{app} = [0.39, 0.60]$, $g_{31} = g_{32} = [0, 0.008]$.

This vertical line also indicates the transition point at which singular-pacemaker rhythms (light blue region in the bifurcation diagram) gain or lose the red pacemaker, at values of $g_{31} = g_{32} < 0.01$ or $g_{31} = g_{32} > 0.01$, respectively, at the outer limits. A small region of two-pacemaker behavior, in which only the blue and green pacemakers occur, exists within the release case, for $g_{31} = g_{32} < 0.01$, and is indicative of inherent pacemaker rhythm formation in release case systems at low synaptic coupling. Pacemaker-related bifurcations (noted by arrows in the bifurcation diagram) occurring in the king-of-the-mountain motif are undergone via a combination of both standard saddle-node and heteroclinic saddle-node bifurcations for both the release and escape case ranges of I_{app} , $I_{app} < 0.45$ and $I_{app} > 0.55$, respectively, and exclusively through standard saddle-node bifurcation for oscillatory ranges in between. Transitions from one-to-three, three-to-one, or one-to-no pacemakers are all heteroclinic in this system. Heteroclinic saddle-node bifurcation from a single red pacemaker is observed in the upper right quadrant for extreme escape cases with very strong coupling and is discussed in further detail in Figure 5.17. Although emphasis here is primarily on changes due to $g_{31} = g_{32}$, pitchfork bifurcation may occur through vertical transitions in I_{app} at system symmetry in asymmetric systems and would be observed here as a direct vertical transition from all three pacemaker rhythms to none. An example of this bifurcation, denoted an x in this figure, and in Figure 4.22, occurs only at the lower bounds of the release case at symmetry with near-knee proximity of the nullclines.

Detailed examination in Figure 4.21 of phase-slip formation separately from other patterns indicates that this transition occurs much more broadly for all oscillatory and escape case ranges of $I_{app} > 0.43$ away from full symmetry ($g_{31} = g_{32} = g_{ij} = 0.01$), line not shown here but visible in Figure 3.11. Before this line, one and two traveling wave patterns appear within oscillatory ranges of I_{app} , while red pacemaker behavior appears from phase-slip within escape ranges, for $g_{31} = g_{32}$

< 0.01 . Beyond the line of symmetry, there is a narrow region (light gray middle region in the bifurcation diagram) for which one or both traveling wave patterns are lost via heteroclinic saddle-node bifurcation. In addition, within the escape case (right gray region in the bifurcation diagram) where the red pacemaker is ultimately lost via a heteroclinic bifurcation, in which the FP-node and saddles collide to form a heteroclinic loop, and phase-slip behavior is observed (examples of this

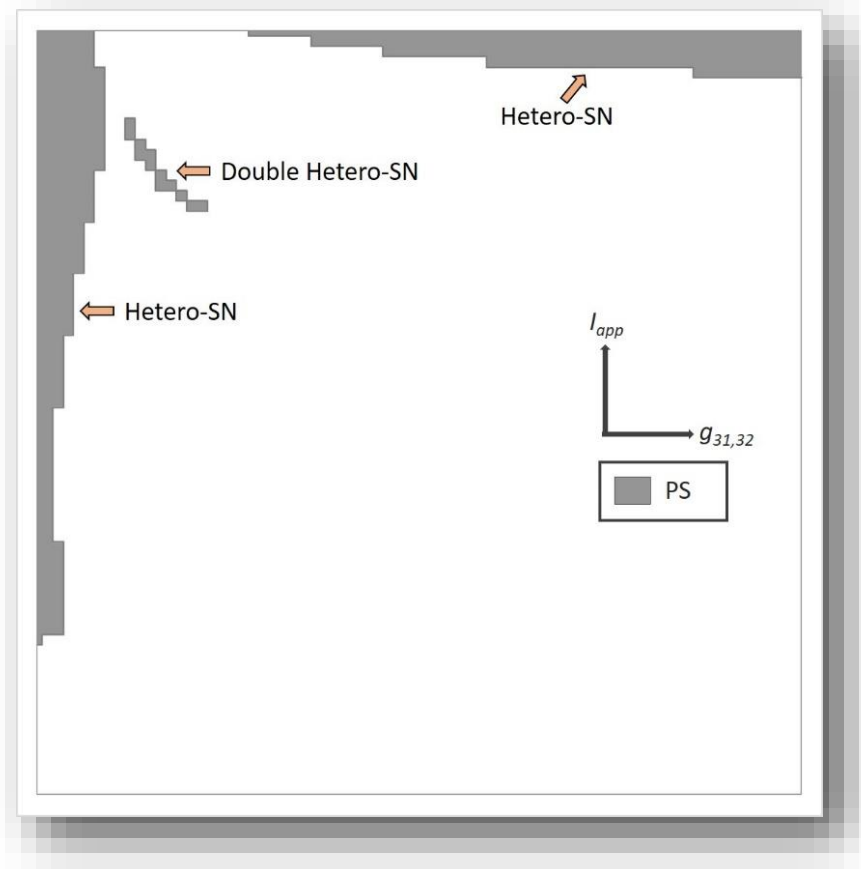


Figure 4.21 Phase-slip within KOM networks

Detailed examination of PS pattern formation separately from other behaviors indicates more extensive phase-slip away from full symmetry ($g_{31} = g_{32} = g_{ij} = 0.01$), line not shown here but visible in Figure 3.11, for all oscillatory and escape case ranges of $I_{app} > 0.43$. This vertical line also indicates the transition point at which 1- or 2-TW patterns appear within oscillatory ranges of I_{app} , or red PM behavior appears from PS within escape ranges, for $g_{31} = g_{32} < 0.01$. Above $g_{31} = g_{32} > 0.01$, there is a narrow region (light gray middle region) for which 1- or 2-TW patterns disappear and within the escape case (right region) where the red PM is lost and PS behavior is observed. All PS-related bifurcations occurring in the KOM motif are heteroclinic SN bifurcations, indicated by arrows. Axes: $I_{app} = [0.39, 0.60]$, $g_{31} = g_{32} = [0, 0.008]$.

can be seen and are discussed further in Figures 3.10 and 5.16. All phase-slip bifurcations occurring in the king-of-the-mountain motif are created via heteroclinic SN bifurcations, indicated by arrows in the figure.

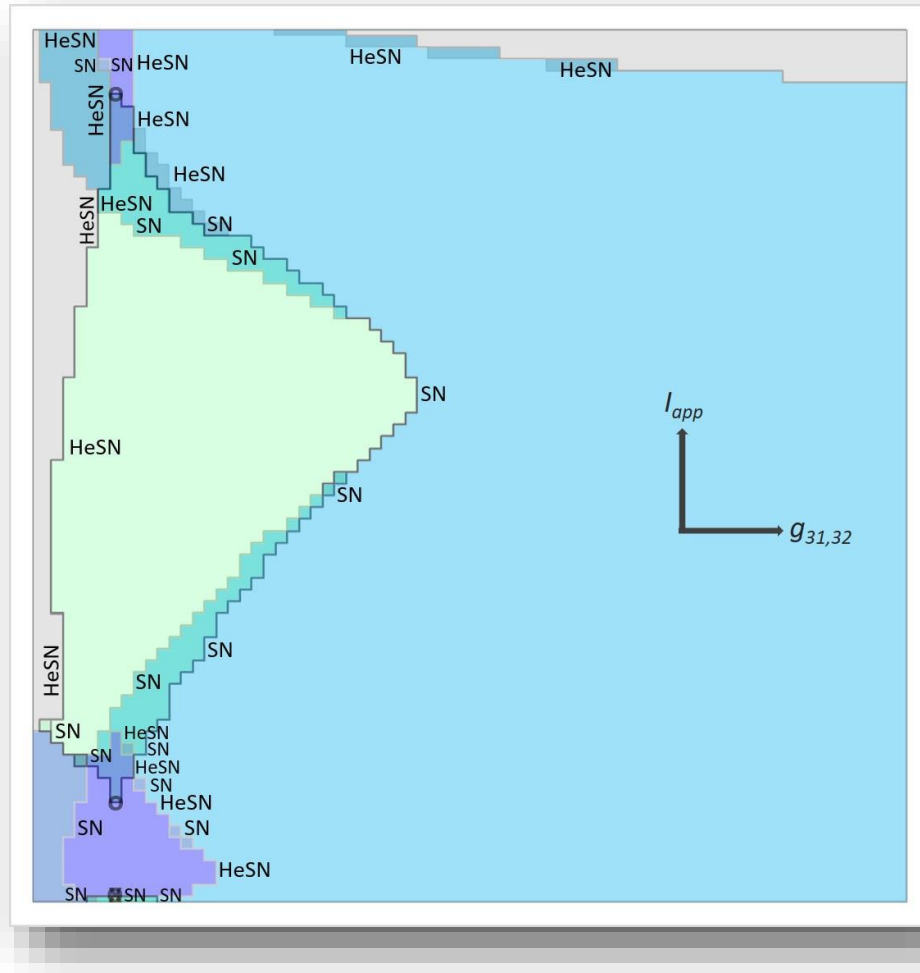


Figure 4.22 Detailed bifurcation transitions within KOM networks

Detailed overlay of bifurcations within the KOM asymmetric motif indicates extensive standard and heteroclinic SN bifurcation behavior. Below system symmetry ($g_{31} = g_{32} < g_{ij} = 0.01$), heteroclinic SN bifurcations are characteristic for movement from PS to either PM or TW rhythms, but have no occurrence within the release case, $I_{app} < 0.45$. Above system symmetry, extensive occurrence of heteroclinic SN bifurcation is observed in direct transitions from 3-to-1 PM regimes within both release and escape, and in the appearance or disappearance of PS in the escape case. No such behavior is observed for the oscillatory ranges in between. The existence of a single pitchfork and three AH bifurcations occurs only at system symmetry with vertical transitions of I_{app} , and is denoted by x and o marks, respectively. Where possible, all transitions are clearly denoted but for complex cases around full symmetry, $g_{31} = g_{32} = g_{ij} = 0.01$, within release or escape cases refer to Figures 4.19-21. Axes: $I_{app} = [0.39, 0.60]$, $g_{31} = g_{32} = [0, 0.008]$.

Combining all three detailed analyses of the three key rhythm types, seen in Figure 4.22, provides a comprehensive view of the occurrence of the bifurcations described. Within the king-of-the-mountain asymmetric motif, only standard saddle-node and heteroclinic saddle-node bifurcations occur with horizontal transitions in $g_{31} = g_{32}$. Three cases of Andronov-Hopf bifurcation are observed for both the release and escape cases at full symmetry ($g_{31} = g_{32} = g_{ij} = 0.01$), occurring with vertical transitions in I_{app} taking the system outside the lowermost and uppermost region of two traveling wave rhythms, respectively, and again for only the extreme release case at near-knee proximity of the nullclines (shown with o marks here and in Figure 4.19). A singular case of pitchfork bifurcation is also observed in the extreme near-knee release case (marked by an x here and in Figure 4.20).

4.6 Discussion and applications

Five key bifurcations have been observed in this research on inhibitory-connected gFN 3-node networks of cells: Andronov-Hopf, pitchfork, saddle-node, heteroclinic SN, and homoclinic SN bifurcations. Both AH and pitchfork bifurcations are found to only occur in cases for which system symmetry exists and all inhibitory connections are of equal strength. This situation exists for all parameters of symmetric motifs, and therefore all bifurcations within this motif are represented by one of these two bifurcations. For the four asymmetric motifs examined, this symmetry only exists along the vertical line represented by $g_{ij} = 0.01$, and we therefore only observe AH and pitchfork bifurcations with vertical movement in I_{app} . Due to the nature of behavior within the release case system at near-knee proximity of the nullclines, $I_{app} < 0.40$, the occurrence of these bifurcations may be observed as many as two times each within the release case and at most once within the escape case. In the mono-biased network, no observations of pitchfork bifurcations are seen at all. Within the king-of-the-mountain network, the only case of an AH bifurcation exists at the near-

knee proximity case just described. These results are summarized in Table 4.1. Standard SN bifurcations dominate all of the asymmetric motifs, as these bifurcations essentially replace both AH and pitchfork for creation or destruction of traveling wave or pacemaker rhythms, respectively, in asymmetric settings, and typically for cases in which there is a single rhythm gained or lost. Heteroclinic SN bifurcations occur extensively within the motifs with double-connection changes, due to the fact that two parameters are required to change in order for heteroclinic transitions to occur, with both pairwise-biased and king-of-the-mountain exhibiting cases of these bifurcations across nearly the full range I_{app} , and both above and below system symmetry. In both cases they are more common in escape ranges of $I_{app} > 0.55$, and there is an interesting switch in the occurrence of heteroclinic SN bifurcations with phase-slip in which they occur in oscillatory ranges of I_{app} only for strong connectivity, $g_{31} = g_{13} \gg g_{ij} = 0.01$, in pairwise-biased systems and weaker connectivity, $g_{31} = g_{32} < g_{ij} = 0.01$, in king-of-the-mountain systems. Homoclinic SN bifurcations occur prolifically within escape range values of $I_{app} > 0.55$ within mono-biased asymmetric networks, both above and below system symmetry. In this work, with focus primarily on bifurcations with horizontal movement in the bi-parametric (g_{31}, I_{app}) -space, this bifurcation is only observed in the mono-biased motif due to the fact that homoclinic transitions can occur only in cases where a single parameter is changed. This does not mean that such bifurcations cannot also occur via vertical transitions in I_{app} as has been observed for both AH and pitchfork bifurcations. An example can be observed indirectly by comparing Figures 3.4(A) and 5.16, where we see a single CTW pattern that is eliminated via collision of the FP-node and saddle seen in Figure 3.5(A), resulting in the diagonal phase-slip rhythm discussed in Figure 5.16. Such cases are not identified in this work, or summarized in the table, but it is important to note that they exist for both heteroclinic and homoclinic SN bifurcations.

5 FURTHER POLYRHYTHMICITY AND POST-INHIBITORY REBOUND

In previous chapters, the focus has been on broader characteristics that can be used to identify and describe shifts in pattern generation across the bi-parametric (g_{ij}, I_{app}) -space. Brief discussion of the effects of fast-slow separation has also been alluded to, but will be discussed in more detail here. Additional polyrhythmicity is also discussed, with specific exceptional cases of rhythm switching, basin-acquisition, and phase-slip behavior with both semi-phase-lock and larger scale rhythmicity. These are added to by several additional cases of asymmetry that do not fall strictly within the five key motifs described thus far. Finally, experiments involving implementation of the post-inhibitory rebound mechanism are discussed with general trends in behavior outlined similarly to what was done in the escape and release mechanism framework, but at a more macro level in which specific cases are limited to I_{app} ranges falling within what would have typically characterized either of those cases or the purely oscillatory ranges between $(0.45 < I_{app} < 0.55)$.

5.1 Additional asymmetric pattern generation

In this section, description of specific asymmetric rhythm switching and basin-acquisition, as well as of unique regions of mono- or poly-invariant circle behaviors, is broken into the general framework within three of the key asymmetric motifs described in detail: (1) Mono-biased systems with a single varying connection, g_{31} , (2) Pairwise-biased systems with two reciprocally changing connections, g_{31} and g_{13} , and (C) King-of-the-mountain (KOM) systems of a single cell with two outgoing varying connections, g_{31} and g_{32} . Less uniquely different pattern generation behavior is possible within the clockwise-biased system but one example of slight asymmetry in this manner is shown in conjunction with strong g_{31} coupling within the mono-biased section. Special emphasis is given here on the types of bifurcations discussed in Chapter 4, and particularly to specific variations in phase-slipping and transient phase-locking behaviors.

5.1.1 Further rhythm switching in mono-biased motifs

For mono-biased systems with a single varying connection, g_{31} , asymmetric transitions in pattern generation and switching are readily obtained away from system symmetry for all ranges of I_{app} . As described in Chapters 3 and 4, these transitions occur almost exclusively via saddle-node bifurcations and often in a homoclinic manner. In Figure 5.1, we observe $(\Delta_{12}, \Delta_{13})$ -Poincaré return maps for a specific case of near-knee release case, where the proximity of the fast cubic and slow sigmoidal nullclines near the lower left knee of the cubic nullcline can drive highly unique pattern generation with very small changes in synaptic coupling. Distinct rhythm switching behavior occurs with increasing mono-biased asymmetric coupling, and traveling wave formation can be induced at low values of I_{app} within this motif. At very weak coupling strength, only the blue pacemaker rhythm dominates for all initial conditions. With increased inhibitory coupling from cell 3 to cell 1, a critical value of g_{31} exists for which a homoclinic bifurcation leads to formation of an invariant circle near the location of the traditional purple CCTW at $(\Delta_{12}, \Delta_{13}) \approx (2/3, 1/3)$. This invariant circle exhibits unique jitter behavior in which traces trapped in this region oscillate in proximity to the purple CCTW, and appear to be traveling waves that jitter, or shift slightly back and forth in relation to one another. With increasing synaptic coupling, this invariant circle acquires an increasingly large basin of attraction before collapsing as the repeller inside this invariant circle undergoes additional homoclinic saddle-node bifurcation and becomes a traditional stable CCTW FP attractor with the black CTW simultaneously taking over what had been the blue basin of attraction through a saddle-node bifurcation. The purple CCTW basin of attraction gradually increases in size with increased synaptic coupling, taking over the black basin of attraction via an additional homoclinic saddle-node bifurcation, with another brief invariant circle appearing near $(\Delta_{12}, \Delta_{13}) \approx (1/3, 2/3)$ before the black attractor ultimately collides with the

remaining nearby saddle and is obliterated. This type of rhythm transition is indicative of systems in which plasticity in synaptic coupling can lead to short- or long-term pattern transitions that could alternate back and forth as the strength of this connection strengthens or weakens.

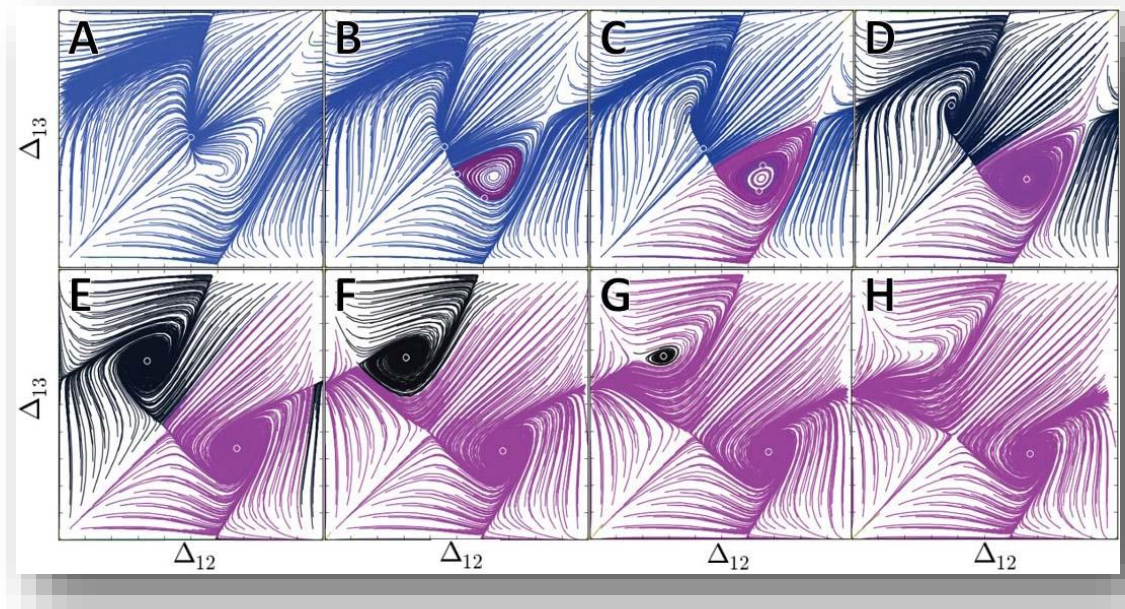


Figure 5.1 Near-knee rhythm switching in mono-biased motifs

$(\Delta_{12}, \Delta_{13})$ -Poincaré return maps for the near-knee release case show distinct rhythm switching behavior with increasing mono-biased asymmetric coupling. At very weak coupling strength (A), only the blue pacemaker rhythm is possible. At a critical value of g_{31} , a homoclinic bifurcation occurs and an invariant circle appears near $(\Delta_{12}, \Delta_{13}) \approx (2/3, 1/3)$ with unique jitter behavior (B). With increasing synaptic coupling, this invariant circle acquires an increasingly large basin of attraction (C) before collapsing as its repeller becomes a traditional stable CCTW FP attractor with the black CTW taking over the blue basin of attraction through a saddle-node bifurcation (D). The purple CCTW basin gradually takes over the black basin of attraction, with another brief invariant circle appearing near $(\Delta_{12}, \Delta_{13}) \approx (1/3, 2/3)$ before the black attractor collides with the nearby saddle and is obliterated. Parameters: $I_{app} = 0.389$, $g_{ij} = 0.001$ except $g_{31} = 0, 0.0004, 0.0006, 0.0007, 0.001, 0.0012, 0.0014, \text{ and } 0.0016$.

A similar transition in behavior, but further from the near-knee release case proximity just described, can be seen in Figure 5.2 where this transition includes similar transient jitter behavior occurring through homoclinic saddle-node bifurcation but with no long-term TW formation. Beginning at full symmetry with $g_{31} = g_{ij} = 0.001$, the system in this example exhibits fully

symmetric PM behavior, with all three pacemakers possible, which disappears as clockwise symmetry is broken with increasing g_{31} strength. Breaking this clockwise symmetry initially gives greater dominance to the red PM pattern due to its asymmetric power to inhibit cell 1, and leads directly to the potential for a transient invariant circle only in the CCTW region due to the existence now of overall increased counter-clockwise connectivity. These bifurcations occur as a green-to-red saddle in the upper left quadrant collapses with the red PM fixed point via SN bifurcation while

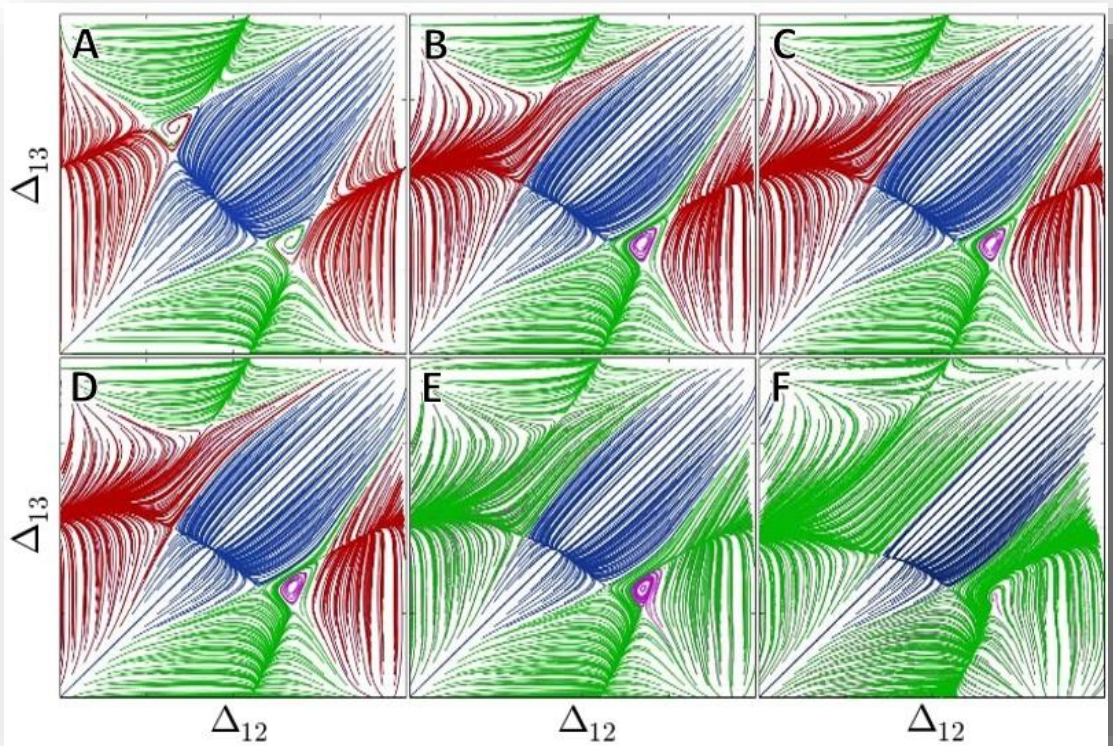


Figure 5.2 PM basin acquisition via fleeting jitter in a mono-biased network

Beginning at full symmetry with $g_{31} = g_{ij} = 0.001$, the system exhibits fully symmetric PM behavior which disappears as clockwise symmetry is broken with increasing g_{31} strength. The green-to-red saddle in the upper left quadrant collapses via saddle-node bifurcation a homoclinic bifurcation occurs near $(\Delta_{12}, \Delta_{13}) \approx (2/3, 1/3)$, in which the transient formation of an invariant circle with purple CCTW behavior is observed for a highly restricted range of g_{31} coupling strengths (B-D). This jitter effect acquires a small basin of attraction (E) before ultimately disappearing as its node and the saddle between it and the green PM fixed point near $(\Delta_{12}, \Delta_{13}) = (1/2, 0)$ collide and obliterate one another. Parameters: $I_{app} = 0.400$, $g_{ij} = 0.001$ except $g_{31} = 0.001, 0.00152, 0.00154, 0.00156, 0.0019$, and 0.0036 .

the homoclinic bifurcation occurs near $(\Delta_{12}, \Delta_{13}) \approx (2/3, 1/3)$, in which the transient formation of an invariant circle with purple CCTW behavior is observed for a highly restricted range of g_{31} coupling strengths. The red PM pattern disappears via saddle-node bifurcation as the saddle between it and the green PM near the invariant circle collide. The remaining jitter effect acquires a small increasing basin of attraction before ultimately disappearing as its node and the saddle between it and the green PM fixed point near $(\Delta_{12}, \Delta_{13}) = (1/2, 0)$ collide and obliterate one another. Ultimate pattern formation in this system will lead to bi-modal PM behavior in which either the green or blue PM will result depending on initial conditions or a external stimulus shifting relative phase-lags between cells.

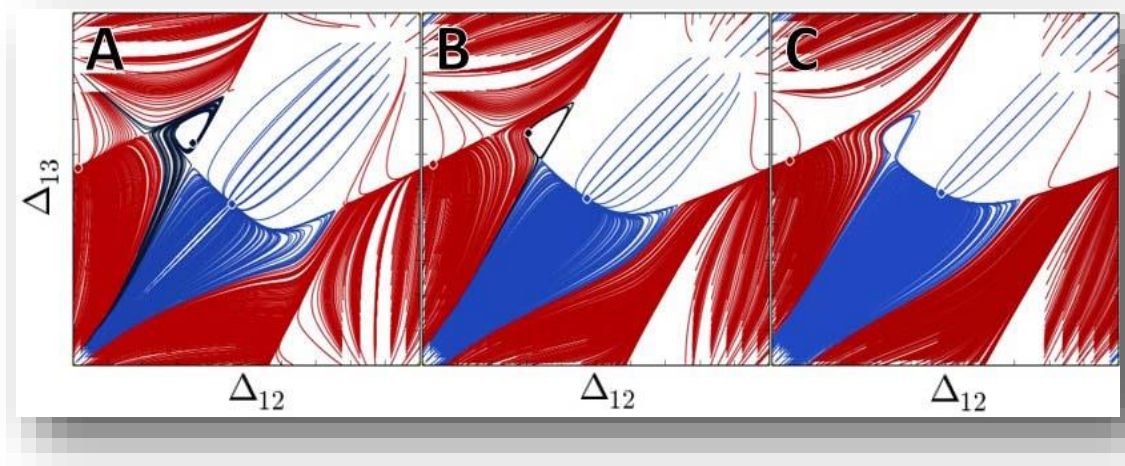


Figure 5.3 TW basin acquisition via invariant circle in mono-biased network

Basin acquisition of the black CTW by the red PM occurs via a homoclinic saddle-node bifurcation with transient formation of an invariant circle near $(\Delta_{12}, \Delta_{13}) \approx (1/3, 2/3)$. As in Figure 5.2, this is due to increases in g_{31} coupling strength above system symmetry at $g_{31} = g_{ij} = 0.001$. The basin for which this jitter effect occurs diminishes in size before disappearing as its repeller node and the saddle between it and the red PM fixed point, near $(\Delta_{12}, \Delta_{13}) = (0, 1/2)$, collide and obliterate one another. Parameters: $I_{app} = 0.582$, $g_{ij} = 0.001$ except $g_{31} = 0.0012162$, 0.0016216 , and 0.0021622 .

In Figure 5.3, an example of more traditional asymmetry in which a black CTW pattern coexisted with both red and blue PMs within escape ranges of I_{app} . In panels A and B, the formation of an

invariant circle with jitter behavior around the CTW, near $(\Delta_{12}, \Delta_{13}) \approx (1/3, 2/3)$, has occurred with increasing g_{31} coupling strength above system symmetry at $g_{31}=g_{ij}=0.001$, with basin acquisition of the black CTW by the red PM occurring via a homoclinic saddle-node bifurcation like that observed in the previous two examples. The basin for which this jitter effect occurs diminishes in size before disappearing as its repellor node and the saddle between it and the red PM fixed point, near $(\Delta_{12}, \Delta_{13}) = (0, 1/2)$, collide and obliterate one another and again lead to bi-modal PM behavior in which either the red or blue PM dominate based on initial conditions or external pulse stimuli or connectivity within larger networks.

Finally, within purely mono-biased asymmetric systems, a transition in rhythmicity can occur (Figure 5.4) at near-knee proximity of the nullclines in the escape case, where the proximity of the fast cubic and slow sigmoidal nullclines near the upper right knee of the cubic can drive the network at strong g_{31} coupling to the point where no attractors, repellers, or saddles exist any longer and the system cycles in a seemingly incoherent manner with quasi periodic covering of the entire 2-D torus occurs with no stable repeating rhythms of any kind. This ergotic behavior is only observed in this system for escape case ranges of $I_{app} > 0.55$, with regions of this specific behavior identified in the upper right corner of the bifurcation diagram detail in Figures 4.17 and 4.18. In this example, a blue PM attractor, near $(\Delta_{12}, \Delta_{13}) = (0, 1/2)$, already coexists with unique phase-slip behavior leading to apparent regular slipping of the system diagonally through ranges of $(\Delta_{12}, \Delta_{13})$ connecting periods of seemingly green or red PM alignment. With increasing g_{31} connectivity, which is already at very strong coupling, the blue basin of attraction decreases in size along the $(\Delta_{12}, \Delta_{13})$ diagonal as the saddles on either side of it converge on the fixed-point node and obliterate one another via homoclinic saddle-node bifurcation.

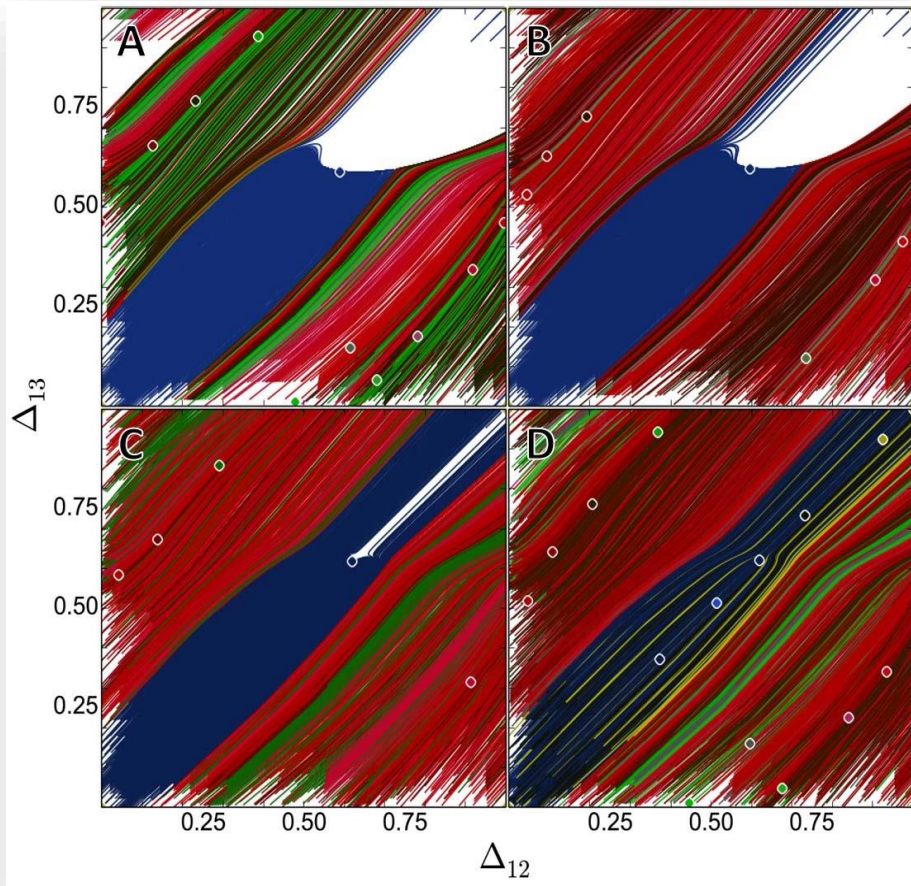


Figure 5.4 Ergodic torus in a mono-biased escape case network

An example of homoclinic saddle-node bifurcation within the escape case ranges of $I_{app} > 0.55$ leading to ergodic torus behavior, in which no stable patterns or coherent rhythmicity of any sort exists any longer. A blue PM attractor, near $(\Delta_{12}, \Delta_{13}) = (0, 1/2)$, coexists with phase-slip behavior leading to apparent regular slipping of the system diagonally through ranges of $(\Delta_{12}, \Delta_{13})$ connecting brief periods of seemingly green or red PM alignment. With increasing g_{31} connectivity, already at very strong coupling, the blue basin of attraction decreases in size as the saddles on either side converge on the fixed-point and obliterate one another. With collapse of these final saddles and node, no attractors, repellers, or saddles exist any longer and the system cycles in a seemingly incoherent manner with quasi periodic covering of the entire 2-D torus. Regions of this specific behavior can be observed in the upper right corner of the bifurcation diagram detail in Figures 4.17 and 4.18. Parameters: $I_{app} = 0.597$, $g_{ij} = 0.001$ except $g_{31} = 0.007027, 0.0077027, 0.0090541$, and 0.0093243 .

An additional unique example of slight clockwise asymmetry in conjunction with increasingly strong g_{31} coupling can be seen in Figure 5.5, and is included here even if not purely mono-biased

asymmetry. Here basin-switching behavior is observed, in which the red PM node and right saddle between the red and blue PM basins of attraction collide and eliminate one another as the blue PM acquires both basins of attraction via a heteroclinic saddle-node bifurcation. This shift from traditional saddle-node or homoclinic saddle-node bifurcation typically observed in mono-biased systems occurs as a direct result of manipulation of more than one key parameter, with both g_{31} and clockwise asymmetry coexisting. The red basin joins the blue PM basin as a direct result of interior occurrence of the trajectories on the blue side of the incoming separatrix of the right blue-green saddle, near $(\Delta_{12}, \Delta_{13}) = (4/7, 1/3)$. With additional increasing g_{31} coupling, and further movement of the instability, a heteroclinic connection between saddles occurs and the incoming trajectories switch side and join the green PM basin of attraction.

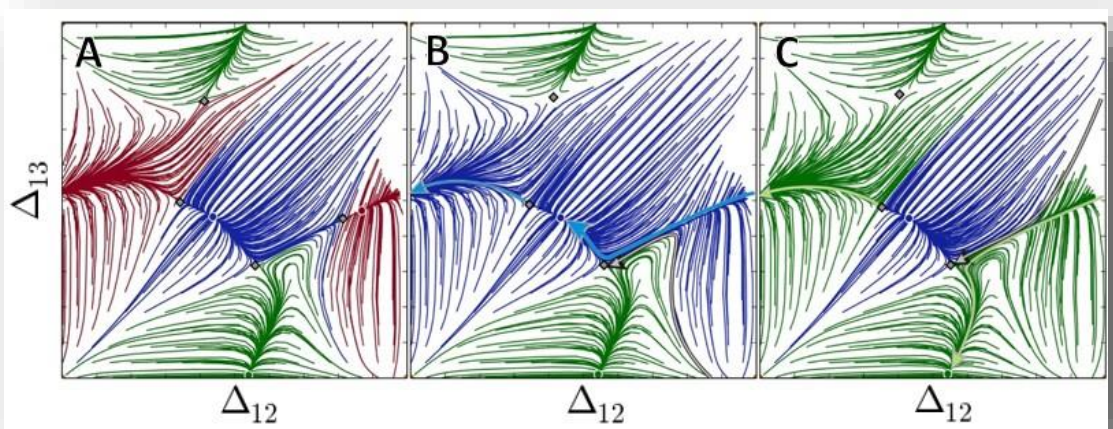


Figure 5.5 Basin-switching in a nearly mono-biased network

An example basin-switching behavior in which the red PM node and right red-blue saddle collide and eliminate one another as the blue PM acquires both basins of attraction. The red basin joins the blue due to interior occurrence of the trajectories on the blue side of the incoming separatrix of the right blue-green saddle, near $(\Delta_{12}, \Delta_{13}) = (4/7, 1/3)$. With additional increasing g_{31} coupling, a heteroclinic connection between saddles forms and the incoming trajectories switch sides and join the green PM basin of attraction. It is important to note that this example of mono-biased increase in g_{31} differs from others shown in previous chapters, where full symmetry existed in the remaining connections. Here there is slight increased counter-clockwise connectivity. Parameters: $I_{app} = 0.400$, $g_{12} = g_{23} = 0.0038$, $g_{13} = g_{32} = g_{21} = 0.0041$, $g_{31} = 0.0061$, 0.0070 , and 0.0071 .

5.1.2 Further rhythm switching in pairwise-biased motifs

For pairwise-biased systems with two varying connections, g_{31} and g_{13} , asymmetric transitions in pattern generation and switching are again readily obtained away from system symmetry for all ranges of I_{app} . As described in Chapters 3 and 4, these transitions occur almost exclusively via saddle-node or heteroclinic saddle-node bifurcations. As in the example in Figure 5.1, here we observe a system in which a blue pacemaker rhythm coexists with an invariant circle near $(\Delta_{12}, \Delta_{13}) = (2/3, 1/3)$. As in Figure 5.5, additional asymmetry is introduced here, here with g_{13} held at half the strength of system symmetry, at $g_{13}=0.005$, but with g_{31} synaptic coupling decreasing in strength from symmetry at $g_{31}=g_{ij}=0.001$ in a mono-biased fashion. With decreasing g_{31} coupling, the blue PM basin of attraction is consumed by the purple invariant circle through heteroclinic saddle-node bifurcation in saddle-node to invariant circle, or SNIC-like, behavior. At a critical value of g_{31} , a heteroclinic loop between the saddles occurs and a system with two different coexisting invariant circles exists, one with s-shaped phase-slip behavior passing through regions that once characterized the red PM, black CTW, and blue PM patterns. This phase-slip pattern then consumes the basin of attraction of the purple invariant circle as its node and remaining saddle collide and eliminate one another. This behavior then converges to stereotypical phase-slip, like that existing in typical pairwise-biased asymmetric systems described in Chapter 4. All initial condition space solutions converge and remain on this phase-slip path, with regular repeating phase shifts passing through regions of all what used to be the standard rhythm patterns (transient seemingly red PM patterns shifting to black CTW, then through blue PM, and purple CCTW rhythms before returning to red PM behavior, and repeating continuously) laying between the position of the remaining saddle near the traditional green PM FP location near $(\Delta_{12}, \Delta_{13}) = (1/2, 0)$ and $(1/2, 1)$. Examples of these temporary shifts in phase-lag behavior can be observed in panel

E' , along with three traces at the lower right showing shifts in seeming PM to TW or vice versa slipping. Traces correspond to the transitions indicated by the arrows in the phase-basin representation in E' .

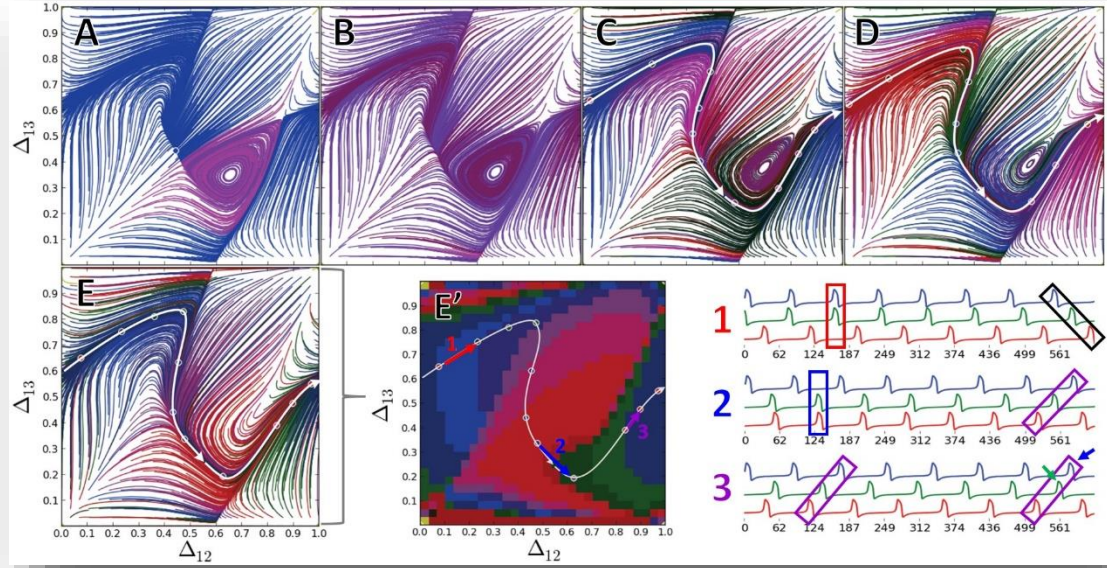


Figure 5.6 Invariant circle multiplicity in pairwise-biased systems

A system in which a blue PM coexists with an invariant circle near $(\Delta_{12}, \Delta_{13}) = (2/3, 1/3)$. Additional asymmetry exists, with g_{13} connectivity weak, at $g_{13} = 0.005$, and g_{31} decreasing in strength from symmetry beginning at $g_{31} = g_{ij} = 0.001$. With decreasing g_{31} coupling, the blue PM basin of attraction is consumed by the purple invariant circle via heteroclinic saddle-node bifurcation in SNIC-like behavior. At a critical value of g_{31} , a heteroclinic loop between saddles forms and two different invariant circles coexist, one purple SNIC-like case and one with s-shaped phase-slip passing through regions that once characterized the red PM, black CTW, and blue PM FP locations. This phase-slip then consumes the purple invariant circle basin as its node and remaining saddle collide. This converges to stereotypical phase-slip existing in typical pairwise-biased asymmetric systems, as $g_{31} = g_{13}$. All solutions converge to this path, with repeating phase shifts passing through regions of all 4 standard rhythm patterns (red PM \rightarrow black CTW \rightarrow blue PM \rightarrow purple CCTW \rightarrow red PM) occurring between the remaining saddle near $(\Delta_{12}, \Delta_{13}) = (1/2, 0)$ and $(1/2, 1)$. Examples of shifts in phase-lag can be seen in E' and the three traces at the lower right, indicated by the arrows in the phase-basin representation shown in E' . Parameters: $I_{app} = 0.413$, $g_{ij} = 0.001$ except $g_{13} = 0.0005$ and $g_{31} = 0.001, 0.0009, 0.0008, 0.0007, 0.0006$.

In Figure 5.7, an example is observed of a pairwise-biased system in which an unstable invariant circle, or ‘river’, along the Δ_{12} -axis repels all trajectories away and toward one of the two traveling wave fixed points, near $(\Delta_{12}, \Delta_{13}) = (1/3, 2/3)$ and $(2/3, 1/3)$. With increasing $g_{13}=g_{31}$ coupling strength, the two remaining TW FPs each approach one of the remaining black-purple saddles, ultimately colliding and eliminating each other in two simultaneous heteroclinic saddle-node bifurcations. All solutions converge to this invariant circle with left-moving phase-slip behavior, with cells 1 and 3 remaining in quasi-antiphase, $\Delta_{13} \approx 0.5$, while cell 2 fires with shorter period slips continuously leftward in traces of bursting activity.

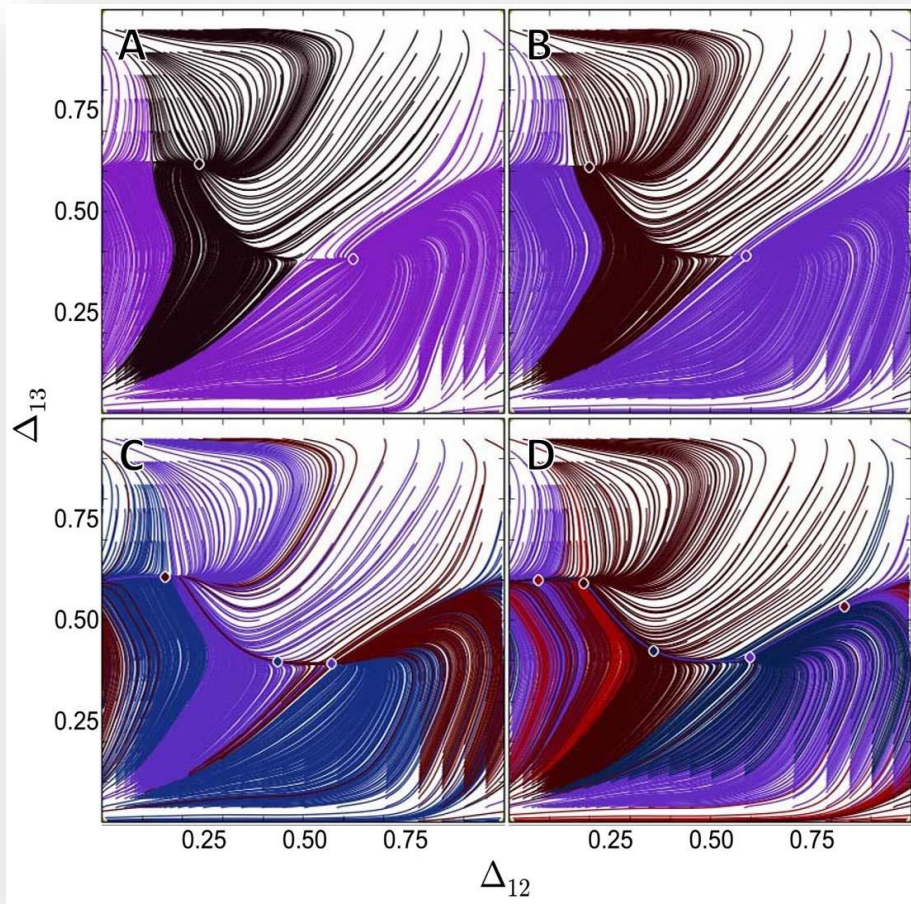


Figure 5.7 Heteroclinic SN bifurcation in pairwise-biased systems

Example of a pairwise-biased system with an unstable invariant circle, or ‘river’, along the Δ_{12} -axis which repels all trajectories away and toward one of the two TW fixed points (A), near $(\Delta_{12}, \Delta_{13}) = (1/3, 2/3)$ and $(2/3, 1/3)$. With increasing $g_{13} = g_{31}$ connectivity, each of the remaining FPs approach one of the two remaining black-purple saddles, ultimately colliding and eliminating each other in two simultaneous heteroclinic saddle-node bifurcations. All solutions converge to this invariant circle with left-moving phase-slip behavior, with cells 1 and 3 remaining in quasi-antiphase, $\Delta_{13} \approx 0.5$, while cell 2 fires with shorter period slips continuously leftward in traces of bursting activity. Parameters: $I_{app} = 0.5006$, $g_{ij} = 0.001$ except $g_{13} = g_{31} = 0.001, 0.0023649, 0.0027027, 0.0028378, \text{ and } 0.0031081$.

ultimately colliding and eliminating each other in two simultaneous heteroclinic saddle-node bifurcations. All initial condition space solutions converge to this invariant circle with left-moving phase-slip behavior, cells 1 and 3 remaining in quasi-antiphase, $\Delta_{13} \approx 0.5$, with oscillatory left- and right-ward jitter, while cell 2 fires with shorter period and appears to slip continuously leftward in observation of individual traces of bursting activity in this system.

5.1.3 *Further rhythm switching in KOM motifs*

For KOM systems with two varying connections, g_{31} and g_{32} , asymmetric transitions occur away from system symmetry for all ranges of I_{app} . As described in Chapters 3 and 4, and in the pairwise-biased systems, these transitions occur almost exclusively via saddle-node or heteroclinic saddle-node bifurcations. In Figure 5.8, like the previous example, a system in which a pair of heteroclinic saddle-node bifurcations occurs is seen, as the traveling wave fixed points, near $(\Delta_{12}, \Delta_{13}) = (1/3, 2/3)$ and $(2/3, 1/3)$, each collide with one of the black-purple saddles and obliterate one another with increasing $g_{31} = g_{32}$ coupling. Unlike in the preceding case, this leads to the disappearance of both black and purple FP attractors with formation of a heteroclinic loop between the incoming separatrices of the remaining red saddles as trajectories are trapped between, with the red pacemaker continuing to coexist. Additional increases in $g_{31}=g_{32}$ coupling lead to additional movement of the remaining two saddles that ultimately results in the switching of trajectories to the other side of the incoming separatrices, as seen in Figure 5.5, and acquisition of the entire initial condition space by the red pacemaker rhythm. This type of behavior could represent transitions in plasticity where some conditions can lead to seemingly erratic rhythmic behavior before settling back to a stability, and parallel brief shocks to a system in which transient seizure or abrupt and sporadic changes in behavior might be explained through network transition.

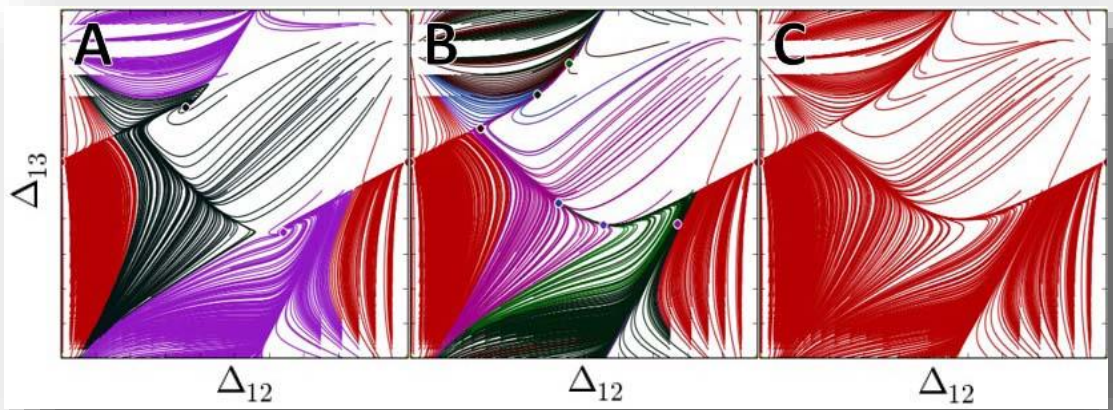


Figure 5.8 Loss of TWs with heteroclinic loops in KOM systems

As in the previous example, a pair of heteroclinic saddle-node bifurcations occur as the TW fixed points, near $(\Delta_{12}, \Delta_{13}) = (1/3, 2/3)$ and $(2/3, 1/3)$, collide with the black-purple saddles and obliterate one another with increasing $g_{31} = g_{32}$ coupling. Unlike Figure 5.7, this leads to disappearance of both black and purple FP attractors with formation of a heteroclinic loop between the incoming separatrices of the remaining red saddles. Additional increases in coupling lead to further shifting of the remaining saddles that results in switching of trajectories to the other side of the incoming separatrices and acquisition of all IC-space by the red PM.

Parameters: $I_{app} = 0.5687$, $g_{ij} = 0.001$ except $g_{31} = g_{32} = 0.0012162, 0.0013514$, and 0.0014865 .

In Figure 5.9, another example of acquisition of the entire initial condition space by the red pacemaker is observed via simultaneous heteroclinic saddle-node bifurcations. In this example, pacemaker rhythms within the escape mechanism ranges of $I_{app} > 0.55$ we can observe asymmetric shifts in the acquisition of both the blue and green PM basins of attraction by the red attractor, as collision of the repellers, near $(\Delta_{12}, \Delta_{13}) = (1/3, 2/3)$ and $(2/3, 1/3)$, with the both the left red-to-blue and lower blue-to-green saddles leads to division of the traces within the original blue and green basins, passing near each of the regions of fleeting CTW and CCTW rhythmicity, by the red and green, and red and blue, basins respectively. Further increases in $g_{31} = g_{32}$ synaptic coupling strength lead to ultimate destruction of both the blue and green fixed point nodes via collision with the saddles near $(\Delta_{12}, \Delta_{13}) = (1/3, 3/5)$ and $(2/3, 1/5)$ through saddle-node bifurcation.

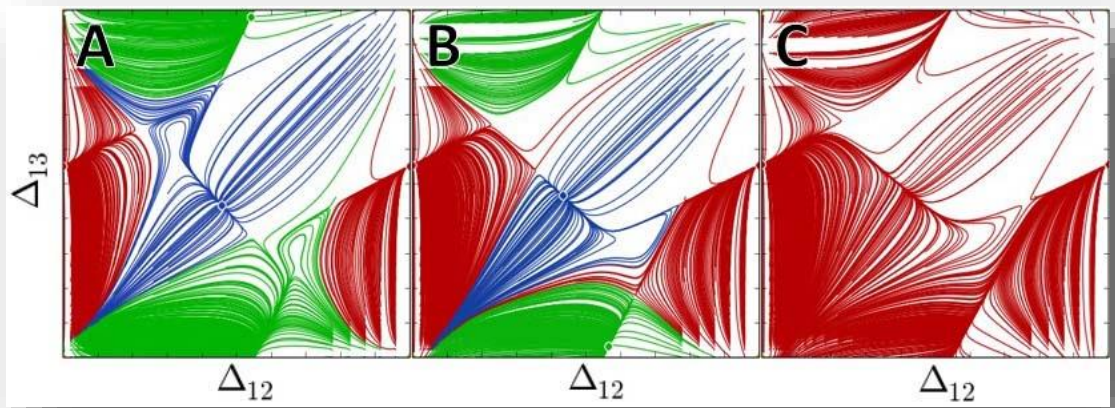


Figure 5.9 PM basin acquisition via heteroclinic SN bifurcations

Another example of acquisition of the entire IC-space by the red PM via simultaneous heteroclinic saddle-node bifurcations. Here, PM rhythms within the escape range of $I_{app} > 0.55$ observe asymmetric shifts in acquisition of the blue and green PM basins of attraction by the red attractor, as collision of the repellers, near $(\Delta_{12}, \Delta_{13}) = (1/3, 2/3)$ and $(2/3, 1/3)$, with the left red-blue and lower blue-green saddles leads to splitting of traces passing near TW rhythmicity within the original blue and green basins by the red and green, and red and blue, basins respectively (B). Further increases in $g_{31} = g_{32}$ coupling strength lead to the destruction of the blue and green FP nodes through collision with the saddles near $(\Delta_{12}, \Delta_{13}) = (1/3, 3/5)$ and $(2/3, 1/5)$ via saddle-node bifurcation (C). Parameters: $I_{app} = 0.5858$, $g_{ij} = 0.001$ except $g_{31} = g_{32} = 0.00094595$, 0.0010811 , and 0.0012162 .

In Figure 5.10, the system begins with coexistence of both a red pacemaker attractor and an unstable invariant circle (or repelling river in this case), near $\Delta_{13} \approx 0.75$. The saddles then split and the red PM basin of attraction becomes blocked to all interior initial conditions by the incoming red saddle separatrices. Heteroclinic connection in the system now passes through all five of the traditional $(\Delta_{12}, \Delta_{13})$ -space fixed-point locations and rhythms will observe phase-slip in which transient portions may appear to briefly pass through regions in which traces mimic green PM, purple CCTW, red PM, blue PM, and black CTW alignment repetitively. With increased $g_{31}=g_{32}$ coupling, the red PM collides with the saddle and all initial condition space now converges to this periodic phase-slip behavior.

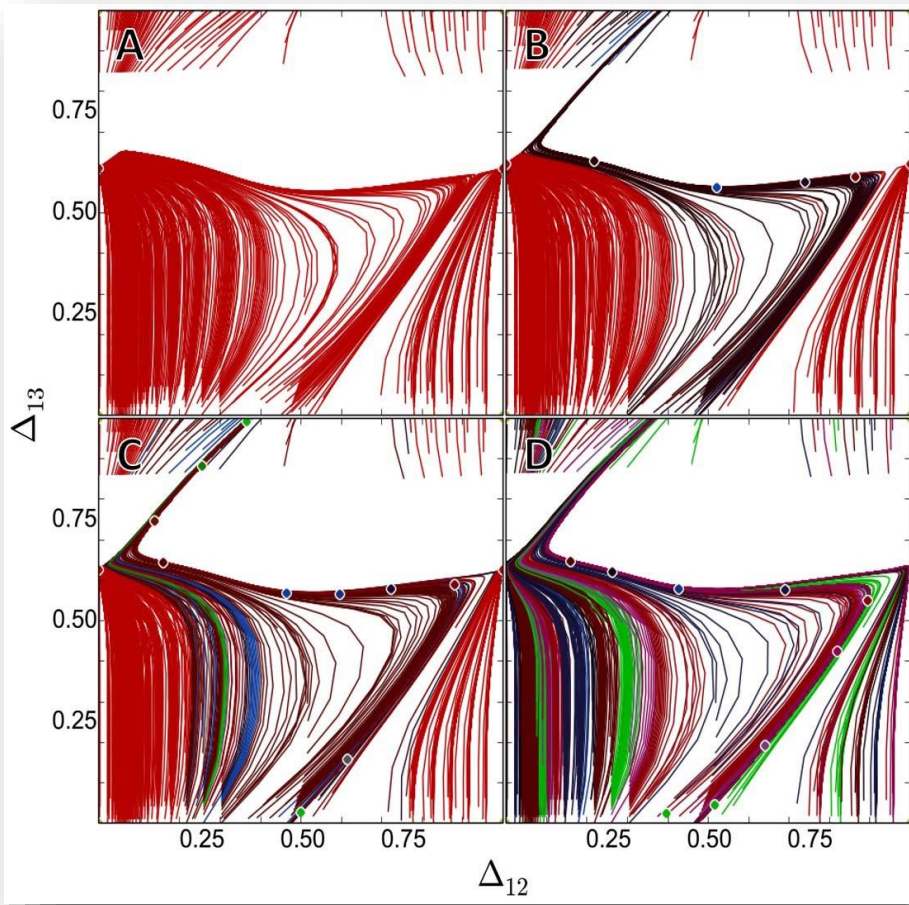


Figure 5.10 Heteroclinic connection between SN separatrices

Beginning in a system with coexistence of a red PM attractor and an unstable invariant circle (or repelling river), near $\Delta_{13} \approx 0.75$, saddles split and the red PM basin of attraction of red PM is blocked to all interior ICs by the incoming saddle separatrices (B). Heteroclinic connection in the system now passes through all the traditional $(\Delta_{12}, \Delta_{13})$ FP locations and rhythms undergo phase-slip, in which transient portions may appear to briefly mimic green PM \rightarrow purple CCTW, red PM \rightarrow blue PM \rightarrow black CTW alignment repetitively. With increased $g_{31} = g_{32}$ coupling, the red PM node collides with the saddle and all IC-space now converges to this periodic phase-slip behavior. Parameters: $I_{app} = 0.5943$, $g_{ij} = 0.001$ except $g_{31} = g_{32} = 0.0044595, 0.005, 0.0052703$, and 0.0055405 .

5.2 Additional fast-slow transition effects on trace patterns

As observed in prior work, and discussed briefly in Chapters 1 and 2, decreasing size of pacemaker regimes in fully symmetric networks has been observed with increasing fast-slow separation

(implemented by decreasing ε). While the region in the bifurcation diagrams in which only traveling waves occur did not grow significantly, wave basins within mixed regions did, and we observe the disappearance of pacemaker-only behaviors entirely as ε gets smaller. Less slowing occurs near the knees when there is greater fast-slow separation, and is inadequate to slow any cell enough to induce pacemaker behavior in truly fast-slow separated symmetric systems. The shape of the orbit limit cycle and the respective traces for systems, as well as respective duty cycles within bursting behavior, also vary with fast-slow separation and will be described in greater detail here. An example of this shift away from the extensive pace-maker rhythm production possible within both release and escape ranges, as well as across all values of I_{app} , can be seen in both the following figures, where their respective basins of attraction compared to similar cases in Chapter 2 are clearly smaller and trajectories exhibit faster convergence.

In Figure 5.11, we observe this situation occurring within the release case symmetric motif as connectivity g_{ij} increases. For direct comparison, these $(\Delta_{12}, \Delta_{13})$ -Poincaré return maps are sampled along the same horizontal pathway at $I_{app}=0.4155$ in Figure 2.9, but with $\varepsilon=0.05$. This gives us a direct representation of the effect of shifts from moderate to high fast-slow separation, moving from weaker to stronger coupling within the same range of values explored there. While both PM and TW behaviors are still observed, much more pronounced dominance of traveling wave patterns exists for all g_{ij} values, with the distinct hard-locking behavior with extremely fast phase-lag convergence, that was previously discussed, occurring much sooner and more dramatically than in the example in Chapter 2 with $\varepsilon=0.30$. Unlike the moderate fast-slow separation previously discussed, the TW basins of attraction do not diminish in size or disappear at all with increasing symmetric coupling strength in release case systems and, in fact, it is the pacemaker rhythms whose basins of attractions are observed to diminish in size and ultimately disappear.

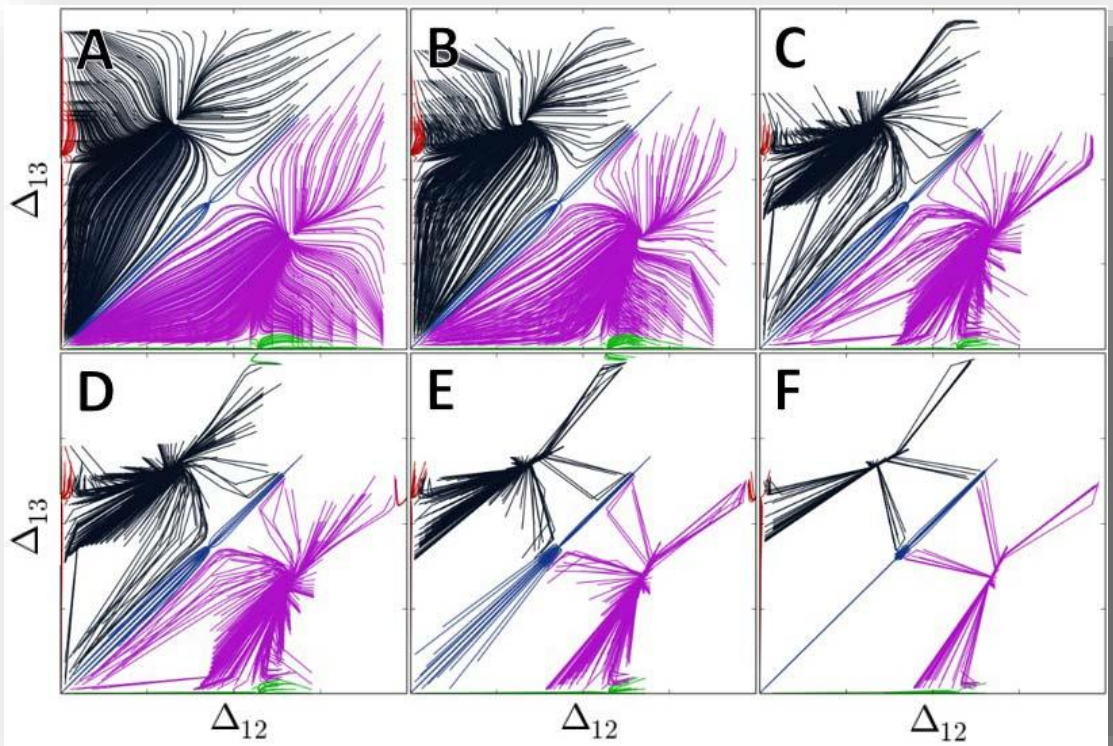


Figure 5.11 Increased fast-slow separation in symmetric release motif

$(\Delta_{12}, \Delta_{13})$ -Poincaré return maps representing the symmetric release motifs as all connection strengths are increased. These maps are sampled along the same horizontal pathway at $I_{app} = 0.4155$ as in Figure 2.9, but with $\varepsilon = 0.05$, and represent shifts from weaker to stronger coupling within the same range of values explored there. While it is still possible for both PM and TW behaviors to occur, much more pronounced dominance of TW patterns exists for all g_{ij} values, with distinct hard-locking behavior with extremely fast phase-lag convergence occurring much sooner and more dramatically. Unlike the moderate fast-slow separation previously discussed, the TW basins of attraction do not diminish in size or disappear at all. Parameters: $g_{ij} = 0.002, 0.008, 0.002, 0.008, 0.002$, and 0.016 .

In an alternate example, in Figure 5.12 we instead observe $(\Delta_{12}, \Delta_{13})$ -Poincaré return maps representing the symmetric release motifs as all connection strengths are held constant and I_{app} spans the range of the bi-parametric space explored. These maps are sampled not only along the same vertical pathway at $g_{ij}=0.0015$, but also at the exact same I_{app} values sampled and shown in Figure 2.5(D1-A1), but with $\varepsilon=0.05$. This permits direct observation representing shifts from

release mechanism ranges of I_{app} , through oscillatory ranges, and finally to those for escape mechanism behaviors. As in the Chapter 2 results, traveling wave patterns occur most prolifically within oscillatory ranges, while pacemaker behaviors are more prominent within the escape and release ranges. Distinct differences exist, however, with greater traveling wave dominance again

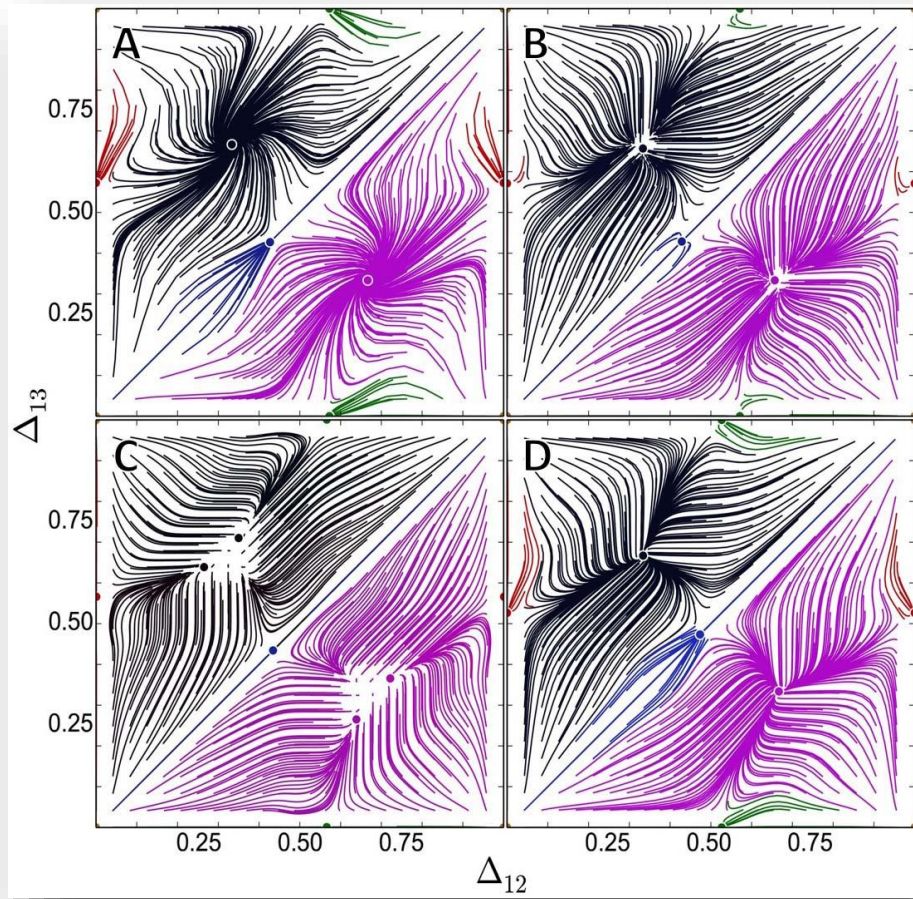


Figure 5.12 Increased TW dominance with high fast-slow separation

$(\Delta_{12}, \Delta_{13})$ -Poincaré return maps representing the symmetric release motifs as connection strengths are held constant and I_{app} spans the range of the bi-parametric space explored. These maps are sampled at the same points along the vertical pathway at $g_{ij} = 0.0015$ shown in Figure 2.5(D1-A1), but with $\varepsilon = 0.05$, and represent shifts from release mechanism ranges of I_{app} through oscillatory ranges to those for escape mechanism behaviors. As in the Chapter 2 results, TW patterns occurring most within oscillatory ranges and PM behaviors more visible within the escape and release ranges. Distinct differences exist, however, with greater TW dominance at all values of I_{app} , decreased PM basin of attraction size, and no ranges for which PM-only behavior can exist. Parameters: $I_{app} = 0.393, 0.419, 0.493, \text{ and } 0.588$.

observed at all values of I_{app} , with the decreased size of pacemaker basins of attraction mentioned previously, and no ranges of I_{app} at this coupling strength for which only pacemaker rhythms can exist. This trend is observed across the system and can be seen in the summary bifurcation diagram of rhythmicity as the fast-slow separation variable is changed that was discussed in the previous chapter (Figure 4.13). Similar effects were also observed across the mono-biased system (Figure 4.14) and in individual sampling within the other network motifs explored.

These effects are a direct result of fast-slow separation and the ability, or inability, of cells to cluster near the knees of the cubic nullcline if not driven to hard by the fast-nullcline. In Figure 5.13, examples of this effect of fast-slow separation on the shape and behavior of the generalized Fitzhugh-Nagumo relaxation oscillator used in this work are explored. At high-fast slow separation, with $\varepsilon = 0.05$, jumps to and from the active and inactive branches of the cubic nullcline are quick as a direct result of the much faster push toward them relative to the sigmoidal nullcline, leading to a crisp black limit cycle with nearly vertical jumps between the branches (A). This effect is also directly observed in the respective sample wave-form (B), with much more square looking behavior relative to the gradual upward and downward sloping observed at less separation with $\varepsilon = 0.30$. This separation is due to vector field convergence to the cubic that is much faster relative to the sigmoidal nullcline. At only moderate fast-slow separation, with $\varepsilon = 0.30$, the convergence toward the sigmoidal nullcline is stronger relatively and both the resulting black orbit and traces are more rounded in appearance (B and D). Both these key examples are sample within the release case, which can be seen with near proximity of the nullclines occurring at the lower left knee of the cubic nullcline. Shown additionally, examples showing further transformation of these transitions in wave-form shape and period can be seen contrasting both release and escape values of I_{app} (0.4 and 0.6, respectively) across intermediate values of decreasing fast-slow separation (ε

$= 0.10 \rightarrow 0.17$) between the two extreme samples already described extensively. The changes in shape are emphasized, becoming more rounded as ε increases, but we can here observe directly the change in period that is also associated with shifts in fast-slow separation. At high-fast slow separation, the period for each burst is much longer due to much slower sigmoidal nullcline drive

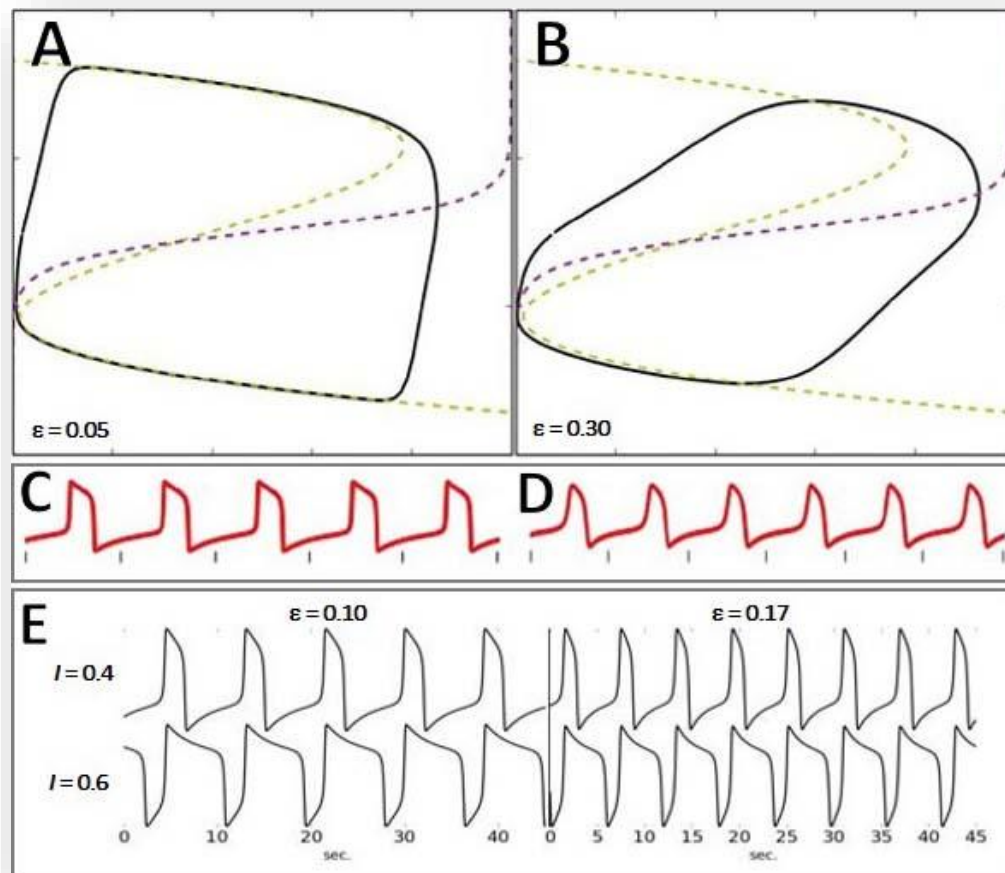


Figure 5.13 Transitions in wave-form patterns with fast-slow separation

Examples of the effect of fast-slow separation on the shape and behavior of the gFN relaxation oscillator explored here. At high-fast slow separation (A), with $\varepsilon = 0.05$, jumps to and from active and inactive branches of the cubic nullcline are quick, resulting in a crisp black limit cycle and wave-forms that are nearly vertical (C). This is due to much faster vector field convergence to the cubic rather than sigmoidal nullcline. At only moderate fast-slow separation (B), with $\varepsilon = 0.30$, the convergence toward the sigmoidal nullcline is stronger and both the resulting black orbit and traces (D) are more rounded in appearance. (E) Additional examples showing transitions in wave-form shape and period can be seen within the context of both release and escape values of I_{app} (0.4 and 0.6, respectively) with decreasing fast-slow separation ($\varepsilon = 0.10 \rightarrow 0.17$).

that results in longer time on both the upper and lower branches of the cubic nullcline. In addition, the effect on duty cycle moving from release to escape ranges of I_{app} is also reiterated, with higher duty cycle in escape cases where the limit cycle slows near the upper right knee and leads to increased time in the active state. This duty cycle shift is valid across all motifs explored.

5.3 Phase slipping across motifs

As described in Chapters 3 and 4, phase-slipping behavior has been observed in asymmetric systems without one-way asymmetry. In clockwise systems, asymmetry is directional and equal and does not permit phase-slip behavior as the system is inherently driven to either clockwise or counter-clockwise rhythmicity away from full symmetry. In the following section, summary of phase-slip behavior mimicking pacemaker-like phase-lock previously observed, as well as additional unique cases observed within the mono-biased and KOM systems with an emphasis on cyclical rhythmicity that varies in time spent within each apparent rhythm pattern.

5.3.1 Pacemaker-like phase-lock in slipping patterns

In $(\Delta_{12}, \Delta_{13})$ -Poincaré return maps, where trajectory convergence is described relative to cell 1, several distinct cases have been observed where phase-lock with phase-slipping behavior is exhibited via an apparent river passing horizontally or vertically through the $(\Delta_{12}, \Delta_{13})$ -space. In Figure 5.14, examples of three of these key phase-slip behaviors with phase-locking behavior are reiterated. A vertical downward-shifting phase-slip observed within the king-of-the-mountain system (from Figure 3.10(A)) is shown with $\Delta_{12} \approx 0.5$ phase-lock of cells 1 and 2, in which voltage traces for cell 3 appear to continuously slip leftward relative to the other two cells, having a shorter period with essentially locked anti-phase bursting by the other two. Similar continuously leftward-shifting phase-slip within a pairwise-biased system is also shown, in this case as an additional point sampled beyond the $g_{31} = g_{13}$ strength of Figure 3.6(D'), occurring after loss of the red

pacemaker node has occurred via saddle-node bifurcation, with $\Delta_{13} \approx 0.5$ phase-lock of cells 1 and 3, in which cell 2 appears to fire with shorter period than the other two cells. Finally, an alternate rightward-shifting phase-slip within the pairwise-biased system (from Figure 3.7(F)) is reiterated, with $\Delta_{13} \approx 0.5$ phase-lock of cells 1 and 3, in which cell 2 appears to continuously fire with longer period than the other two cells in observation of traces of bursting activity.

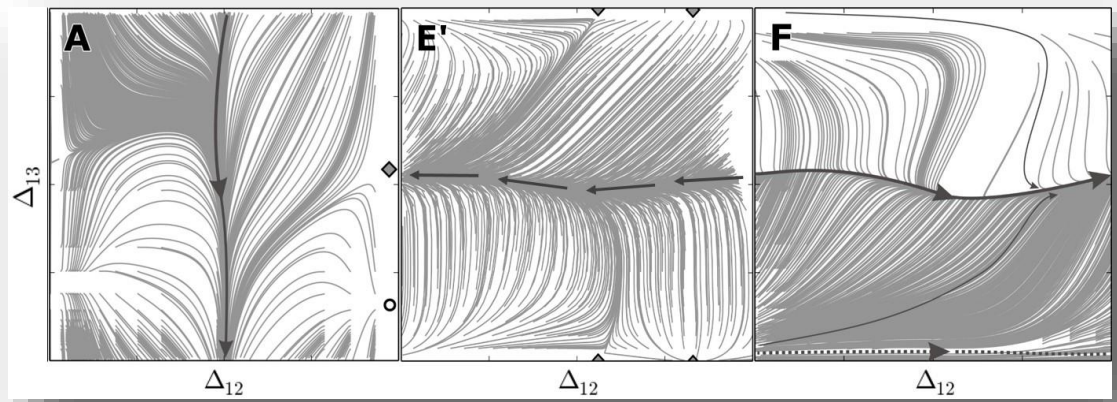


Figure 5.14 Vertical and horizontal phase-slip with quasi phase-lock

Examples of three different phase-slip behaviors with phase-locking behavior. (A) Downward-shifting phase-slip within a KOM system (from Figure 3.10(A)) with $\Delta_{12} \approx 0.5$ phase-lock of cells 1 and 2, in which cell 3 fires with shorter period than the other two cells. (E') Similar leftward-shifting phase-slip within a pairwise-biased system (additional point extending past the $g_{31}=g_{13}$ strength of Figure 3.5(D')) after loss of red PM node) with $\Delta_{13} \approx 0.5$ phase-lock of cells 1 and 3, in which cell 2 fires with shorter period than the other two cells. (F) Rightward-shifting phase-slip within a pairwise-biased system (from Figure 3.7(F)) with $\Delta_{13} \approx 0.5$ phase-lock of cells 1 and 3, in which cell 2 appears to fire with longer period than the other two cells.

Parameters: $I_{app} = 0.57, 0.399, \text{ and } 0.5716$ and $g_{ij} = 0.001$ except $g_{31} = g_{32} = 0.00001$, $g_{31} = g_{13} = 0.004$, and $g_{31} = g_{13} = 0.00331$.

5.3.2 Mono-biased S-patterns within the escape mechanism

Additional phase-slip with apparent phase-lock behavior is also possible, and less apparent with representation here with respect to cell 1. In Figure 5.15, an example of diagonal phase-slip with a slight s-shaped behavior can be seen within the mono-biased system. In this case, we shift from the base case in Figure 3.5(A) by inducing an additional vertical shift in I_{app} , which would be a

heteroclinic bifurcation if both were made simultaneously. This case exhibits different quasi phase-locking behavior with the phase-lock of cells 2 and 3, $\Delta_{23} \approx 0.5$, in which phase-lags for both cells appear to continuously slip leftward in the return maps, with shorter period than cell 1. This example, which has undergone an additional saddle-node bifurcation, contrasts with the system convergence to black clockwise traveling wave dominance that was shown previously at zero coupling of cell 3 to cell 1, and occurs manipulating a single parameter by increasing I_{app} .

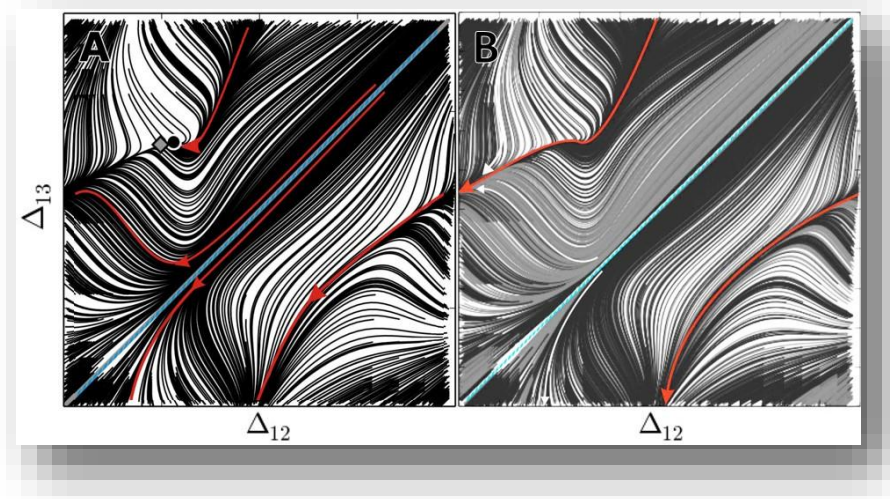


Figure 5.15 S-pattern phase-slip in mono-biased systems

Example of diagonal phase-slip behavior within mono-biased system (from Figure 3.5(A), with effect of vertical shift in I_{app} shown in panel B) with different quasi phase-locking behavior with $\Delta_{23} \approx 0.5$ phase-lock of cells 2 and 3, in which phase-lags both cells appear to continuously slip leftward (diagonally downward but staying approximately in anti-phase with each other) on the return map and fire with shorter period than the cell 1. This contrasts with system convergence to CTW behavior (A) shown previously for zero coupling of cell 3 to cell 1, and occurs via saddle-node bifurcation with increasing I_{app} . Parameters: $g_{ij} = 0.001$ except $g_{31} = 0$ and $I_{app} = 0.582$ and 0.586 .

5.3.3 KOM S-patterns within the release mechanism

An entirely different kind of s-shaped phase lag is possible, one example observed previously in Figure 3.10(E), where phase-slip occurs with repetitive transitions in wave-form phase-lag relationships with both an extended period of apparent stereotypical phase-lock behavior between cells 1 and 3, $\Delta_{13} \approx 0.5$, followed by relatively fast transitions diagonally, with apparent phase-lock

between cells 2 and 3, $\Delta_{23} \approx 0.5$, like that described in Figure 5.15. This overall pattern is like that observed in Figure 5.11, but coexisting with the red pacemaker, near $(\Delta_{12}, \Delta_{13}) = (0, 1/2)$ and $(1, 1/2)$, and with much more stable and rapid convergence to this river of periodic behavior. A detailed view of this invariant circle phase-slip is represented in Figure 5.16, in which a pair of heteroclinic saddle-node bifurcations have led to formation of a heteroclinic loop between the incoming separatrices of the remaining red saddles. All initial space conditions between the saddles on either side of the red basin converge and remain on this s-shaped path, with regular

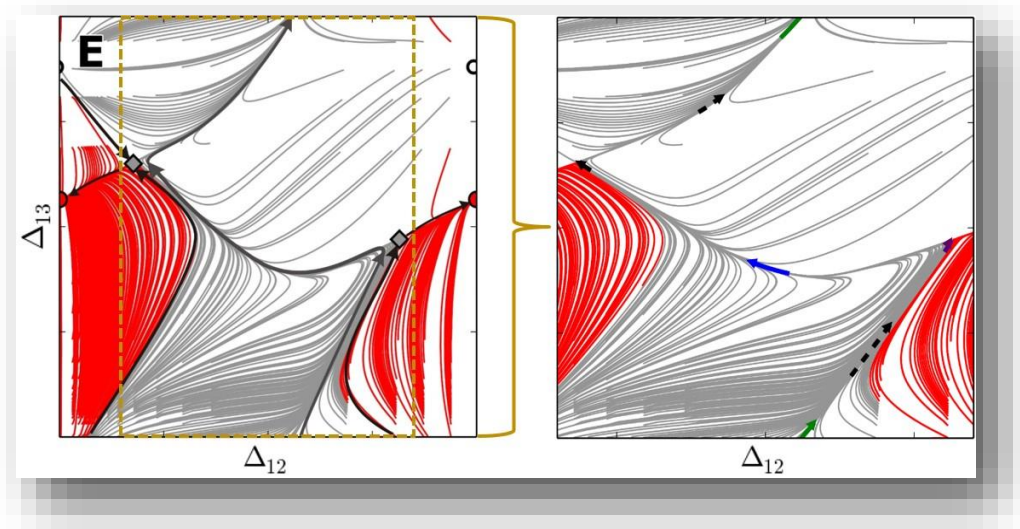


Figure 5.16 S-pattern phase-slip in KOM systems

Detailed view of the invariant circle phase-slip observed in Figure 3.10(E), and like Figure 5.8, in which a pair of heteroclinic saddle-node bifurcations lead to formation of a heteroclinic loop between the incoming separatrices of the remaining red saddles. All solutions beginning within these separatrices converge and remain on this s-shaped path, with regular repeating phase shifts passing through regions of all 4 standard rhythm patterns (green PM → purple CCTW → blue PM → black CTW → green PM) laying between the remaining saddles near the traditional red PM FP location near $(\Delta_{12}, \Delta_{13}) = (0, 1/2)$ and $(1, 1/2)$. Examination of traces along this path exposes difference in the time spent at different locations, with lines representing 20 cycles shown along this river. More time is spent near TW-like rhythms (very short black and purple lines), and the fastest transitions (dashed black lines) occur between locations of traditional FP locations. The most time is spent in the horizontal traversal from near $(\Delta_{12}, \Delta_{13}) = (0.9, 0.5)$ to $(\Delta_{12}, \Delta_{13}) = (0.1, 0.6)$, and results in the system appearing for extended periods to have phase-locked phase-slipping behavior with cells 1 and 3 in anti-phase. Parameters: $I_{app} = 0.570$ and $g_{ij} = 0.001$ except $g_{31} = g_{32} = 0.00136$.

repeating phase shifts passing through regions of all four of the remaining standard rhythm patterns. This begins at the bottom, near $(\Delta_{12}, \Delta_{13}) = (1/2, 0)$, with green pacemaker alignment, which transitions relatively quickly to purple CCTW alignment before then passing for an extended period horizontally through the blue PM and arriving at black CTW alignment, after which more rapidly converging back to its starting green PM position. A look at traces along this path exposes difference in the time spent at different locations along this river. More time is spent near TW-like rhythms, and the fastest transitions occur between locations of traditional FP locations. During the faster diagonal traversal from the black CTW location to the purple CCTW location, passing through the green PM FP location, apparent phase locked anti-phase behavior exists between cells 2 and 3, with cell 1 now firing with shorter period relative to the other two.

5.4 Post-inhibitory rebound mechanism

Post Inhibitory Rebound (PIR) is a mechanism through which some neurons are activated, where the cell can respond to hyperpolarization with depolarization above the level of the normal potential to create bursting-like behavior once hyperpolarizing stimulus is removed [49, 50]. Traditionally, excitation increases a post-synaptic cell's activity and inhibition decreases it. In some cases, inhibition changes the values of the ion gating variables. The gating variable values determine the voltage threshold which needs to be exceeded to fire an action potential. Once inhibition stops, the window of potential for PIR behavior can be explained as the time in which increased neuronal excitability exists, and is the property by which many CNS neurons can exhibit action potential bursting immediately after inhibitory synaptic stimulus. It is thought that PIR may contribute to the maintenance of oscillatory activity in networks that are characterized by mutually inhibitory connections, like those involved in locomotor behaviors [51-52].

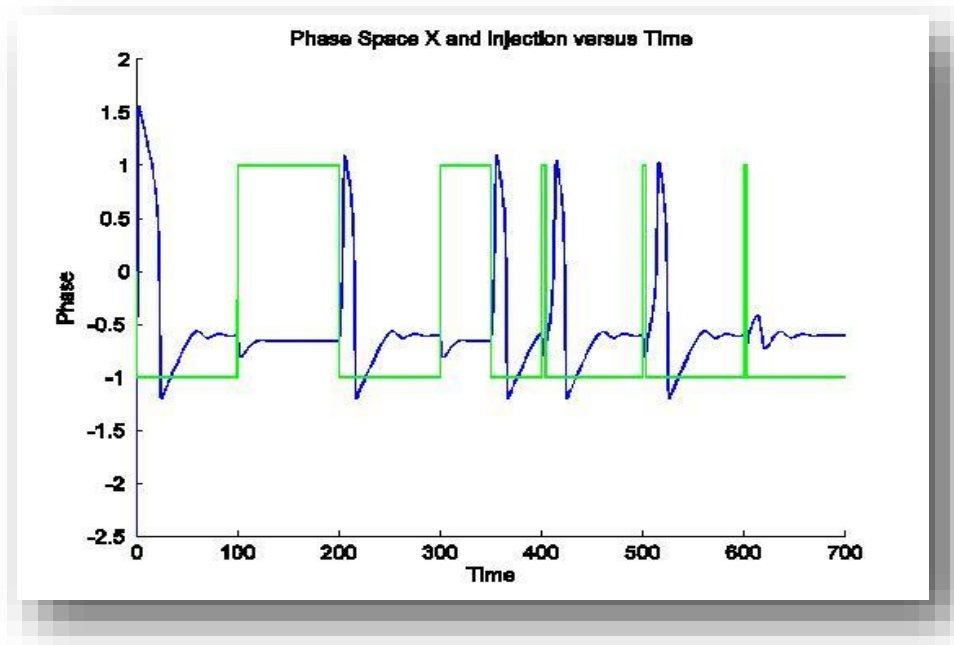


Figure 5.17 Minimum external perturbation required for PIR

Inducing an external stimulus to hyperpolarize a cell can lead to firing of a cell (spikes in the blue trace) upon release of the stimulus. This effect is directly related to the length of the stimulus (shown in the green trace for a fixed negative current input), however, with a minimum duration for which activity can be induced. Below this duration, cells in coupled inhibitory networks will remain in their natural quiescent state.

Again, in some cases, strong inhibition or mild inhibition applied for a sufficiently long duration (see Figure 5.17) will decrease the threshold for firing below the uninhibited quiescent voltage, allowing a cell to fire a spike or packet of spikes following a period of hyperpolarization before returning to rest [48]. In this case, rapid release from inhibition can cause the post cell to fire an action potential from inhibition alone. In the Fitzhugh-Nagumo model the quiescent state is considered to occur at the bottom left knee, near what is normally considered release case mechanism ranges of I_{app} . Strong inhibition shifts this knee to the left (see Figure 2.6) and the equilibrium point shifts left and down to the new stable intersection of nullclines. When the inhibition is released, if the intersection shifts back faster than the post cell's slow variable can

change, the post cell can pass by the original knee (on the left of the knee) and jump to the upper branch of the fast cubic nullcline to initiate a burst of active behavior.

5.4.1 Post-inhibitory rebound methods

During investigation of this phenomena, modeling parameter sets were tested to verify that the PIR mechanism was at work. This was accomplished by running the model with no inhibition and confirming stable quiescence for the cells and then running the model with inhibition present and with one cell starting on the active branch, an initial condition restriction not used during the release and escape cases discussed in Chapters 2-4. This confirmed that internal inhibition can generate branch jumping in all cells, and verified previous work and observation that some networks of neurons, which do not intrinsically oscillate, may be induced to generate coherent rhythms, often in the form of globally synchronous cluster states for slow synapses with sufficiently large coupling strength [48]. For most parameter sets some or all the initial condition states result in quiescence persisting. For some range of inhibition values most initial condition space resulted in stable PIR rhythmic generation. All parameter sets had minimum synaptic coupling strength required to produce stable rhythm patterns, a minimum which directly results in typical hard-locking behavior within these networks that causes the system to very rapidly converge to final equilibrium. Below this minimum all initial condition space results in stable quiescent network behavior (Figure 5.19(A)). This nature requires use of the phase-basin approach to representing phase-lag convergence, as described in Figure 2.4, since representation of traces makes it difficult to discern transitions which are abrupt and can shift dramatically between computational iterations (Figure 5.18). This makes for unattractive looking 2-D Poincaré return maps but may lend itself to quick CPG decision making and possibly forms of logic gating. While increasing coupling strength is required to induce greater, or ongoing, bursting duration above the

minimum thresholds described to initiate it, this can often ultimately lead to cases where too strong synaptic coupling can ultimately lead to chaotic behavior in which activity may occur seemingly randomly with no rhythmic behavior observable (Figure 5.19). This can be avoided by applying appropriate additional constraints, specifically by inducing PIR in systems avoiding canard-like limit cycle behavior, upon which there does not seem to be maximum value of coupling strength for non-chaotic behavior. For the generic synapse mechanism, with strong fast and slow system separation, and near the left nullcline, pacemaker rhythms are not observed.

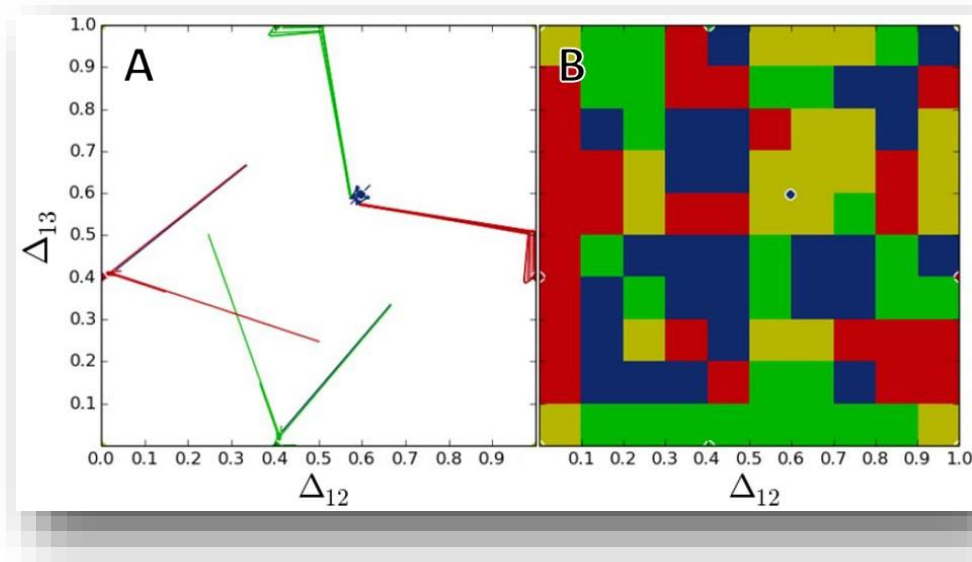


Figure 5.18 Hard-locking effects in PIR systems

The hard-locking nature of strong synaptic coupling required in PIR networks causes rhythmic jumping. The traces make only a few very big jumps, rapidly converging to their final rhythmic pattern. Parameters: $\varepsilon = 0.069$, $I_{app} = 0.5528$, and $g_{ij} = 0.03$.

Another method to induce PIR is with modification of the synapse mechanism, such that there is a band of state space between the active and inactive states, and prohibiting inhibition from acting on cells in the state space of the upper branch, permits pacemaker rhythms to emerge stably for conditions which they could not within the generic synapse mechanism just described. Changing the timing parameter, ε , to be closer to a value of 1 also allows the emergence of pace maker

rhythms. In all cases for which the stable pacemaker rhythms exist, the initial condition space that results in pacemaker rhythms is a very narrow minority of the total initial condition space. This behavior also lends itself to the fast CPG decision making mentioned.

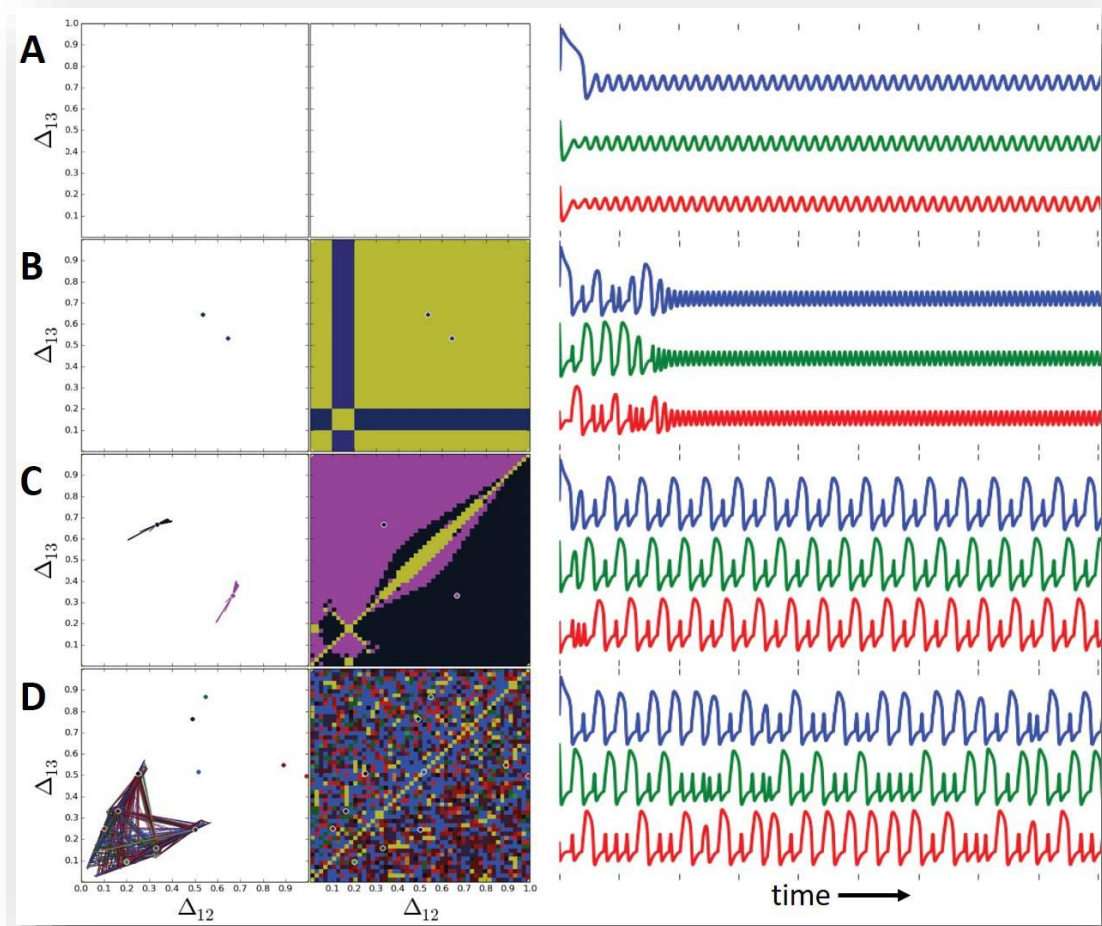


Figure 5.19 Coupling strength effects of on PIR behavior

With increasing synaptic strength, a small region of persistent activity may emerge and grow from initial quiescence (shown by yellow in phase-basins) until almost all the phase space results in rhythmic network activity (traces for B and C). Here we observe TW patterns represented by the black and purple basins. Most initial conditions settle to their respective fixed points in only two or three steps (characteristic of hard-locking in PIR cases, see Figure 5.18) and observed in the jagged trace convergences in the left panels. At too strong connectivity, chaos may result (D) and is represented by random multi-color coding. Parameters: $\varepsilon = 0.30$, $I_{app} = 0.6107$, and $g_{ij} = 0, 0.2304, 0.2575$, and 0.2902 .

A third method exists to induce pacemaker rhythms, which is also available in combination with either the generic synapse or strong fast slow system separation methods described. By shifting the cubic nullcline, such that the gap at the right knee is much smaller compared to the left knee, the time a cell effectively spends on the upper branch can be manipulated for longer duration. This results in increased total inhibition on the other cells, and can push the cells further out leftward from the lower knee of the cubic nullcline, making them jump immediately to the upper branch of the cubic upon release, even if the cells on the bottom branch were not at the knee when the inhibition began. Normally a cell needs to be close to this knee when another cell begins to apply inhibition to cause a PIR event, and is a primary reason why traveling wave patterns dominate the initial condition space for this mechanism.

5.4.2 *Symmetric PIR results*

To remain coherent with previous results discussed for escape and release case mechanisms, results in this section will be organized in terms of shifting the nullclines from right proximity (escape-like) through oscillatory middle ranges to left proximity of the nullclines (release-like) for fully symmetric motif PIR systems. This is then followed by general discussion of some results for the four key asymmetric motifs described in previous chapters. It is important to note that most of the results will parallel the rhythms observed previously (generic PM or TW behavior), but that much of PIR initial condition (IC) space will still often remain or return to quiescent states rapidly after external stimulus is applied. In addition, there are times in which PM behavior may be identified (and other times not recognized) for unique cases where the system drives one cell to quiescence while the other two manage to remain active in anti-phase (Figure 5.20). For simplicity, these are not described or distinguished separately from the general results.

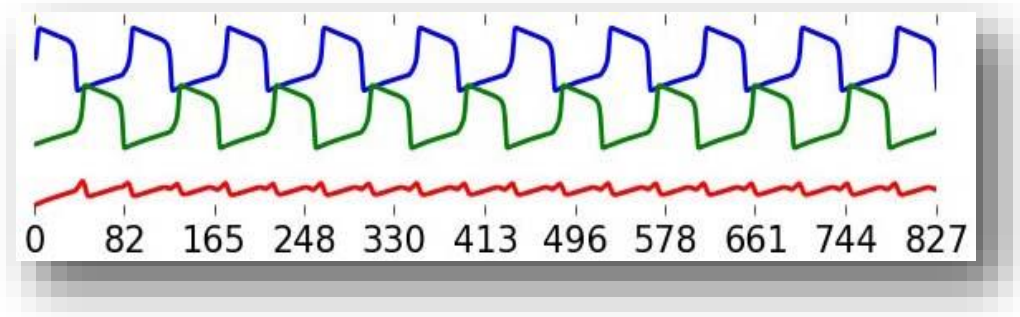


Figure 5.20 Half-center oscillator reduction in PIR systems

An interesting case when the system reduces to a half center oscillator, with the green and blue cells remaining active and in anti-phase ($\Delta_{12} = 1/2$) but the red cell remains quiescent. This is pacemaker behavior but does not fall within the framework of the classic case discussed in previous chapters. Parameters: $g_{ij} = 0.02$, beginning with ($\Delta_{12} = 0.5$).

In the right nullcline proximity case, in ranges of I_{app} close to those observed for the escape case mechanism, pacemakers are the first rhythms to emerge with increasing synapse strength. For a certain range of values, pace makers occupy all the initial condition space (Figure 5.21). At some of these values the IC space for one pacemaker is divided into multiple islands (shown zoomed in for a special case in Figures A.8 and A.9). Phase basin diagrams show the system with most or all IC space resulting in network silence. At low coupling strengths, quiescence dominates (in yellow), but increasing coupling can cause the appearance of stable regions of the IC state space for which PM rhythms can exist (green and red). Beyond a certain threshold, however, these patterns lose stability and then return to the typical regimes of TW-dominant parameter space, occupying all none silent initial conditions.

As mentioned, PMs in these systems have interesting conditions for separating initial condition space with the final stable rhythms. The bulk of the blue, red, and green basins remain around their respective fixed points. However, for certain synapse strengths there are ambiguous boundaries for these basins. On certain boundaries, crossing parameter space vertically, for ICs beginning with cells 1 and 2 in anti-phase ($\Delta_{12} = 0.5$), and beginning cell 3 at different relative positions, we

observe cases where final stable rhythm outcomes will switch from green to blue and back and forth in short ranges of initial condition space (Figure A.8). These changes are due to small differences of the cells starting or leaving a bursting or quiescent state and how this affects final stability. Similar behavior is observed moving across parameter space horizontally, for ICs beginning with cells 1 and 3 in anti-phase ($\Delta_{13} = 0.5$), but with rhythms switching between either red or blue PM behavior (Figure A.9).

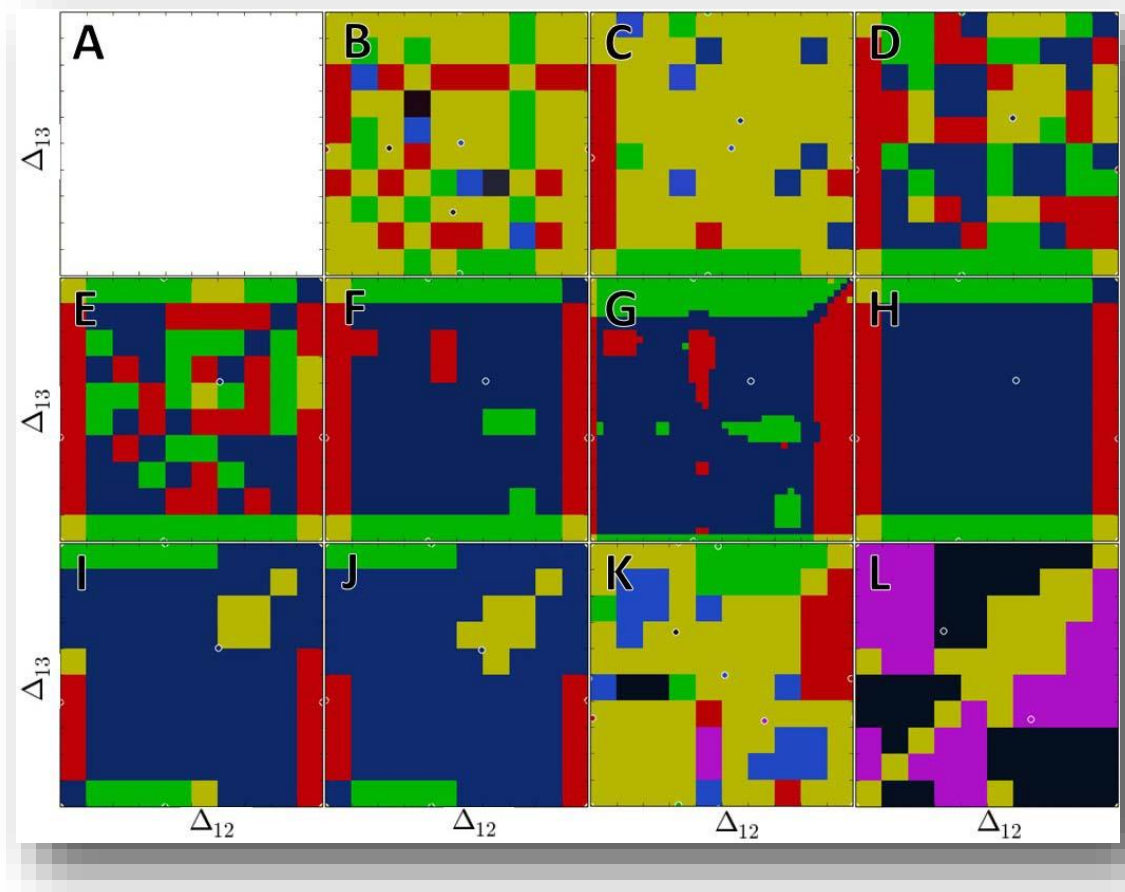


Figure 5.21 Panel of return maps for symmetric 'escape' range PIR

Phase basin diagrams showing the system with most or all initial condition space resulting in network silence. At low coupling strengths, quiescence dominates (in yellow), but increasing coupling can cause the appearance of stable regions of the IC state space for which PM rhythms can exist (here green and red). Beyond a certain threshold, however, these patterns lose stability and then return to the typical regimes of TW-dominant parameter space. Parameters: $\varepsilon = 0.067$, $h = -0.433$, $I_{app} = 0.592$, $g_{ij} = 0.001, 0.01, 0.02, 0.03, 0.04, 0.05, 0.05_{\text{zoom}}, 0.06, 0.09, 0.1, 0.2, 0.3$, and 1.3

For oscillatory ranges of nullcline proximity, when the fast null-cline is in the middle and both knee gaps are about equal, there is strong fast slow system separation. This results in systems for which the traveling waves are the only stable rhythmic outputs (Figure 5.22). With low synapse strengths PM rhythms emerge but only last a couple network cycles before transitioning to stable network quiescence, with only the unstable and transient pace makers existing. With increasing synapse strength, stable traveling waves emerge and grow. Initially silence occupies most the initial condition space. With increasing synapse strength, the basins of attraction, for the traveling wave cases, grows to occupy most the initial condition space. For this same system, introduction

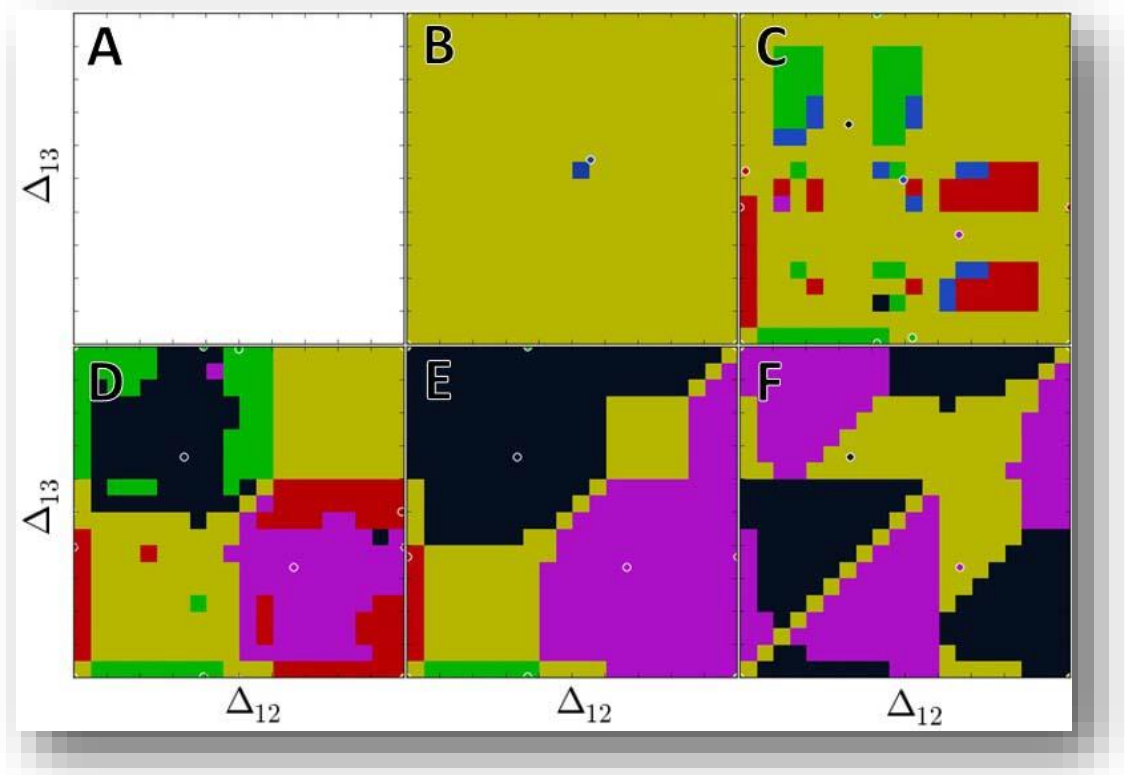


Figure 5.22 Panel of return maps for oscillatory symmetric case PIR

Panels showing the system with symmetric network connectivity and increasing coupling strength. Large regions of quiescent ICs (yellow regions) are gradually acquired by increasing basins of attraction of the TWs (black and purple) in the symmetric case, while in the mono-biased system this is paired with regions of increased PM behavior (green PM regions).

Parameters: $\varepsilon = 0.067$, $h = -0.394$, $I_{app} = 0.496$, $g_{ij} = 0.01, 0.02, 0.03, 0.04, 0.08, 0.1, 0.2, 0.45, 1.5$.

of a synaptic mono-biased anti-symmetry increasing the connection from cell 1 to cell 2, g_{12} , gives some similar results but with clearly asymmetric behavior (Figure A.11, right panels). This system begins, as did the symmetric one, at an initial synaptic coupling strength, $g_{ij} = g_{12} = 0.07$, where both TW basins are present and occupy just under 50% of the IC space was used. With increasing

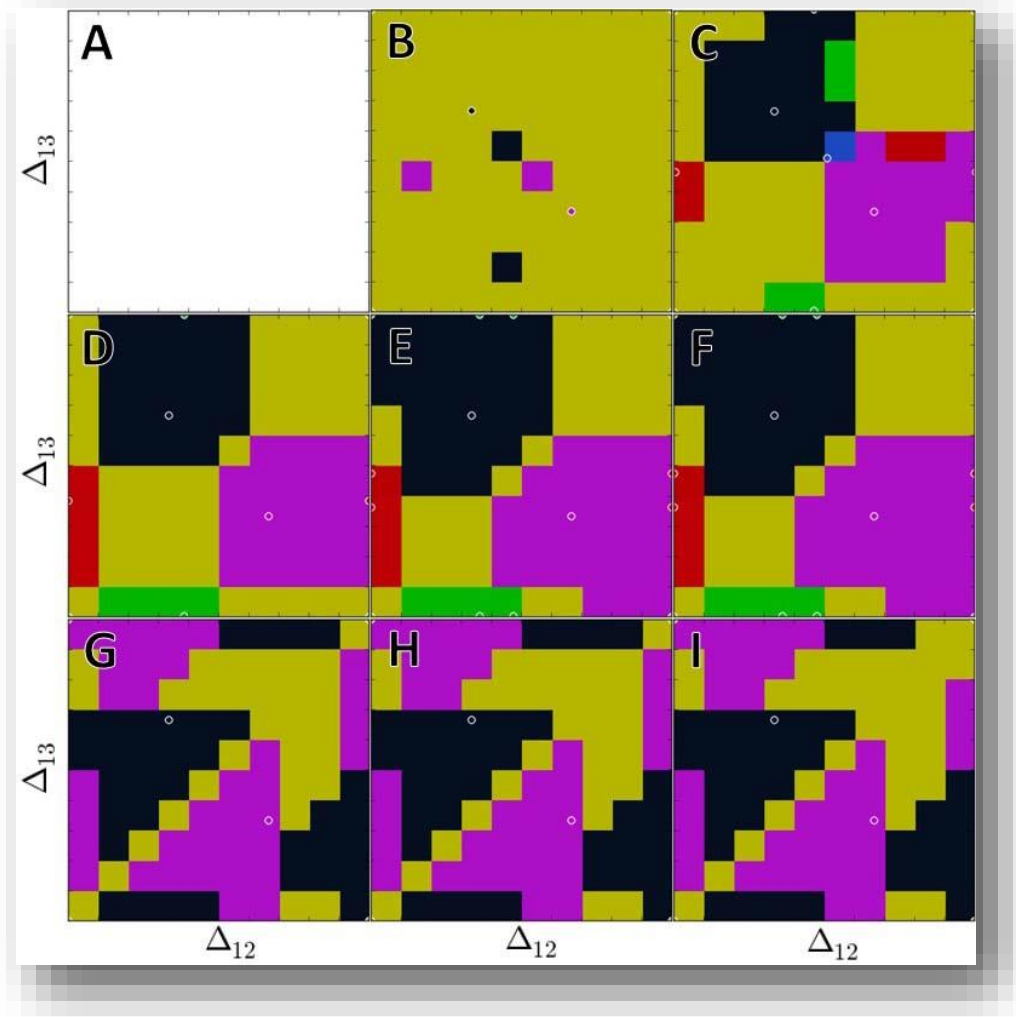


Figure 5.23 Panel of return maps for symmetric ‘release’ range PIR

Phase basin diagrams showing the system again beginning with most or all IC space resulting or returning to network silence (in yellow). Increasing coupling again causes the appearance and growth of stable regions of the IC state space for which PM rhythms can exist (green and red) with TW behavior. Beyond a certain threshold, these patterns lose stability and return to the typical regimes of primarily TW-dominant parameter space. This is emphasized by stability of rhythm outputs in panels G-I with increasing coupling strength not inducing any further rhythm changes. Parameters: $\varepsilon = 0.069$, $h = -0.311$, $I_{app} = 0.465$, $g_{ij} = 0.001, 0.02, 0.04, 0.06, 0.09, 0.15$, and 1.5.

g_{12} strength, the TW basins grew, with the purple CCTW basin growth outpacing that of the black CTW, eventually occupying significantly more IC space. Unlike the symmetric case, the transient green pace maker never disappears with increasing g_{12} strength. Significant differences only appear if the anti-symmetric connection is that of the others, looking like the symmetric case prior. In the left nullcline proximity case, in ranges of I_{app} close to those observed for the release case mechanism, the gap between the slow sigmoidal and left knee of the fast cubic nullclines is much smaller than that on the right. This system behaviors very similarly to the oscillatory ranges just described, with the early emergence of PMs being unstable and transient. TWs are the only stable network outputs, with basins of attraction growing with increasing synaptic strength to include most, but never all, of IC space (Figure 5.23). This finding might support the conclusion that small PIR networks are more rugged and resist perturbations to network behavior for small variations in synaptic configuration. If a single connection can be 5 times as large as the other connections, others all being equivalent, and the same basic network behavior is preserved, then this CPG will perform its specific task even with significant damage to the network. If this is true, one would expect small PIR networks to be found in essential and consistent behavior governing CPGs. One would not expect to find these networks in behaviors that need to be fine-tuned in response to varying environmental conditions.

Comparison of the emergence and existence of regions of possible rhythmic behavior within otherwise largely quiescent ICs for the entire bi-parametric (g_{ij}, I_{app}) -space (Figure 5.24) indicates dominance of TW patterns when PIR succeeds in initiating rhythms. This occurrence of TW behavior (shown in green) increases with decreasing values of I_{app} , and only appears with increasing coupling strength, g_{ij} , PM rhythms (dark and light blue) only appearing at near right-knee nullcline proximity and only for midranges of g_{ij} , with the presence of increasing regions of

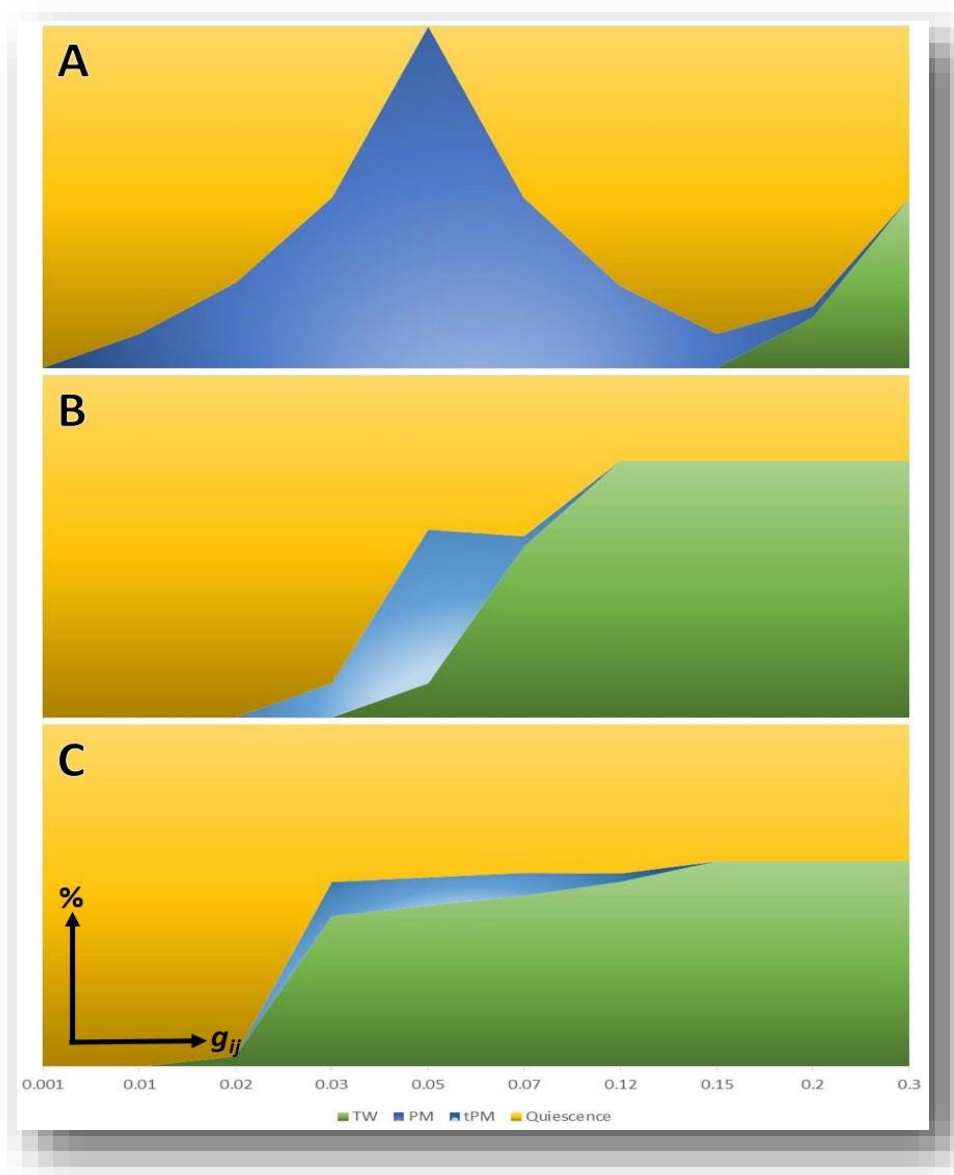


Figure 5.24 Pattern contribution with shifts in I_{app} for symmetric PIR

Set of 3 graphs showing the contribution of TWs, PMs, and transient PMs at increasing synapse strengths, each box spanning the range from 0-100%. Quiescent behavior (shown in yellow) dominates ICs for the bi-parametric (g_{ij}, I_{app}) -space, with the presence of increasing regions of stable TW behavior (green) in all cases but primarily transient pockets of PM behavior otherwise. For right-knee proximity of the nullclines (A), with $I_{app} > 0.55$, we observe a critical point at which PM behavior (darker blue) entirely dominates, increasing until that point and decreasing afterward. For oscillatory ranges of I_{app} (B), only transient PM behaviors (lighter blue) are observed and appear to peak at the same range of $g_{ij} \approx 0.05$. For right-knee proximity of the nullclines (A), with $I_{app} < 0.45$, we observe a similar but much reduced range of tPM activity and increased dominance of TW rhythms, an increasing trend observed with decreasing I_{app} .

stable TW behavior (green) in all cases but primarily transient pockets of PM behavior otherwise. For right-knee proximity of the nullclines where PM activity is most prevalent, with $I_{app} > 0.55$, we observe a critical point at $g_{ij} \approx 0.05$ where PM behavior (darker blue) entirely dominates, increasing up to that point and decreasing afterward. For oscillatory and left-knee proximity ranges of $I_{app} < 0.55$, only transient PM behaviors (lighter blue) are observed and appear to peak near the same range of g_{ij} . These are patterns in which PM behavior is only temporarily induced (transient PM, or tPM, shown in light blue) and then falls back into quiescence over time. These fleeting periods of transient PM activity increase to dominate as much as 40% of the bi-parametric (g_{ij} , I_{app})-space within oscillatory ranges but are much less present at low ranges of I_{app} . This behavior is nearly the reverse of that observed for escape-to-release shifts in I_{app} within the symmetric motif explored in the previous chapters.

5.4.3 Asymmetric PIR results

For asymmetric motifs, two different experiments are explored and begin for cases with moderate and strong synaptic coupling within the right knee proximity of the nullclines case with high fast-slow separation ($I_{app}=0.592$ and $\varepsilon=0.067$). The first case, $g_{ij} = 0.0663$, begins at full symmetry near a peak PM region while the second case, $g_{ij} = 0.1724$, begins at full symmetry in a null space between stable PM and TW regimes (Figure 5.25(A and B), respectively). An additional experiment is also described in the Appendix in Figure A.11.

For the first case, in which we observe a system with only moderate symmetric synaptic coupling, with $g_{ij} = 0.0663$, both PM and TW behavior exists. Beginning from this state, decreasing or increasing the relevant coupling strengths for each asymmetric motif from this initial state (shown by vertical line), we observe shifts in pattern formation unique to each connectivity network (Figure 5.27). For the mono-biased motif (panels across A), in which g_{31} is manipulated, we

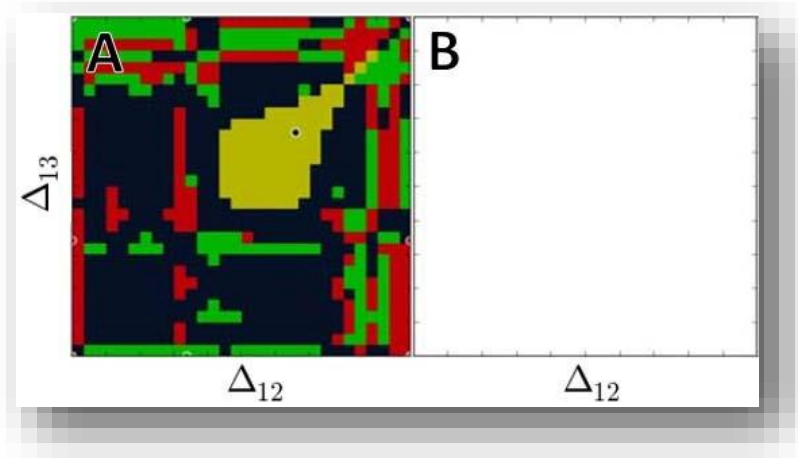


Figure 5.25 Initial symmetric states for asymmetric PIR examples

Panels showing phase-basin return maps for the two cases of asymmetric PIR explored here. In panel A, we observe a system with only moderate symmetric synaptic coupling in which PM behavior exists and panels in Figure 5.26 describe shifts in this system by decreasing or increasing respective asymmetric g_{ij} values from this initial state, beginning the system with ICs within one of the peak PM regions visible. In panel B, we observe a system with strong symmetric synaptic coupling in which only quiescence exists (no trajectories in B, or yellow in A), with panels in Figures 5.27 and 5.28 describing shifts by decreasing or increasing respective asymmetric g_{ij} from here. Parameters: $I_{app} = 0.592$, $\epsilon = 0.067$, and $g_{ij} = 0.0663$ or 0.1724 .

observe increasing dominance of the red PM only briefly with increased g_{31} , and followed by an overall increase in green PM activity where rhythms exist. Red PMs decrease, and then disappear entirely, with decreasing g_{31} coupling, with green PM behavior increasing slightly. For the pairwise-biased motif (panels across B), in which $g_{31} = g_{13}$ is manipulated, we observe increasing dominance of the red PM activity above and green PM activity below symmetry, green PMs occupying nearly the entire IC-space at low coupling values. For the KOM motif (panels across C), in which $g_{31} = g_{32}$ is manipulated, we observe increasing complete dominance of the red PM above symmetry, while it nearly disappears entirely with shifts below. For the clockwise-biased motif (panels across D), in which $g_{31} = g_{12} = g_{23}$ is manipulated, we observe increasing dominance of one or the other TW pattern, clockwise below and counterclockwise above symmetry, while it nearly disappears entirely with shifts below, with asymmetric reduction in the green PM.

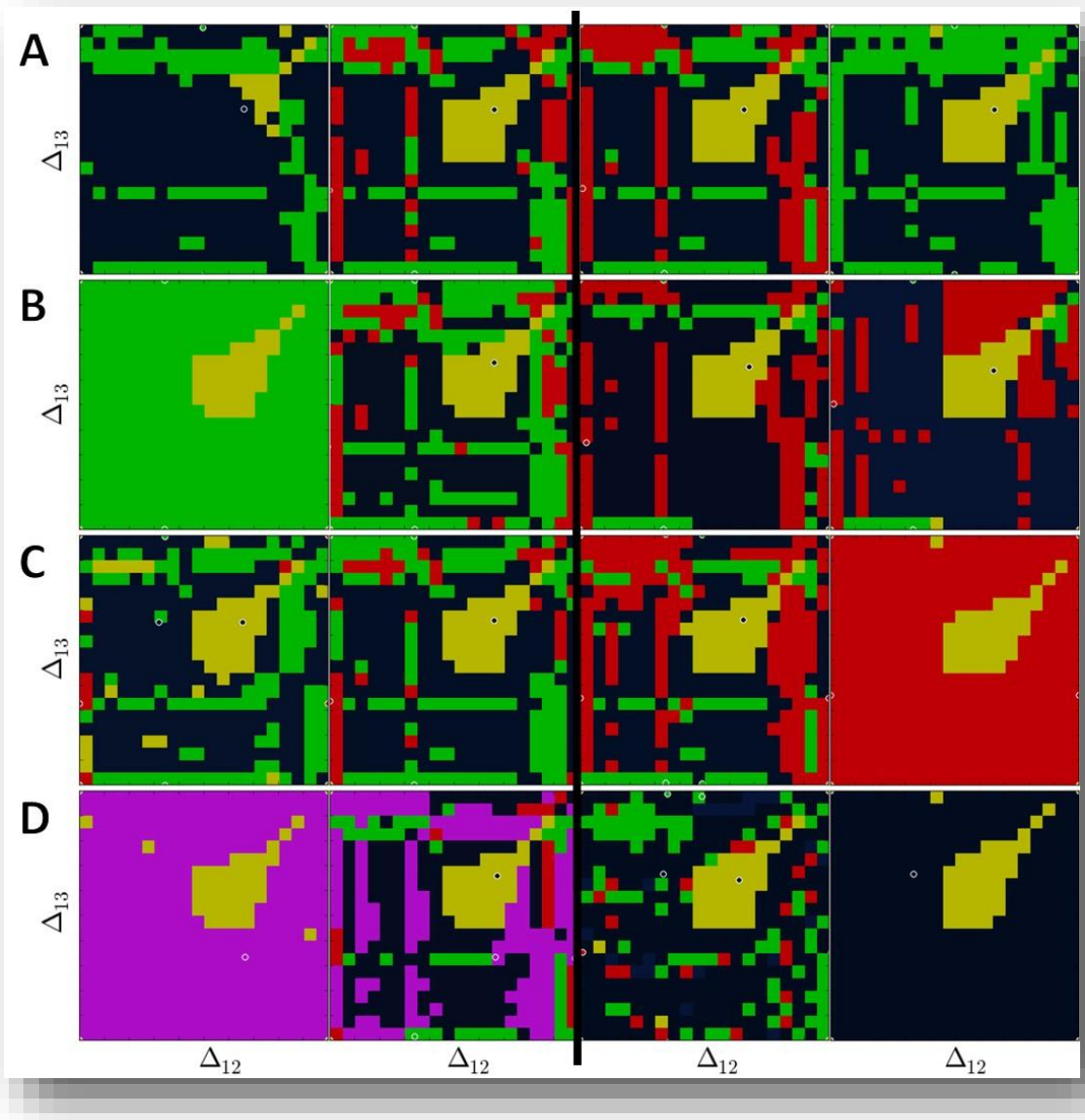


Figure 5.26 Asymmetry in moderately coupled right-knee PIR systems

Series of phase maps for asymmetric motifs above and below full symmetry (vertical line) with moderate coupling strength. Beginning from a system with large PM activity (Figure 5.25(A)), differences are observed in pattern emergence or disappearance with decreasing or increasing asymmetric coupling strength, left and right panels in each row, respectively. Mono-biased (A), pairwise-biased (B), and KOM (C) motifs all show shifts emphasizing a singular PM rhythm, while the clockwise (D) motif sees these rhythms disappear with increasing dominance on a single TW pattern. Yellow regions again indicate ICs leading to quiescence. Parameters: $\varepsilon = 0.067$, $I_{app} = 0.592$, and $g_{ij} = 0.0663$; A: $g_{31} = 0.0464, 0.0654, 0.0689$, and 0.0902 , B: $g_{31} = g_{13} = 0.0623, 0.0642, 0.0714$, and 0.0831 , C: $g_{31} = g_{32} = 0.0599, 0.0638, 0.0724$, and 0.0896 , D: $g_{31} = g_{12} = g_{23} = 0.0593, 0.063, 0.0736$, and 0.0893 .

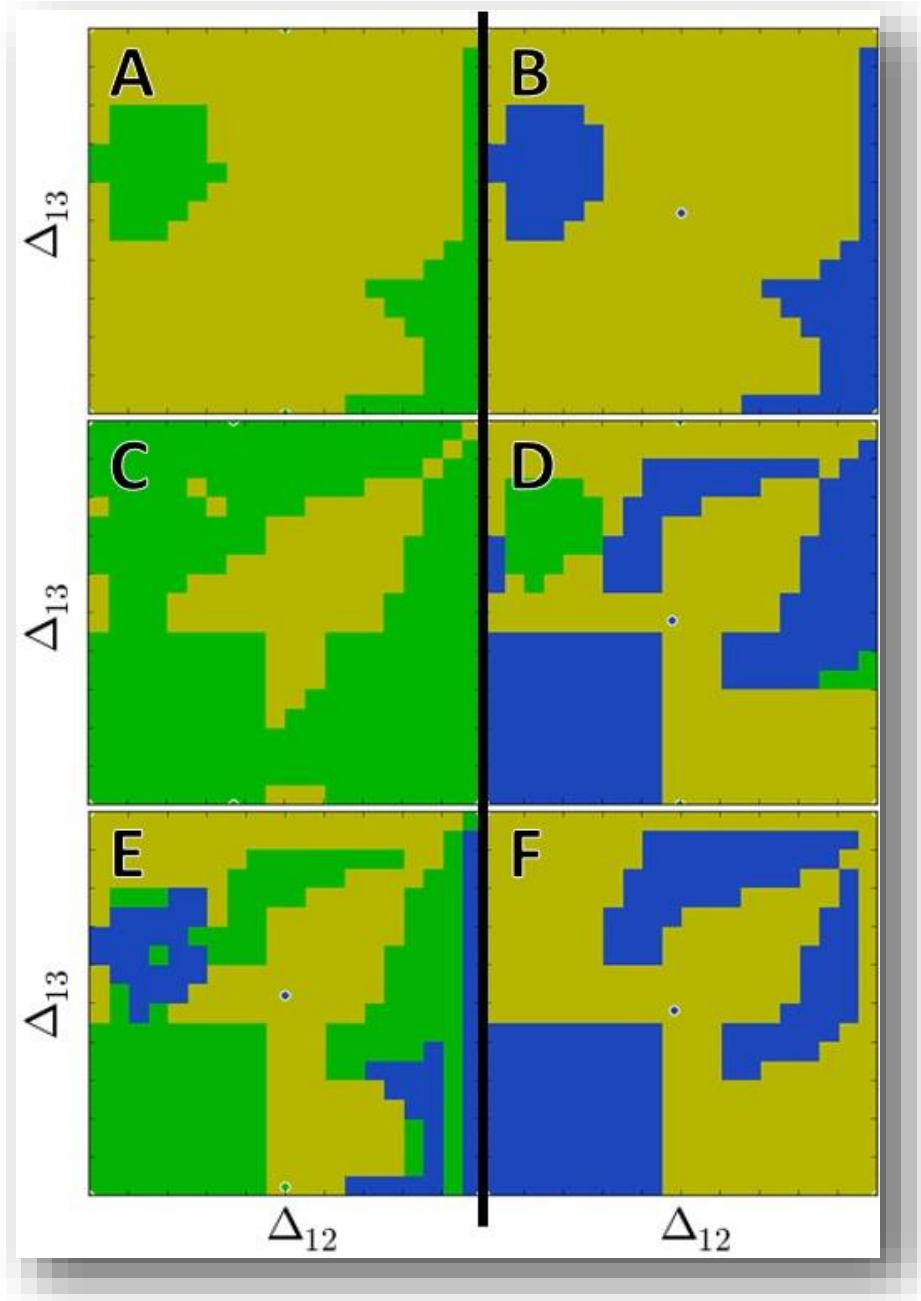


Figure 5.27 Asymmetry in strongly coupled right-knee PIR systems

Phase maps for asymmetric motifs above and below full symmetry (vertical line) with strong coupling strength. Beginning from a system with no rhythmic activity (Figure 5.25(B)), differences are observed in pattern emergence decreasing or increasing asymmetric coupling strength, left and right panels in each row, respectively. Mono-biased (A), pairwise-biased (B), and KOM (C) motifs again all show shifts emphasizing a singular PM rhythm, but with much greater dominance than observed at moderate coupling (Figure 5.26(A-C)). Yellow regions indicate ICs leading to quiescence. Parameters: $\varepsilon = 0.067$, $I_{app} = 0.592$, and $g_{ij} = 0.1724$; A: $g_{31} = 0.1421$ and 0.1590 , B: $g_{31} = g_{13} = 0.1218$ and 0.2490 , C: $g_{31} = g_{32} = 0.1508$ and 0.2031 .

For the second case, in which we observe a system with strong symmetric synaptic coupling, with $g_{ij} = 0.1724$, we begin with ICs in the null-space for which no stable patterns exist (Figure 5.25(B)). Decreasing or increasing the relevant coupling strengths for each asymmetric motif from this initial state (shown by vertical or horizontal lines), we observe shifts in pattern formation unique to each connectivity network (Figures 5.27-28). For all three cases involving only connections to or from cell 3 (shown in Figure 5.27), g_{31} for mono-biased (A), $g_{31} = g_{13}$ for pairwise-biased (B), and $g_{31} =$

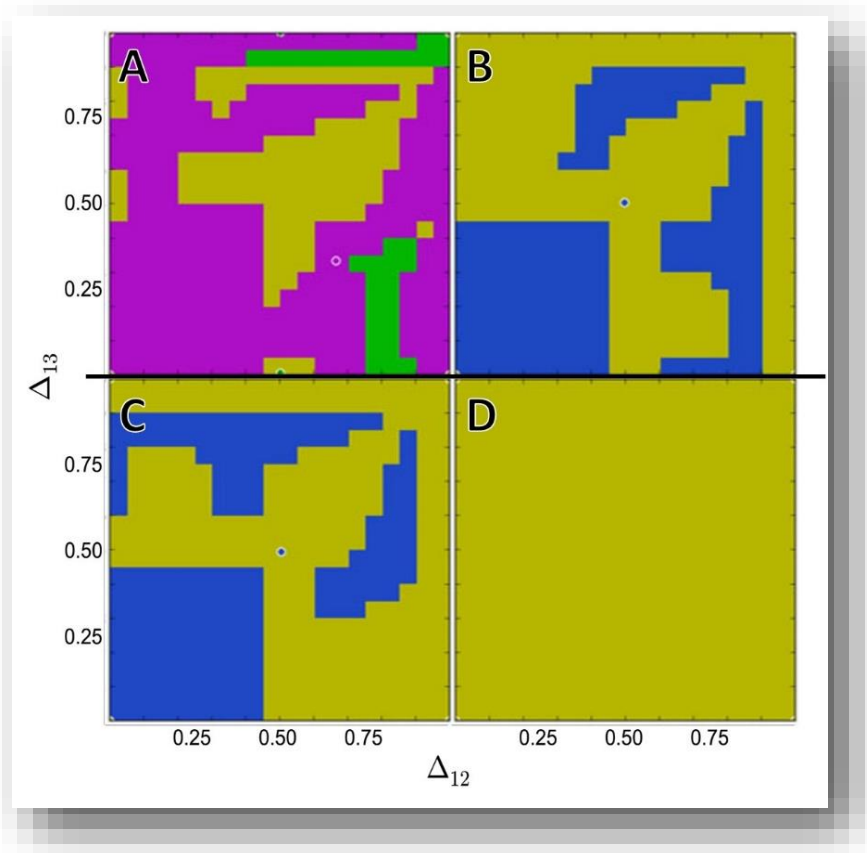


Figure 5.28 Strongly coupled clockwise right-knee PIR motifs

Phase maps for clockwise asymmetric motif above and below full symmetry (horizontal line) with strong coupling strength. Beginning from a system with no rhythmic activity (Figure 5.25(B)), we observed the asymmetric appearance and then disappearance of blue PM activity in both directions, ultimately leading to dominance of the CCTW pattern (A) at high coupling strength or, unlike in both release-escape and the moderately coupled PIR system previously described in which CTW patterns dominated, system-wide quiescence (D) at low synaptic coupling. Yellow regions indicate ICs leading to quiescence. Parameters: $\varepsilon = 0.067$, $I_{app} = 0.592$, and $g_{ij} = 0.1724$ except $g_{31} = g_{12} = g_{23} = 0.1970, 0.1844, 0.1542$, and 0.1190 .

g_{32} for KOM (C), we again observe shifts emphasizing a singular PM rhythm, green below and blue above full symmetry, but with much greater dominance than was observed at moderate coupling. All three systems remain dominated primarily by quiescence for most of the bi-parametric (g_{ij}, I_{app}) -space. For the clockwise motif (panels across D), in which $g_{31} = g_{12} = g_{23}$ is manipulated, we observe increasing dominance of one or the other TW pattern, clockwise below and counterclockwise above symmetry, while it nearly disappears entirely with shifts below, with asymmetric reduction in the green PM on either side. For the clockwise asymmetric motif shown in Figure 5.28, however, we observe the asymmetric appearance and then disappearance of blue PM activity in both directions. This occurs transiently, ultimately leading to dominance of either the CCTW pattern at high coupling strength (D) or, unlike in both release- and escape-like systems and the moderately coupled PIR systems previously described in which CTW patterns dominated, system-wide quiescence occurs at low synaptic coupling (A).

5.4.4 Summary of PIR results

The PIR mechanism is a challenging system to broadly sweep and analyze, as was done within the escape-release framework discussed in previous chapters. The range of inhibition strengths for which PIR activity can exist is relatively narrow compared to the other mechanisms investigated. When this behavior does exist, there are always significant dead zones of system quiescence for the mechanism in the (g_{ij}, I_{app}) bi-parametric state space. TWs remain the dominant stable rhythmic pattern for most ranges and initial conditions for this system. PM rhythms require particular conditions to exist within this framework, and are nearly always a minor rhythm regime when compared to TW rhythms or static equilibrium. PIR networks jump quickly to final rhythm states due to both the required strong coupling and its inherent hard-locking nature. This makes PIR a viable candidate for CPG decision making in complex logic systems.

Results for symmetric near left-knee proximity of the nullclines indicate that PIR may induce transitions from TW-specific network outputs to PM rhythms. This results directly from changes in the duty cycle of the cells in the network as the move from smaller to larger values for affected coupling strengths. This relationship between duty cycle and rhythmic output is directly opposite that observed in both the escape and release cases, where TW typically remain dominate stable outputs with large duty cycle values. This could be a result of the hard-locking nature of PIR, and merits additional comparison to escape and release cases with definite hard locking characteristics. On the other end of the spectrum, when near right-knee proximity of the nullclines exists, transitions to PM behaviors are significantly reduced and only exist transiently, with TW rhythms occurring with much greater frequency. Within asymmetric PIR motifs, additional deviations from release-escape stereotypical behavior are observed, and most particularly for the clockwise-biased system. The general response of clockwise-biased increases in coupling strength, causing the emergence and or domination of a singular TW rhythm well above or below symmetry, holds true for only one of the two asymmetric synapse cases investigated. The other loses stability for all network output with decreasing clockwise anti-symmetry, becoming dominated entirely by quiescent output. This illustrates how much more dependent the PIR mechanism is on non-synaptic parameters than are the other mechanisms, with some cases where no magnitude of synaptic anti-symmetry can induce network outputs.

5.5 Discussion and applications

An examination of these further rhythmicity patterns, bifurcations, and the addition of additional asymmetry in several of the systems via coupling strength shifts or changes in fast-slow separation, aids in understanding these networks in a broader context in which manipulation of increasing numbers of parameters, plasticity, or residence within the framework of most of these patterns

occurs because of saddle-node bifurcations, often either homoclinic or heteroclinic. The unexpected regularity with which different phase-slipping behaviors can be observed in all three of the asymmetric motifs explored further lends itself to analysis of macro-scale rhythmic behaviors in which we may see periods of apparently stable patterns interspersed by fast rhythm switching to another apparently stable rhythm even without the need for external stimuli. These may present novel applications to experimental research of small local networks in which multi-stable rhythm production can be observed with the same network connectivity.

Further examination of changes in fast-slow separation within a system reiterate the increased dominance of oscillatory behavior with TW behaviors within the entire (g_{ij}, I_{app}) bi-parametric state space. This has been demonstrated directly both in this chapter and in the previous one, in which bifurcation detail across changing values of ε was performed more extensively both for symmetric and mono-biased networks, and is a direct result of the increased drive of the fast-cubic nullcline in drawing trajectories toward it relative to the slow sigmoidal nullcline. This leads to squarer limit cycle orbits and waveforms, as little or no clustering of cells can occur for very long at the knees of the cubic nullcline, even with near-knee proximity in either the release or escape case ranges of I_{app} . Changes in increased duty cycle for escape cases was described specifically here in the context of fast-slow separation as well, but are valid with increases in $I_{app} > 0.55$ for all network motifs explored, as well as within the framework of PIR.

In results described for exploration of PIR, there was a relatively narrow range of inhibitory coupling strengths for which bursting activity can be induced. When it does exist, it is generally a minority relative to the large zones of quiescence typically observed. TWs remain the dominant rhythmic output of the network for most ranges and initial conditions, with PM rhythms requiring highly restrictive conditions and typically coexisting with TW patterns and for an even more

restricted volume of IC space. PIR networks jump quickly to final rhythm states due to both the required strong coupling and its inherent hard-locking nature. Within asymmetric PIR motifs, additional deviations from release-escape stereotypical behavior are observed, most emphatically for the clockwise system, and underlines the increased dependence of the PIR mechanism on non-synaptic parameters.

6 TRANSITIONS IN 3-CELL MODULAR NETWORKING

Work in previous chapters has extensively explored the nature and behavior of local three-cell networks, with allusion to use of these not only in hypothesis generation for experimental studies, but also as a potential framework for using results from this work as 3-node building blocks for modular networking. Larger networks formed in this manner become more complicated, and visualization of dynamics observed in these systems becomes challenging within the framework of trace analysis and even using the phase-lag reduction employed thus far to reduce visualization to a two-dimensional system that could be displayed using the Poincare return maps extensively employed in this research. Some discussion is made here about ways in which higher-order networks could be readily analyzed and visualized, beginning with the simpler case of connection of a single additional node to one of the five key network motifs explored. This becomes more complicated with the addition of two cells, or the combination of two motifs, and an additional approach to doing this while continuing to use this methodology is described later in this chapter. Initial observations and results connecting 3-cell motifs into larger six-cell networks is described in the context of inhibitory connectivity, maintaining the reciprocally inhibitory HCO dynamics explored extensively thus far. Use of excitatory connections is not described here, but would be another method in which one network could be used to stimulate rhythm switching in the other, and is a recommended direction for future work building on this research. Finally, exploration of the addition of electrical between motifs is examined, with emphasis on transitions in rhythmogenesis and rhythm switching with increasing electrical connectivity. This approach is specifically used to describe a method for creating five-cell networks using strong electrical connection to effectively merge two cells together. This approach can also be used, and is described for a couple examples in the Appendix, to define even four-cell networks as coupled

three-cell motifs with two cells from each network being strongly electrically coupled. Broad transitions in rhythmicity are described, with the hope that future research can use some of these preliminary guiding principles in hypothesis generation and in furthering extensive bi-parametric exploration of these systems similarly to what has been done for the five key motifs described in this research, effectively building a growing library of bifurcation diagrams that can aid in continuing to bridge the gap between well-known small local network dynamics and behavioral outputs and rhythm generation in much larger interconnected networks.

6.1 Visualization of higher-dimension phase-lag return maps

6.1.1 4-cell networks and 3-D visualization

Addition of a single cell to previously described three-cell networks lends itself to three-dimensional visualization using the same phase-lag reduction approach used thus far, continuing to use cell 1 as a reference from which all results are described. The simplest case would be connection of this fourth cell to only one of the three-cell network, and preliminary work by others in our lab indicates that this method can effectively capture and describe dynamics previously alluded to as a single external pulse or stimulus to cause rhythm switch within a polyrhythmic 3-node network. A single cell can induce rhythm switch using a single incoming inhibitory stimulus to the network, which would depend on the intrinsic mechanism, whether release or escape, in which its I_{app} value resides. For a release case system, in which $I_{app} < 0.45$, the fourth cell would be an endogenous burster, moving along its orbit cycle continuously oscillating without any inhibitory stimulus, and provide a periodic inhibitory stimulus to the cell it is connected to. For escape case systems, in which $I_{app} > 0.55$, this cell would instead fire continuously without any inhibitory stimulus, as it remains trapped in the active state on the upper branch of the cubic nullcline without inhibitory effects to shift the sigmoidal nullcline and allow it to escape said

inhibition, and provide instead a continuous inhibitory stimulus to the cell it is connected to. This would have much more significant effect on network dynamics, as the connected cell would effectively become continuously inhibited and require unique parameter values or much stronger 3-cell network coupling to overwhelm and escape this drive. For either of these cases, this system is relatively easy to visualize using a three-dimensional representation, as shifts will tend to be linear in their effects and traces will not generally cross one another and complicate visualization and interpretation (see Figure 6.1).

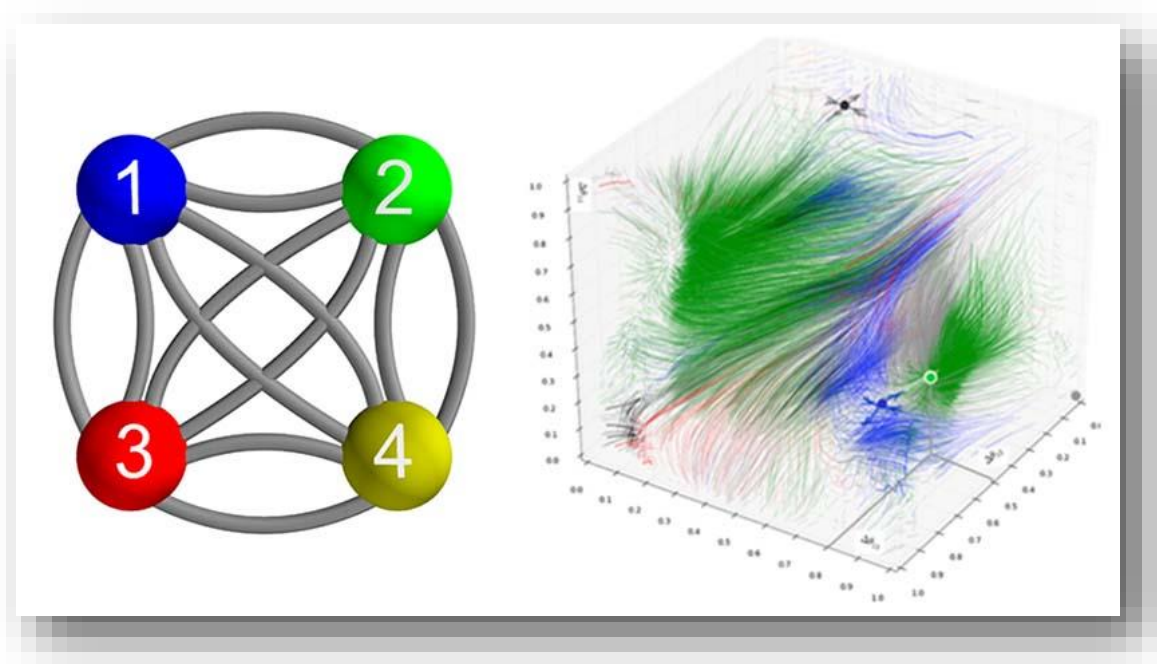


Figure 6.1 Sample 4-cell configuration and 3-D visualization

(A) Doubling of potential number of synaptic connections observed with addition of a fourth cell to the network. (B) 3-D visualization for an originally 3-PM symmetric 3-cell motif with the addition of additional symmetric coupling only between cells 3 and 4, where $g_{ij} = g_{43} = g_{34}$ and $g_{4j} = 0$ otherwise. Cell 3 becomes silenced relative to the other two cells in the original 3-cell network, and cannot induce enough inhibition to become dominant for any of the three-dimensional $(\Delta_{12}, \Delta_{13}, \Delta_{14})$ -space. All traces within the 3-cell motif will converge to either blue or green PM dominance, with the relative positions of cells 3 and 4 remaining in anti-phase, $\Delta_{34} = 0.5$, and positioned in an alternate anti-phase position to the dominant cell depending whether cell 4 was initially active relative to cell 3.

At the opposite end of the spectrum, this additional fourth cell could instead be fully connected to the network, forming an HCO relationship with all three other cells and doubling the number of connections that could be manipulated either symmetrically or asymmetrically. An example of full connectivity can be seen in Figure 6.1(A), where cell 4 is shown in yellow. The 3-D visualization shown in the (B) is for a symmetric motif but with only reciprocal inhibitory coupling of cells 3 and 4, as was described in the second simpler case in which the fourth cell only connects to one within the 3-node motif. Here we can see a three-cell motif that originally exhibited all three pacemaker rhythms driven to only two pacemakers instead. For the symmetric connectivity of cell 4 onto cell 3, where $g_{ij} = g_{43} = g_{34}$, cell 3 becomes effectively silenced relative to the other two cells in the 3-cell network with this additional inhibitory stimulus, and cannot induce enough inhibition on either cell 1 or 2 to become dominant for any of the three-dimensional $(\Delta_{12}, \Delta_{13}, \Delta_{14})$ -space. All traces within the 3-cell motif will converge to either blue or green pacemaker behavior, with the relative positions of cells 3 and 4 remaining in anti-phase, $\Delta_{34} = 0.5$, and positioned depending on whether cell 4 was initially active or not relative to cell 3. It is important to note that this PM behavior may result in a staggered anti-phase location by either the red or yellow cell which is dictated by initial conditions. The effect of adding additional cell 4 connectivity results in traces which will cross over one another even on a 3-dimensional surface, and makes this visualization inadequate to properly describe or identify overall behavior. For such cases, as in the higher-order networks described later, use of two 2-D return maps is required, with the optimal choice of which lags are shown being dictated by both the connectivity and the needs of the experimentalist, typically Δ_{14} and a second lag relationship of choice. Such representations are not shown here, as emphasis is on use of 3-cell motifs as building blocks for larger networks.

6.1.2 Larger network visualization technique

Connectivity of larger networks with 5, 6, or more cells involves many more relationships between cells, with appropriate references becoming more challenging to identify and describe, particularly if more than a couple connections between networks exist. This can become complicated very rapidly, and additional visualization may need to be developed to describe complex systems, an example of multiple inhibitory and electrical connections, as well as an excitatory connection replacing zero connectivity of g_{31} in two otherwise mono-biased motifs, can be seen in Figure 6.2 for a hypothesized network inducing synchronicity between cells in each system. This type of connectivity is not currently conducive to the methods employing broad spanning of parameters described in this work, and is currently restricted to continuing to visualize individual traces to characterize behaviors for specific parameter combinations.

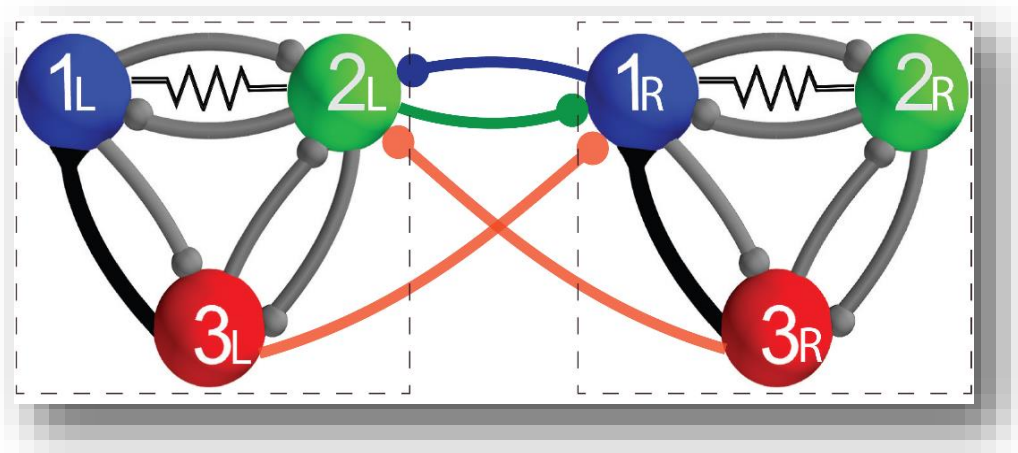


Figure 6.2 Anti-phase connectivity of mono-biased motifs with internal complexity
 Example of additional connectivity between to otherwise mono-biased motifs with $g_{31} = 0$. Replacement of g_{31} by an excitatory connection, as well as weak electrical connection of cells 1 and 2 in each motif adds significant internal complexity to network dynamics not explored in this research. Further coupling of two such identical modified mono-biased inhibitory motifs is shown with HCO connectivity of left cell 2 and right cell 1, as well as incoming inhibitory connections to the same two cells from cell 3 of the opposing network. This helps drive an anti-phase relationship between the two local networks and this circuitry is representative of a hypothesized network inducing synchronicity between respective cells on each side.

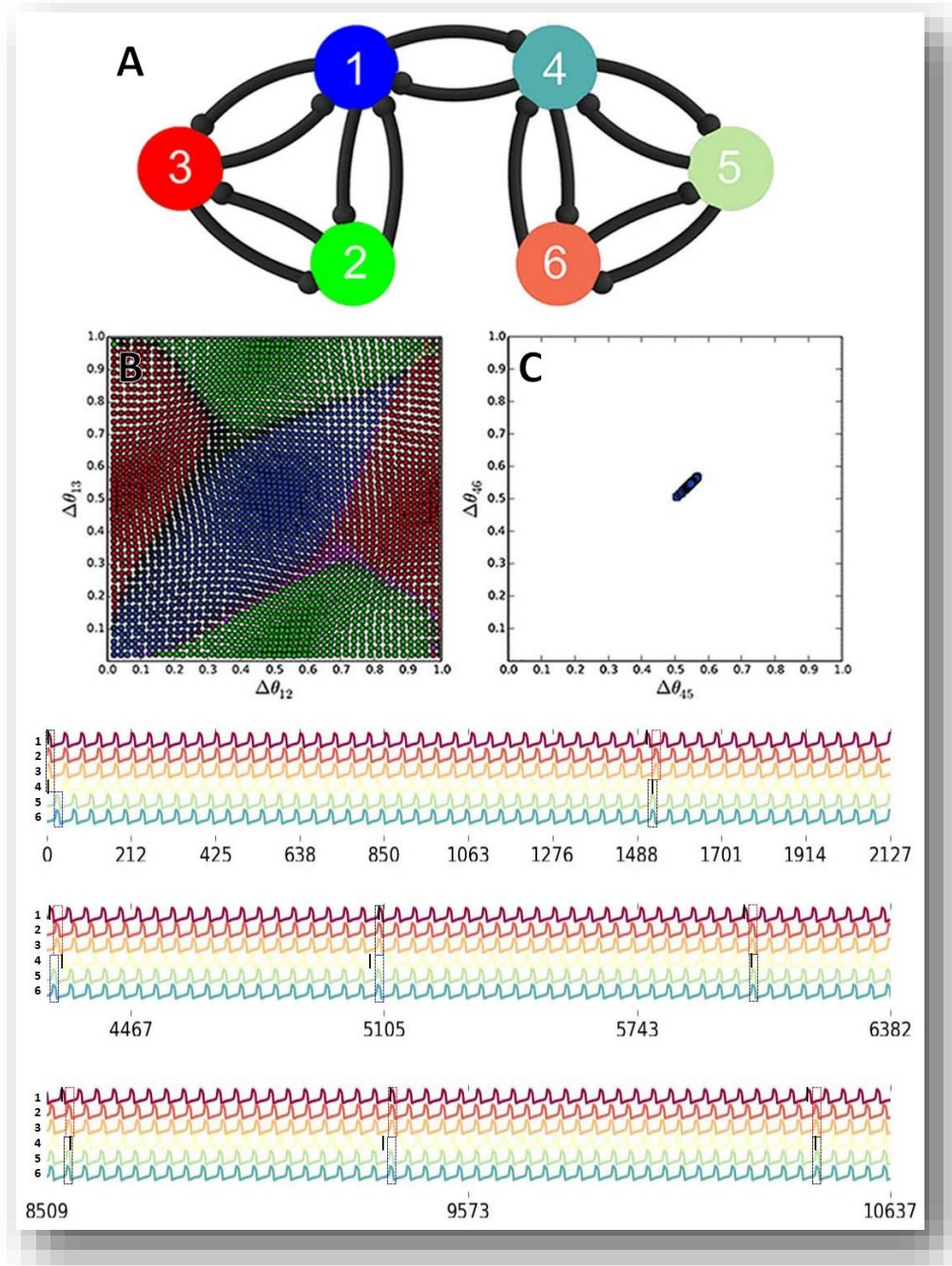


Figure 6.3 2-panel phase basin visualization for 6-cell networks

Example using two phase-basin return maps to describe two symmetric 5-rhythm motifs with reciprocally inhibitory coupling of cells 1 and 4. Here a fixed initial condition is set for one network, here the [456]-network begins at the blue PM position, $(\Delta_{45}, \Delta_{46}) = (0.5, 0.5)$, shown at right (C), beginning [123] with all $(\Delta_{12}, \Delta_{13})$ -space as usual. In this case, the left phase basin diagram (B) shows final outcomes for [123], with significant reduction in the size of the TW basins. Traces converging to system-wide red PM behavior, with [456] synchronicity (not shown for left phase-basin).

Maintaining the structure of research performed thus far, connection of three cell motifs is examined initially using only inhibitory coupling within the framework of the five key network motifs described. This permits use of the two phase-return map approach described, in which each of the two 3-cell networks is described with respect to its primary cell, cell 1 in the first network and cell 4 in the second network, and additional understanding of connectivity between the two primary cells is required to interpret outcomes. A simplified version of this approach to representation can be seen in Figure 6.3, using two phase-basin return map visualizations to describe the connection of two symmetric motifs with reciprocal inhibitory coupling of cells 1 and 4. This approach requires setting a fixed starting initial condition for one network, here [456] at the blue PM position $(\Delta_{45}, \Delta_{46}) = (0.5, 0.5)$ shown at right, while beginning [123] with all $(\Delta_{12}, \Delta_{13})$ -space as usual. In this case, the left phase basin diagram shows final outcomes for [123], with significant reduction in the size of the TW basins, which was originally a stereotypical oscillatory network with all five basic rhythm patterns present in equal distribution. Shown as well are panels zooms of traces converging from an initial system condition of [123] synchronous and [456] blue-pacemaker with 1 and 4 in-phase, $(\Delta_{12}, \Delta_{13}, \Delta_{14}, \Delta_{45}, \Delta_{46}) = (0, 0, 0, 0.5, 0.5)$. This specific starting condition leads to system-wide red pacemaker behavior with [456] synchronicity (phase-basin representation not shown here). This system is at fully symmetric synaptic coupling, with $g_{ij}=g_{kl}=g_{14}=g_{41}$, additional detail on this approach, as well as the effects of weak-to-strong mono- and pairwise-biased inter-motif coupling is described in the following section.

6.2 Inhibitory coupling of symmetric motifs

Extending on the approach of a double phase-basin return map representation of system dynamics, reference to the left motif will be described as was done in Figure 6.3, with [123] represented by coupling strength, g_{ij} , and phase-lag references, $(\Delta_{12}, \Delta_{13})$. The right motif, [456] is represented by

coupling strength, g_{kl} , and phase-lag references, $(\Delta_{45}, \Delta_{46})$. Careful description of the relevant relationships g_{14} , g_{41} , and Δ_{14} will permit larger network characterization. In preliminary work shown here, only these relationships are manipulated, but the number of additional potential g_{il} and g_{kj} connections creates a total number of possible connections having the relationship $\sum_{i=1}^n 2(i-1)$, where n is the number of nodes present in the larger network, as was first seen in the simple case of adding only a fourth cell. If fully interconnected, this network could potentially have $\sum_{i=1}^6 2(i-1) = 30$ connections to manipulate. This vastly compounds the complexity of the network, particularly for any introduced asymmetry, and here work focuses primarily only describing effects of addition of either one, a mono-biased single-coupling using g_{41} , or two, pairwise-biased single-coupling using $g_{14} = g_{41} > 0$, inhibitory connections between symmetric motifs. It is important to note that here, and through the remainder of this work, the term single-coupled is used to represent the number of pairs of cells interconnected between the two motifs, and not necessarily the number of connections, which could be one or two for each pair of cells. Some examples of such double- or triple-connected networks are shown in the Appendix but are not an emphasis of initial modular networking done in this research.

6.2.1 *Mono-biased single inhibitory-coupled symmetric networks*

For simplicity, the following examples employ equi-symmetric motifs, in which all connections within each of the two symmetric motifs are equal those in the other, $g_{ij} = g_{kl}$. Only the coupling connection(s) between the two symmetric motifs are manipulated, and are done so in terms of weak, equal, and strong coupling of motifs. For single-coupled symmetric networks, this relationship can be expressed as $g_{41} = 0.5 \cdot g_{ij} = 0.5 \cdot g_{kl}$, $g_{41} = g_{ij} = g_{kl}$, and $g_{41} = 2 \cdot g_{ij} = 2 \cdot g_{kl}$, for weak, equal, and strong, respectively. In all cases, the [456]-motif is driving the [123]-motif via this single incoming connection. An example for visualization of trace convergence for the [123]-motif

with increasing mono-biased g_{41} coupling in Figure 6.4 shows increased sensitivity to driving influences by the incoming connection from cell 4 that cause trajectories to initially move less smoothly, often crossing one another, before stabilizing to final rhythm outcomes in relationship to cell 1. This is due to increasing push by the driving cell as g_{41} becomes stronger and drives the initially in-phase relationship of cells 1 and 4, $\Delta_{14} = 0$, to anti-phase, $\Delta_{14} = 0.5$. In inhibitory mono-biased single-coupled networks, the [456]-motif remains unaffected, as it is not driven in any way by [123]. This means that local network will remain in the stable blue pacemaker rhythm in which it started, and there is no need to observe visualization of its phase-lag relationship. The blue pacemaker outcome originally present in [123] is largely diminished because of this additional inhibitory influence on it, and portions of its basin are lost to green and red pacemaker outcomes

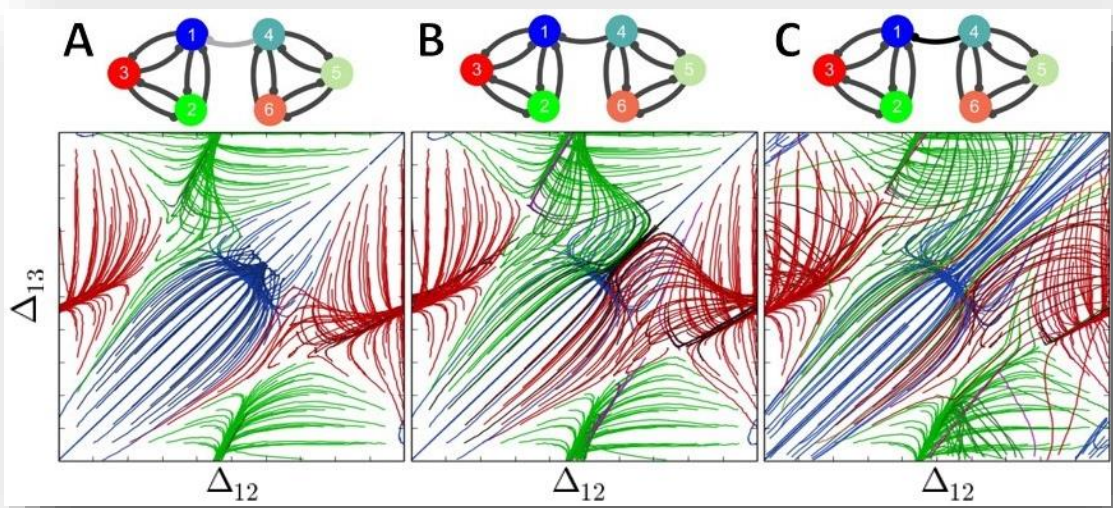


Figure 6.4 Trace convergence in mono-biased single-coupled symmetric networks. Addition of a single inhibitory synapse, g_{41} , between two symmetric motifs. The [456]-motif is begun with fixed initial condition with a blue PM rhythm at $(\Delta_{45}, \Delta_{46}) = (0.5, 0.5)$ driving the [123]-motif, which is fully explored using a grid of ICs. Cells 1 and 4 begin in-phase, and rapidly driven to anti-phase with increased g_{41} coupling. With weak g_{41} coupling, little overall effect is observed in final $(\Delta_{12}, \Delta_{13})$ fixed point outcomes, but initial trajectories fluctuate as cell 1 is pushed away from cell 4. With increasing g_{41} coupling, these initial fluctuations become more complex and interpretation is complicated by crossing trajectories. Parameters: $\Delta_{14,init} = 0$, $g_{41} = 0.5 \cdot g_{ij} = 0.5 \cdot g_{kl}$, $g_{41} = g_{ij} = g_{kl}$, and $g_{41} = 2 \cdot g_{ij} = 2 \cdot g_{kl}$.

in that motif. Some initial conditions, particularly for stronger g_{41} coupling, experience extensive ‘wandering’ effects in which longer cycle time is required to observe final convergence, and some initial conditions may in fact appear to exhibit seemingly chaotic behavior.

Even in this simple connectivity case, a trajectory-based approach to phase-lag return maps is inadequate for rapid analysis of rhythm outcomes, and phase-basin representations will be used here instead, as was done for some previous strong-coupling or post-inhibitory rebound systems in which this method was employed. This simplifies interpretation of the effects of increasing g_{41} coupling on [123] rhythm outcomes by ignoring entirely the individual trajectories of each initial condition and instead plotting at its position only the color of the final rhythm outcome for that

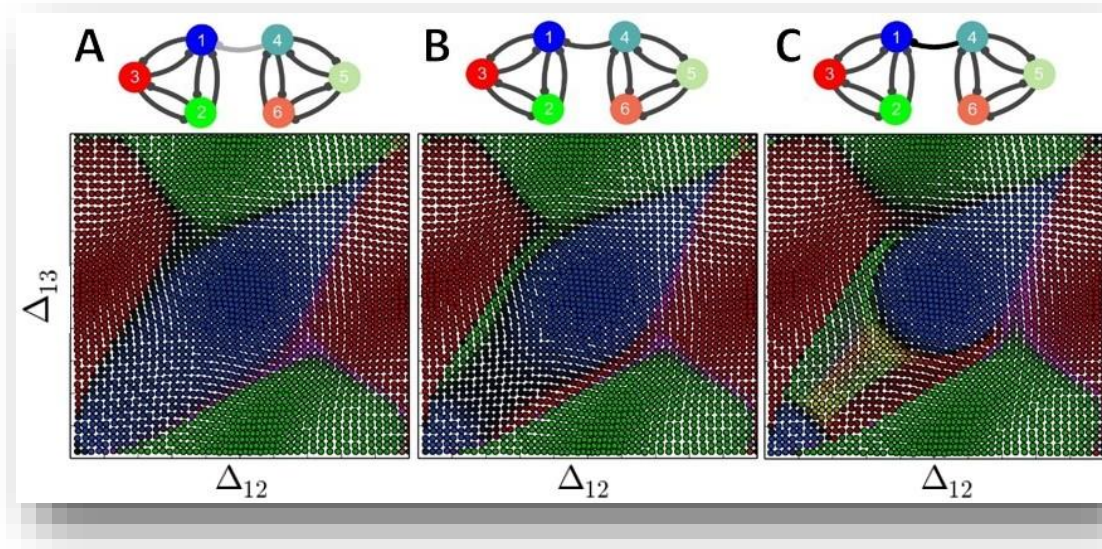


Figure 6.5 Basin visualization for mono-biased single-coupled symmetric networks

As in Figure 6.4, a single inhibitory synapse, g_{41} , connects two symmetric motifs with [456] beginning as a blue PM rhythm, $(\Delta_{45}, \Delta_{46}) = (0.5, 0.5)$ driving the [123]-motif, with cells 1 and 4 in-phase. Here, however, phase-basin representation simplifies interpretation of the effects of this coupling on [123] rhythm outcomes by ignoring entirely the trajectories of each IC and instead plotting only the color of the final rhythm outcome for that starting position. This reiterates dominance of green and red PM outcomes, and emphasizes additional complexity for some ICs originally starting in the blue PM basin that now converge to one of the other two or exhibit seeming chaotic behavior. Longer cycle time would be required to observe final convergence for some of these states. Parameters: $\Delta_{14,init} = 0$, $g_{41} = 0.5 \cdot g_{ij} = 0.5 \cdot g_{kl}$, $g_{41} = g_{ij} = g_{kl}$, and $g_{41} = 2 \cdot g_{ij} = 2 \cdot g_{kl}$.

initial condition. Interpretation reiterates dominance of both the green and red pacemaker outcomes, and emphasizes additional complexity for some initial conditions originally starting in the blue PM basin that now converge to one of the other two or may even exhibit seeming chaotic behavior (denoted by multi-colored or yellow regions in the phase-basin diagram). Longer cycle times would typically be adequate to observe final convergence for some of these states, while in other systems this may indeed represent phase-slip, quiescence, or ergotic tendency.

This approach much more clearly represents final rhythm outcomes by avoiding complexity introduced by trajectories crossing over one another within the phase-lag return map, and is employed for all remaining results described in this chapter and in the supplemental results found in the index for modular networking using connected 3-node motifs. In this previous example, increasing the driving force of [456] on [123] by increasing g_{41} coupling leads to increasing reduction in the ability of the blue pacemaker rhythm to dominate the [123]-network. Since [456] was itself unaffected, its rhythm generation remained in the blue pacemaker rhythm in which it began, $(\Delta_{45}, \Delta_{46}) = (0.5, 0.5)$, but in local network anti-phase relative to [123], as cell 4 affectively turns off cell 1 whenever it is active, $\Delta_{14} = 0.5$. This means that final rhythm outcomes, in relationship to cell 1, could be described as $(\Delta_{12}, \Delta_{13}, \Delta_{14}, \Delta_{15}, \Delta_{16}) = (x, y, 0.5, 0, 0)$, with x and y each representing the final return map solutions for each initial $(\Delta_{12}, \Delta_{13})$ starting position.

6.2.2 Pairwise-biased single inhibitory-coupled symmetric networks

In the mono-biased connection of symmetric motifs just described, one network will always remain in its original state, receiving no reciprocal or other external driving force to push its system away from its beginning equilibrium. The introduction of a second, reciprocal connection, between cells 1 and 4 leads to feedback between the two networks that can lead to rhythm changes in both. This single additional connection adds increasing complexity that now requires visualization of

both phase-basin outputs, since [456] will not necessarily remain in the starting position it which it begins. This approach still requires a fixed $(\Delta_{45}, \Delta_{46})$ -space initial condition for which the results in both phase basins are valid, with full sweeping of possible rhythm generation outcomes requiring a collection of paired [123]-[456] phase-basin return maps for the entire $(\Delta_{45}, \Delta_{46})$ -space being sampled. For complex asymmetric networks, where many rhythms are possible and symmetry does not exist between specific pacemaker or traveling wave outcomes, this problem may be too complex for this approach to properly explore full network potential. For symmetric systems, however, this problem does not exist due to equivalency that exists between each pacemaker or each traveling wave pattern. Outcomes that are valid for one of each set will apply symmetrically to the other(s). In this section, results are therefore described for initial conditions sampling only one key rhythm type (PM, TW, or one of each) with the knowledge that the results will be transitive to the others. One further simplifying assumption is made here, however, in using initial conditions that have already converged to stable equilibrium in the unconnected motif. Results obtained in this manner may not always be valid for any other initial conditions within the original basin of attraction for the rhythm in the connected network, as system-wide convergence once both networks are connected can be heavily influenced by the specific relative phase-lag separation of each cell. For clarity, the first example of this approach will use the same system settings and parameters previously observed for the stereotypical symmetric release case, described in Figure 2.8(C). In this case, all five rhythm outcomes are originally possible, but with vastly reduced basins of attraction for the two traveling wave outcomes. In Figure 6.6, the phase-lag return map obtained previously for this is shown, as well as visualization of the connection of two such identical motifs via reciprocally inhibitory pairwise-biased single coupling. In future examples, the initial phase-basin result prior to connection will be shown instead.

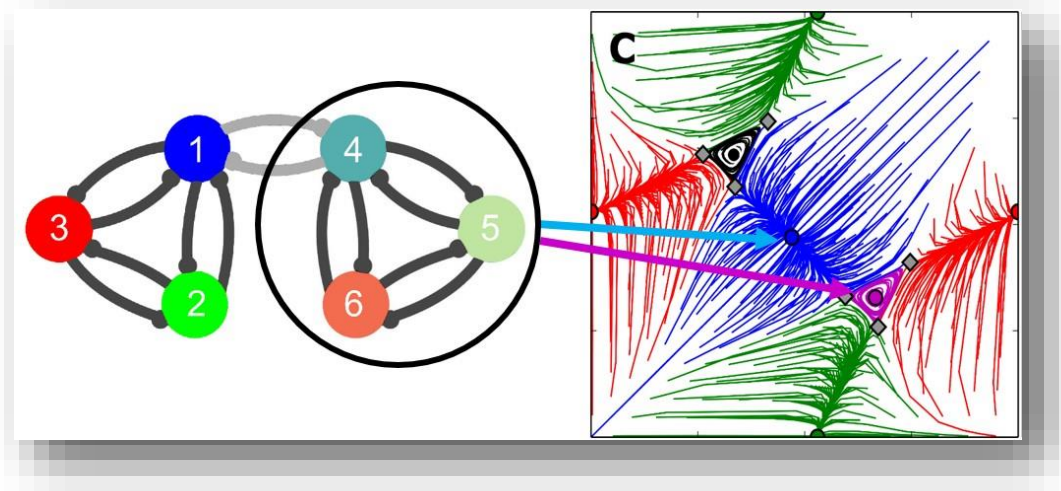


Figure 6.6 Weak inhibitory pairwise-biased symmetric mixed release

Introduction of weak reciprocal inhibition between cells 1 and 4 ($g_{14} = g_{41}$) of identical symmetric release case motifs described in Figure 2.8(C). Sample outputs for this network are shown in the Figure 6.7 for [456] beginning in either blue PM or purple CCTW rhythmicity, near $(\Delta_{45}, \Delta_{46}) = (0.5, 0.5)$ or $(2/3, 1/3)$, respectively. Parameters: $I_{app} = 0.4155$, $g_{ij} = g_{kl} = 0.015$ except $g_{14} = g_{41} = 0.0075$.

As in the example in Figure 6.4, introduction of weak reciprocal inhibition between in-phase cells 1 and 4, $\Delta_{14} = 0$, at half the strength of the other connections, with $g_{14} = g_{41} = 0.0075$, leads to initial loss of the traveling wave rhythms. In Figure 6.7, we observe the effect of this reciprocal inhibition on [123] is the same for either $(\Delta_{45}, \Delta_{46})$ beginning position for [456] (left panels of A and B). Traveling wave patterns completely disappear and the entire $(\Delta_{12}, \Delta_{13})$ -space is evenly shared by the three pacemaker rhythms, but with an interesting whorl of split divergence to these three patterns from the locations where the black CTW and purple CCTW rhythms had previously existed. Introduction of this additional inhibitory coupling has successfully driven the system through torus bifurcation in which collapse of saddles around each point has resulted in a stability shift. All three pacemaker rhythms are possible in [123] in either initial condition for $(\Delta_{45}, \Delta_{46})$, depending on initial $(\Delta_{12}, \Delta_{13})$ -relationships. The outcomes for [456] are very different, however, depending on which of the two initial conditions for $(\Delta_{45}, \Delta_{46})$ are used. When begun as a blue

pacemaker rhythm, $(\Delta_{45}, \Delta_{46}) = (0.5, 0.5)$, the system remains in this stable rhythm even with reciprocal coupling with [123] via the $g_{14} = g_{41}$ connection. This is a direct result of the fact that coupling between motifs is weak and there is not a strong drive to push cells 1 and 4 into anti-phase, which would have potentially led to abrupt early transitions in convergence trajectories.

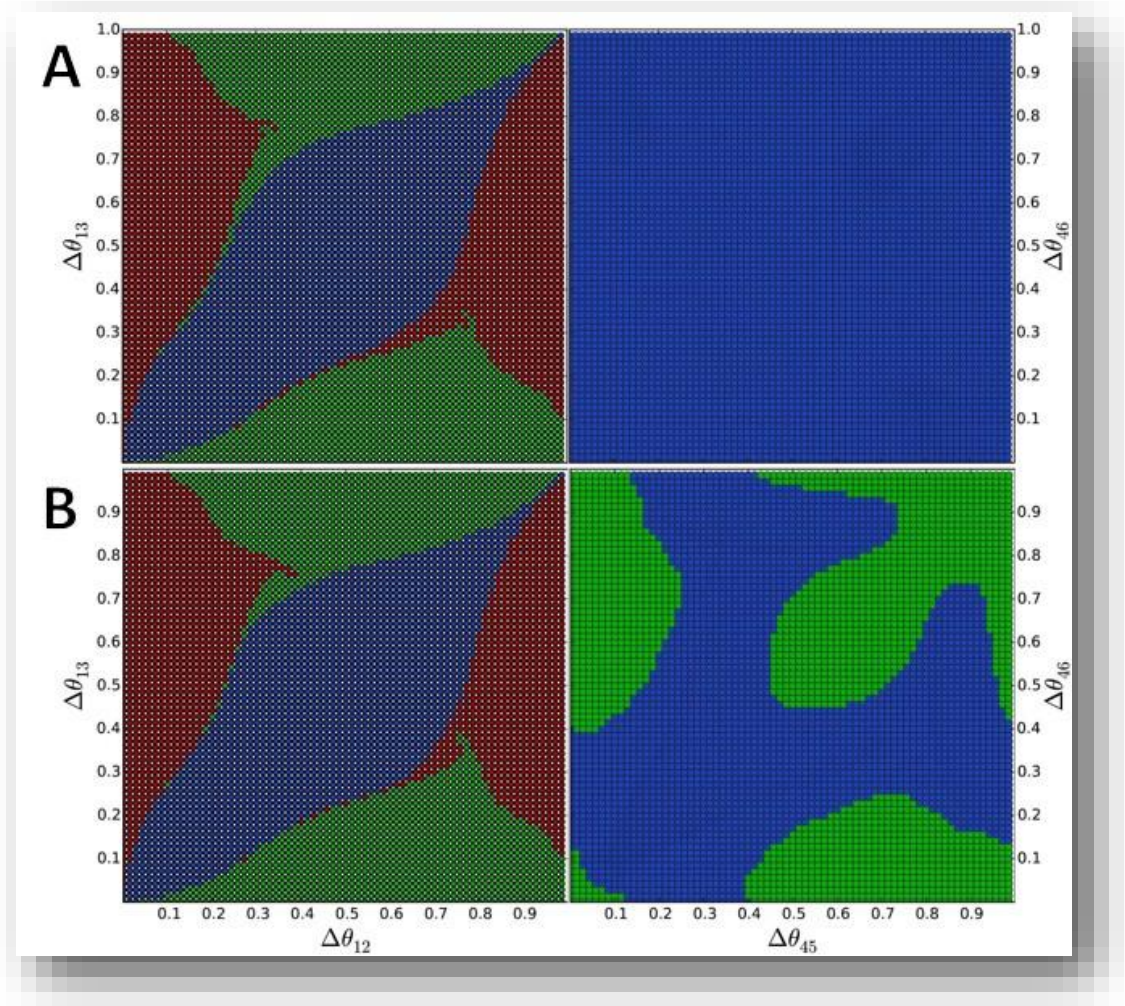


Figure 6.7 Weak inhibitory pairwise-biased symmetric release

Symmetric release case system, as in Figure 2.8(C), with introduction of weak reciprocal inhibition, $g_{14} = g_{41}$, between in-phase cells 1 and 4. Panels represent system outcomes for both networks, exploring all $(\Delta_{12}, \Delta_{13})$ -space, but starting [456] as either blue PM (A) or purple CCTW (B) with $(\Delta_{45}, \Delta_{46}) = (0.5, 0.5)$ or $(2/3, 1/3)$, top and bottom panels respectively. For both cases, [123] converges equally to one of three PM rhythms based on ICs, TW patterns disappearing completely. For the first case, [456] will remain in blue PM rhythmicity with weak coupling, while for the second it rapidly diverges from this pattern to either the blue or green PM. Parameters: $\Delta_{14,initial} = 0$, $I_{app} = 0.4155$, $g_{ij} = g_{kl} = 0.015$ except $g_{14} = g_{41} = 0.0075$.

When [456] is begun as a counterclockwise traveling wave, $(\Delta_{45}, \Delta_{46}) = (2/3, 1/3)$, however, it is not guaranteed that it will remain in a stable blue PM rhythm and the green PM rhythm outcome now occurs half of the time, depending on the initial conditions of $(\Delta_{12}, \Delta_{13})$, which in turn affect when and how strongly cell 1 is activated and exerts inhibition on cell 4. It is important to note here that interpretation of the $(\Delta_{45}, \Delta_{46})$ using this approach is different from that used thus far for $(\Delta_{12}, \Delta_{13})$ -return maps. Since we begin the [456]-motif at a specified initial condition, its return map does not represent the outcome for each $(\Delta_{45}, \Delta_{46})$ -space condition but instead represents for the singular initial condition being examined what rhythm [456] will exhibit given that specific pairing of shown $(\Delta_{12}, \Delta_{13})$ -return map outcomes. For example, if we wanted to know the outcome of pairing a red PM [123] network condition, $(\Delta_{12}, \Delta_{13}) = (0, 0.5)$, with a black CTW [456] network condition, $(\Delta_{45}, \Delta_{46})$, using initially in-phase coupling of cells 1 and 4, the $\Delta_{14} = 0$, we need only look at the $(0, 0.5)$ position in each of the two panels in Figure 6.7(B). In the left panel, a red dot is present at $(\Delta_{12}, \Delta_{13}) = (0, 0.5)$, indicating that network [123] remains a red PM even after the networks are connected in this manner. In the right panel, however, a green dot is present at $(\Delta_{45}, \Delta_{46}) = (0, 0.5)$, indicating that network [456] will transition from its initial black CTW rhythm, with relationship $(\Delta_{45}, \Delta_{46}) = (1/3, 2/3)$, to become a green PM system, with relationship $(\Delta_{45}, \Delta_{46}) = (0.5, 0)$, when cell 4 begun in phase with cell 1 when [123] begins as a red-PM, with $(\Delta_{12}, \Delta_{13}) = (0, 0.5)$. In this manner, we can pair each matching point on the two return maps to determine the rhythm outcomes for both local networks given that specific starting position in [123] for the fixed beginning point selected for [456]. To be specific, this system could be represented in this example with either of the two following relationship transformations: $(\Delta_{12}, \Delta_{13}, \Delta_{14}, \Delta_{45}, \Delta_{46}) = (0, 1/2, 0, 1/3, 2/3) \rightarrow (0, 1/2, z, 1/2, 0)$ or $(\Delta_{12}, \Delta_{13}, \Delta_{14}, \Delta_{15}, \Delta_{16}) = (0, 1/2, 0, 1/3, 2/3) \rightarrow (0, 1/2, z, z+1/2, z)$, where z is the amount of anti-phase behavior induced by the strength of the coupling

between the two networks, and indicates the importance of also knowing the final outcome for Δ_{14} when using this method. In this case, coupling is too weak to push them to full anti-phase and, depending on the initial conditions for $(\Delta_{12}, \Delta_{13})$, generally Δ_{14} remains close to zero.

Extending on this example, but using weaker network connectivity, with $g_{ij} = g_{kl} = 0.0005$, and very slightly higher I_{app} , the size of the basins of attraction for the traveling wave patterns is more equivalent to those observed for pacemakers (see Figure 6.8). This change permits more system dynamics, and sensitivity to change, than the previous one did, for which traveling waves were eliminated with the introduction of even weak inter-network coupling. In Figure 6.9, system changes can be observed beginning this larger network with [456] in either the blue PM or black CTW rhythm, near with $(\Delta_{45}, \Delta_{46}) = (0.5, 0.5)$ or $(1/3, 2/3)$. As before, both cases are explored (A and B, respectively) beginning with cells 1 and 4 in-phase, with $\Delta_{14} = 0$, but now followed by an example beginning in anti-phase, with $\Delta_{14} = 0.5$, for the black CTW initial conditions (C).

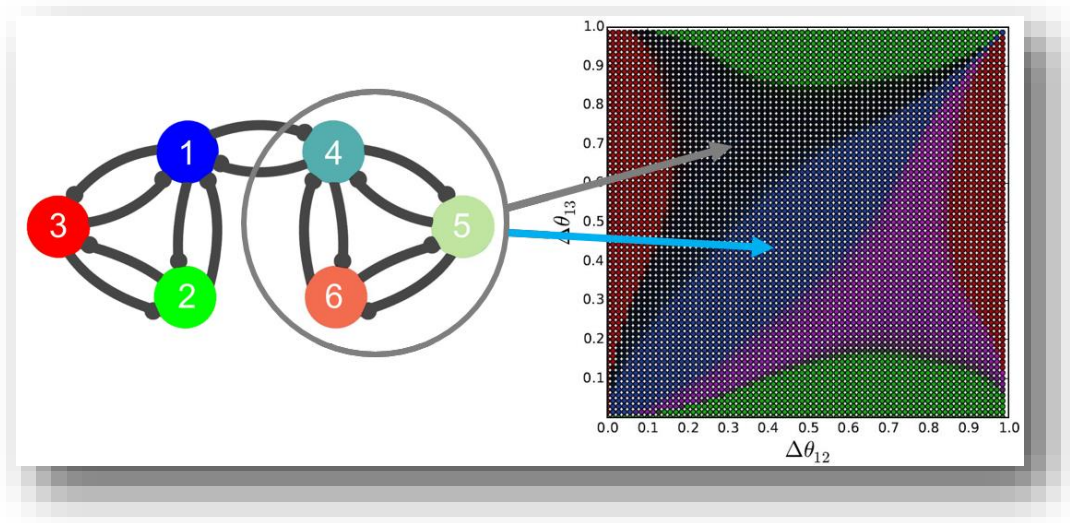


Figure 6.8 Moderate inhibitory pairwise-biased symmetric mixed release
Introduction of moderate reciprocal inhibition between cells 1 and 4 ($g_{14} = g_{41}$) of identical symmetric release case motifs with weaker inner-network connectivity, and larger initial basins of attraction for the TW rhythms. Sample outputs for this network are shown in Figure 6.9 for [456] beginning in either blue PM or black CTW rhythmicity, near $(\Delta_{45}, \Delta_{46}) = (0.5, 0.5)$ or $(1/3, 2/3)$, respectively. Parameters: $I_{app} = 0.42$, $g_{ij} = g_{kl} = g_{14} = g_{41} = 0.0005$.

In the top two panels, where the system begins with cells 1 and 4 in-phase, $\Delta_{14} = 0$, examining the full $(\Delta_{12}, \Delta_{13})$ -space of initial conditions with blue PM [456], having $(\Delta_{45}, \Delta_{46}) = (1/2, 1/2)$, much greater effect resulting from moderate coupling is observed than was seen with weak coupling. Here $g_{ij} = g_{kl} = g_{14} = g_{41}$, and the reciprocal inhibition between the two local networks at cells 1 and 4 is just as strong as connections within each network to other cells. Both local networks are much more susceptible to $(\Delta_{12}, \Delta_{13})$ initial condition effects, and frequently driven away from whatever original pattern had dictated its rhythmicity. The [123]-motif sees significant reduction in potential pacemaker outcomes, with increasing traveling wave regimes and complex basin boundary relationships with multiple non-contiguous pockets of $(\Delta_{12}, \Delta_{13})$ -space for which each pattern can occur. The [456]-motif continues to retain much ability to stay in a blue pacemaker (BPM) rhythm relationship for about 45% of the $(\Delta_{12}, \Delta_{13})$ -space initial conditions, with an equal portion of these initial conditions now driving it instead to black traveling wave behavior. Of interest, however, are the new regions of very slow convergence or of either apparent chaotic or quiescent behavior shown in yellow. These regions must be recognized with care, as this color coding only indicates that the numerical methods employed in this computational approach did not converge to a solution within the number of cycles specified (typically 150 were used). To broadly span results and connect regions of differing rhythmicity, these specific cases have not been investigated in much depth in this research as they generally form a minority of overall outcomes and would require individual trace analysis (in this case for up to 10% of the 75x75 grid, or approximately 562 traces for this map alone).

In the middle two panels, all $(\Delta_{12}, \Delta_{13})$ -space of initial conditions are again explored with cells 1 and 4 beginning in-phase, $\Delta_{14} = 0$, but with a fixed black CTW initial condition for [456], having $(\Delta_{45}, \Delta_{46}) = (1/3, 2/3)$. Patterns in both networks are again frequently driven away from the pattern

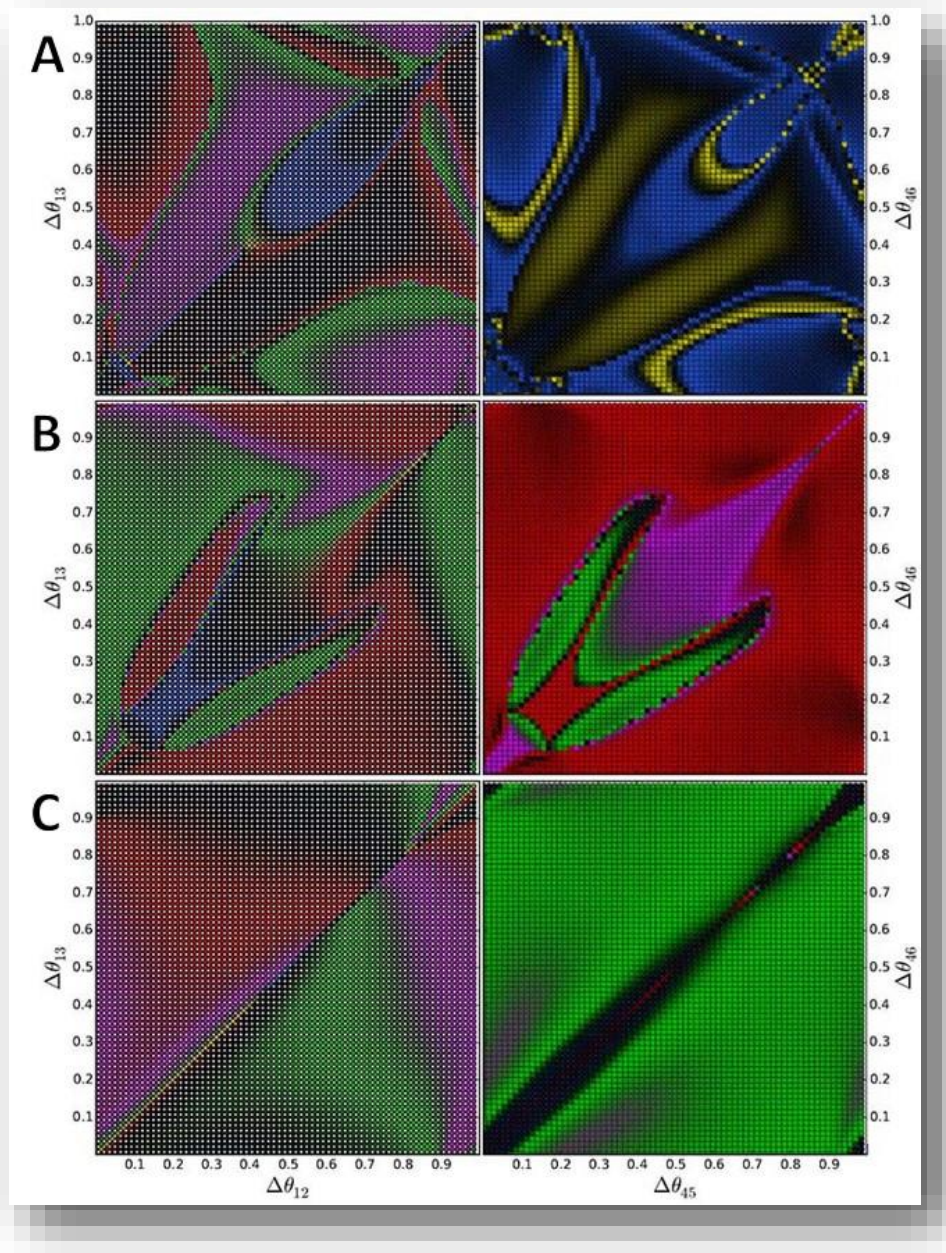


Figure 6.9 Moderate inhibitory pairwise-biased symmetric mixed release

Symmetric release case, with introduction of moderate reciprocal inhibition, $g_{14} = g_{41}$, between cells 1 and 4. Panels represent system outcomes for both networks, exploring all $(\Delta_{12}, \Delta_{13})$ -space, [456] starting as blue PM or black CTW, $(\Delta_{45}, \Delta_{46}) = (0.5, 0.5)$ or $(1/3, 2/3)$, cells 1 and 4 beginning in-phase for A and B and anti-phase black CTW for C. PM rhythms outcomes for [123] significantly diminish in A, with most [456] outcomes remaining blue PM or shifting to CTW. Conversely, most TW rhythms are lost in both networks for initial black CTW [456], with red and green PM rhythms gaining dominance for both networks in opposite fashion for each case. Unique diagonal and origin initial conditions $(\Delta_{12} = \Delta_{13})$ or $(\Delta_{12}, \Delta_{13}) \approx 0$ with convergence to black CTW rhythms in anti-phase. Parameters: $I_{app} = 0.42$, $g_{ij} = g_{kl} = g_{14} = g_{41} = 0.005$.

dictating its starting rhythmicity, but this time with significant reduction in potential traveling wave outcomes for both motifs, and complete or nearly complete elimination of the blue pacemaker as a possible outcome for the [456] and [123] motifs, respectively. Both networks are dominated, in different ways, by red and green pacemaker, as well as counterclockwise traveling wave, rhythms, again with complex basin boundary relationships with multiple non-contiguous pockets of $(\Delta_{12}, \Delta_{13})$ -space for which each pattern may occur. Reiterating upon the same example used for interpretation in the weakly connected motifs in Figure 6.7, pairing of a red PM [123] network condition, $(\Delta_{12}, \Delta_{13}) = (0, 0.5)$, with a black CTW [456] network condition, $(\Delta_{45}, \Delta_{46})$, using initially in-phase coupling of cells 1 and 4, the $\Delta_{14} = 0$, is indicated by the color of the dot in the $(0, 0.5)$ position in each of the two panels in Figure 6.9(B). The green dot in the left panel indicates that network [123] shifts from red to green PM rhythmicity, with $(\Delta_{12}, \Delta_{13}) = (0.5, 0)$, after connection with [456]. The red dot at this position in the right panel that network [456] shifts from black CTW to red PM rhythmicity after coupling. Unlike the weak coupling case, however, the stronger $g_{14} = g_{41}$ coupling in this system is adequate to push cells 1 and 4 into near anti-phase for nearly all $(\Delta_{12}, \Delta_{13})$ -space, with $\Delta_{14} \approx 0.5$. This specific initial condition set for the system could therefore be represented with either of the two following relationship transformations: $(\Delta_{12}, \Delta_{13}, \Delta_{14}, \Delta_{45}, \Delta_{46}) = (0, 1/2, 0, 1/3, 2/3) \rightarrow (0, 1/2, 1/2, 1/2, 0)$ or $(\Delta_{12}, \Delta_{13}, \Delta_{14}, \Delta_{15}, \Delta_{16}) = (0, 1/2, 0, 1/3, 2/3) \rightarrow (0, 1/2, 1/2, 0, 1/2)$.

For the anti-phase starting condition of a black CTW [456] network, with $\Delta_{14} = 0.5$, a significantly different outcome is observed than that for the black CTW starting in-phase. The [123] network again is primarily dominated by red and green pacemaker, as well as counterclockwise traveling wave, rhythms but without most of the complex basin boundaries and non-contiguous pockets of $(\Delta_{12}, \Delta_{13})$ -space observed for which each pattern may occur. The [456] network is driven for nearly

all initial conditions of the $(\Delta_{12}, \Delta_{13})$ -space to green pacemaker rhythmicity, with a narrow band of black CTW rhythms possible along the diagonal or near the origin, where starting conditions of either $\Delta_{12} = \Delta_{13}$ or $(\Delta_{12}, \Delta_{13}) \approx (0, 0)$ existed, respectively. The same example of interpretation used thus far would result in an outcome for pairing of a red PM [123] network with a black CTW [456] network using anti-phase initial connection of cells 1 and 4 would give the final relationship $(\Delta_{12}, \Delta_{13}, \Delta_{14}, \Delta_{45}, \Delta_{46}) = (0, 1/2, 1/2, 1/3, 2/3) \rightarrow (2/3, 1/3, 1/2, 1/2, 0)$ or $(\Delta_{12}, \Delta_{13}, \Delta_{14}, \Delta_{15}, \Delta_{16}) = (0, 1/2, 1/2, 5/6, 1/6) \rightarrow (2/3, 1/3, 1/2, 0, 1/2)$. Examples reading these maps continues in this manner and will not be performed for remaining results shown here.

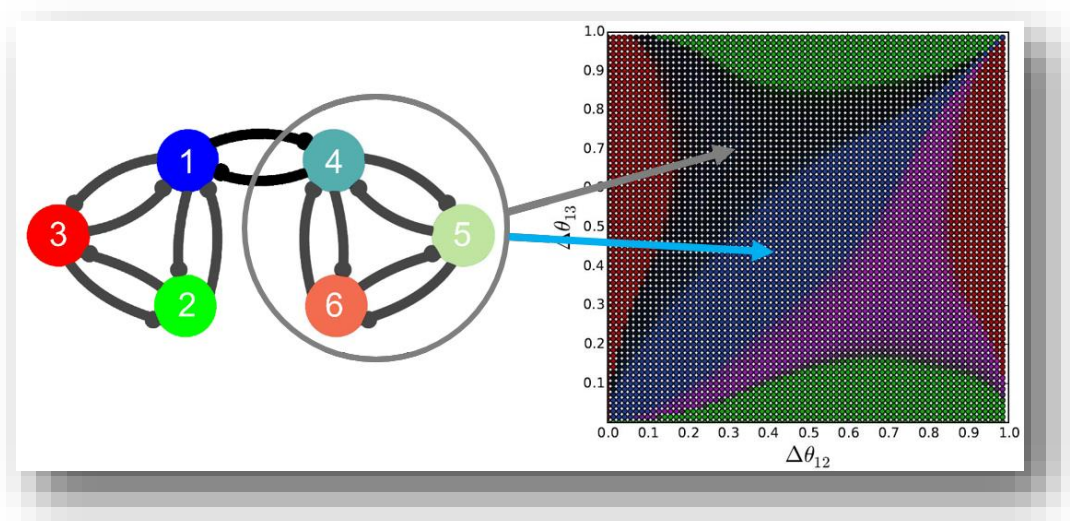


Figure 6.10 Strong inhibitory pairwise-biased symmetric mixed system

Introduction of very strong reciprocal inhibition between cells 1 and 4 ($g_{14} = g_{41}$) of identical symmetric release case motifs with weaker inner-network connectivity, and larger initial basins of attraction for the TW rhythms. Sample outputs for this network are shown in Figure 6.11 for [456] beginning in either blue PM or black CTW rhythmicity, near $(\Delta_{45}, \Delta_{46}) = (0.5, 0.5)$ or $(1/3, 2/3)$, respectively. Parameters: $I_{app} = 0.42$, $g_{ij} = g_{kl} = 0.0005$ except $g_{14} = g_{41} = 0.050$.

Finally, for strong reciprocally inhibitory coupling between the two networks, with $g_{14} = g_{41}$ ten times as strong within-network connections, similar trends in behavior are observed in Figure 6.11 as were seen in the moderately coupled networks just described. Traces in this connectivity

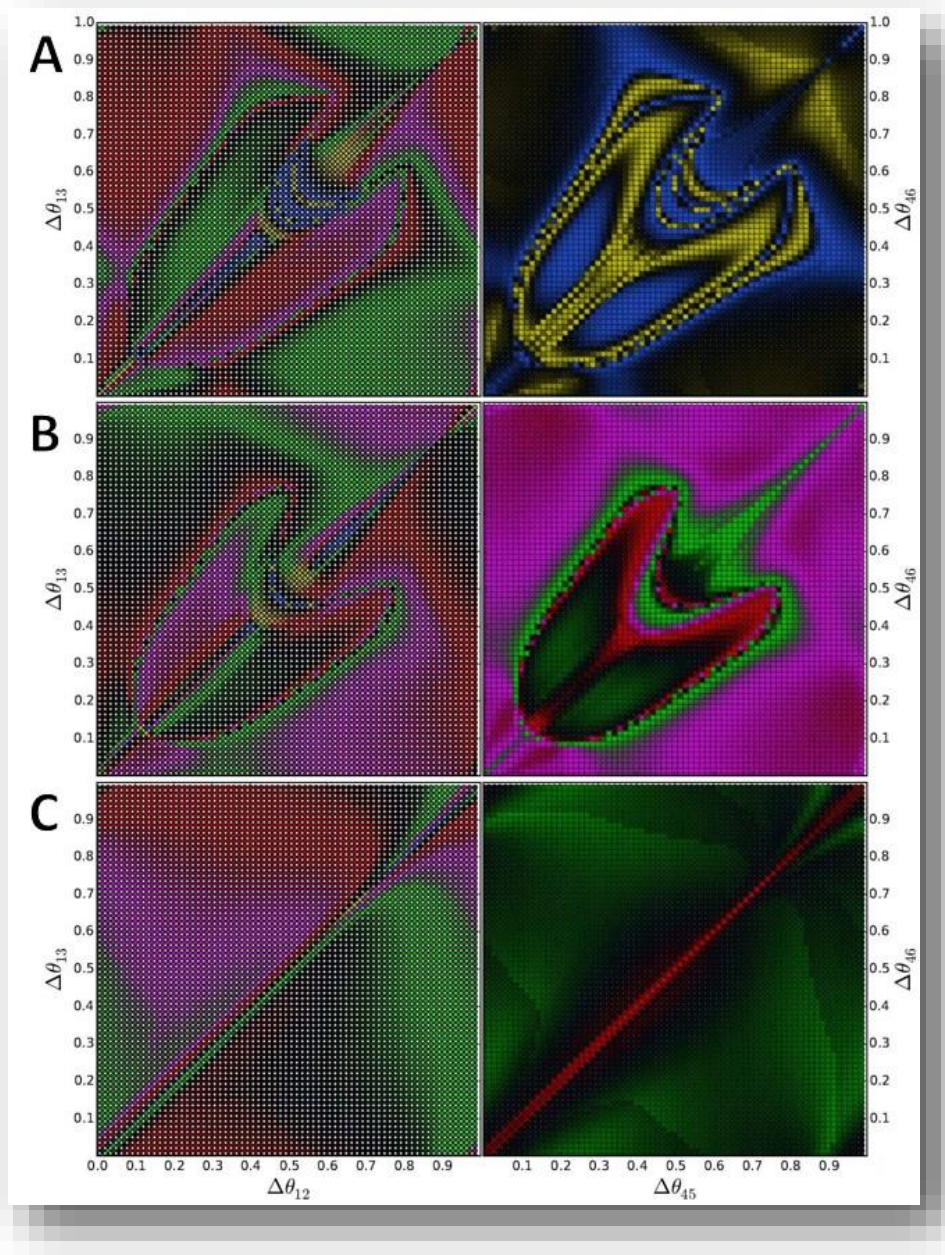


Figure 6.11 Strong inhibitory pairwise-biased symmetric mixed release

Symmetric release case with strong reciprocal inhibition, $g_{14} = g_{41}$. Panels represent system outcomes for both networks, exploring all $(\Delta_{12}, \Delta_{13})$ -space, [456] starting as blue PM or black CTW, $(\Delta_{45}, \Delta_{46}) = (0.5, 0.5)$ or $(1/3, 2/3)$, cells 1 and 4 beginning in-phase for A and B and anti-phase black CTW for C. In this case, TW rhythms outcomes for [123] significantly diminish in A, with most [456] outcomes again remaining blue PM or shifting to CTW. Also conversely, most PM rhythms are lost in both networks for initial black CTW [456], TW rhythms gaining dominance and particularly the CCTW rhythm for the in-phase [456] network. Green PM behavior dominates anti-phase [456] unique diagonal initial red PM outcomes at $\Delta_{12} = \Delta_{13}$ initial conditions. Parameters: $I_{app} = 0.42$, $g_{ij} = g_{kl} = 0.0005$ except $g_{14} = g_{41} = 0.050$.

framework converge much more quickly, however, and this induces some additional complexity in basin boundary and non-contiguous rhythmicity pocket outcomes than previously. In addition to overall increased complexity in all three visualized outcomes, a distinct new region of possible red PM [456] outcomes now exists in the anti-phase black CTW example in the right panel of C for initial conditions in which $\Delta_{12} = \Delta_{13}$.

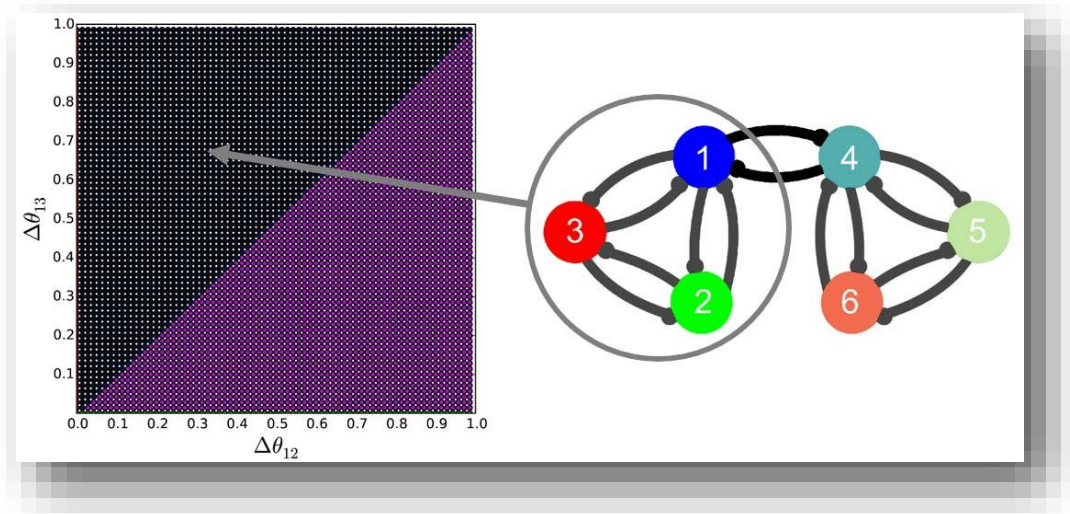


Figure 6.12 Strong inhibitory pairwise-biased symmetric TW system

Introduction of very strong reciprocal inhibition between cells 1 and 4 ($g_{14} = g_{41}$) of identical symmetric oscillatory case motifs in which only TW rhythms are possible when unconnected. Sample outputs for this network are shown in Figure 6.13, this time instead spanning all $(\Delta_{45}, \Delta_{46})$ -space while beginning [123] in black CTW rhythmicity, near $(\Delta_{12}, \Delta_{13}) = (1/3, 2/3)$. Parameters: $I_{app} = 0.50$, $g_{ij} = g_{kl} = 0.010$ except $g_{14} = g_{41} = 0.050$.

Finally, as examples shown thus far all resided in release case ranges of I_{app} , for which all five primary rhythm outcomes were possible for either network when unconnected, an example of strong coupling between two purely oscillatory networks, in which only the two traveling wave patterns exist when uncoupled, is explored here (see Figure 6.12). In this example, the full $(\Delta_{45}, \Delta_{46})$ -space of initial conditions is explored while [123] is begun in each case with the black CTW initial condition, at $(\Delta_{12}, \Delta_{13}) = (1/3, 2/3)$. This is only shown for the in-phase initial condition,

with $\Delta_{14} = 0$ at initiation of coupling of the two networks. This results in initial conditions for most of $(\Delta_{45}, \Delta_{46})$ -space converging to green PM behavior, with the blue PM outcome not possible at all due to the very strong inhibitory effects on it by the [123] network. Both traveling wave and the red PM rhythm remain possible in minority. The [123]-motif, which began with wave-forms in the black CTW phase-lag, with $(\Delta_{12}, \Delta_{13}) = (1/3, 2/3)$, will by and large remain a traveling wave but is equally likely to be pushed in counter-clockwise rotation depending on the initial conditions for $(\Delta_{45}, \Delta_{46})$. Additional regions of both red and green PM outcomes are also possible, with blue rhythms again not possible at all. Interestingly, there is now an increased region of multi-colored phase-basin outcomes near what could almost be considered the wing-tips of a butterfly pattern.

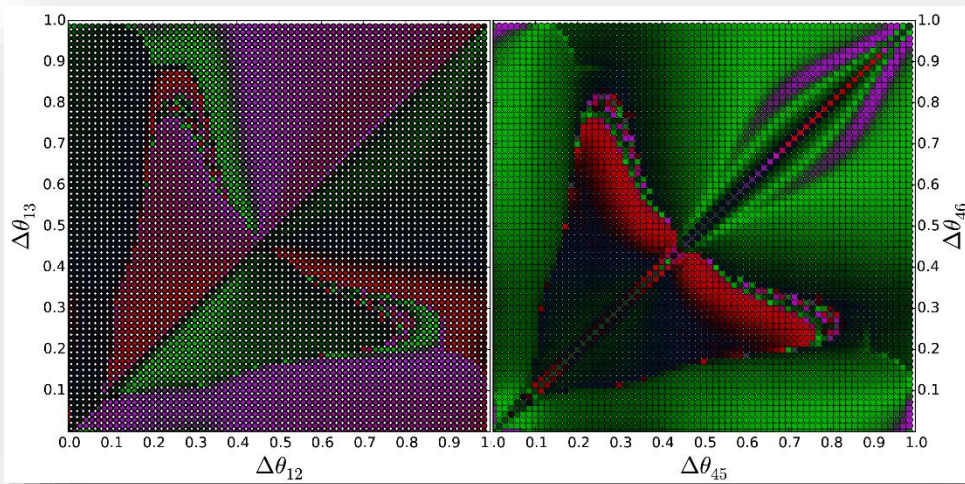


Figure 6.13 Strong inhibitory pairwise-biased symmetric TW networks

Symmetric case in oscillatory range of I_{app} , with strong reciprocal inhibition, $g_{14} = g_{41}$. Panels represent system outcomes for both networks, exploring all $(\Delta_{45}, \Delta_{46})$ -space, [123] starting as black CTW, $(\Delta_{45}, \Delta_{46}) = (1/3, 2/3)$ and cells 1 and 4 beginning in-phase, with $\Delta_{14} = 0$. Green PM rhythms outcomes dominate the IC-space of [456], with the presence of all other patterns except the blue PM. Most [123] outcomes remain oscillatory traveling waves for all [456] ICs as but with equal distribution of CTW and CCTW and the appearance of some previously impossible red and green PM behaviors. More dynamic rhythm behavior is seen, with appearance of multiple PM regions, as well as regions of multi-colored phase-varying lag, or ‘rivers’, similar to those seen in asymmetric 3-node motifs previously described. Parameters: $I_{app} = 0.50$, $g_{ij} = g_{kl} = 0.010$ except $g_{14} = g_{41} = 0.050$.

Previously it was observed that yellow color-coding indicated outcomes for which the numerical method employed in this computational approach had not yet, or could not, converge to a solution either as a result of the need for longer cycle time to converge or due to quiescence or chaos reigning for those particular initial condition combinations. Here, however, where multicolored points are all clustered together, examination of the individual traces results in determination that phase-slip behaviors can be induced for these particular initial condition combinations and thereby creates the ‘river of fixed points’ effect previously described in Chapters 3-5. This type of phase-slip was not possible in symmetric 3-node motifs independent of external connectivity, so this is a novel result of reciprocal coupling of such networks. Closer examination of several of the previous figures also indicate smaller regions where this behavior may also exist but the effect is particularly emphatic with very strong coupling, and additional research is required to verify the consistent existence of such phase-slip at moderate coupling ranges. The specific shape and direction of this phase-slip behavior is also not an emphasis or described here.

6.3 Electrical coupling of symmetric motifs

Unlike both inhibitory, which has been an emphasis of this research, and excitatory coupling, which are both chemical, electrical coupling is a conductive link formed in a narrow gap between two neighboring cells [54]. This is often called a gap junction and impulses transmitted this way are much faster but do not have the advantage of gain that is available to chemical connections, and signals relayed will be the same or smaller than that of the originating neuron. Electrical synapses are mostly bidirectional and often found in systems requiring fastest possible response time, such as escape reflexes, as they allow for many neurons to fire synchronously [55-56]. Mixed networks with both oscillating and hyperpolarized, passive neurons can even see strengthening of such a connection between them result in increasing or decreasing the frequency of the oscillator

depending on the properties of the oscillator. In networks coupling oscillatory cells, such as the purely traveling wave examples at mid-range values of I_{app} shown later, the effects of electrically coupling depend significantly on membrane potentials, intrinsic properties, and coupling strength [53]. Here electrical connection will be explored first in connecting symmetric motifs, as was done with inhibitory coupling, and then in exploring effects of introducing electrical coupling between a symmetric motif and a purely clockwise one in a hybrid system. For each of these two modular networks, experiments are demonstrated of using networks that exist in purely pacemaker, purely traveling wave, or mixed rhythm outcome potentials prior to being connected. Only single-coupling will be explored again, with some additional examples for double- and triple-coupling shown in the Appendix.

6.3.1 *Single electrically-coupled symmetric PM networks*

For these first examples, two networks of symmetric motifs within release ranges of I_{app} are connected via electrical coupling between cells 1 and 4, as seen in Figure 6.14. These unconnected motifs are not capable of producing traveling wave rhythmicity without external input, but are selected here for their near-bifurcation parameter set in which we see a whorl of differing pacemaker generation capability around the traditional locations of the black CTW and purple CCTW rhythms, near $(\Delta_{12}, \Delta_{13}) = (1/3, 2/3)$ and $(2/3, 1/3)$. Electrical coupling is not able to induce such dramatic rhythm switch even for this carefully selected example.

Since both networks are identical, we can consider the phase-basin in Figure 6.14 as the reference from which network rhythmicity will deviate with the introduction of coupling. In Figure 6.15, the effect of beginning the [456]-motif with cells 1 and 4 in-phase, $\Delta_{14} = 0$, and with blue pacemaker rhythmicity can be observed. Spanning all of the $(\Delta_{12}, \Delta_{13})$ initial condition space results in the immediate disappearance of the previous whorl behavior in [123], and a growing region of blue

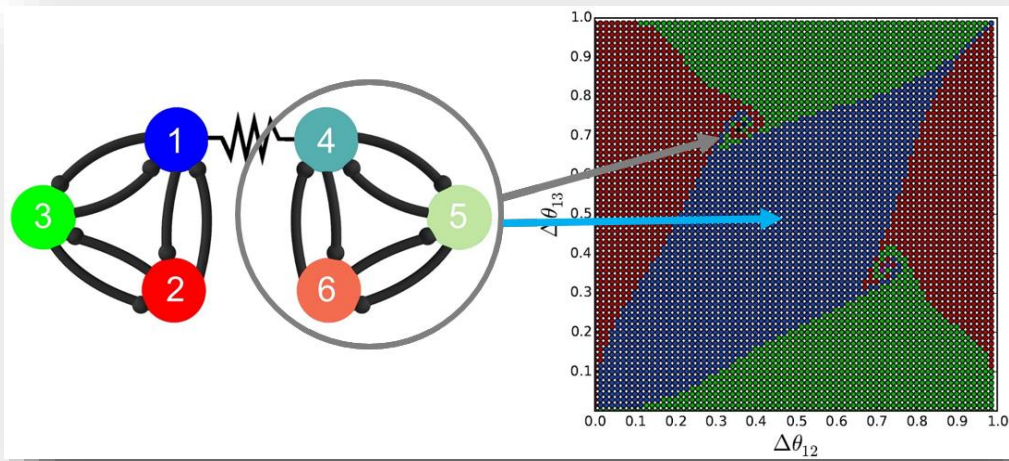


Figure 6.14 Single electrically-coupled symmetric PM systems

Electrical coupling of identical symmetric release networks for which only PM outcomes originally exist. Sample outputs for this network are shown in Figures 6.15-17, spanning all $(\Delta_{12}, \Delta_{13})$ -space ICs while beginning [456] in either blue PM or black CTW phase-lag, near $(\Delta_{45}, \Delta_{46}) = (1/2, 1/2)$ and $(1/3, 2/3)$, respectively. Both begin with in-phase cells 1 and 4, $\Delta_{14} = 0$, followed by an anti-phase example for CTW. Parameters: $I_{app} = 0.4$, $g_{ij} = g_{kl} = 0.005$.

pacemaker rhythmicity for initial conditions in that network beginning near the origin, $(\Delta_{12}, \Delta_{13}) \approx 0$, with increasing electrical coupling. The [456]-motif remains fixed as a blue pacemaker (BPM) network, as no force exists to push cells 1 and 4 out of phase. Starting the [456]-motif in Figure 6.16 with initial conditions appearing as a black clockwise traveling wave, near $(\Delta_{45}, \Delta_{46}) = (1/3, 2/3)$, with cells 1 and 4 still in-phase at $\Delta_{14} = 0$, the previous whorl behavior again unfolds, but only slightly, as it thickens in the [123]-motif. A growing region of blue pacemaker rhythmicity is again observed with increasing electrical coupling for initial conditions beginning near the origin. The [456]-motif continues to remain largely fixed as a blue pacemaker network, with some potential for green or red pacemaker rhythmicity, the former disappears entirely while the latter only increases with stronger electrical coupling. This occurs largely for [123]-ICs beginning near the origin, but with unusual symmetric occurrence occurring along the $\Delta_{12} = \Delta_{13}$ diagonal.

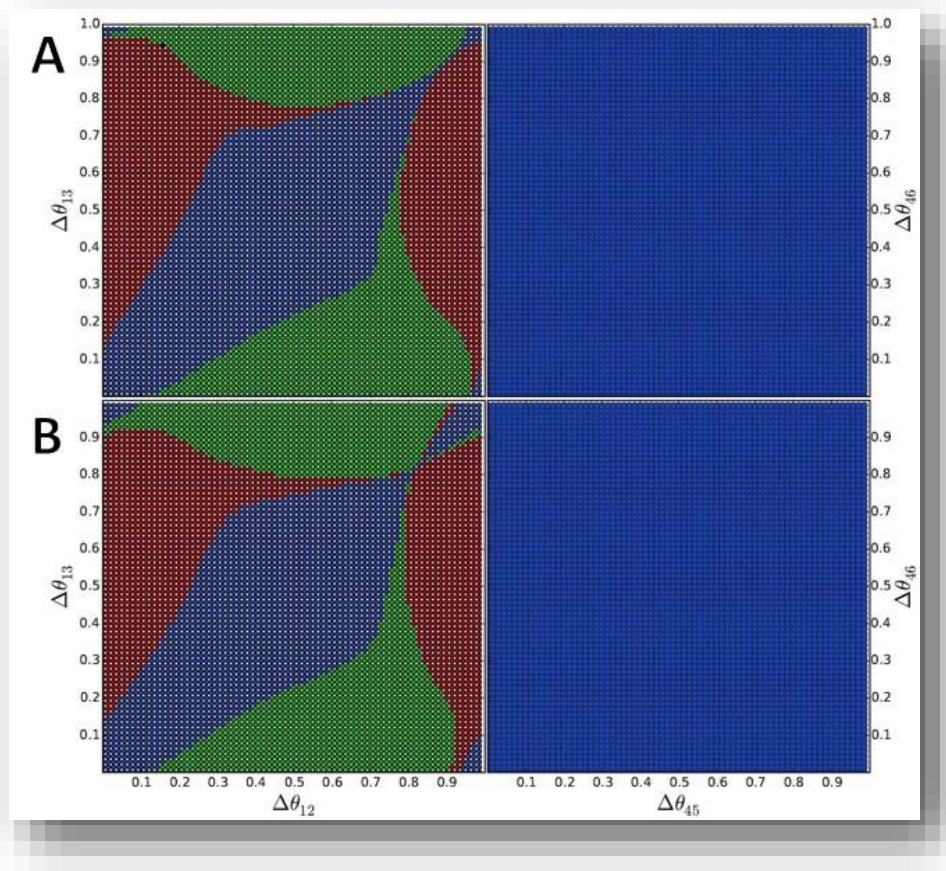


Figure 6.15 Single electrically-coupled symmetric PM systems, in-phase BPM

Symmetric release networks, for which only PM rhythms are possible, connected via increasing electrical coupling of cells 1 and 4. Panels represent outcomes for both networks, spanning all $(\Delta_{12}, \Delta_{13})$ -space ICs while beginning [456] in blue PM phase-lag, near $(\Delta_{45}, \Delta_{46}) = (1/2, 1/2)$, cells 1 and 4 in-phase, with $\Delta_{14} = 0$. Previous whorl behavior disappears immediately in [123], with a growing region of blue PM rhythmicity for ICs beginning near the origin at higher electrical coupling, while [456] remains fixed as a blue PM network. Parameters: $I_{app} = 0.4$, $g_{ij} = g_{kl} = 0.005$, $g_{elec} = 0.005$ and 0.010 .

Finally, for the case where cells 1 and 4 begin in anti-phase, $\Delta_{14} = 1/2$, with [456] in black CTW phase-lag, near $(\Delta_{45}, \Delta_{46}) = (1/3, 2/3)$, observed in Figure 6.17, the previous whorl behavior disappears at weak coupling in [123] only to then be reintroduced and thickened as coupling increases. Blue pacemaker rhythmicity again increases but with shifting behavior, more so around the $\Delta_{12} = \Delta_{13}$ diagonal, while only moderately for initial conditions beginning near the origin. [456]

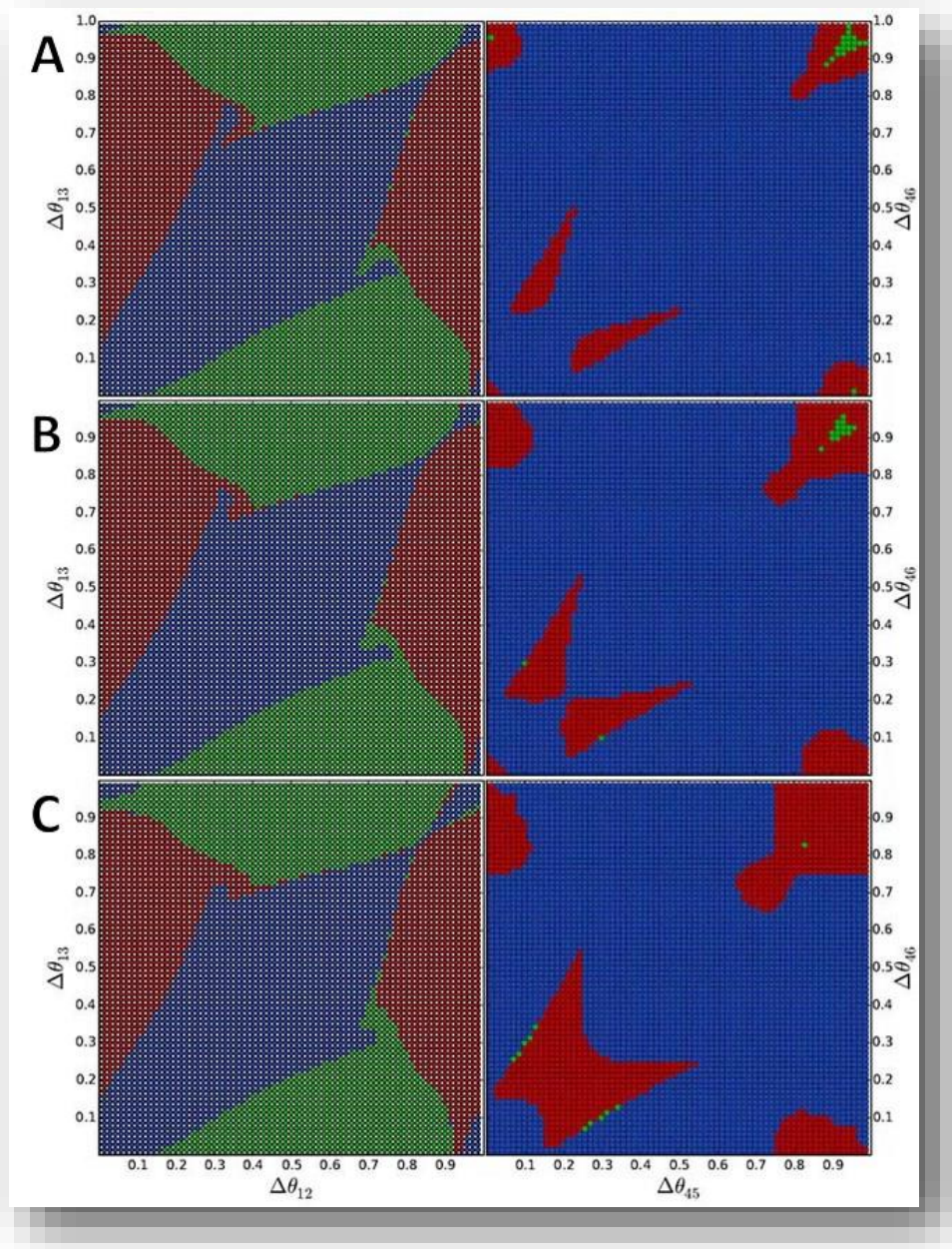


Figure 6.16 Single electrically-coupled symmetric PM systems, in-phase CTW

Symmetric release networks, for which only PM rhythms are possible, connected via increasing electrical coupling of cells 1 and 4. Panels represent outcomes for both networks, spanning all $(\Delta_{12}, \Delta_{13})$ -space ICs while beginning [456] in black CTW phase-lag, near $(\Delta_{45}, \Delta_{46}) = (1/3, 2/3)$, cells 1 and 4 in-phase, with $\Delta_{14} = 0$. Previous whorl behavior unfolds slightly but thickens in [123], with a growing region of blue PM rhythmicity again observed for ICs beginning near the origin at higher electrical coupling. [456] remains largely fixed as a blue PM network, with some potential for green or red PM rhythmicity, the latter of which increases with stronger electrical coupling while green disappears entirely. Parameters: $I_{app} = 0.4$, $g_{ij} = g_{kl} = 0.005$, $g_{elec} = 0.005$, 0.010, and 0.05.

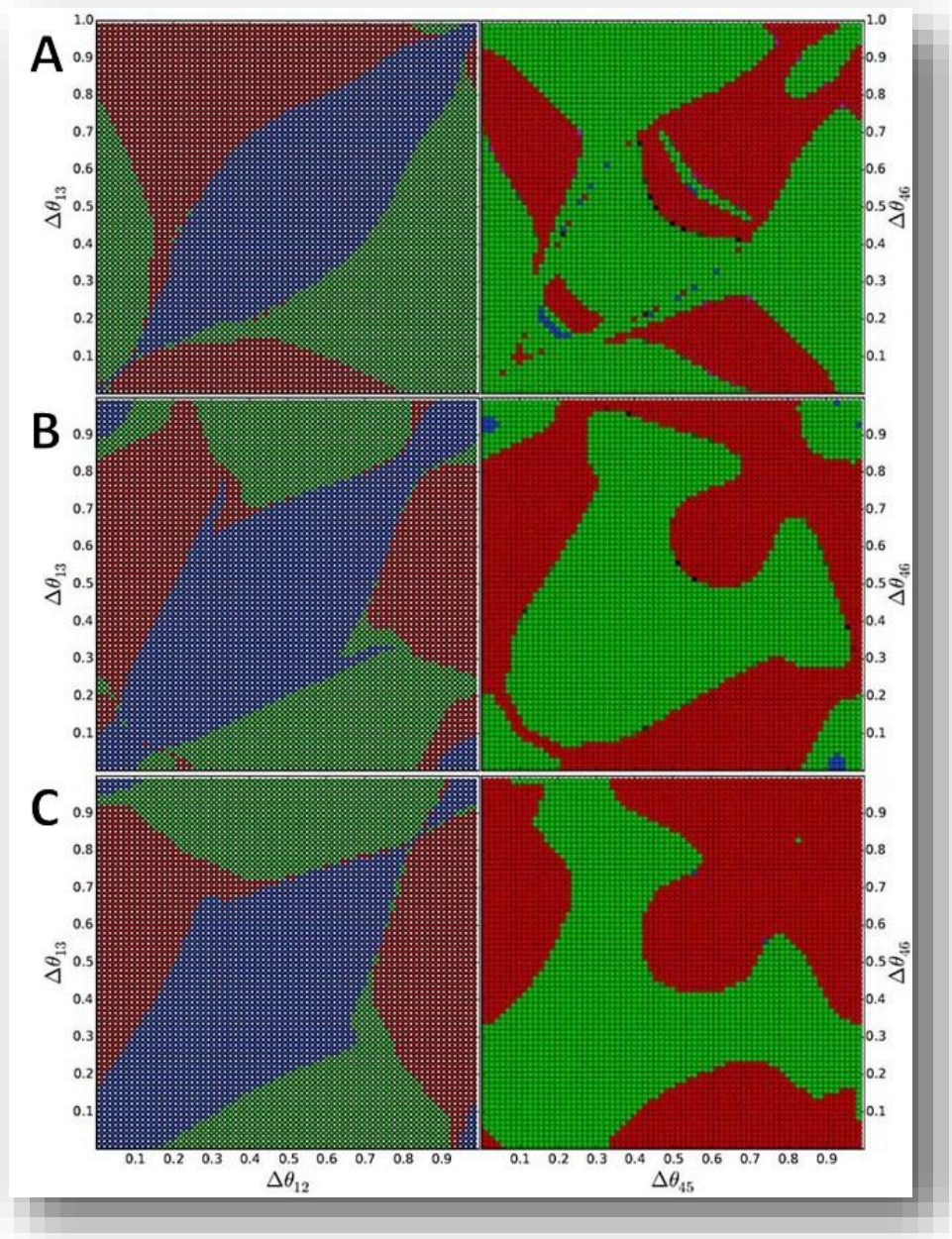


Figure 6.17 Single electrically-coupled symmetric PM systems, anti-phase CTW
Symmetric release networks, for which only PM rhythms are possible, connected via increasing electrical coupling of cells 1 and 4. Panels represent outcomes for both networks, spanning all $(\Delta_{12}, \Delta_{13})$ -space ICs while beginning [456] in black CTW phase-lag, near $(\Delta_{45}, \Delta_{46}) = (1/3, 2/3)$, cells 1 and 4 in anti-phase, with $\Delta_{14} = 1/2$. Previous whorl behavior disappears in [123] at weak coupling only to be reintroduced and thickened at stronger coupling. Blue PM rhythmicity again increased but with shifting behavior and only somewhat for ICs beginning near the origin. [456] can only produce small pockets blue PM behavior, which disappear entirely as red and green PM behavior dominate and stabilize with increasing electrical coupling. Parameters: $I_{app} = 0.4$, $g_{ij} = g_{kl} = 0.005$, $g_{elec} = 0.005, 0.010$, and 0.05 .

can now only produce small pockets blue pacemaker behavior, which disappear entirely as red and green pacemaker behavior dominate and stabilize with increasing electrical coupling, eventually forming single continuous basins for each at initial conditions within the $(\Delta_{12}, \Delta_{13})$ -space.

6.3.2 Single electrically-coupled symmetric TW networks

Next, electrical coupling of oscillatory networks exhibiting only traveling wave rhythms when connected, base case shown in Figure 6.18, results in both networks remaining fairly exclusively in traveling wave outcomes for all initial conditions explored. The networks described here are sampled at mid-range values of I_{app} , with sample outputs shown in Figures 6.19-20, using the same full span of initial $(\Delta_{12}, \Delta_{13})$ -space conditions being typically employed in this chapter, but here sampling only the in-phase case of [456] black CTW phase-lag, near $(\Delta_{45}, \Delta_{46}) = (1/3, 2/3)$, with $\Delta_{14} = 0$, and the anti-phase case of [456] purple CCTW phase-lag, near $(\Delta_{45}, \Delta_{46}) = (2/3, 1/3)$, with space are explored with a fixed starting position for the [456]-network in black clockwise phase-

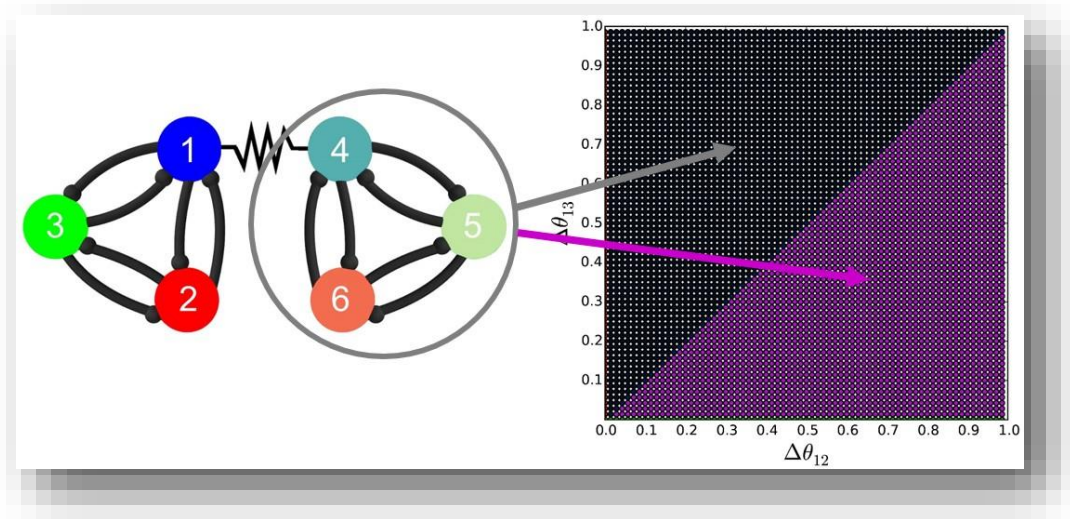


Figure 6.18 Single electrically-coupled symmetric TW systems

Electrical coupling of identical oscillatory symmetric networks for which only TW outcomes originally exist at mid-range values of I_{app} . Sample outputs for this network are shown in Figures 6.19-20, spanning all $(\Delta_{12}, \Delta_{13})$ -space ICs while beginning [456] in either black CTW phase-lag, near $(\Delta_{45}, \Delta_{46}) = (1/3, 2/3)$, with in-phase cells 1 and 4, $\Delta_{14} = 0$, or in purple CCTW phase-lag, near $(\Delta_{45}, \Delta_{46}) = (2/3, 1/3)$, in anti-phase at $\Delta_{14} = 0.5$. Parameters: $I_{app} = 0.5$, $g_{ij} = g_{kl} = 0.005$.

$\Delta_{14} = 0.5$. This change is made for novelty to test the ability of electrical coupling to synchronize networks as alluded to earlier. In the first example, in Figure 6.19, all of the initial conditions for the $(\Delta_{12}, \Delta_{13})$ -lag position, near $(\Delta_{45}, \Delta_{46}) = (1/3, 2/3)$. The relationship between cells 1 and 4 is begun in-phase, with $\Delta_{14} = 0$. The original phase-basin map in Figure 6.18 indicates even division along the $\Delta_{12} = \Delta_{13}$ diagonal between the clockwise and counter-clockwise rhythms in unconnected networks. This division is maintained symmetrically about this line but is perturbed, with basin

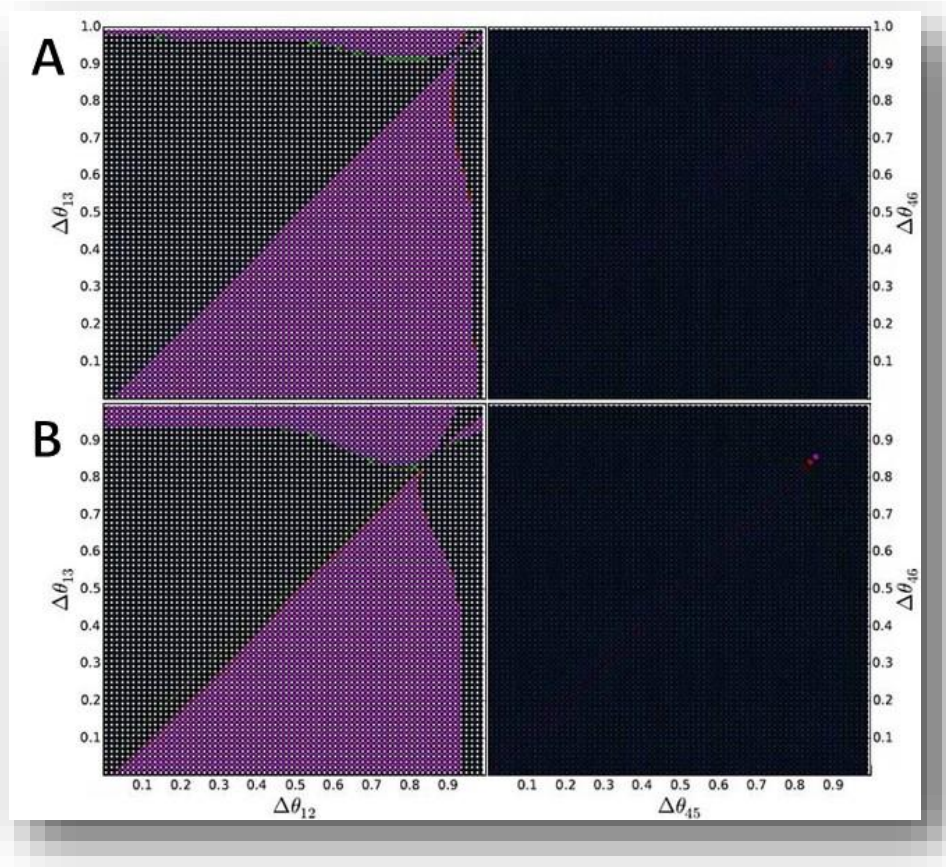


Figure 6.19 Single electrically-coupled symmetric TW systems, in-phase CTW
Oscillatory symmetric networks, for which only TW rhythms are possible, connected via increasing electrical coupling of cells 1 and 4. Panels represent outcomes for both networks, spanning all $(\Delta_{12}, \Delta_{13})$ -space ICs while beginning [456] in black CTW phase-lag, near $(\Delta_{45}, \Delta_{46}) = (1/3, 2/3)$, cells 1 and 4 in-phase, with $\Delta_{14} = 0$. Previous division of the $(\Delta_{12}, \Delta_{13})$ -space along the $\Delta_{12} = \Delta_{13}$ diagonal in [123], is perturbed symmetrically around this line to increasing effect in the upper right quadrant as coupling increases. [456] remains fixed as a black CTW network. Parameters: $I_{app} = 0.5$, $g_{ij} = g_{kl} = 0.005$, $g_{elec} = 0.005$ and 0.05 .

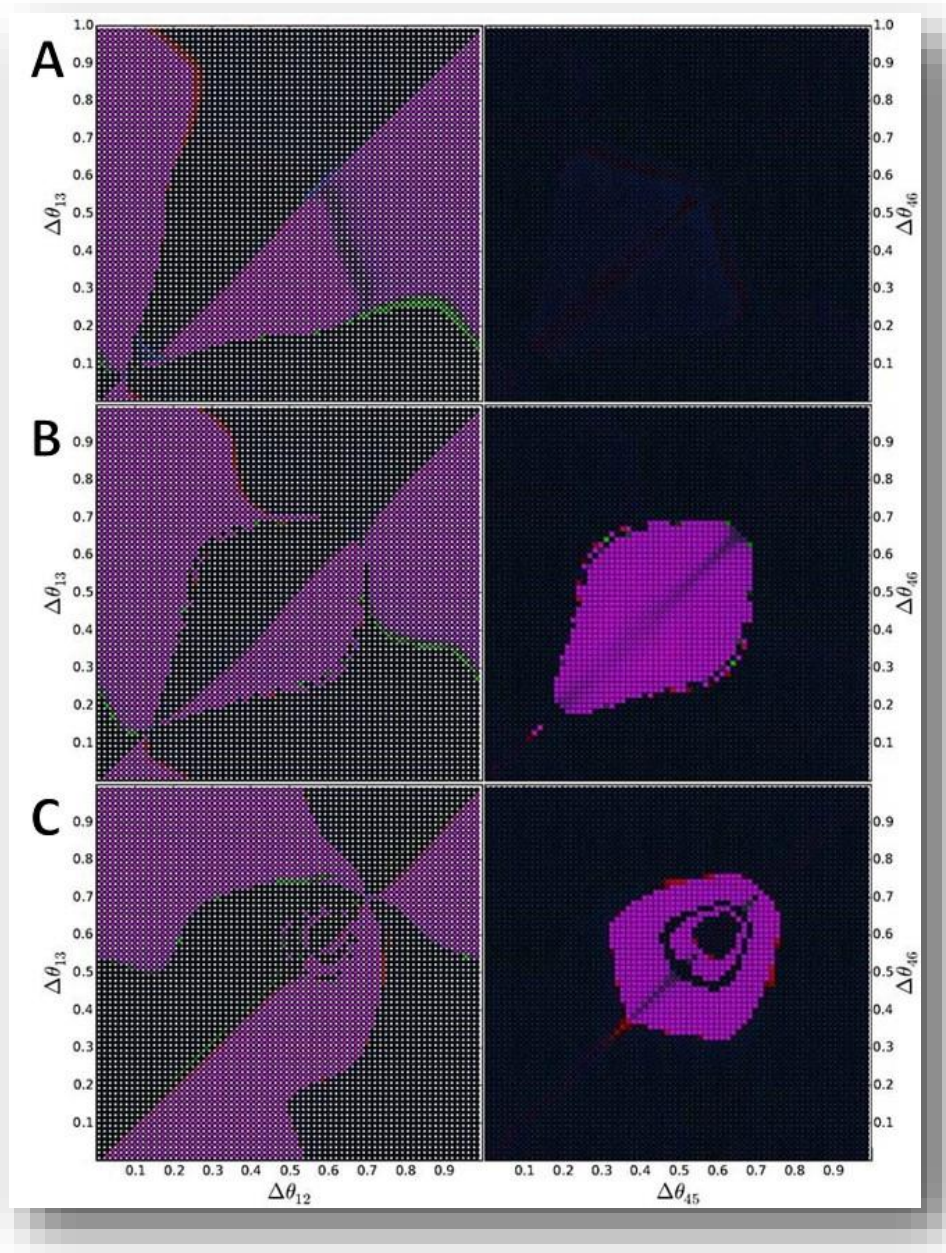


Figure 6.20 Single electrically-coupled symmetric TW systems, anti-phase CCTW
Oscillatory symmetric networks, for which only TW rhythms are possible, connected via increasing electrical coupling of cells 1 and 4. Outcomes again span $(\Delta_{12}, \Delta_{13})$ -space ICs, but beginning [456] with purple CCTW phase-lag, near $(\Delta_{45}, \Delta_{46}) = (1/3, 2/3)$, and cells 1 and 4 in $\Delta_{14} = 1/2$ anti-phase. Division of the $(\Delta_{12}, \Delta_{13})$ -space along the $\Delta_{12} = \Delta_{13}$ diagonal in [123], is even more profoundly perturbed around this line but beginning at the lower left quadrant before extending along it with coupling increases. [456] continues to remain largely fixed as a black CTW network, but observes $(\Delta_{12}, \Delta_{13})$ -ICs around $(0.5, 0.5)$ where [456] can be driven to purple CCTW rhythmicity. These effects increase with coupling as the system is forced to bring cells 1 and 4 back into phase. Parameters: $I_{app} = 0.5$, $g_{ij} = g_{kl} = 0.005$, $g_{elec} = 0.005, 0.010$, and 0.05 .

switching occurring at the top and right boundaries and with even more increasing effect in the upper right quadrant as coupling increases. The [456]-motif continues to remain fixed in its original black clockwise traveling wave rhythm, with these system initial conditions and beginning in-phase behavior not being adequate to drive it to any other pattern.

For the anti-phase case in Figure 6.20, however, very different effects are observed, particularly for the [456]-motif that has up to this point seemed unresponsive to $(\Delta_{12}, \Delta_{13})$ -space initial condition effects. In this case [456] was begun with the purple counter-clockwise traveling wave pattern, near $(\Delta_{45}, \Delta_{46}) = (1/3, 2/3)$, with $\Delta_{14} = 1/2$ anti-phase. Because electrical coupling drives the cells to burst together with increasing strength, the stronger the electrical coupling becomes, the more dramatic and quickly the system conditions will change. The division of the $(\Delta_{12}, \Delta_{13})$ -space along the $\Delta_{12} = \Delta_{13}$ diagonal in [123] that was seen previously is now even more profoundly perturbed around this line but with reverse effect. This perturbation begins at the lower left quadrant before extending along the diagonal with coupling increases. The [456]-motif continues to remain mostly convergent to black clockwise rhythmicity, but observes a very specific range of $(\Delta_{12}, \Delta_{13})$ -space initial conditions near $(\Delta_{12}, \Delta_{13}) = (0.5, 0.5)$ where the [456] local network can instead be driven to purple CCTW rhythmicity, particularly with very strong electrical coupling. These effects increase with coupling as the system is forced to bring cells 1 and 4 back into phase much more quickly.

6.3.3 *Single electrically-coupled symmetric penta-rhythmic networks*

Finally, exploring electrical coupling of symmetric release networks in which all five rhythm outcomes are initially possible gives additional similar results. As before, all of the $(\Delta_{12}, \Delta_{13})$ -space of initial conditions are explored while sampling cases where $(\Delta_{45}, \Delta_{46}) = (1/2, 1/2)$ or $(1/3, 2/3)$, beginning in either blue pacemaker or black clockwise traveling wave rhythmicity. These are

indicated in the phase-basin diagram shown in Figure 6.21. Both cases are again shown beginning with cells 1 and 4 in-phase, at $\Delta_{14} = 0$, with an additional anti-phase example then shown for the black clockwise traveling wave case. When the system is initiated with the [456]-motif beginning with in-phase blue pacemaker phase-lag, near $(\Delta_{45}, \Delta_{46}) = (1/2, 1/2)$, all capability of the [123]-network to produce traveling wave rhythms is immediate lost with electrical coupling. All three pacemaker rhythms grow and take over what used to be the basin of attraction for each of the traveling wave rhythms, but with lesser growth of the blue region as the red and green patterns take over most of this $(\Delta_{12}, \Delta_{13})$ -space. As in previous examples, the blue rhythm acquires a growing region of initial condition space near the origin where all three cells fire initially in near synchronicity. The [456]-network, on the other hand, remains unaffected in these initial conditions and remains in blue pacemaker activity with cell 4 continuing to remain in-phase with cell 1.

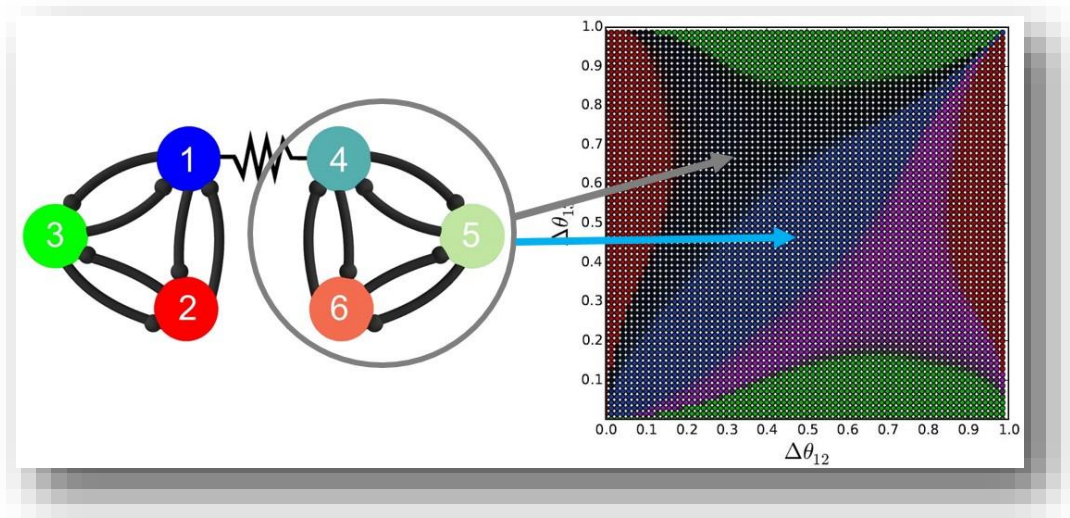


Figure 6.21 Single electrically-coupled symmetric mixed rhythm

Electrical coupling of identical symmetric release networks for which all five rhythm outcomes are possible when unconnected. Sample outputs for this network are shown in Figures 6.22-24, spanning all $(\Delta_{12}, \Delta_{13})$ -space ICs while beginning [456] in either blue PM or black CTW phase-lag, near $(\Delta_{45}, \Delta_{46}) = (1/2, 1/2)$ and $(1/3, 2/3)$, respectively. Both begin with in-phase cells 1 and 4, $\Delta_{14} = 0$, followed by an anti-phase example for the black CTW case. Parameters: $I_{app} = 0.42$, $g_{ij} = g_{kl} = 0.005$.

When the [456]-motif begins in-phase but with a black clockwise traveling wave, phase-lag near $(\Delta_{45}, \Delta_{46}) = (1/3, 2/3)$, all five rhythms remain possible in [123]. This is paired, however, with a shift in the pacemaker basins from the lower left to upper right quadrant, with growth again of the blue pacemaker near the origin at $(\Delta_{12}, \Delta_{13}) \approx (0, 0)$, both continuing with increased coupling. The [456]-network experiences significant shifting for half of the $(\Delta_{12}, \Delta_{13})$ -space of initial conditions, as the black clockwise traveling wave may be pushed into red pacemaker rhythmicity. The $(\Delta_{12},$

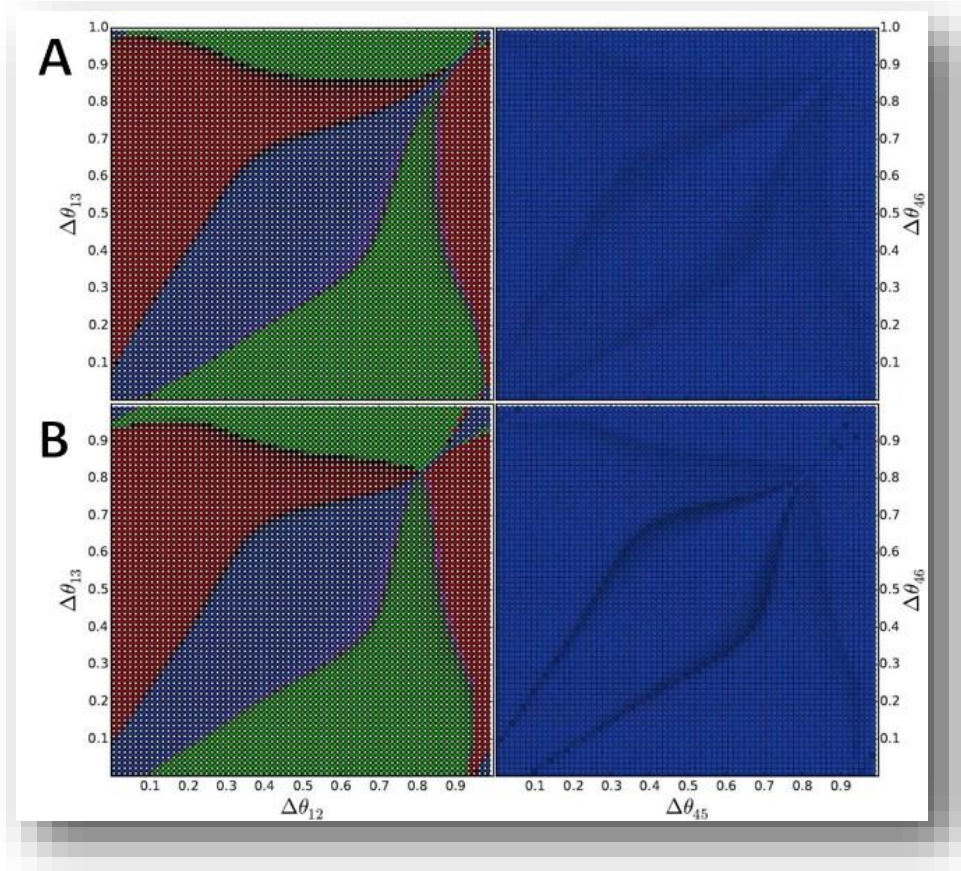


Figure 6.22 Single electrically-coupled symmetric mixed rhythm, in-phase BPM
Symmetric release networks, for which all five rhythm outcomes are possible, connected via increasing electrical coupling of cells 1 and 4. Panels represent outcomes for both networks, spanning all $(\Delta_{12}, \Delta_{13})$ -space ICs while beginning [456] in blue PM phase-lag, near $(\Delta_{45}, \Delta_{46}) = (1/2, 1/2)$, and cells 1 and 4 in-phase at $\Delta_{14} = 0$. TW rhythms are completely eliminated in [123], with only slight growing of the blue PM region at higher electrical coupling. The [456]-motif continues to observe primarily blue PM rhythm outcomes, with narrow bands of CTW rhythms shown by black bands. Parameters: $I_{app} = 0.42$, $g_{ij} = g_{kl} = 0.005$, $g_{elec} = 0.005$ and 0.05 .

Δ_{13})-space of initial conditions for which this red pacemaker behaviors outcome occurs aligns with the same conditions for which [123] itself converges to pacemaker behaviors, resulting in both networks exhibiting either all pacemaker or all traveling wave rhythms at system equilibrium.

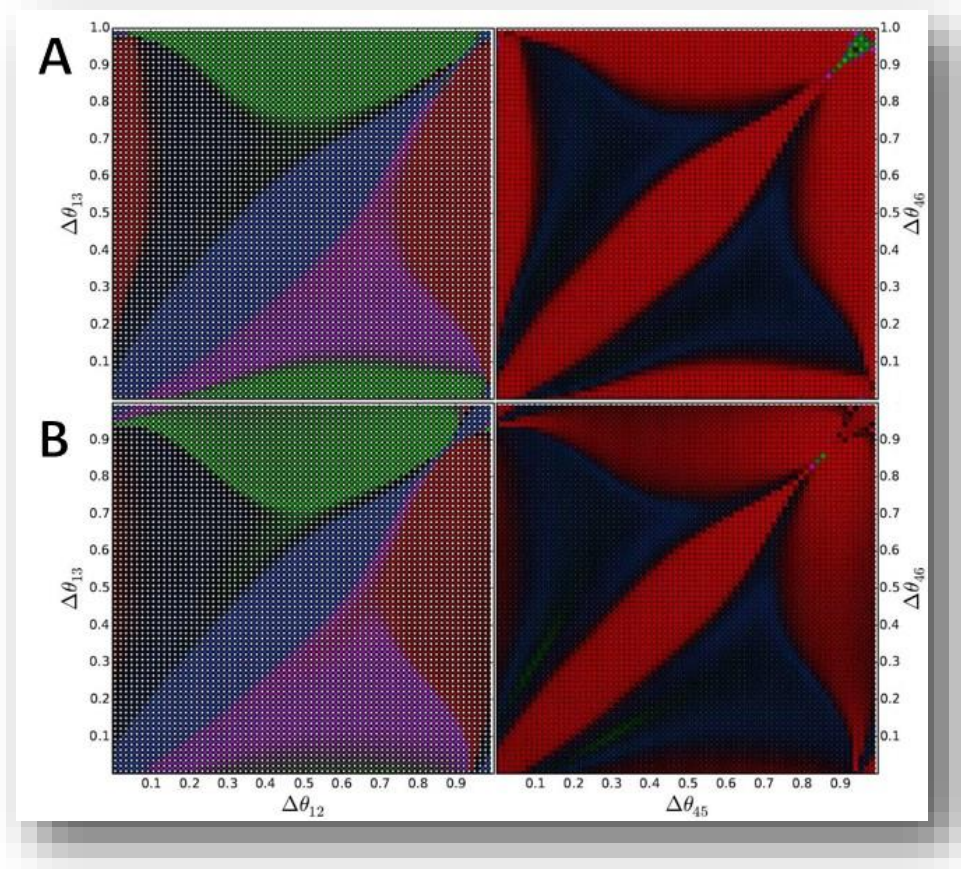


Figure 6.23 Single electrically-coupled symmetric mixed rhythm, in-phase CTW

Symmetric release networks, for which all five rhythm outcomes are possible, connected via increasing electrical coupling of cells 1 and 4. Panels represent outcomes for both networks, spanning all $(\Delta_{12}, \Delta_{13})$ -space ICs while beginning [456] in black CTW phase-lag, near $(\Delta_{45}, \Delta_{46}) = (1/3, 2/3)$, with in-phase cells 1 and 4 at $\Delta_{14} = 0$. All five rhythms remain in [123], with an interesting shift in the PM basins of attraction from the lower left quadrant to the upper right, as well as growth of the blue PM near the origin at $(\Delta_{12}, \Delta_{13}) \approx (0, 0)$. [456] sees a dramatic shift from its starting position as a black CTW to that of a red PM for half of the $(\Delta_{12}, \Delta_{13})$ -space ICs. These red PM behaviors all align with outcomes in [123] for which PM behaviors were induced, with either all PM or all TW rhythms visible in both local networks at once. Parameters: $I_{app} = 0.42$, $g_{ij} = g_{kl} = 0.005$, $g_{elec} = 0.005$ and 0.05 .

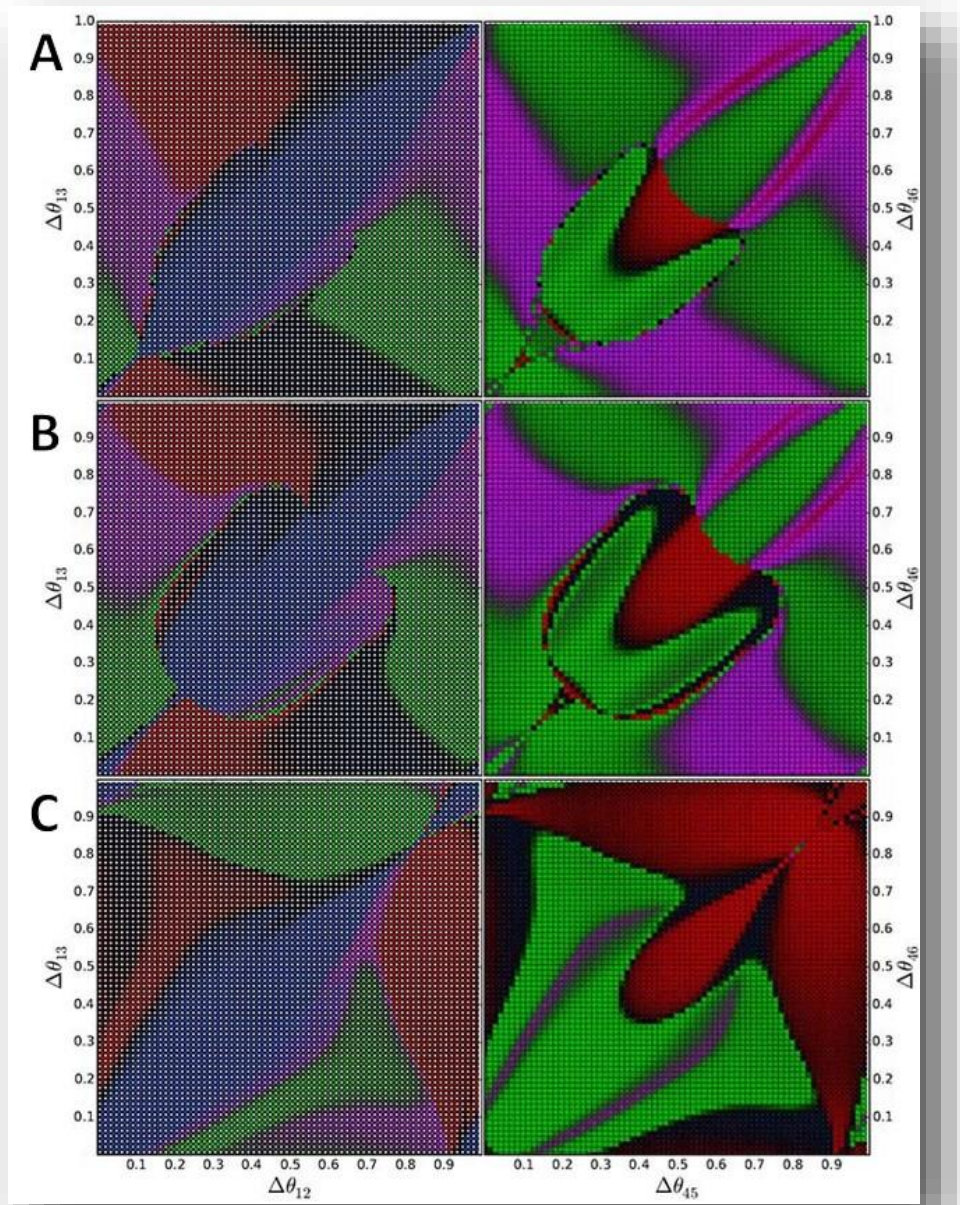


Figure 6.24 Single electrically-coupled symmetric mixed rhythm, anti-phase CTW

Symmetric release networks, with all five rhythm outcomes are possible, connected via electrical coupling of cells 1 and 4. Panels represent outcomes, spanning all $(\Delta_{12}, \Delta_{13})$ -space ICs while beginning [456] as a black CTW, near $(\Delta_{45}, \Delta_{46}) = (1/3, 2/3)$, with cells 1 and 4 in anti-phase at $\Delta_{14} = 1/2$. Results are most striking, all five rhythm outcomes remaining possible in [123] but with complex boundaries and non-contiguous basins which stabilize somewhat with increasing coupling. At lower coupling, the [456] motif splits most of the $(\Delta_{12}, \Delta_{13})$ -IC outcomes, converging to CCTW or green PM rhythmicity in [456]. A red PM basin also emerges in [456] for $(\Delta_{12}, \Delta_{13})$ -ICs near $(1/2, 1/2)$, which grows and then dominates at strong electrical coupling in lieu of the purple CCTW. Parameters: $I_{app} = 0.42$, $g_{ij} = g_{kl} = 0.005$, $g_{elec} = 0.005, 0.010$, and 0.05 .

Finally, when the [456]-motif begins with a black clockwise traveling wave instead in anti-phase, $\Delta_{14} = 1/2$, all five rhythms still remain possible in [123], but with increasingly complex boundaries and non-contiguous regions for each rhythms basins of attraction. The blue pacemaker is the only rhythm in that network which remains located within its traditional region of $(\Delta_{12}, \Delta_{13})$ -space initial conditions and behaves very similar to the past two examples. Every other pattern observes significant basin switching, as beginning the system with cells 1 and 4 in anti-phase forces rapid shifting to bring them into phase with electrical coupling. At lower values of electrical coupling, the [456] motif is pushed rapidly from its initial clockwise rotation and splits most of the $(\Delta_{12}, \Delta_{13})$ -space of initial conditions by converging to counterclockwise traveling wave or green pacemaker rhythmicity. A small red pacemaker basin also emerges in [456] for $(\Delta_{12}, \Delta_{13})$ -ICs near $(1/2, 1/2)$, which continues to grow with strong electrical coupling until it dominates with the frequency in with the counterclockwise rhythm did at lower coupling strengths.

6.4 Electrical coupling of symmetric-clockwise hybrid networks

As symmetric motifs are the simplest to model and manipulate, and have the most straight-forward responses to shifts in the bi-parametric (g_{ij}, I_{app}) -space, these have been used extensively in this research as the first step in elucidating behavioral outcomes for parameter shifts in these network. This was done first in Chapter 2 with the 3-node motif and again in this chapter as the basis for use of 3-node motifs in modular networking, first with a simple 4-cell example and now within the framework of coupled motifs. As before, the next step is to introduce additional asymmetry and observe changes in behavior from that seen in the purely symmetric modular networks. In this section, research describes connection of the simplest asymmetric motif, the clockwise-biased one in which no phase-slipping behavior was observed in the unconnected network. To further simplify this first step at modular asymmetry, this clockwise-biased network is not only connected with a

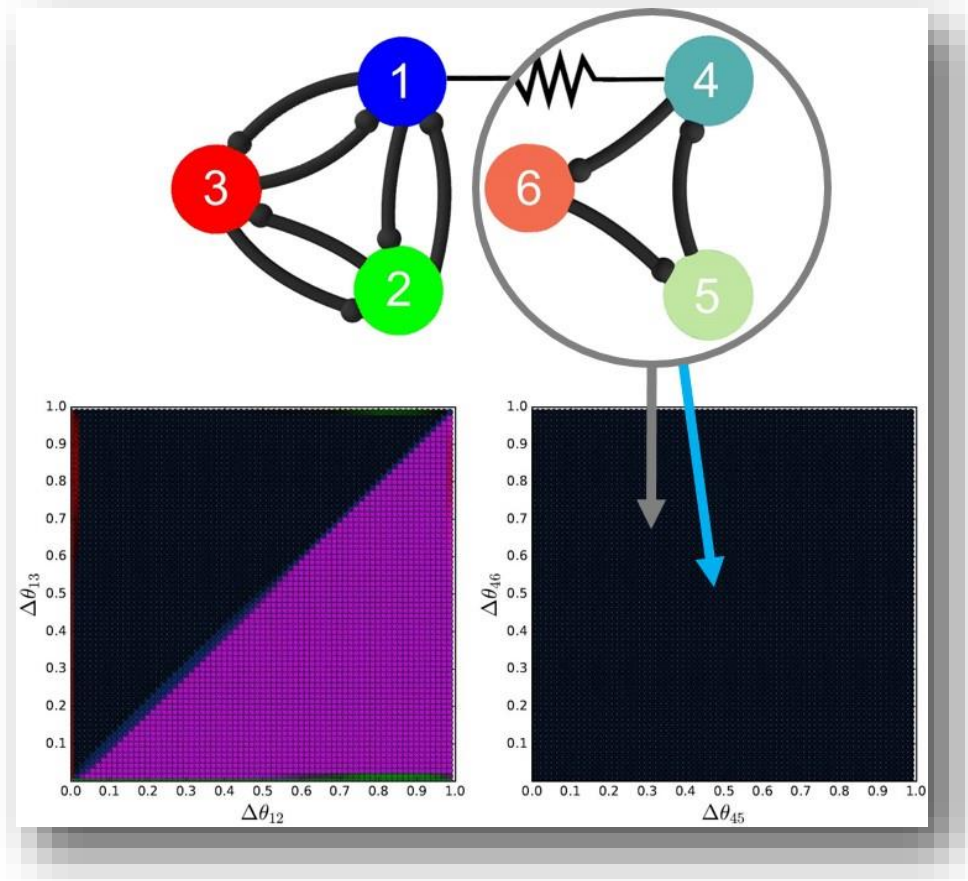


Figure 6.25 Single electrically-coupled symmetric-clock hybrid system

Electrical coupling of a symmetric network for which TW outcomes almost entirely dominate with a purely clockwise network for which only the black CTW pattern exists. Sample outputs for this network are shown in Figures 6.26-28, spanning all $(\Delta_{12}, \Delta_{13})$ -space ICs while beginning [456] in either blue PM or black CTW phase-lag, near $(\Delta_{45}, \Delta_{46}) = (1/2, 1/2)$ and $(1/3, 2/3)$, respectively. Both begin with in-phase cells 1 and 4, $\Delta_{14} = 0$, followed by an anti-phase example for the CTW IC. Parameters: $I_{app} = 0.45$, $g_{ij} = g_{kl} = 0.008$.

fully symmetric one, but is also held in the unique case where only counterclockwise connectivity exists (in other words, $g_{46} = g_{65} = g_{54} = 0$). An example of this symmetric-clockwise hybrid can be seen in Figure 6.25, along with phase-basin diagrams representing the initial state of both the [123]- and [456]-motifs when uncoupled. A nearly oscillatory symmetric release case network is employed for [123], in which traveling wave entirely dominate. This is paired with a purely clockwise network for which only the black clockwise rhythm is possible initially.

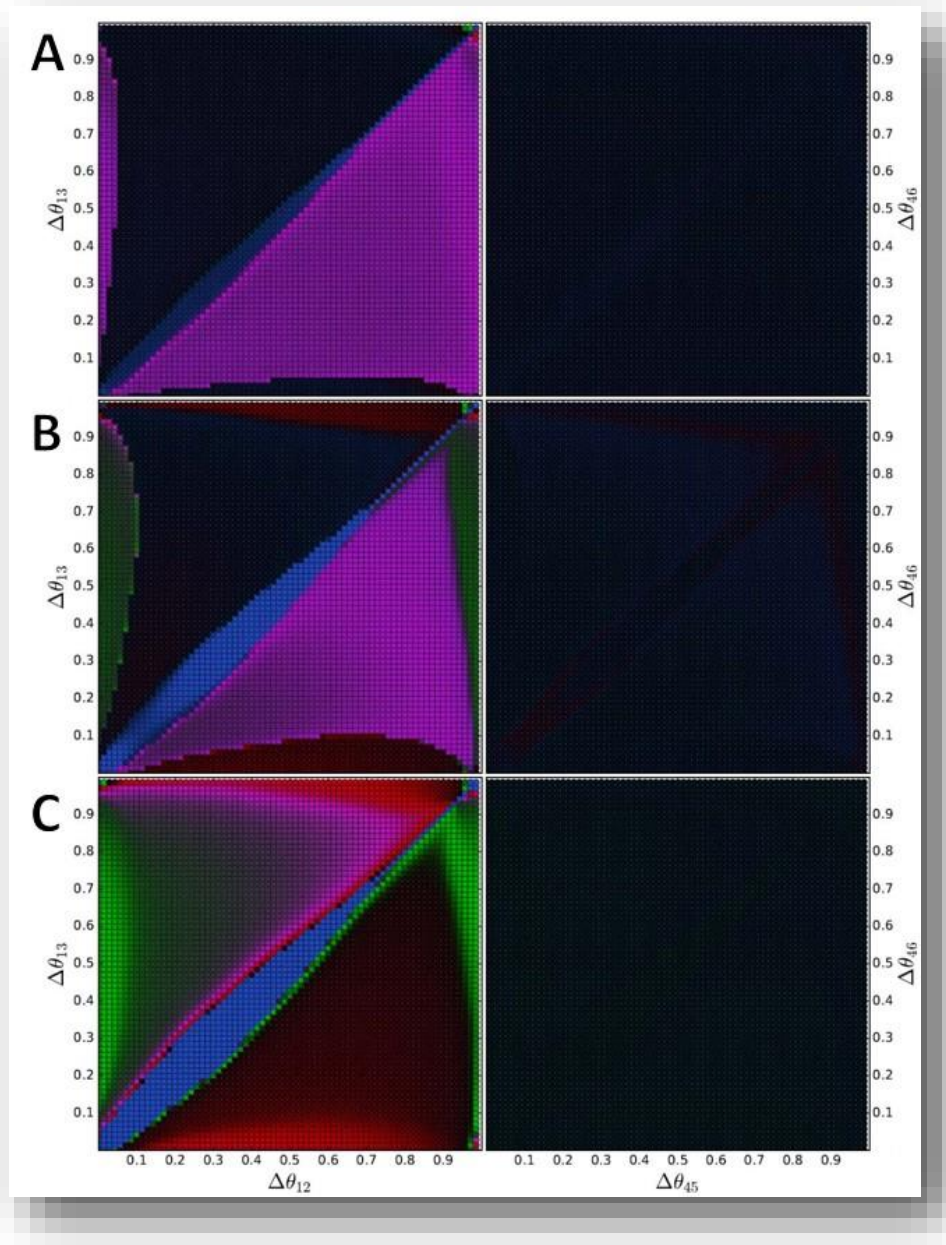


Figure 6.26 Single electrically-coupled symmetric-clock hybrid, in-phase BPM Connection of an almost entirely TW-dominated symmetric network with a purely clockwise network, with only black CTW patterns possible, via increasing electrical coupling of cells 1 and 4. Panels represent outcomes for both networks, spanning all $(\Delta_{12}, \Delta_{13})$ -space ICs while beginning [456] in blue PM phase-lag, near $(\Delta_{45}, \Delta_{46}) = (1/2, 1/2)$, with cells 1 and 4 in-phase at $\Delta_{14} = 0$. [123] converges primarily to TW rhythms at weaker electrical coupling due to continued clockwise rhythmicity of [456], but with increasing presence of possible PM outcomes which grow to dominate at stronger coupling. [456] remains fixed as a black CTW at all coupling values. Parameters: $I_{app} = 0.45$, $g_{ij} = g_{kl} = 0.008$, $g_{elec} = 0.002, 0.005$, and 0.01 .

As in examples previously shown, all initial conditions for the $(\Delta_{12}, \Delta_{13})$ -space shown in Figure 6.26 are spanned in the symmetric [123] motif while beginning the clockwise [456] motif, which can initially only converge to black clockwise rhythms, first in the blue pacemaker phase-lag position, near $(\Delta_{45}, \Delta_{46}) = (1/2, 1/2)$, and with cells 1 and 4 beginning in phase. At weaker electrical coupling, the [123]-network converges primarily to traveling wave rhythms as a result of the $1/3$ period inhibitory stagger to cell 1 provided by continued clockwise rhythmicity of [456]. With increasing electrical coupling, however, an increasing presence of possible pacemaker outcomes grows to dominate at stronger coupling with red and green pacemaker behaviors switching stereotypical positions. The [456]-network remains constantly in black clockwise pattern generation at all coupling values, electrical coupling and in-phase initiation unsurprisingly inadequate to drive it to other rhythmicity.

This lack of power to drive the purely clockwise [456]-network out of black clockwise traveling wave behavior remains valid for all systems explored in which cells 1 and 4 began in-phase. There is therefore no immediate push on cell 4 with electrical coupling that would cause it to deviate from its original outcome. The example in Figure 6.27, for which that network begins in fact in this starting position is unsurprising in maintaining the same outcomes for the [456]-motif. This is compounded further by the observation that the [123]-motif also seems to be unaffected in any way different from what was just observed in the blue pacemaker starting position of Figure 6.26. Beginning in-phase, with no impetus to push abruptly from starting conditions, the clockwise [456]-network will immediately converge to its black clockwise rhythmicity no matter its starting position and will therefore have the same long-term effects on the [123]-network for all couplings and initial conditions observed (in this case not only of the $(\Delta_{12}, \Delta_{13})$ -space but also the $(\Delta_{45}, \Delta_{46})$ -space). This is therefore an extremely robust modular network.

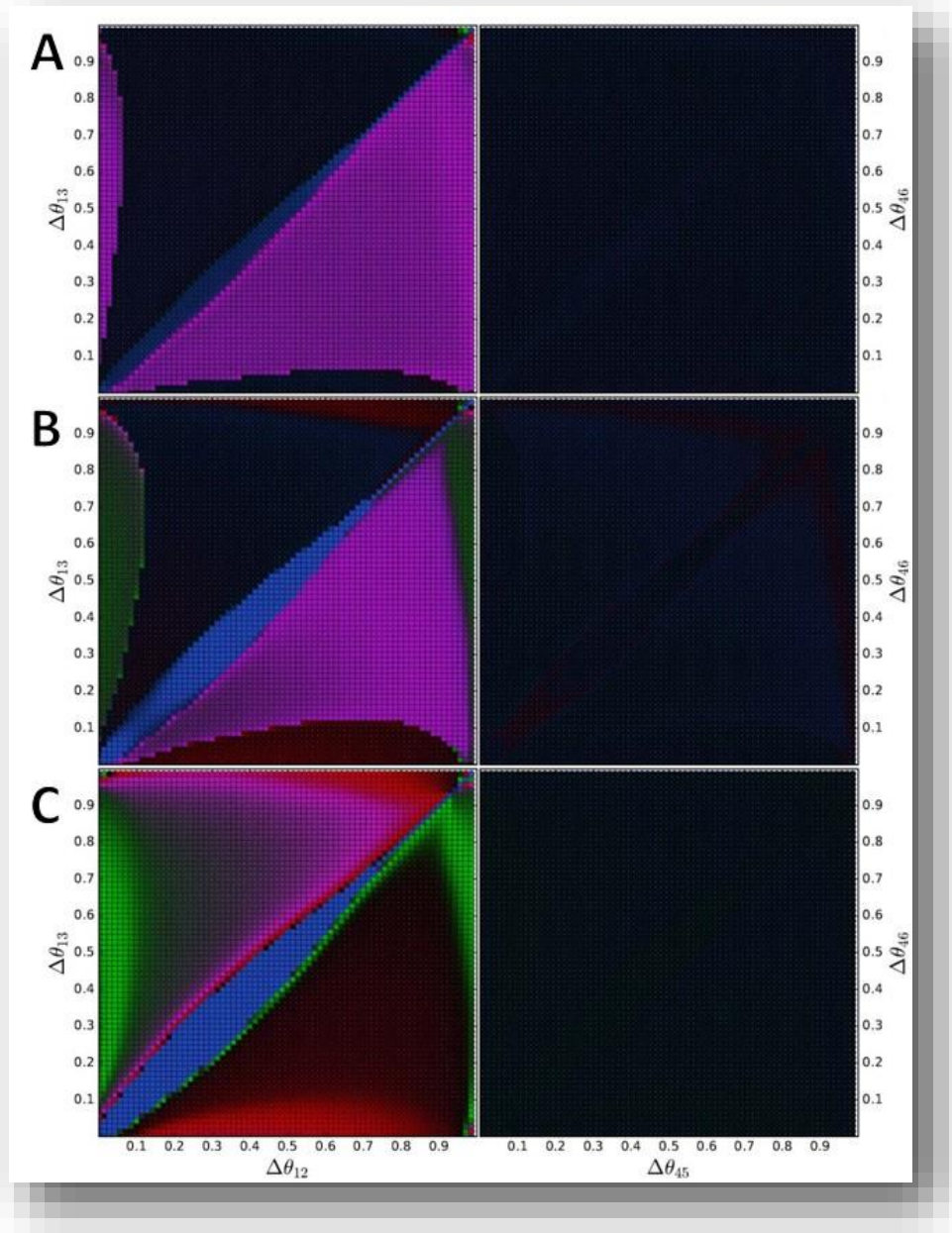


Figure 6.27 Single electrically-coupled symmetric-clock hybrid, in-phase CTW Connection of an almost entirely TW-dominated symmetric network with a purely clockwise network, with only black CTW patterns possible, via increasing electrical coupling of cells 1 and 4. Panels represent outcomes for both networks, spanning all $(\Delta_{12}, \Delta_{13})$ -space ICs while beginning [456] in black CTW phase-lag, near $(\Delta_{45}, \Delta_{46}) = (1/3, 2/3)$, cells 1 and 4 in-phase, with $\Delta_{14} = 0$. Entire system converges to nearly identical outcomes as in the in-phase blue PM example of Figure 6.26, with the purely clockwise connectivity of [456] resulting in its immediate convergence to black CTW behavior in both cases, which in turn drives outcomes in [123]. Parameters: $I_{app} = 0.45$, $g_{ij} = g_{kl} = 0.008$, $g_{elec} = 0.002, 0.005, 0.01$.

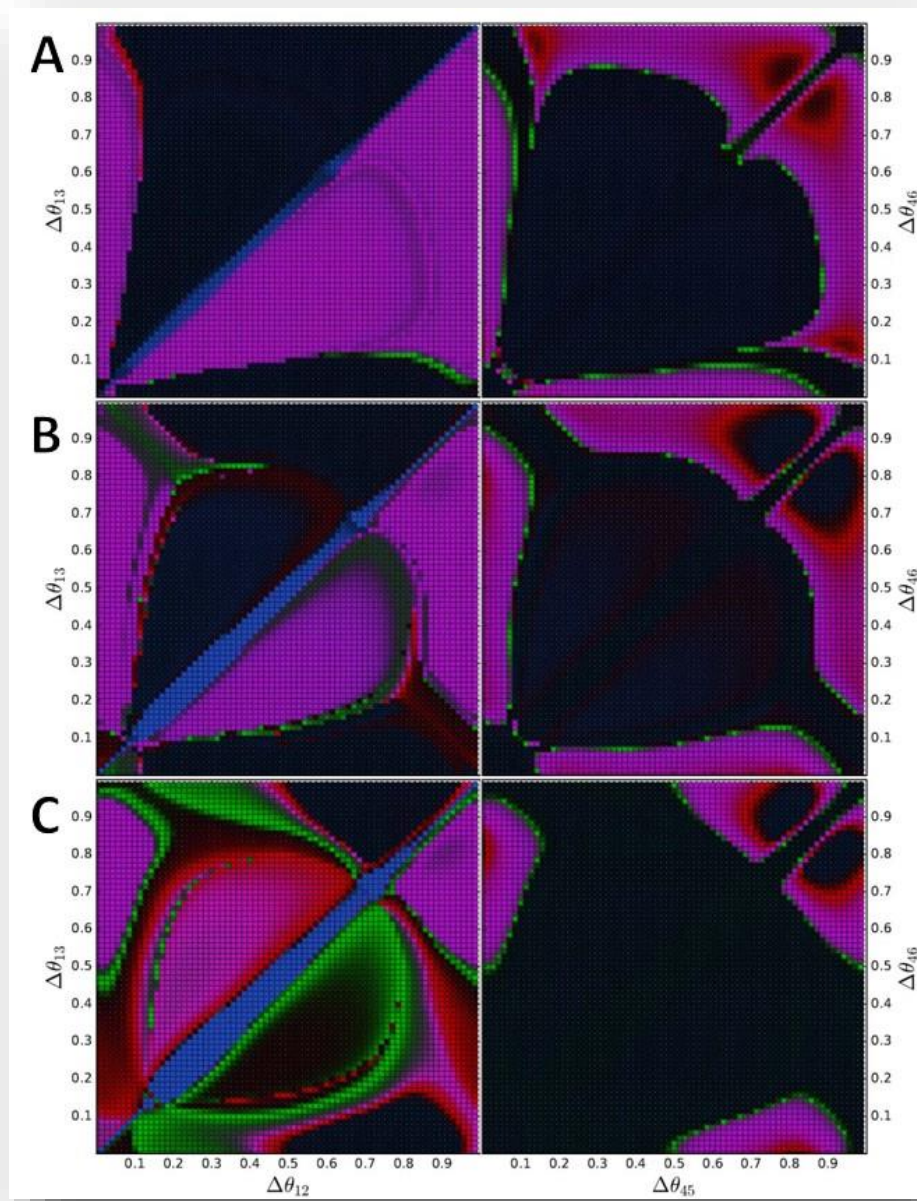


Figure 6.28 Single electrically-coupled symmetric-clock hybrid, anti-phase CTW

Almost entirely TW-dominated symmetric network electrically coupled with a purely clockwise one, where only black CTW patterns exist, via connection of cells 1 and 4. Panels represent outcomes spanning all $(\Delta_{12}, \Delta_{13})$ -space ICs beginning [456] in black CTW phase-lag, near $(\Delta_{45}, \Delta_{46}) = (1/3, 2/3)$, in cells 1 and 4 anti-phase at $\Delta_{14} = 1/2$. [123] results mostly in TW rhythms at weaker coupling due to CTW dominance of [456], but with possible PM outcomes growing to dominate at stronger coupling with complex boundaries. [456] remains mostly black CTW, but now exhibits CCTW and regions of red PM activity for some $(\Delta_{12}, \Delta_{13})$ -ICs, decreasing in size with coupling. Parameters: $I_{app} = 0.45$, $g_{ij} = g_{kl} = 0.008$, $g_{elec} = 0.002, 0.005$, and 0.01 .

Finally, and of most interest, is the case beginning the [456]-motif in Figure 6.28 again with black clockwise traveling wave rhythmicity but connecting cells 1 and 4 electrically beginning in anti-phase, with $\Delta_{14} = 1/2$. As in both previous examples, the [123]-motif remains largely dominated by traveling wave rhythms at weaker coupling due to the clockwise traveling wave dominance of [456], but with more extensive basin switching between the two patterns than was previously observed. With increased electrical coupling, possible pacemaker outcomes also again grow to occupy much of the phase-basin diagram but with complex boundaries and multiple regions of non-contiguous basins of attraction for each rhythm. More surprisingly, while the [456]-network continues to remain mostly in black clockwise traveling wave rhythmicity, it can now be induced to exhibit not only counterclockwise traveling wave patterns but also small regions of red pacemaker activity for some $(\Delta_{12}, \Delta_{13})$ -space initial conditions. Both additional patterns see decreasing basin sizes with stronger electrical coupling.

While initial coupling even what might be considered the simplest asymmetric network with a symmetric one led to many straight-forward and intuitive results, particularly for the [456]-network with the existence of only counterclockwise-directional inhibition, but exhibited dramatic shifts in behavior with anti-phase initial coupling of cells 1 and 4, and sometimes with increasingly strong electrical coupling. Even with only the single electrical connection explored in this chapter, dramatic results were sometimes achieved in establishing apparent synchronicity of cells 1 and 4 for both the symmetric-symmetric and the symmetric-clock. This is not enough to force full network symmetry between the two local networks, however, and additional electrical coupling of cells would be required. Some preliminary results for adding this type of coupling for the symmetric-clock hybrid network can be found in the Appendix for both double and triple electrical coupling of the two networks.

6.5 Very strong electrical coupling for node reduction

In addition to establishing apparent node synchronicity, and even local network synchronicity using two or three electrical couplings, use of this method of connecting networks can permit the use of this 3-node modular structure in constructing larger networks that are not necessarily of modulus 3 dimension. Precisely because electrical coupling generally drives connected cells to in-phase relationships, and therefore at very strong coupling to full synchronicity, introduction of very strong electrical coupling effectively makes two nodes identical to one another. This reciprocal identity assumption via very strong coupling and synchronicity can be used to collapse two nodes onto one another or, in the case of connecting two 3-node networks, combine a modular 6-cell network into an effectively 5-cell configuration. This is potentially a highly useful technique, in permitting the rich range of results and parameter sweeping that has been done in this, and other similar, research to be applied not only within networks with 3-cell kernels or with modular 3-node multiplicity but also to essentially any number and configuration of cells by simply collapsing cells upon one another where necessary to create the desired larger network structure.

In the following figures this is shown as an extension of the results discussed in the previous sections, first with the three types of coupled symmetric networks explored (pacemaker-only release, traveling-wave only oscillatory, and five rhythm release), and then with the symmetric-clockwise hybrid motif explored. In Figure 6.29, for example, we observe three panels extending results for the combined pacemaker-only symmetric release networks described in Figures 6.14-6.17. The top pair of panel represents the extension to Figure 6.15, with [456] beginning in blue pacemaker rhythmicity and cells 1 and 4 in-phase, but with electrical coupling now set at $g_{elec} = 0.1$, or twenty times as strong as the rest of the network connections, in addition to acting faster as an electrical connection. All outcomes in this node-reduction lead to pacemaker rhythms in both

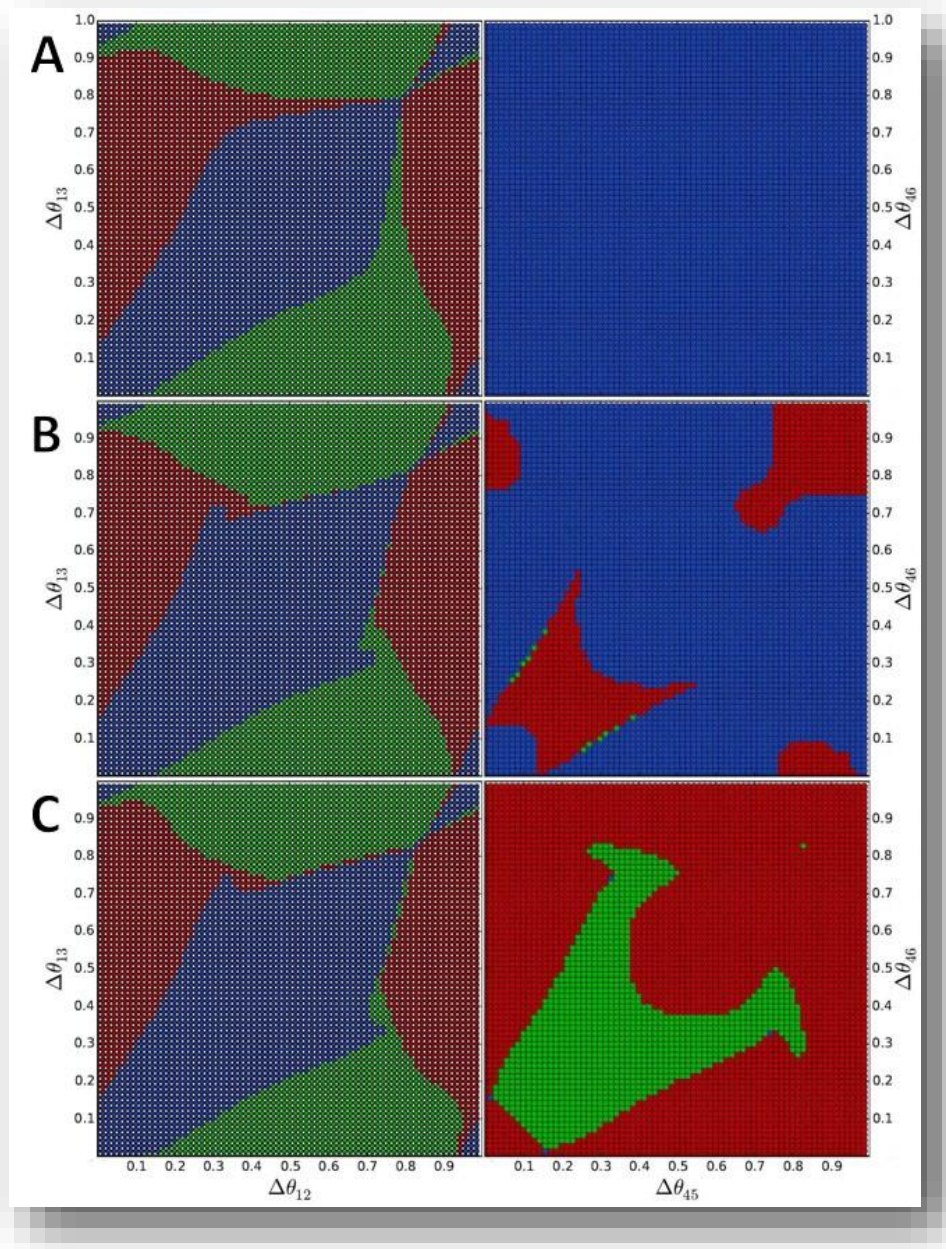


Figure 6.29 Very strong single electrically-coupled symmetric PM systems

Very strong coupling of two purely symmetric release case motifs initially exhibiting only PM rhythms, extensions on Figures 6.15-17. All $(\Delta_{12}, \Delta_{13})$ -space ICs are spanned for the [123]-motif. (A) [456] starts as in-phase BPM, $(\Delta_{14}, \Delta_{45}, \Delta_{46}) = (0, 0.5, 0.5)$. (B) [456] starts as in-phase CTW, $(\Delta_{14}, \Delta_{45}, \Delta_{46}) = (0, 0.33, 0.67)$, (C) [456] starts as anti-phase CTW, $(\Delta_{14}, \Delta_{45}, \Delta_{46}) = (0.5, 0.33, 0.67)$. In all three cases, we observe final system outcomes emphasizing the trends seen earlier and now having stabilized to final rhythm generation patterns that will remain constant for any additional increases in electrical coupling. Parameters: $I_{app} = 0.4$, $g_{ij} = g_{kl} = 0.005$, $g_{elec} = 0.1$.

networks, final rhythms in the [456]-motif dependent entirely on its beginning state. This is followed then by a pair of panels extending Figure 6.16 by representing the same strength electrical coupling with [456] beginning in-phase again but in the blue pacemaker position, and then in anti-phase with initial purple counterclockwise phase-lag. In both cases, the [123] network sees basin switching of the CTW and CCTW regimes across the $\Delta_{12} = \Delta_{13}$ diagonal in the upper right quadrant with initial conditions placing cell 2 or 3, or both, late in the initial period of bursting cell 1. This

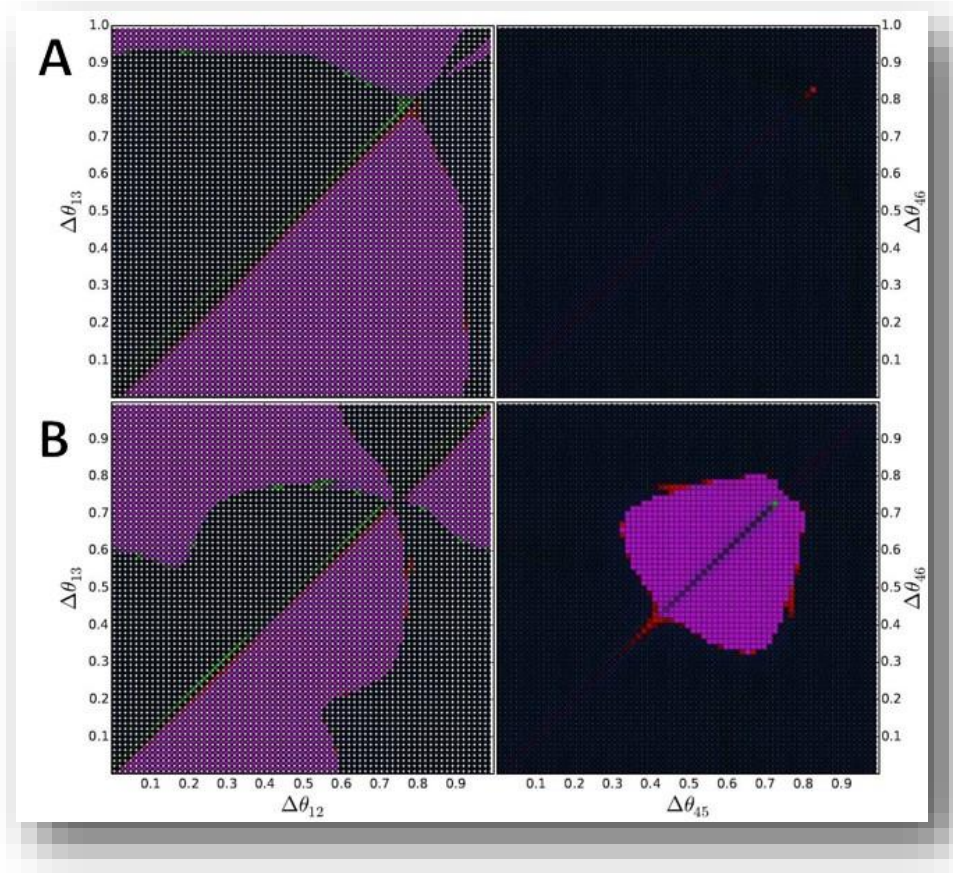


Figure 6.30 Very strong single electrically-coupled symmetric TW systems

Very strong coupling of two purely symmetric release case motifs initially exhibiting only TW rhythms, extensions on Figures 6.19-20. All $(\Delta_{12}, \Delta_{13})$ -space ICs are spanned for the [123]-motif. (A) [456] starts as in-phase BPM, $(\Delta_{14}, \Delta_{45}, \Delta_{46}) = (0, 0.5, 0.5)$. (B) [456] starts as anti-phase CCTW, $(\Delta_{14}, \Delta_{45}, \Delta_{46}) = (0.5, 0.83, 0.17)$. In both cases, symmetric outcomes around the 45-degree line, in which only TW patterns exist, are observed for both networks. A unique region of CCTW rhythmicity occurs when beginning [456] in anti-phase. Parameters: $I_{app} = 0.5$, $g_{ij} = g_{kl} = 0.005$, and $g_{elec} = 0.1$.

switch is even more pronounced when cells 1 and 4 begin in anti-phase, as rapid convergence of the two cells by strong electrical coupling forces them to come into phase immediately and all other cells receive resulting inhibitory stagger altering normally stable convergence to fixed outcomes. The [456]-motif is immediately driven to only clockwise traveling wave rhythms when begun in-phase with $(\Delta_{14}, \Delta_{45}, \Delta_{46}) = (0, 0.5, 0.5)$, but can be driven to either clockwise or counterclockwise rhythmicity when begun in anti-phase.

In Figure 6.31, where very strong coupling of two symmetric release case motifs capable of producing all five standard rhythms, as seen in Figure 6.21, extends on observations of Figures 6.22-24, we again observe stable fixed outcomes that emphasize the trends seen previously while having stabilized to outcomes that will no longer vary with additional electrical coupling strength. For the extension on the example beginning with in-phase blue pacemaker activity in [456], with $(\Delta_{14}, \Delta_{45}, \Delta_{46}) = (0, 0.5, 0.5)$, only pacemaker rhythm outcomes are possible in both networks because of both the cell 1 and 4 synchronicities and the pacemaker stimulus induced by [456] onto [123]. For the case where [456] begins with in-phase clockwise traveling wave phase-lag, with $(\Delta_{14}, \Delta_{45}, \Delta_{46}) = (0, 0.33, 0.67)$, all rhythms remain possible in [123] with only either clockwise traveling wave or red pacemaker outcomes present in [456], pacemaker rhythms in [456] aligning with conditions where pacemakers also stabilize in [123]. Finally, when [456] begins in an anti-phase clockwise traveling wave position, at $(\Delta_{14}, \Delta_{45}, \Delta_{46}) = (0.5, 0.17, 0.83)$, abrupt transitions forcing cells 1 and 4 back into synchronicity lead to additional green pacemaker rhythms in [456] which align with interesting growth of the blue pacemaker basin in [123]. Basin switch is again observed in upper right quadrant of [123] along the $\Delta_{12} = \Delta_{13}$ diagonal for all three cases, with increasingly complex pattern transitions and boundaries for both networks beginning in anti-phase. Lastly, we introduce very strong electrical coupling of a symmetric network for which TW

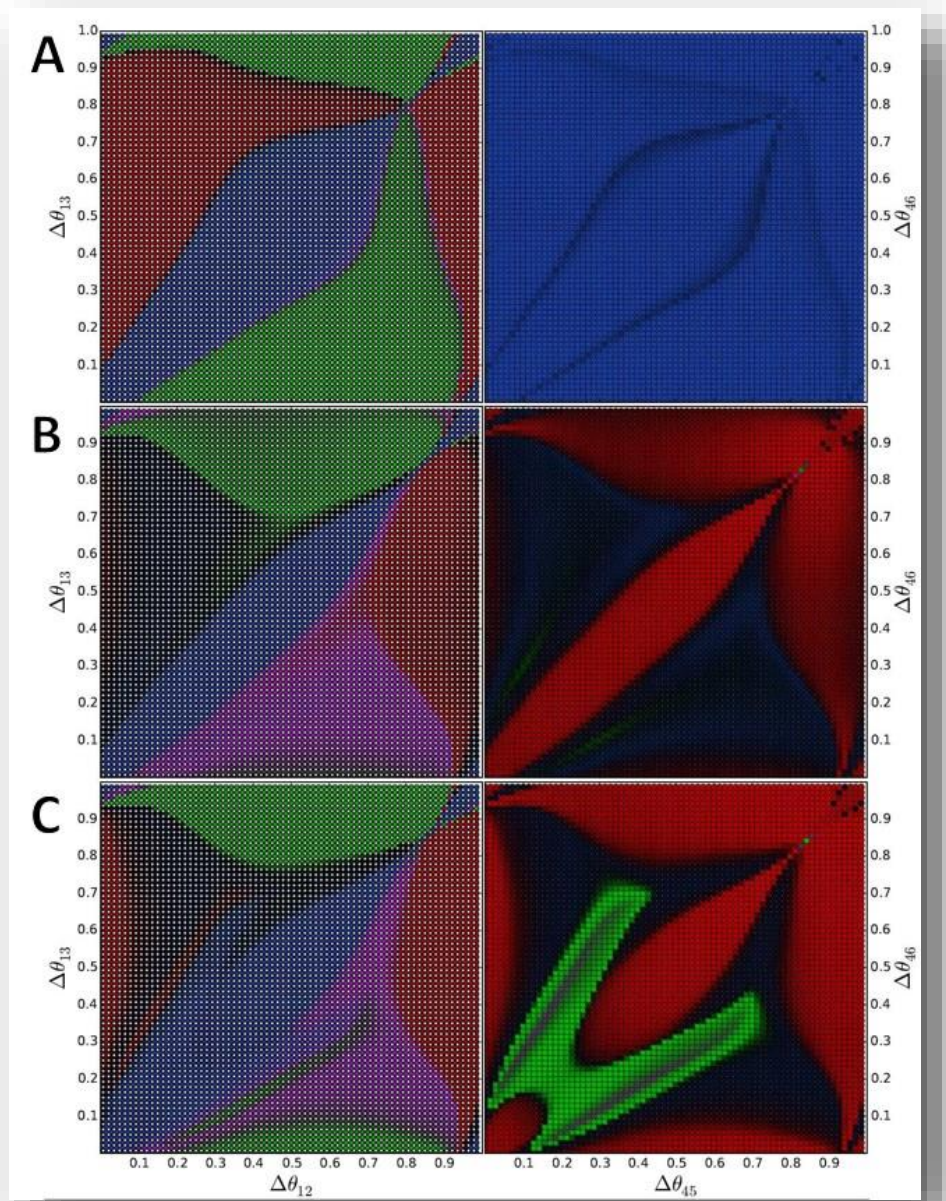


Figure 6.31 Very strong single electrically-coupled symmetric multi-rhythm systems
 Very strong coupling of two symmetric release case motifs initially capable of producing all five standard rhythms, extensions on Figures 6.22-24. All $(\Delta_{12}, \Delta_{13})$ -space ICs are spanned for the [123]-motif. (A) When [456] begins in-phase BPM, $(\Delta_{14}, \Delta_{45}, \Delta_{46}) = (0, 0.5, 0.5)$, only PM rhythm outcomes are possible in both networks. (B) When Motif (456) begins in-phase CTW, $(\Delta_{14}, \Delta_{45}, \Delta_{46}) = (0, 0.33, 0.67)$, all rhythms are possible in [123] with only CTW and RPM present in [456]. (C) When [456] begins anti-phase BTW, $(\Delta_{14}, \Delta_{45}, \Delta_{46}) = (0.5, 0.17, 0.83)$, abrupt transitions lead to additional green PM rhythms in [456]. Basin switch in upper right quadrant of [123] is observed in all cases, with complex pattern transitions for both networks when begun in anti-phase. Parameters: $I_{app} = 0.42$, $g_{ij} = g_{kl} = 0.005$, and $g_{elec} = 0.1$.

outcomes almost entirely dominate with a purely clockwise network for which only the black CTW pattern exists, as seen in Figure 6.25, as an extension of the results in Figures 6.26-28, but with modifications to the third case introducing it first beginning instead in counter-clockwise rhythmicity and then as an in-phase clockwise example instead. Outcomes here again emphasize the trends seen previously, but stabilized to outcomes that will no longer vary with additional increasing electrical coupling strength. As before, the [123]-motif is explored using all $(\Delta_{12}, \Delta_{13})$ -space initial conditions are spanned for the [123]-motif. As before, when the [456]-motif begins with in-phase blue pacemaker rhythmicity, with $(\Delta_{14}, \Delta_{45}, \Delta_{46}) = (0, 0.5, 0.5)$, all five rhythms continue to remain possible in [123] but with significantly reduced capability to produce traveling wave patterns. When [456] begins instead with in-phase clockwise traveling wave phase-lag, at $(\Delta_{14}, \Delta_{45}, \Delta_{46}) = (0, 0.33, 0.67)$, this trend is even more pronounced with very few initial conditions in the $(\Delta_{12}, \Delta_{13})$ -space for which they can occur. In both cases, the blue basin of attraction is also significantly reduced. This is even more emphatically reduced in the case in which [456] begins in anti-phase with a counterclockwise traveling wave, $(\Delta_{14}, \Delta_{45}, \Delta_{46}) = (0, 0.67, 0.33)$. This system is forced to abruptly transition to bring cells 1 and 4 into immediate synchronicity with very strong electrical coupling, and complex basins of rhythm potential appear in both networks. The [123]-network is now primarily occupied by traveling wave rhythms, which are paired with complex outcomes in [456] which do not always converge to the clockwise rhythm and may indicate artificial rhythmicity induced by the strongly-coupled inhibition provided from [123] and require additional investigation. This anti-phase example was selected here as an alternative to the view of the black clockwise initial state shown in Figure 6.28. Finally, results of strong coupling for that network beginning in-phase, but with slight stagger from the original position now at $(\Delta_{14}, \Delta_{45}, \Delta_{46}) = (0.5, 0.17, 0.83)$ instead, show that observed trends continue for the [456]-motif, with both

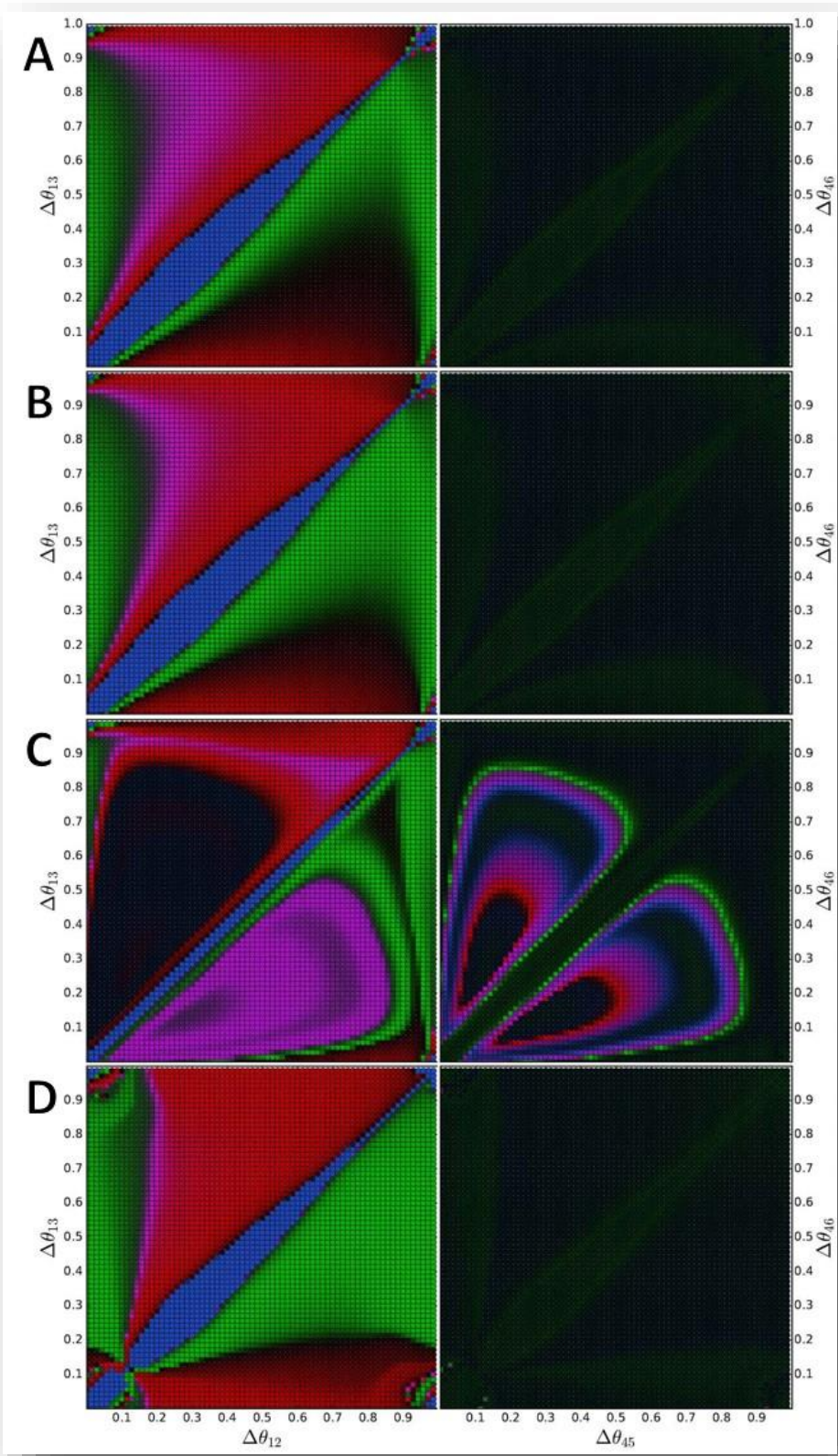


Figure 6.32 Very strong single electrically-coupled symmetric-clock hybrid system

Very strong coupling of a symmetric motif producing primarily TW rhythms with a purely clockwise network with only CTW initially, extensions on Figures 6.26-28. All $(\Delta_{12}, \Delta_{13})$ -space ICs are spanned for the [123]-motif. (A) When [456] begins in-phase BPM, $(\Delta_{14}, \Delta_{45}, \Delta_{46}) = (0, 0.5, 0.5)$, all five rhythms remain possible in [123] but with decreasing TW patterns. (B) When [456] begins in-phase CTW, $(\Delta_{14}, \Delta_{45}, \Delta_{46}) = (0, 0.33, 0.67)$, this trend is more emphatic. (C) When [456] begins in-phase CCTW, $(\Delta_{14}, \Delta_{45}, \Delta_{46}) = (0, 0.67, 0.33)$, TW rhythms instead dominate most of [123] and additional complex regions of non-CTW behavior become possible in [456]. (D) When [456] begins anti-phase in staggered CTW, $(\Delta_{14}, \Delta_{45}, \Delta_{46}) = (0.5, 0.17, 0.83)$, almost purely PM behavior in [123] is paired with fixed CTW outcomes in [456]. Parameters: $I_{app} = 0.45$, $g_{ij} = g_{kl} = 0.008$, and $g_{elec} = 0.05$.

the counterclockwise traveling wave and red pacemaker rhythms now eliminated. In this case, however, almost purely pacemaker behavior exists in [123] with much less complex basin boundaries than beginning in the traditional position. This underlines the sensitivity of the network

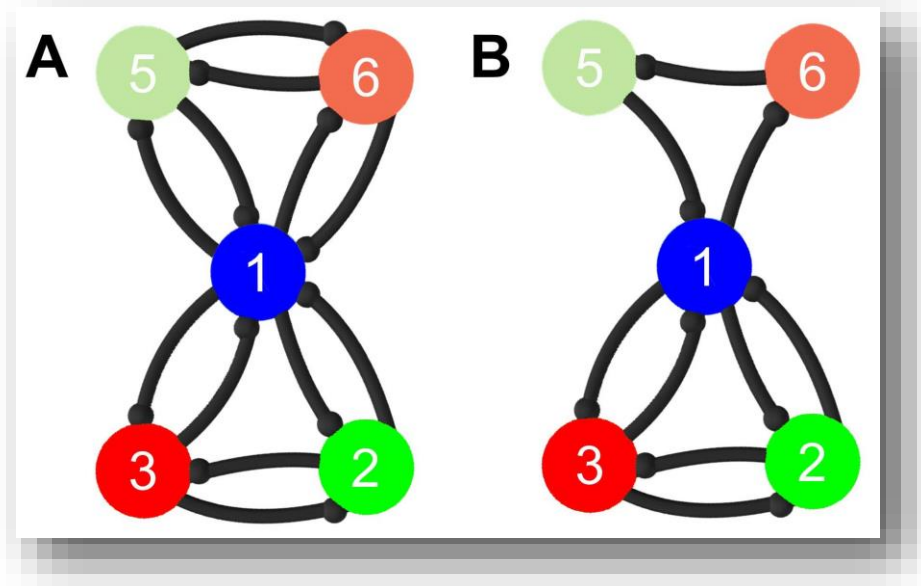


Figure 6.33 Effective 5-node reduction of Sym-Sym and Sym-Clock networks

The effect of very strong electrical coupling cells between two networks forces them into fixed synchronicity, effectively collapsing them into a single cell with outgoing connections into both original local-networks. The effect of this node-reduction is shown here for the two systems explored with: (A) two symmetric 3-node networks into a 5-node configuration, collapsing cells 1 and 4 into a single cell with four incoming and four outgoing connections, and (B) a symmetric 3-node motif combined with a purely clockwise one, collapsing cells 1 and 4 into a single cell with only three incoming and three outgoing connections.

to initial conditions in both networks, and the need to develop even further techniques to adequately span and explore all initial condition spaces for both networks. The effect of introducing this very strong electrical coupling cells between two three-node motifs forces them into fixed synchronicity, effectively collapsing any connected cells into single cells with outgoing connections into both original local-networks. The effect of this node-reduction can be observed in Figure 6.33 for the two examples discussed here.

6.6 Discussion and applications

In this chapter, we discussed the use of three-node motifs in modular networking, as building blocks for construction of larger networks with embedded local networks. An initial example of use of this approach in developing a 3+1 configuration, in which an additional cell is added to a known three-cell network to introduce additional dynamics and potential rhythmicity. Expansion of the motifs in this manner effectively doubled the number of potential connections possible for parameter sweeping from six to twelve, vastly compounding the complexity of these systems and the ability to visualize such systems. With a single additional cell, it is still possible to retain all of the key features of phase-lag return maps previously described, but using a three-dimensional visualization. This approach is relatively easy to interpret for simplistic cases, where only one or two additional connections are used, but becomes difficult to analyze outcomes with additional connectivity or asymmetry, with traces challenging to untangle visually when viewing return maps of these outcomes. An example of the simplest case, for a symmetric motif with a fourth cell only connected to one of the original three, was shown and gave a good idea for usable cases in which this method could be valuable.

With increasing complexity, or with larger network coupling using two three-cell motifs, this three-dimensional visualization is inadequate and a technique for using phase-basin diagrams for

outcomes in both networks was introduced. This technique requires beginning one of the two networks in a fixed initial condition, while permitting full spanning of the initial condition space of the other network as had been done previously. Phase-basin diagrams for the outcomes then indicate the outcomes of each of the two networks, but relative to the initial conditions of the spanned network. In this research, results were typically demonstrated spanning the full $(\Delta_{12}, \Delta_{13})$ -space for the [123] network while beginning the [456] network at several fixed rhythmicity positions to represent general outcomes. For symmetric networks, or coupled networks using at least one symmetric network, this method is useful in teasing out general trends in behavior, as selection of the specific traveling wave or pacemaker rhythm used in [456] can typically be applied to results picking any other traveling wave or pacemaker rhythm instead. For further introduced asymmetry, this method would require more extensive spanning of paired initial conditions in order to evaluate asymmetric outcomes in beginning positions for the [456]-motif. For simplicity, this work focused on beginning positions that represented initial blue pacemaker or black clockwise traveling wave phase-lag, with starting conditions for connectivity of cells 1 and 4 in either in-phase or anti-phase relationships, with $\Delta_{14} = 0$ or 0.5 respectively. This permits exploration of the effect of either inhibitory or electrical coupling of those two cells on rhythms in both networks when synchronous or asynchronous initial conditions exist or are imposed.

Results of connecting three-node motifs in this way were explored first with single inhibitory connection of only cells 1 and 4, both with mono-biased and pairwise-biased coupling. In the mono-biased case, this represented driving input onto the [123]-motif by oscillatory rhythms generated in the [456]-motif and could be interpreted as almost any kind of external input, including single-cell addition or a single incoming connecting from another external local network of any size. This impulse effect had influences on the rhythm generation of the driven network that

aligned well with hypothesized outcoming using both results from work in earlier chapters and known effects of external impulse stimuli. Visualization only of the affected network was necessary in this case, as no feedback was provided to the driving network that would affect its beginning rhythm in any way. In the pairwise-biased case, however, more significant effects were observed and visualization of both network outcomes was required. It was here that we introduced in further detail the concept of pairing phase-basin representations both to avoid the complexity of interpreting phase-lag return map trajectories that could now cross over one another but also because the driving network could also be induced to change rhythm. Only symmetric motifs were paired in these preliminary examples, but similar effects and methods would remain equally viable for other paired network combinations.

This approach was then extended to introduction of electrical coupling of three-node motifs, where relative synchronicity is generally achieved rapidly between connected cells even with moderate coupling strength, and full synchronicity becomes normal with increasing strengths. As this type of connectivity was new to research discussed thus far, more extensive sampling was provided and results were again shown first using paired symmetric networks as a base case to work from. We showed the effect of pairing symmetric motifs with differing mechanisms, both release case and fully oscillatory systems, with examples of symmetric motifs capable of producing pacemaker-only, traveling wave only, or full penta-rhythmicity each shown. The effect of electrical coupling is significant in many cases, but highly dependent on whether the connected cells begin in-phase or anti-phase, as electrical coupling will push them to synchronize. The stronger the electrical coupling, the more significant the observed effect of shifts in rhythmicity due to eventual synchronization of cells 1 and 4. In nearly every example, many of which were chosen precisely because they existed in bi-parametric (g_{ij} , I_{app})-space near observed bifurcation effects, dramatic

rhythm shifts could be induced eliminating or creating rhythms possible in each network. At times these effects were immediate even at very low coupling, while requiring stronger coupling to drive networks in other cases. In all cases, rhythm outcomes tended to stabilize with increasing coupling strength. These trends were observed as well in the paired symmetric-clockwise motifs, with surprising capability to drive a network which did not even have the capability by itself to produce a specific rhythm to do so when paired, particularly when strongly connected in anti-phase.

Finally, as an extension of this stabilizing behavior with increasing electrical coupling strength, the effect of very strong coupling in forcing cells 1 and 4 to immediately synchronize was explored. Experiments described in connecting the previous systems with increasingly strong electrical coupling were all extended by inducing electrical coupling at 10-20 times the strength of previous results shown. In each case the trend previously observed was extended, or sometimes repeated if the system was already at full synchronicity of cells 1 and 4. All examples shown here were validated by testing double the strength shown to verify that no further rhythm changes were observed in either network. In every case, cells 1 and 4 are immediately driven to in-phase synchronicity, with $\Delta_{14} = 0$, and behave as one unit with no time differentiation between waveform observations of either cell. This permits these cells to effectively be treated as a single cell and is a novel method for node-reduction that permits extensions of the work described to networks that are not necessarily multiples of the three-node motifs characterized. This outcome may be valuable in bridging the gap between well-known and characterize local dynamics of two- or three-cell networks to the behavioral outcomes driven by much larger networks, and is a first step in using this and other research in modular networking to build larger networks with known dynamics.

7 CONCLUSIONS

This focus of this research has been to explore the robustness of synchronized oscillatory patterns, revealing universal principles of rhythmogenesis and multi-functionality, or stability of multiple phase-locked outcomes, in circuits with the same parameter set. This type of multi-functionality is important in rhythm switching behaviors and vital in the understanding of systems capable not only of generating a multitude of rhythmic motor control behaviors like walking, swimming, and breathing, but also in other networks facilitating tasks with periodic stability, like circadian rhythms, and even perhaps in memory formation and retrieval. Understanding general principles which can lead either functional and dysfunctional behaviors in neural networks is a goal that may benefit future study of abnormal neurological diseases and other biological arrhythmias that result from perturbations of the mechanisms governing normal rhythmic states.

While building upon previous work using Hodgkin-Huxley-type equations to capture a full range of biologically feasible parameter effects in inhibitory three-cell networks, this work focused on qualitative and quantitative stability analysis of a family of reciprocally coupled neural circuits, constituted of generalized Fitzhugh–Nagumo neurons, while retaining some general biologically relevant parameters that can be readily manipulated in an experimental setting. This permits a reduction in complexity that allows much more extensive parameter sweeping and exploration of system-wide outcomes. Extensive use of the methods of bifurcation analysis and phase reduction were used to reduce this complexity even further, allowing much broader elucidation of qualitative changes in rhythm stability by permitting extensive exploration of pivotal parameters that was previously impossible to describe biologically plausible network connectivity.

This work has explored both symmetric and asymmetric connectivity within three-cell motifs, which often form constituent blocks within larger networks, with the goal of characterizing key

network connectivity commonly observed and building a framework to use these results for hypothesis generation and validation with experimental work in either laboratory or natural settings. Intrinsic mechanisms of synaptic release, escape, and post-inhibitory rebound were all examined, and each lead to differing poly-rhythmicity, where a single parameter or perturbation may trigger rhythm switching in otherwise robust networks. Additional rhythm outcomes were also discovered and elucidated, including phase-varying lags and broader cyclical behaviors, helping to characterize system capability and robustness that could reproduce or anticipate experimentally observed outcomes.

Finally, by developing a suite of visualization approaches and computational tools, some accessible online through the lab at the site NuerDS.net, for use in the three-cell networks, to catalog and describe the potential for robustness of network rhythmogenesis, and extending these tools for use in characterizing outcomes in larger network settings, novel new methods have been disclosed for principles in neuroscience applications and modeling that may be applicable to systems beyond central patterns generators and simple motor-control. A framework for approaching this modular organization was introduced, by using both inhibitory and electrical coupling of well-characterized 3-node motifs, employing these local circuits as building blocks within larger networks to describe underlying cooperative mechanisms.

7.1 Polyrhythmicity in local 3-node networks

In Chapters 2 and 3, methods of phase-reduction and phase-lag return maps were described and paired with use of bifurcation diagrams to systematically and extensively explore bi-parametric outcomes and rhythm switching behaviors. The focus here, and in the following chapters, was primarily on exploration of the bi-parametric (g_{ij}, I_{app}) -space to represent changes readily observed in nature or manipulatable in a laboratory setting. Changes in connectivity strength, g_{ij} , between

cells can be used to represent the formation of new connectivity in learning or development, or through changing circuit connection strength that may either occur with use (or lack thereof) or be induced by additional chemical or electrical internal or external stimulus causing a connection to strengthen or weaken. In Hodgkin-Huxley-type models, these types of changes could be represented through a variety of gating variables or other parameters that are now all enveloped within this single coupling parameter in the gFN model employed here. Similarly, the current shift parameter, I_{app} , also encompassed what could be a combination of internal ionic flows with differing parameters and behaviors in more complex models and here envelop all such changes.

This approach allows for broad sweeping of parameter space but would require teasing out individual sub-components to determine appropriate connectivity or current changes to manipulate in a lab setting. One other limitation here is the simplicity of the waveform, as the focus here is on bursting patterns and rhythmicity and not on fluctuations within those bursts that would represent interspike intervals (ISIs) or other tapering effects observed in nature and captured by more complex models. The benefit gained here, however, is the ability to much more broadly categorize macro-scale bursting behaviors and transitions that could then be used to identify areas of interest in which to introduce additional layers of complexity to the current gFN model to examine other effects of interest regarding subtler waveform variations in initiation and onset, or the effect of ISIs on additional cellular interactions not encompassed by the overall bursting pattern itself.

Results from examination of the fully-symmetric three-node network were as expected, and distinct trends in pattern formation and collapse were observed within the framework connecting release-type mechanisms at low ranges of $I_{app} < 0.45$, through oscillatory mid-ranges, to escape-type mechanisms occurring at higher $I_{app} > 0.55$. Pacemaker patterns are more readily apparent at the two extremes, with the nature of null-cline proximity for the release and escape cases

permitting more ready clustering of the cells near each knee of the nullcline as transitions slowed and induced longer periods of inhibition on one or more cells in the network. Opposite effects were observed for the two mechanisms, with inherently bursting release-case cells more likely to produce traveling wave outcomes at low coupling strength and escape-case ones at higher coupling strengths. The reverse was true for pacemaker rhythms, which tended to still dominate both these mechanisms relative to traveling wave formation. Truly oscillatory ranges of I_{app} tended toward pure traveling wave regimes of behavior, with no nullcline slowing effects to push the cells to not simply divide the limit cycle space equally when all connections are of equal strength. The effects of post-inhibitory rebound described in Chapter 5 were characterized by a small growing traveling wave regime as coupling increases, strong coupling generally required to induce any activity whatsoever in these otherwise quiescent systems, with no pacemaker behavior observed for the symmetric motif.

Extending this approach to four additional key asymmetric motifs in Chapter 3, traveling wave and pacemaker rhythms are again observed in both the inherently bursting release and quiescent escape mechanisms, with each dominated more by one (PM and TW respectively again) for most motifs and the other occurs mostly at lower asymmetric coupling strengths. In nearly all motifs explored, unique behaviors occur around full symmetry where the strength of the connection being manipulated was close to those being held fixed at 0.0010. This is most apparent in the clockwise-biased motif in which the bifurcation looks nearly symmetrical around the vertical line representing this equipotent connectivity, but is also clear in the extended ‘peaks’ and ‘troughs’ of mixed behavior observed in either the pairwise-biased or king-of-the-mountain motifs. Pacemaker behavior is least likely to occur in clockwise-biased motifs, as this connectivity induces traveling wave behavior at any strength coupling, and pacemaker-only behavior is only induced near

symmetry for very small ranges of $g_{12} = g_{23} = g_{31}$ at the extremes of both release and escape. It is important to note that, while four key asymmetric circuit configurations are explored in detail, these results are symmetric with results for identical changes affecting different cells within the network. Results obtained, both in phase-lag return map outcomes and bifurcation diagrams summarizing them, need only be oriented and viewed with correct reference to the cell or cells being affected. An example of symmetric equivalence of asymmetric motifs is describe in Figure 7.1, where equivalent motifs for each of the four key asymmetric motifs are represented.

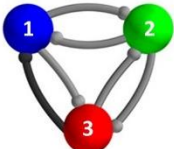
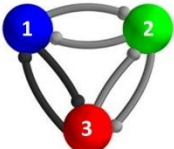
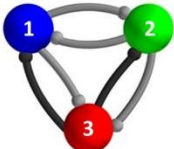
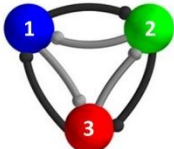
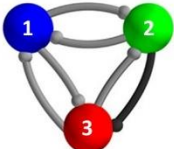
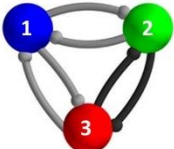
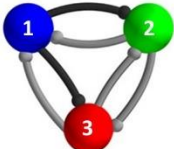
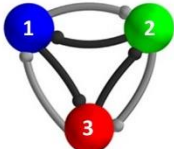
Motif	Mono-biased	Pairwise-Biased	King-of-Mountain	Clockwise
Base Case				
Alternate Example				
Symmetrically Equivalent List	$g_{31}, g_{32},$ $g_{12}, g_{21},$ g_{23}^*, g_{32}	$g_{31}=g_{13},$ $g_{12}=g_{21},$ $g_{23}=g_{32}^*$	$g_{31}=g_{32},$ $g_{12}=g_{13}^*,$ $g_{21}=g_{23}$	$g_{31}=g_{12}=g_{23},$ $g_{13}=g_{32}=g_{21}^*$

Figure 7.1 Symmetrically equivalent asymmetric 3-node motifs

Examples of alternate circuitry in 3-node networks which remain symmetrically equivalent to each of the four key motifs described. For each key motif, shown as the base case and in **bold** in the equivalence list, one visual alternate example is provided, and denoted with an *, along with a list of all possible equivalent networks which could be described using the outcomes from Chapters 3-5 of this work.

Phase-slipping behaviors were observed with unexpected regularity in the mono-biased or the two double-connection motifs, and lend themselves to analysis of macro-scale rhythmic behaviors in which periods of apparently stable patterns interspersed by fast rhythm switching to another

apparently stable rhythm without the need for external stimuli might be observed. These may present novel applications to experimental research of small local networks in which multi-stable rhythm production can be observed with the same connectivity. Rhythm switching for non-phase-slipping systems is also readily obtained in both release and escape cases, either by external stimulus in the form of a current pulse (abrupt temporary shift up or down in effective I_{app} value seen in the bifurcation diagrams) or by either natural or artificial connection plasticity (abrupt temporary shift up or down in effective g_{ij} value seen in the bifurcation diagrams). Some of these types of effects are observed in the coupled network outcomes described in Chapter 6.

Further investigation into the specific types of bifurcations observed, and the cases in which these could be induced was a primary focus of Chapter 4. Andronov-Hopf and pitchfork bifurcations, which characterized all rhythm transitions observed within the fully symmetric motif, were not typical for changes observed within the asymmetric motifs. As most results in this work are described in detail with movement across the bifurcation diagram, changing g_{ij} , the symmetric requirement for the existence of either Andronov-Hopf or pitchfork bifurcation exists only along the vertical line in each bifurcation diagram representing full system symmetry and these are therefore only observed with vertical shifts in I_{app} along that line. Asymmetric motifs bifurcate primarily through saddle-node bifurcation, with frequent observation of homoclinic saddle-node bifurcation in mono-biased systems and heteroclinic saddle-node bifurcation in either pairwise-biased or king-of-the-mountain motifs. Further examples and details for these rhythm transitions were described in the detailed bifurcation diagrams for both the mono-biased and king-of-the-mountain networks in Chapter 4, and in further images described in Chapter 5. A summary of the stereotypical rhythm transitions within the release and escape mechanism, as well as the existence of phase-slip behavior and the key bifurcations observed for each motif, can be seen in Table 7.1.

Table 7.1 Summary of 3-node network polyrhythmicity and bifurcations

3-Node Motif	Stereotypical Release	Stereotypical Escape	Phase-slip	Key Bifurcations
Symmetric	TW \rightarrow Mix \rightarrow PM PM Dominates	PM \rightarrow Mix \rightarrow TW TW Dominates	None	Andronov-Hopf, Pitchfork
Mono-Biased	PM \rightarrow Mix \rightarrow TW TW Dominates	TW \rightarrow Mix \rightarrow PM PM & PS Dominate	Escape case only	Saddle-node, Homoclinic saddle-node Andronov-Hopf*
Pairwise-Biased	PM \rightarrow Mix \rightarrow PM/PS PM & PS Dominate	PM \rightarrow Mix \rightarrow PM/PS PM & PS Dominate	Both release ¹ and escape	Saddle-node, Heteroclinic saddle-node, Andronov-Hopf*, Pitchfork*
King-of-the-Mountain	PM \rightarrow Mix \rightarrow PM PM Dominates	PS \rightarrow Mix \rightarrow PM/PS PM & PS Dominate	Both release and escape	Saddle-node, Heteroclinic saddle-node, Andronov-Hopf*, Pitchfork*
Clockwise	TW \rightarrow Mix \rightarrow TW TW Dominates	TW \rightarrow Mix \rightarrow TW TW Dominates	None	Saddle-node, Andronov-Hopf*, Pitchfork*

*Only through vertical transitions in I_{app} at system symmetry. ¹Only occurs for $g_{31} = g_{13} < g_{ij}$ for near-knee proximity of nullclines.

As mentioned, a narrow range of inhibitory coupling strengths exists for which bursting activity can be induced post-inhibitory rebound and generally requires very strong coupling relative to the other results described. When bursting activity does exist, it generally occupies a small fraction of the $(\Delta_{12}, \Delta_{13})$ -space of initial conditions relative to the large zones of quiescence typically observed. Traveling waves remain dominant for most ranges and initial conditions, with pacemaker rhythms requiring highly restrictive conditions to occur, and typically coexist with traveling wave patterns for an even more restricted volume of initial condition space. PIR networks jump quickly to final rhythm states due to both this required strong coupling and its inherent hard-locking nature. Within asymmetric PIR motifs, additional deviations from release-escape stereotypical behavior were observed within the other systems continued, most emphatically for the clockwise system, and underlines the increased dependence of the PIR mechanism on non-synaptic parameters.

Most of the work described here is in terms of the four key motifs, and examined in the simple case where each of these asymmetries were equivalent within themselves (i.e., in pairwise-biased both g_{31} and g_{13} were changed equally). Specifically, that any introduced asymmetry was equal for all connections being manipulated. For example, results for the pairwise-biased case are described in terms of $g_{31} = g_{13}$, with $g_{12} = g_{21} = g_{23} = g_{32}$ held constant at another connectivity strength. A couple very specific cases for asymmetry in this pairwise-biased case where $g_{31} \neq g_{13}$ were examined, but in general this additional asymmetry was not explored here, and represents another direction in which future work could extend these results. Additional asymmetry in this manner is not possible for the mono-biased motif, but can be applied in each of the other three key motifs explored, with some examples for such additional asymmetry described in Figure 7.2.

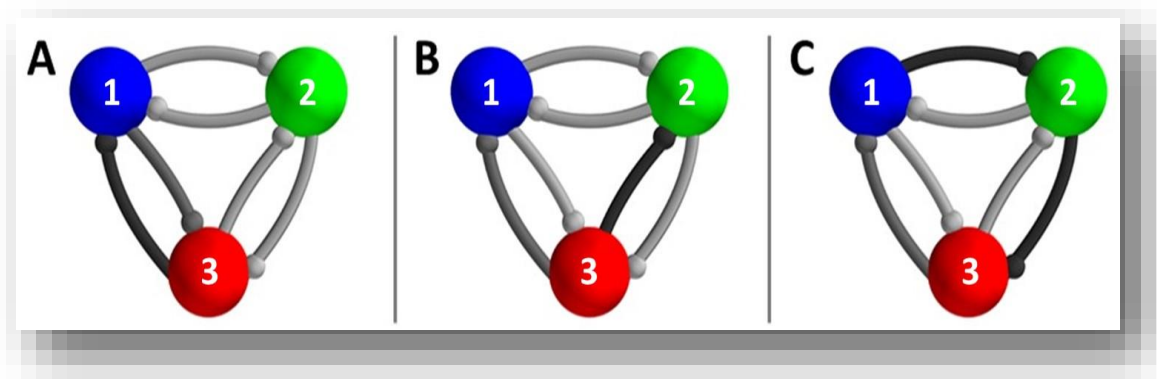


Figure 7.2 Additional asymmetry within asymmetric 3-node motifs

Examples of introducing additional asymmetry within the changing connections of three of the key asymmetric motifs explored. (A) As done in Figure 5.6, unequal changes in g_{31} (black) and g_{13} (grey) can lead to additional rhythm transitions. (B) Example of asymmetric effects of unequal king-of-the-mountain outgoing connections, $g_{31} \neq g_{32}$. (C) As done in Figure 5.5, unequal changes in the clockwise connections, $g_{12} = g_{23} \neq g_{31}$, may lead to additional changes in rhythmicity. In all of these cases, results would be symmetric changing any other connection.

Finally, while most of this work has focused on shifts in the (g_{ij}, I_{app}) bi-parametric state space, the same approach could be implemented using any bi-parametric pair or by spanning bifurcation diagrams across changes in a third parameter to create a panel of changes or a three-dimensional

tri-parametric bifurcation diagram visualization. Examination of changes in fast-slow separation, parameter ε , in this manner in Chapter 5, and in several specific-case examples in earlier chapters, emphasized the increasing dominance of oscillatory behavior at high fast-slow separation, with traveling wave behaviors growing to dominate the entire (g_{ij}, I_{app}) bi-parametric state space. This is a direct result of the increased drive of the fast-cubic nullcline in drawing trajectories toward it relative to the slow sigmoidal nullcline, leading to squarer limit cycle orbits and more abrupt waveforms transitions, as little or no clustering of cells is permitted to occur at the knees of the cubic nullcline, even with near-knee proximity in either the release or escape case ranges of I_{app} . Changes in duty in the context of fast-slow separation was described as well.

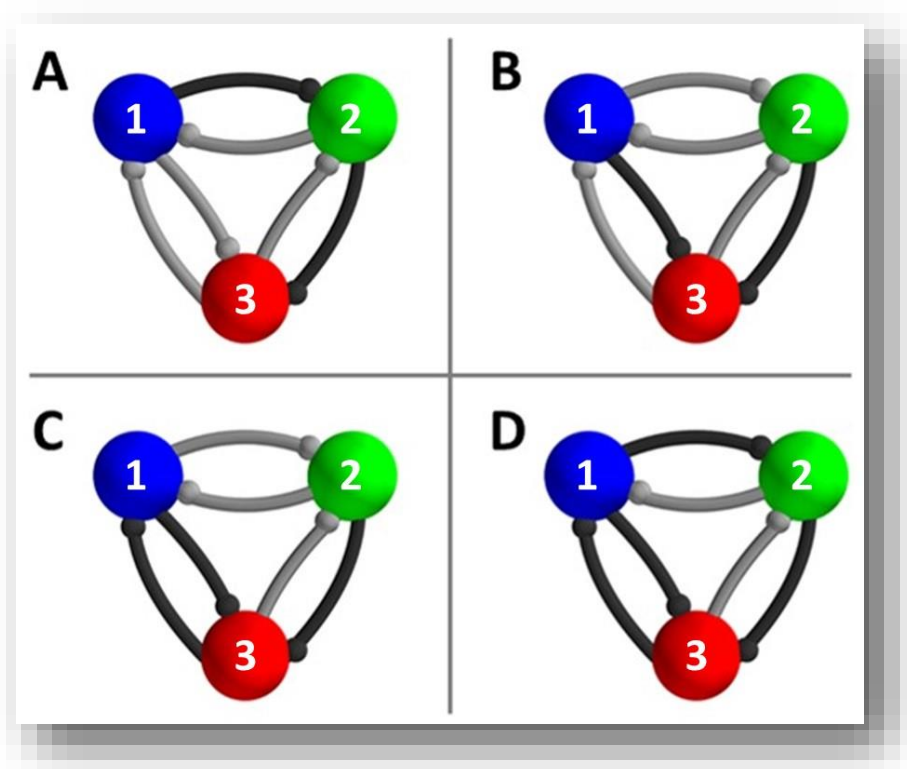


Figure 7.3 Examples of alternate key motifs observed in nature

Other key motif configurations could be examined in similar fashion, and represent cases for extension in future work. (A) Semi-clockwise biased, with g_{ij} held constant but changing $g_{12} = g_{23}$. (B) Serf-of-the-valley, with g_{ij} held constant but changing $g_{13} = g_{23}$. (C), Pairwise-affective with g_{ij} held constant but changing $g_{13} = g_{31} = g_{23}$. (D) Paired-clockwise, with g_{ij} held constant but changing $g_{12} = g_{23} = g_{31} = g_{32}$.

Lastly, future work could extend on the atlas of figures and results that have been described thus far for the four key asymmetric motifs by adding additional key motifs observed in nature to a growing collection of results and bifurcation diagrams describing outcomes for key asymmetries observed in natural settings. An example of four additional motifs that could be explored can be seen in Figure 7.3, some with very different connectivity than those examined here (semi-clockwise biased and serf-of-the-valley), while others could be performed independently or potentially represent a pairing of results obtained in the four key motifs explored in this work. Pairwise-affective could be considered a pairwise-biased motif affected by an additional mono-biased connection to one cell in the pairwise couple, and paired-clockwise could be considered a pairwise-biased motif with the addition of full clockwise asymmetry (or conversely as a clockwise-biased motif with the addition of mono-biased asymmetry onto a single node). This emphasizes the broad range of outcomes that could be effectively explored using the analytical and computational tools developed in this research, and aid in a growing atlas of results from which future work could hypothesize outcomes pairing well-characterized motifs.

7.2 Modular networking and expansion techniques

Finally, in Chapter 6, use of the three-node local network outcomes as building blocks to connect and describe larger networks was introduced. This required an extension of the analytical tools and visualization approaches employed up to that point to extend the phase-reduction and return map techniques for application in higher-dimensional settings. The methods employed in Chapters 2-5 readily lend themselves to analysis of 4-node networks in which only one or two connections are added, with an example of 3-D visualization of such a network demonstrated there. For further circuit connectivity, however, this approach may be inadequate and additional methods of

visualization would be required in order to rapidly span and evaluate parameter changes within more complex networks.

Work in this area moved directly to connection of two three-cell motifs to each other, as any results obtained here for release case outcomes would immediately apply to 3+1 circuit connectivity for mono-biased coupling of the two networks. If either a single release-case cell or one cell from another release-case 3-cell motif drives only a single cell in the other 3-cell local network without reciprocal inhibition, the effects observed will be identical for purely traveling wave rhythmicity in the driving network. In such a case, the fully oscillatory distribution of bursting will maintain the original period of a single inherently bursting release mechanism cell. This may change, however, if the driving network is in pacemaker rhythmicity and is not begun with the connected cells in-phase. This type of outcome was not discussed in this work but presents another area in which interesting outcomes might be observed.

As an extension to using the original visualization approach, a method is introduced for beginning one network with fixed initial conditions while spanning the full bi-parametric (g_{ij} , I_{app})-space of initial conditions for the other network. Use of phase-basin return maps was required, as phase-lag return maps would describe trajectories crossing over one another and be difficult to interpret. Since one network begins with fixed initial conditions, its phase-basin map represented instead the final outcome to which it converged from that initial position, given the corresponding (Δ_{12} , Δ_{13}) initial condition in the other network. This approach proved useful in describing initial results of introducing mono-biased and pairwise-biased inhibitory coupling of cells 1 and 4 between two networks, a summary of results for connectivity explored can be seen in Table 7.2. Results from these examples validated the capability of 3-node network outcomes to hypothesize rhythm shifts induced by coupling within a larger network framework. Further exploration of this type of

coupling was not described here, either with mixed three-node networks or with additional coupling between networks, but indicates similar outcomes while underlining the need for additional tools to effectively span all possible parameter combinations.

Table 7.2 Summary of coupled symmetric 3-node network outcomes

Circuit Diagram	Figures	Initial Rhythmicity	[456]-ICs	Rhythm Outcome with Increasing g_{ij}
	6.4-6.5 Not shown	Pentarhythmic (O) increasing g_{ij}	BPM, $\Delta_{14}=0$ CTW, $\Delta_{14}=0$	[123] TWs diminish, [456] unaffected [123] TWs diminish, [456] unaffected
	6.7	Pentarhythmic (R) weak coupling	BPM, $\Delta_{14}=0$ CCTW, $\Delta_{14}=0$	[123] TWs eliminated, [456] remains BPM [123] TWs diminish, [456] BPM/GPM split
	6.9	Pentarhythmic (R) moderate coupling	BPM, $\Delta_{14}=0$ CTW, $\Delta_{14}=0$ CTW, $\Delta_{14}=0.5$	[123] 5 complex, [456] BPM/CTW/Q [123] TW↓ PM↑, [456] RPM /GPM/CCTW [123] TW↓ PM↑, [456] GPM /CCTW
	6.11	Pentarhythmic (R) strong coupling	BPM, $\Delta_{14}=0$ CTW, $\Delta_{14}=0$ CTW, $\Delta_{14}=0.5$	[123] 5 complex/Q, [456] BPM/CTW/Q [123] 5 complex/Q, [456] RPM/GPM/CTW/ CCTW [123] TW↓ PM↑, [456] GPM/CTW
	6.13	Pentarhythmic (O)	CTW, $\Delta_{14}=0$	[123] TW↑ PM↓, [456] GPM /RPM/CTW/CCTW
	6.15 6.16 6.17	PM-only (R), $g_{elec} \uparrow$	BPM, $\Delta_{14}=0$ CTW, $\Delta_{14}=0$ CTW, $\Delta_{14}=0.5$	[123] complex PM, [456] BPM [123] complex PM, [456] complex PM/GPM↓ [123] complex PM, [456] GPM/RPM complexity↑
	6.19 6.20	TW-only (O), $g_{elec} \uparrow$	CTW, $\Delta_{14}=0$ CTW, $\Delta_{14}=0.5$	[123] complex TW, [456] CTW [123] complex TW, [456] CTW-complex CTW /CCTW
	6.22 6.23 6.24	Penta (R), $g_{elec} \uparrow$	BPM, $\Delta_{14}=0$ CTW, $\Delta_{14}=0$ CTW, $\Delta_{14}=0.5$	[123] TW↓ PM↑, [456] BPM /CTW↑ [123] 5 complex, [456] complex RPM/CTW [123] 5 complex, [456] GPM/RPM↑/CCTW↓
*Systems either Oscillatory (O) or Release (R), Q represents quiescence, BPM/GPM/RPM for pacemakers, bold for dominant rhythm				

Coupling of three-node networks was then described using electrical coupling, where relative synchronicity was generally achieved rapidly between connected cells even with moderate coupling strength, full synchronicity induced with increasing strength. Pairing of symmetric motifs within both release case and fully oscillatory systems was examined, with examples of local networks capable of producing pacemaker-only, traveling wave only, or full penta-rhythmicity initially. The effect of electrical coupling is typically significant but highly dependent on whether the connected cells begin in-phase or anti-phase, as electrical coupling will push them eventually

to synchronicity. These effects are summarized in Tables 7.2 and 7.3, where circuits are shown with all initial conditions and final outcomes. In all cases, rhythm outcomes tended to stabilize with increasing coupling strength, a trend which continued as well in the paired symmetric-clockwise motifs, with surprising capability to drive a network which did not even have the circuit capability by itself to produce a specific rhythm to do so when paired.

Table 7.3 Summary of coupled symmetric-clock 3-node network outcomes

Circuit Diagram	Figures	Initial Rhythmicity	[456]-ICs	Rhythm Outcome with Increasing g_{ij}
	6.26	TW-only/CTW (O) increasing g_{elec}	BPM, $\Delta_{14}=0$	[123] TWs/BPM → PMs/TWs ↓ [456] CTW
	6.27		CTW, $\Delta_{14}=0$	[123] TWs/BPM → PMs/TWs ↓ [456] CTW
	6.28		CTW, $\Delta_{14}=0.5$	[123] TWs/PMs → PMs/TWs ↓ [456] CTW/CCTW/RPM
	A.13	TW-only/CTW (O) increasing g_{elec}	BPM, $\Delta_{14}=0$	[123] TWs→ PMs/CTW/CCTW [456] CTW→ CTW/CCTW
	A.14		CTW, $\Delta_{14}=0$	[123] TWs→ PMs/CTW [456] CTW
	A.15		CTW, $\Delta_{14}=0.5$	[123] TWs/BPM/GPM → BPM/GPM/CTW/CCTW [456] CTW/CCTW/GPM
	A.18	TW-only/CTW (O) increasing g_{elec}	BPM, $\Delta_{14}=0$	[123] TWs→ CTW/CCTW/RPM → CTW/CCTW [456] CTW→ CTW/CCTW
	A.19		CTW, $\Delta_{14}=0$	[123] TWs→ CTW/CCTW/RPM → CTW [456] CTW→ CTW/GPM → CTW
	A.20		CTW, $\Delta_{14}=0.5$	[123] TWs→ CTW/CCTW/GPM → CTW/CCTW [456] CTW/CCTW/GPM → CTW/CCTW
*Oscillatory (O) systems, BPM/GPM/RPM for pacemakers, bold for dominant rhythm, <i>italics</i> for synchronous IC outcomes				

This stabilizing behavior with increasing electrical coupling strength was used to explore the effect of inducing immediate synchronicity through very strong coupling of cells 1 and 4, at 10-20 times the strength of previous results shown. Results validated that no further rhythm changes could be induced with any further increase in electrical connectivity. In each case, cells 1 and 4 were immediately driven to in-phase synchronicity, with $\Delta_{14} = 0$, and behaved as a single unit with no time differentiation between waveform observations of either cell, permitting these cells to

effectively be treated as a single cell in a novel method for node-reduction. This result indicates the capability to extend the three-node outcomes, comprising most this research, not only to larger networks of multiplicity three, but also to networks of almost any dimension. This outcome may be valuable in bridging the gap between well-known and characterized local dynamics of two- or three-cell networks to the behavioral outcomes driven by much larger networks, and is a first step in using this and other research in modular networking to construct larger networks.

7.3 Future extensions and applications

A primary focus of this work has been to introduce methods to rapidly and cohesively sweep parameters describing polyrhythmicity and bifurcation transitions in three-node networks, with a specific eye toward applying these results to describe outcomes in natural settings where these behaviors are observed. While the results are interesting in themselves, the goal of this research is to create a framework from which both hypothesis generation for experimental work and construction of large modular networks can be extended, aiding studies bridging the gap between small local network rhythms and large-scale behavioral outputs in biological systems. Some of these applications are immediately available, with experimental results validating outcomes observed in the three-node results discussed in this work. Two examples of this can be seen in Figure 7.2, where rhythm generation and bifurcation within either a mono-biased or pairwise-biased three-node motif may effectively capture rhythmicity like that of the pyloric stomatogastric circuit. By first eliminating the g_{23} connection in the left panels, to create what could be viewed as the zero-state mono-biased case, a system exists in which the blue-black saddle and the black fixed point are in proximity to one another and prepared to undergo further saddle-node bifurcation with an additional parameter change. By then decreasing the coupling strength from cell 3 to cell 2, g_{32} , this saddle and node converge and obliterate one another, as the blue pacemaker takes over the

original basin of attraction of the clockwise traveling wave. With increasing g_{32} strength, the blue-green saddle and green FP node move together and undergo an additional saddle-node bifurcation in which blue acquires both basins of initial condition space. Finally, at strong g_{32} coupling, the remaining traveling wave collapses and the blue pacemaker dominates nearly all the $(\Delta_{12}, \Delta_{13})$ -space of initial conditions. The pattern here now appears similar to the specific phase-lag combination observed for rhythms in the pyloric STG circuit. This is of course an example of additional asymmetry not present in bifurcation diagrams shown in earlier chapters, but mimics the dual-connection asymmetry mentioned for several specific examples in Chapter 5, and represents an additional key motif that might be added to the collection of key motifs in future

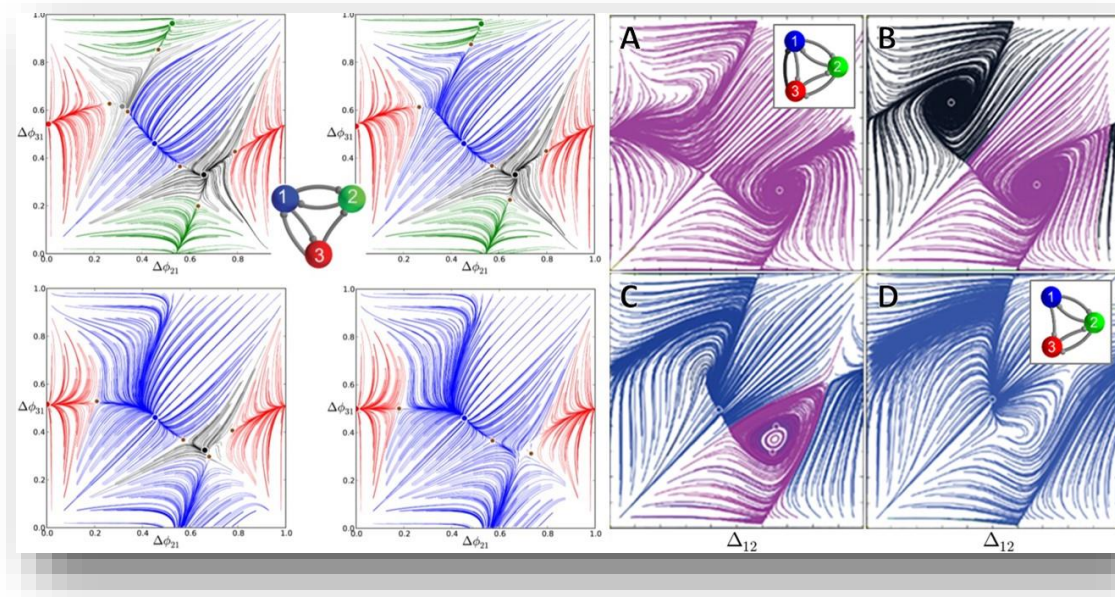


Figure 7.4 Hypothesized pyloric replication

Left: Poincaré return maps for phase-lags in an inhibitory HH-model CPG, all five rhythms observed. As single connection g_{32} is eliminated, 3 of the 5 fixed points disappear through a series of saddle-node bifurcations, resulting in (D) with a dominant blue PM, like the rhythm observed in the pyloric STG circuit [from 18]. Right: Similar outcome observed with different parameters using gFN-model. Beginning with strong g_{31} connection, in which only the CCTW rhythm is possible, decreasing g_{31} leads to emergence of CTW (B), which is then captured by the BPM rhythm (C), with only the BPM rhythm possible when the connection is removed entirely (D). Parameters: $I_{app} = 0.389$, $g_{ij} = 0.001$ except $g_{31} = 0.0016, 0.001, 0.0006$, and 0.

work. The example in the right panels shows similar transition to PM-only outcomes at different parameter values using the mono-biased motif described in this work and eliminating g_{31} .

Extensions of this approach for coupled networks can also be made, and in Figures 7.3 and 7.4 a description for using strong electrical coupling to use two of the well-characterized three-cell motifs to represent a 5-cell circuit is provided. Examination of the larger five-cell gastric network lends itself readily to decomposition into two key three-cell local networks, and in Figure 7.3 we observe how two subsets of three cells could each be considered either a mono-biased or a king-

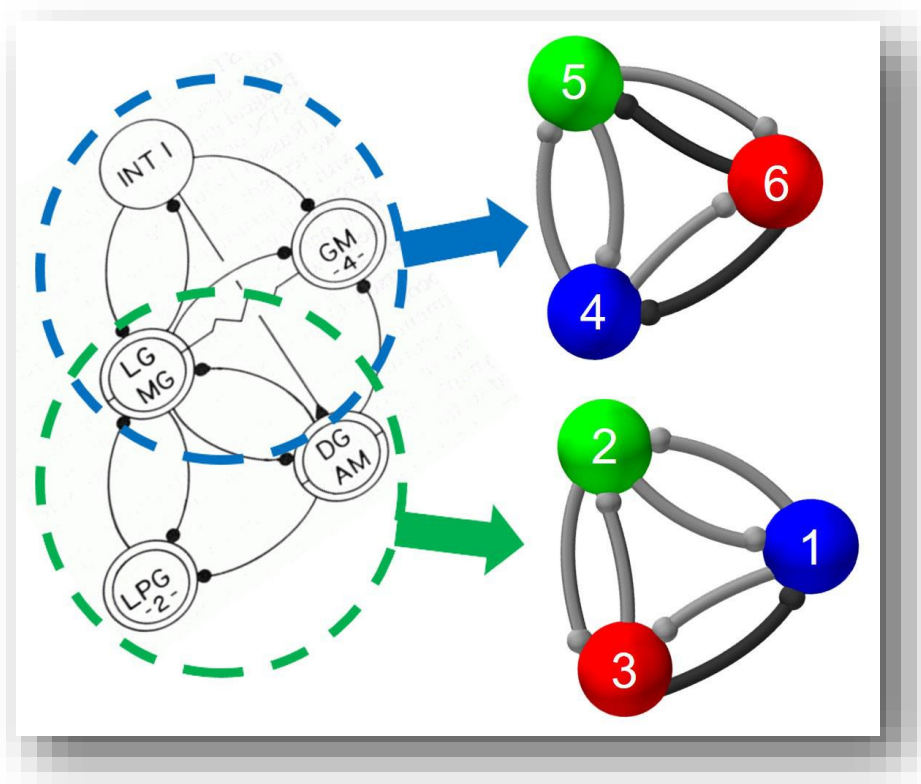


Figure 7.5 3-cell motif identification within the gastric network

The gastric network can be described in general terms as the coupling of two characterized three-node motifs: a mono-biased motif, removing the connection $g_{31} = 0$, and a king-of-the-mountain motif, removing the connections $g_{64} = g_{65} = 0$. These networks can be collapsed via strong electrical coupling reducing cells 2 and 4 into one effectively synchronous cell with outputs into both networks (Figure 7.6). Additional coupling is required to mimic the effect of the remaining connections and could be introduced stepwise (Figure 7.7).

of-the-mountain local network. By rotating and orienting the networks in the manner shown, we can maintain the local network relationships that permit direct use of results in Chapters 3-5. Each of these could be studied individually, and compared to experimental results as was done in the previous example, or as a cohesive network in which strong electrical coupling is used to collapse cell 2 of the left network onto cell 1 of the right network. This permits construction of an effective 5-node network of purely inhibitory connections which captures most of the circuit connectivity observed in the original network, and would represent a first step in transitioning from three-cell results to five-cell outcomes that can be validated experimentally. The effective larger network circuit achieved at this intermediate step can be seen in Figure 7.6.

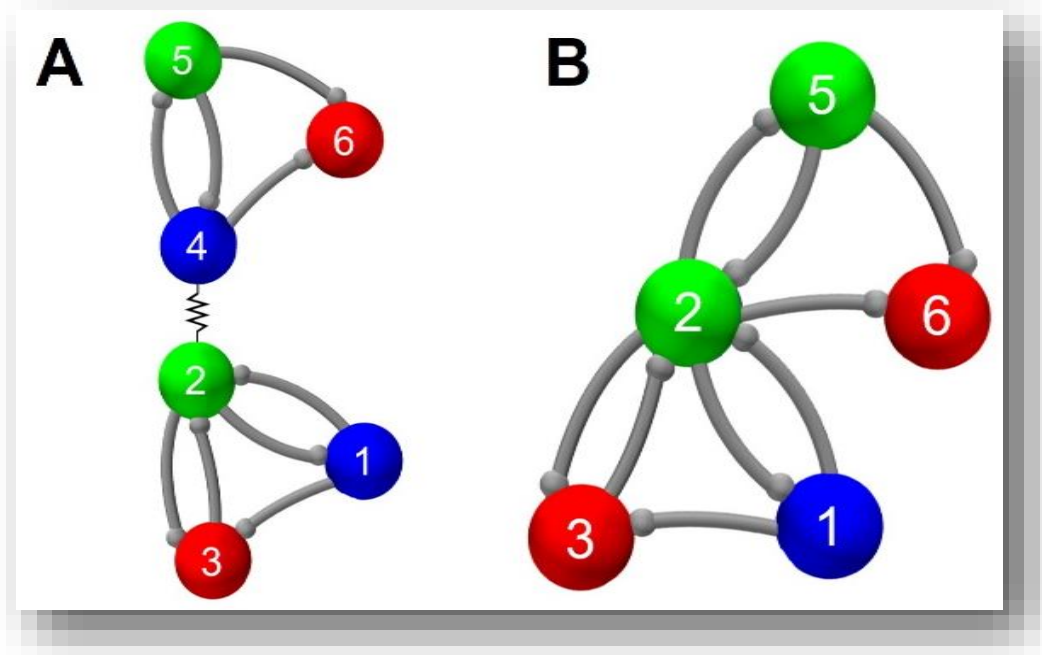


Figure 7.6 Effective 5-cell configuration with strong electrical coupling
 Creation of a fully inhibitory 5-node network approximating a first step toward the full gastric network, using very strong electrical coupling to collapse a node from a king-of-the-mountain local network, with $g_{65} = g_{64} = 0$, onto a node in a mono-biased local network, with $g_{31} = 0$. Examination of extended inhibitory networks in this fashion is a logical next step in using outcomes of this research toward applications in larger circuits observed in nature.

Further research using this approach could characterize this 5-node network, as was done in Chapter 6, in order to both validate this experimentally, if the other missing connections can someday be turned off in the laboratory setting with chemical or electrical interaction, and to hypothesize changes in rhythmicity observed by introducing one or more of the missing connections. An approach to this that would maintain the structure of this research would first introduce the inhibitory connection from cell 1 of the left network to cell 3 of the right network. Secondly, introduction of the electrical connection between cells 1 and 3 of the right network would be the logical next step, if practically feasible. And finally, introduction of excitatory coupling, which has not been done in this research, from cell 2 of the right network onto cell 1 of the left network (Figure 7.7). This is of course a simplistic approach and assumes equal connectivity of all inhibitory connections, and additional steps would be required in transitions to the full network if any asymmetry exists in these.

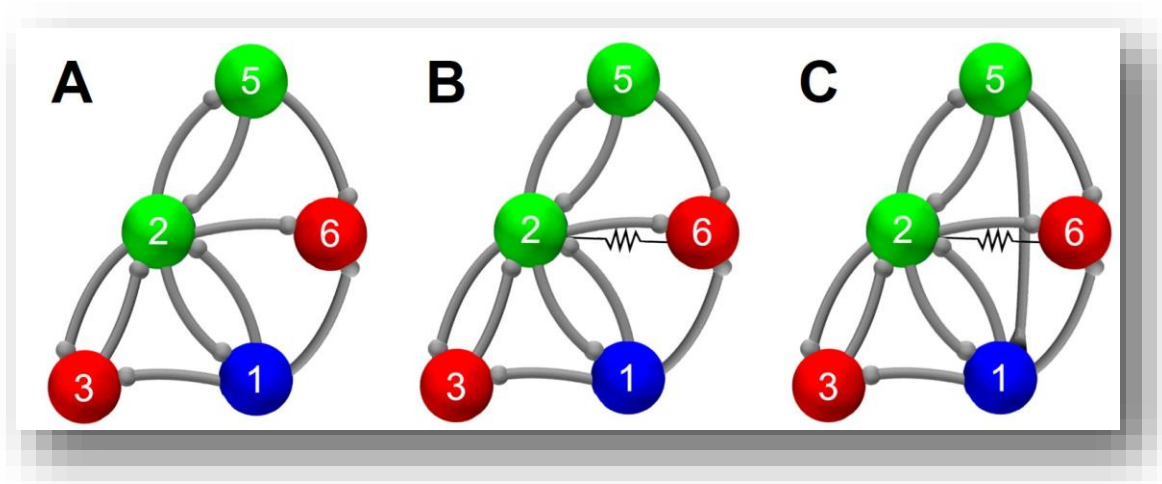


Figure 7.7 Stepwise approach to analysis of 5-node gastric network

Outcomes using well-characterized three-node networks, and observed results of strong electrical coupling of mono-biased and KOM networks could be extended to more accurately approximate the full gastric circuit by stepwise introduction of (A) first an additional inhibitory connection between cells 1 and 6, g_{16} , followed by (B) electrical coupling of cells 2 and 6, $g_{elec,26}$ and finally (C) an excitatory connection from cell 5 to cell 1, $g_{exc,51}$.

In addition to this specific application of construction of a larger network using a modular approach employing well-characterized three-node outcomes, another next step for future research would be scaling this modular networking methodology up on a large scale. Three-node motifs could be connected to create vast networks of interconnected cells, using fully symmetric, fully fixed asymmetric, or mixed networks of multiple three-node motifs. There is no limit to the network size to which this extension could be made, but additional restrictions may be required to facilitate analysis and create realistic networks in which some size restriction or other boundary conditions may exist. An example of two frameworks in which boundary conditions of this sort could be employed can be found in Figure 7.7, where either a torus or flat-cube approach to introducing both network boundaries and additional cyclical interaction are each described. In torus network connectivity, where a flat network of cells may be connected cyclically both horizontally and vertically and create a doughnut shaped relationship, appearing similar to the way in which we

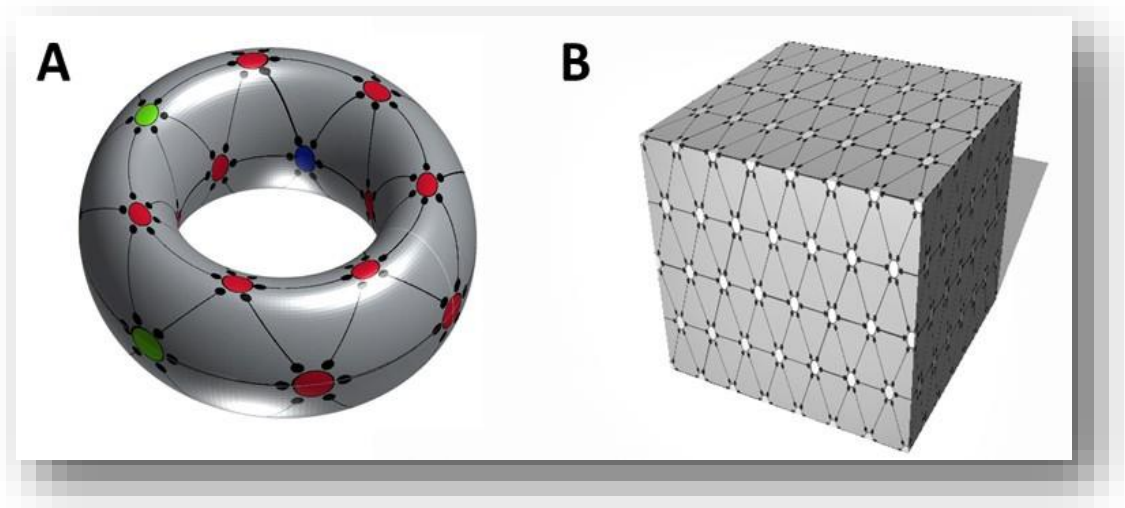


Figure 7.8 Sample boundary conditions in modular networking

Example of (A) torus network connectivity, where a flat network of cells may be connected cyclically both horizontally and vertically and create a doughnut shaped relationship, and (B) flat cubic network connectivity, where a flat network of cells may be folded and connected into a hollow cube upon the surface of which network activity occurs.

unfolded the phase-return map torus to create 2-D return maps in Chapter 2. In flat cubic network connectivity, a flat network of cells may similarly be folded and connected into a hollow cube upon the surface of which network activity is observed. This approach could also be made three-dimensional, with interior three-node motifs connecting the exterior network boundaries in more complex ways. In any of these applications, additional tools would be required to aid in visualization of outcomes, and some thought may be required to optimize computational performance with ever-increasing network size.

Finally, it is important to point out that this research emphasized outcomes in networks of heterogeneous cells, in which all cells employed the same cellular capabilities, and it would be interesting to observe the outcomes of mixing cells with differing intrinsic mechanisms. In particular, as opposite trends were observed for outcomes in the bifurcations of three-node networks in either the release or escape ranges of I_{app} , it would be interesting to connect mixed networks of these cells to describe other potential rhythmicity outcomes. Other parameter changes or additions, influencing the nature of the nullclines or the speed of the synapses could also dramatically influence outcomes and would be of interest in future work. Natural networks of cells within animals are typically comprised of many kinds of cells and connections with differing capabilities and mechanisms, and the next logical step would be to begin systematic observation of outcomes achievable when studying such mixed networks.

REFERENCES

- [1] T Bal, F Nagy, and M Moulins. The pyloric central pattern generator in crustacea: a set of conditional neural oscillators. *Journal of Comparative Physiology A*, 163:715–727, 1988.
- [2] RJ Calin-Jageman, MJ Tunstall, BD Mensh, PS Katz, and WN Frost. Parameter space analysis suggests multi-site plasticity contributes to motor pattern initiation in tritonia. *J. Neurophysiol.*, 98:2382, 2007.
- [3] WN Frost and PS Katz. Single neuron control over a complex motor program. *Proc.Nat.Acad. Sc.*, 93(1):422–426, 1996.
- [4] PS Katz and SL Hooper. Invertebrate central pattern generators. In G North and R R. Greenspan, editors, *Invertebrate Neurobiology*. Cold Spring Harbor Laboratory Press, NY, New York, 2007.
- [5] WB Kristan, RL Calabrese, and WO Friesen. Neuronal control of leech behavior. *Prog. in Neurobiology*, 76:279, 2005.
- [6] E Marder and RL Calabrese. Principles of rhythmic motor pattern generation. *Physiol Rev.*, 76(3):687–717, July 1996.
- [7] JM Newcomb, A Sakurai, JL Lillvis, CA Gunaratne, and PS Katz. Homology and homoplasy of swimming behaviors and neural circuits in the nudipleura (mollusca, gastropoda, opisthobranchia). *Proc. Natl. Acad. Sci.*, 109(1):10669–76, 2012.
- [8] A Sakurai, JM Newcomb, JL Lillvis, and PS Katz. Synaptic patterning of left-right alternation in a computational model of the rodent hindlimb central pattern generator. *Curr. Biol.*, 21:1036, 2011.
- [9] A Selverston, editor. *Model Neural Networks and Behavior*. Springer, Berlin, 1985.

- [10] IV Belykh and AL Shilnikov. When weak inhibition synchronizes strongly desynchronizing networks of bursting neurons. *Phys Rev Lett*, 101:078102, Aug 2008.
- [11] J Best, A Borisyuk, J Rubin, D Terman, and M Wechselberger. The dynamic range of bursting in a model respiratory pacemaker network. *SIAM J. Appl. Dyn. Syst.*, 4:1107–1139, 2005.
- [12] RL Calabrese, BJ Norris, A Wenning, and TM Wright. Coping with variability in small neuronal networks. *Integrative and Comparative Biology*, 51(6):845–855, 2011.
- [13] H Koch, AJ Garcia, and JM Ramirez. Network reconfiguration and neuronal plasticity in rhythm-generating networks. *Integrative and Comparative Biology*, 51(6):856–868, 2011.
- [14] E Marder. Neuromodulation of neuronal circuits: back to the future. *Neuron*, 76:1, 2012.
- [15] AL Shilnikov, R Gordon, and I Belykh. Polyrhythmic synchronization in bursting networking motifs. *Chaos*, 18(3):037120, Sep 2008.
- [16] WE Sherwood, R Harris-Warrick, and JM Guckenheimer. Synaptic patterning of left-right alternation in a computational model of the rodent hindlimb central pattern generator. *J Comp Neuro*, 30(2):323, 2010.
- [17] J Wojcik, R Clewley, and AL Shilnikov. Order parameter for bursting polyrhythms in multifunctional central pattern generators. *Phys Rev E*, 83:056209–6, 2011.
- [18] J Wojcik, R Clewley, J Schwabedal, and AL Shilnikov. Key bifurcations of bursting polyrhythms in 3-cell central pattern generators. *PLoS ONE*, 9(4), 2014.
- [19] R Milo, S Shen-Orr, S Itzkovitz, N Kashtan, D Chklovskii, and U Alon. Network motifs: Simple building blocks of complex networks. *Science*, 298(5594):824–827, 2002.
- [20] Sporns and R Kötter. Motifs in brain networks. *PLoS Biol*, 2(11):e369, 2004.

- [21] MI Rabinovich, P Varona, AL Silverston, and HD Abarbanel. Dynamical principles in neuroscience. *Reviews of Modern Physics*, 78(4):1213–1265, 2006.
- [22] AGM Bulloch and NI Syed. Reconstruction of neuronal networks in culture. *Trends in Neurosciences*, 15(11):422 – 427, 1992.
- [23] PS Katz. Tritonia swim network. *Scholarpedia*, 4(5):3638, 2013.
- [24] E Marder. Invertebrate neurobiology: Polymorphic neural networks. *Current Biology*, 4(8):752–754, 1994.
- [25] N Kopell and B Ermentrout. Chemical and electrical synapses perform complementary roles in the synchronization of interneuronal networks. *Proc Natl Acad, Sci* 101:15482–15487, 2004.
- [26] N Kopell. Toward a theory of modelling central pattern generators. In: Cohen A, Rossingol S, Grillner S, editors, *Neural Control of Rhythmic Movements in Vertebrates*, New York: Wiley, 1988.
- [27] F Skinner, N Kopell, and E Marder. Mechanisms for oscillation and frequency control in networks of mutually inhibitory relaxation oscillators. *Comput Neurosci* 1: 69, 1994.
- [28] WB Kristan. Neuronal decision-making circuits. *Curr Biol*, 18:R928–R932, Oct 2008.
- [29] KL Briggman and WB Kristan. Multifunctional pattern-generating circuits. *Annu Rev Neurosci*, 31:271–294, 2008.
- [30] A Sakurai and PS Katz. Distinct neural circuit architectures produce analogous rhythmic behaviors in related species. *Soc. Neurosci. Abstr.*, 37.918.04, 2011.
- [31] S Jalil, D Allen, J Youker, and AL Shilnikov. Toward robust phase-locking in melibe swim central pattern generator models. *J. Chaos*, 6:046105–15, 2013.

- [32] AA Prinz, V Thirumalai, and E Marder. The functional consequences of changes in the strength and duration of synaptic inputs to oscillatory neurons. *The Journal of neuroscience*, 23(3):943–954, 2003.
- [33] AA Prinz, D Bucher, and E Marder. Similar network activity from disparate circuit parameters. *Nature neuroscience*, 7(12):1345–1352, 2004.
- [34] A Sakurai, AN Tamvacakis, PS Katz. Hidden synaptic differences in a neural circuit underlie differential behavioral susceptibility to a neural injury. *eLife* 10.7554/eLife.02598, 2014.
- [35] E Marder and D Bucher. Central pattern generators and the control of rhythmic movements. *Current Biology*, 11(23):R986-96, 2001.
- [36] D Alaçam and AL Shilnikov. Making a swim central pattern generator out of latent parabolic bursters. *Bifurcation and Chaos* 25(7), 1540003, 2015.
- [37] AI Selverston, DF Russell, JP Miller, and DG King. The stomatogastric nervous system: Structure and function of a small neural network. *Progress in Neurobiology*. 7(3):215-246, 1976.
- [38] RM Harris-Warrick and BR Johnson. Checks and balances in neuromodulation. *Frontiers in Behavioral Neuroscience*, 4:47, July 2010.
- [39] JT Schwabedal, DE Knapper, AL Shilnikov. Qualitative and Quantitative Stability Analysis of Penta-rhythmic Circuits, *Nonlinearity* 29:3647-3676, 2016
- [40] Luo, Dingjun (1997). *Bifurcation Theory and Methods of Dynamical Systems*. World Scientific. p. 26. ISBN 981-02-2094-4.
- [41] Steven Strogatz, *Non-linear Dynamics and Chaos: With applications to Physics, Biology, Chemistry and Engineering*, Perseus Books, 2000.

- [42] LP Shilnikov, AL Shilnikov, DV Turaev, and LO Chua. *Methods of Qualitative Theory in Nonlinear Dynamics. Parts I & II*, World Scientific, 2001.
- [43] YA Kuznetsov. *Elements of Applied Bifurcation Theory*, Springer, 3rd edition, 2004.
- [44] AA Andronov, EA Leontovich, II Gordon, and AG Maier. *Theory of Bifurcations of Dynamical Systems on a Plane*. Israel Program Sci. Transl, 1971.
- [45] EM Izhikevich. *Dynamical Systems in Neuroscience: The Geometry of Excitability and Bursting*. The MIT Press, 2007.
- [46] S Wiggins. *Introduction to Applied Nonlinear Dynamical Systems and Chaos*, Springer-Verlag, 1990.
- [47] F Dercole and S Rinaldi. *Dynamical Systems and Their Bifurcations*. Chapter in *Advanced Methods of Biomedical Signal Processing*, eds. S Cerutti & C Marchesi, IEEE-Wiley Press, New York, NY, 2011.
- [48] D Chik, S Coombes, and ZD Wang. Clustering through postinhibitory rebound in synaptically coupled neurons. *Physical Review E* 70:011908, August 2004.
- [49] MD Binder, N Hirokawa, and U Windhorst, editors. *Encyclopedia of Neuroscience*, Springer Berlin Heidelberg, 2009.
- [50] JD Angstadt, JL Grassmann, KM Theriault, and SM Levasseur. Mechanisms of postinhibitory rebound and its modulation by serotonin in excitatory swim motor neurons of the medicinal leech. *J. Comp. Physiol. A Neuroethol. Sens. Neural. Behav. Physiol.* 191(8):715–32, August 2005.
- [51] DH Perkel and B Mulloney (July 1974). Motor pattern production in reciprocally inhibitory neurons exhibiting postinhibitory rebound. *Science*. 185:181–3, 1974.

- [52] VD Gerasimov, PG Kostyuk, and VA Maiskii. Reactions of giant neurons to break of hyperpolarizing current. *Fed. Proc. Transl. Suppl*, 25:T438-T442, 1966.
- [53] AA Sharp, LF Abbott, and E Marder. Artificial Electrical Synapses in Oscillatory Networks. *Journal of Neurophysiology*, Vol. 67, No. 6, June 1992.
- [54] ER Kandel, JH Schwartz, and TM Jessell *Principles of Neural Science* (4th ed.). New York: McGraw-Hill, 2000.
- [55] JR Gibson, M Beierlein, and BW Connors. Functional properties of electrical synapses between inhibitory interneurons of neocortical layer 4. *J. Neurophysiol.* 93(1):467–80, January 2005.
- [56] D Purves, GJ Augustine, D Fitzpatrick, WC Hall, AS LaMantia, JO McNamara, and LE White. *Neuroscience* (4th ed.). Sinauer Associates. pp. 85–88, 2008.
- [57] D Somers and N Kopell. Rapid synchronization through fast threshold modulation. *Biol. Cybernetics* 68(5):393-407, 1993.
- [58] ST Alford and MH Alpert. A synaptic mechanism for network synchrony. *Frontiers Cellular Neuroscience*, 2014.
- [59] A Szucs, RD Pinto, MI Rabinovich, HD Abarbanel, and AI Selverston. Synaptic modulation of the interspike interval signatures of bursting pyloric neurons. *J. Neurophysiol.* 89(3):1363-77, March 2003.
- [60] AI Selverston and J Ayers. Oscillations and oscillatory behavior in small neural circuits. *Biol Cybern.* 95(6):537-54, December 2006.
- [61] E Marder. Motor pattern generation. *Curr. Opin. Neurobiol.* 10:691–698, 2000.

- [62] JR Cazalets, F Nagy, and M Moulins. Suppressive control of the crustacean pyloric network by a pair of identified interneuron. I. Modulation of the motor pattern. *J Neurosci* 10:448–457, 1990.
- [63] GS Cymbalyuk, Q Gaudry, MA Masino, and RL Calabrese. Bursting in leech heart interneurons: cell-autonomous and network-based mechanisms. *J Neurosci* 22:10580–10592, 2002.
- [64] M Denker, A Szucs, RD Pinto, HDI Abarbanel, and AI Selverston. A network of electronic neural oscillators reproduces the dynamics of the periodically forced pyloric pacemaker group. *IEEE Trans Biomed Eng* 52:792–799, 2005.
- [65] RC Elson and AI Selverston. Slow and fast synaptic inhibition evoked by pattern-generating neurons of the gastric mill network in spiny lobsters. *J Neurophysiol* 74:1996–2011, 1995.
- [66] M Gola and AI Selverston. Ionic requirements for bursting activity in lobster stomatogastric neurons 145:191–207, 1981.
- [67] DM Maynard and AI Selverston. Organization of the stomatogastric ganglion of the spiny lobster. IV. The pyloric system. *J Comp Physiol* 100:161–182, 1975.
- [68] JP Miller and AI Selverston. Mechanisms underlying pattern generation in lobster stomatogastric ganglion as determined by selective inactivation of identified neurons. IV. Network properties of pyloric system. *J Neurophysiol* 48:1416–1432, 1982.
- [69] JM Ramirez, AK Tryba, and F Pena. Pacemaker neurons and neuroonal networks: an integrative view. *Curr Opin Neurobiol* 14:665–674, 2004.
- [70] DW Richter and KM Spyer. Studying rhythmogenesis for breathing: comparison of in vivo and in vitro models. *TINS* 24:464–472, 2001.

- [71] JC Smith, RJ Butera, C Koshiya, C Del Negro, CG Wilson, and SM Johnson. Respiratory rhythm generation in neonatal and adult mammals: The hybrid pacemaker-network model. *Resp Physiol* 122:131–148, 2000.
- [72] C Soto-Trevino, KA Thoroughman, E Marder, and LF Abbott. Activity-dependent modification of inhibitory synapses in models of rhythmic neural networks. *Nat Neuro* 4:297–303, 2001.
- [73] X-J Wang and J Rinzel. Alternating and synchronous rhythms in reciprocally inhibitory model neurons. *Neural Comp* 4:844–897, 1992.
- [74] A Szücs, R Huerta, MI Rabinovich, and AI Selverston. Robust microcircuit synchronization by inhibitory connections. *Neuron* 61(3):439-53, February 2009.
- [75] K Matsuoka. Mechanisms of frequency and pattern control in the neural rhythms generators. *Biol Cybernetics* 1:1, 1987.
- [76] Canavier, DA Baxter, JW Clark, and JH Byrne. Multiple modes of activity in a model neuron suggest a novel mechanism for the effects of neuromodulators. *J Neurophysiol* 72: 872–882, 1994.
- [77] AA Prinz, C Billimoria, and E Marder. Alternative to hand-tuning conductance based models: construction and analysis of databases of model neurons. *JNeurophysiol* 90:3998–4015, 2003.
- [78] J Rubin and D Terman. Geometric analysis of population rhythms in synaptically coupled neuronal networks. *Neural Comput* 12:597–645, 2000.
- [79] F Skinner, L Zhang, J PerezVelazquez, and P Carlen. Bursting in inhibitory interneuronal networks: A role for gap-junctional coupling. *J Neurophysiol* 81:1274, 1999.

- [80] C Vreeswijk, L Abbott, and G Ermentrout. When inhibition not excitation synchronizes neural firing. *J Comput Neuroscience* 1:313–321, 1994.
- [81] S Jalil, IV Belykh, and AL Shilnikov. Fast reciprocal inhibition can synchronize bursting neurons. *Phys Rev E* 81:45201R, 2010.
- [82] S Jalil, IV Belykh, and AL Shilnikov. Spikes matter in phase-locking of inhibitory bursting networks. *Phys Rev E* 85:36214, 2012.
- [83] J Rubin and D Terman. Explicit maps to predict activation order in multiphase rhythms of a coupled cell network. *J, Math Neuroscience* 2:1–28, 2012.
- [84] IV Belykh, E de Lange, and M Hasler. Synchronization of bursting neurons: What matters in the network topology. *Phys Rev Lett* 94:188101, 2005.
- [85] AL Shilnikov, L Shilnikov, and D Turaev. On some mathematical topics in classical synchnization: a tutorial. *J Bifurcations and Chaos* 14:2143–2160, 2004.
- [86] W Kristan and R Calabrese. Rhythmic swimming activity in neurons of the isolated nerve cord of the leech. *The Journal of experimental biology* 65:643–68, 1976.
- [87] M Masino and R Calabrese. Phase relationships between segmentally organized oscillators in the leech heartbeat pattern generating network. *Journal of neurophysiology* 87:1572–85, 2002.
- [88] M Masino and R Calabrese. Period differences between segmental oscillators produce intersegmental phase differences in the leech heartbeat timing network. *Journal of neurophysiology* 87:1603–15, 2002.
- [89] D Lamb and R Calabrese. Neural circuits controlling behavior and autonomic functions in medicinal leeches. *Neural Systems & Circuits* 1:13, 2011.

- [90] P Ashwin, O Burylko, and Y Maistrenko. Bifurcation to heteroclinic cycles and sensitivity in three and four coupled phase oscillators. *Physica D* 237: 454–466, 2008.
- [91] AL Shilnikov. Complete dynamical analysis of an interneuron model. *J Nonlinear Dynamics* 68:305–328, 2012.
- [92] B Van der Pol and J Van der Mark. The Heartbeat Considered as a Relaxation Oscillation, and an Electrical Model of the Heart. *Phil. Mag.* 6:763, 1928.
- [93] L Mandelstam, N Papalexi, A Andronov, S Chaikin and A Witt. Report on recent research on nonlinear oscillations. NASA Technical Translation F-12:678, 1969.
- [94] A Andronov, A Vitt and S Khaikin. *Theory of Oscillators* (London: Pergamon) (tr. F. Immerzi from the Russian, first edition Moscow 1937), 1966.
- [95] R Fitzhugh. Impulses and Physiological States in Theoretical Models of Nerve Membrane. *Biophys. J.* 1(6):445-466, 1961.
- [96] J Hasty, F Isaacs, M Dolnik, D McMillen and JJ Collins. Designer gene networks: Towards fundamental cellular control. *Chaos* 11(1):207-220, 2001.
- [97] R Guantes and JF Poyatos. Dynamical Principles of Two-Component Genetic Oscillators. *PLoS Comput. Biol.* 2 e30, 2006.
- [98] M Brøns and R Kaasen. Canards and mixed-mode oscillations in a forest pest model. *Theor. Popul. Biol.* 77(4):238-42, 2010.
- [99] HA Braun, H Bade and H Hensel. Static and dynamic discharge patterns of bursting cold fibers related to hypothetical receptor mechanisms. *Pflugers Arch.* 386:1-9, 1980.
- [100] J Rinzel. *Ordinary Partial Differential Equations*. Berlin: Springer, pp 304–16, 1985.
- [101] J Rinzel. A formal classification of bursting mechanisms in excitable systems. *Math. Top. Popul. Biol. Morphogenesis Neurosci.* 71:267, 1987.

- [102] S Coombes and PC Bressloff, *Bursting: the Genesis of Rhythm in the Nervous System*. Singapore: World Scientific, 2005.
- [103] AL Shilnikov and G Cymbalyuk Transition between tonic spiking and bursting in a neuron model via the blue-sky catastrophe. *Phys. Rev. Lett.* 94 048101, 2005.
- [104] TJ Lewis and J Rinzel. Dynamics of spiking neurons connected by both inhibitory and electrical coupling. *J. Comput. Neurosci.* 14(3):283-309, 2003.
- [105] MV Bennett and RS Zukin. Electrical coupling and neuronal synchronization in the Mammalian brain. *Neuron* 41(4):495-511, 2004.
- [106] D McMillen, N Kopell, J Hasty and JJ Collins. Synchronizing genetic relaxation oscillators by intercell signaling. *Proc. Natl Acad. Sci. USA* 99(2): 679-84, 2002.
- [107] D Terman, JE Rubin and CO Diekman. Irregular activity arises as a natural consequence of synaptic inhibition, *Chaos* 23:4, 046110, 2013.
- [108] A Sakurai and PS Katz. State-, Timing-, and Pattern-Dependent Neuromodulation of Synaptic Strength by a Serotonergic Interneuron. *J. Neurosci.* 29(1):268-279, 2009.
- [109] AI Selverston. Invertebrate central pattern generator circuits. *Phil. Trans. R. Soc. B* 365:2329-2345, 2010.
- [110] PS Katz. Neural mechanisms underlying the evolvability of behavior. *Phil. Trans. R. Soc. B* 366:2086-2099, 2011.
- [111] E Marder, AE Tobin and R Grashow. How tightly tuned are network parameters? Insight from computational and experimental studies in small rhythmic motor networks. *Prog. Brain. Res.* 165:193-200, 2007.

- [112] C Günay and AA Prinz. Model calcium sensors for network homeostasis: Sensor and readout parameter analysis from a database of model neuronal networks. *J. Neurosci.* 30:1686-1698, 2010.
- [113] AN Pisarchik and U Feudel. Control of multistability. *Phys. Rep.* 540(4):167-218, 2014.
- [114] S Daun, JE Rubin and IA Rybak. Control of oscillation periods and phase durations in half-center central pattern generators: a comparative mechanistic analysis. *J. Comput. Neurosci.* 27:3, 2009.
- [115] JE Rubin, NA Shevtsova, GB Ermentrout, JC Smith and IA Rybak. Multiple rhythmic states in a model of the respiratory CPG. *J. Neurophysiol.* 101:2146-2165, 2009.
- [116] JR Dunmyre and JE Rubin. Optimal intrinsic dynamics for bursting in a three-cell network. *SIAM J. Appl. Dyn. Syst.* 9:154-187, 2010.
- [117] JTC Schwabedal, AB Neiman and AL Shilnikov. Robust design of polyrhythmic neural circuits. *Phys. Rev. E* 90:022715, 2014.
- [118] A Franci, G Drion, V Seutin and RA Sepulchre. Balance Equation Determines a Switch in Neuronal Excitability. *PLoS Comput. Biol.* 9:e1003040, 2013.
- [119] GB Ermentrout and DH Terman. *Mathematical Foundations of Neuroscience. Interdisciplinary Applied Mathematics Vol 35*, Springer, 2010
- [120] MG Rosenblum, AS Pikovsky and J Kurths. Phase Synchronization of Chaotic Oscillators. *Phys. Rev. Lett.* 76:1804, 1996.
- [121] WJ Beyn, A Champneys, E Doedel, W Govaerts, YA Kuznetsov and B Sandstede. *Handbook of Dynamical Systems, Volume 2*. London: Elsevier, p. 149, 2002.
- [122] M Golubitsky and I Stewart. Nonlinear dynamics of networks: the groupoid formalism. *Bull. Am. Math. Soc.* 43:305-364, 2006.

- [123] M Golubitsky, D Romano and Y Wang. Network periodic solutions: patterns of phase-shift synchrony. *Nonlinearity*, 25:1045-1074, 2012.
- [124] F Antoneli and I Stewart. Two-colour patterns of synchrony in lattice dynamical systems. *Int. J. Bifurcation Chaos* 16:559, 2006.
- [125] AP Dias and RC Paiva. Hopf bifurcation in coupled cell networks with Abelian symmetry. *Bol. Soc. Port. Mat.* 110–115, 2010.

APPENDICES

Appendix A: Supplementary Methods

Appendix A.1: Rhythm Pattern Identification

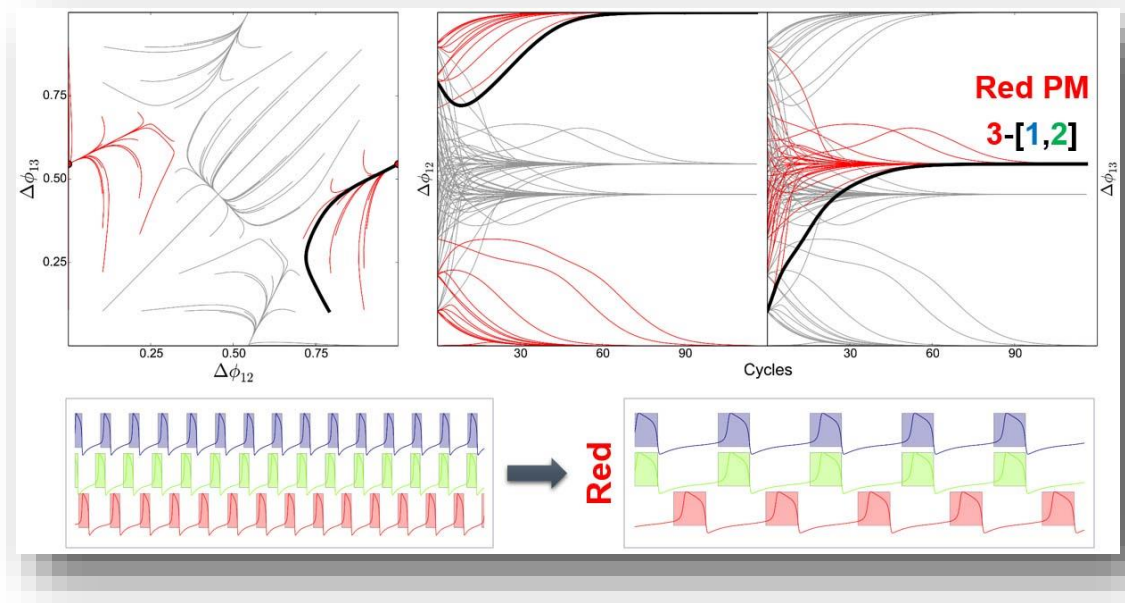


Figure A.1 Identification of red pacemaker using traces and phase lag
Detailed examination of convergence to the red PM rhythm, near $(\Delta\phi_{12}, \Delta\phi_{13}) \approx (0, 1/2)$, with full phase-lag return map in (A). Convergence of $\Delta\phi_{12}$ to zero is observed in (B) with similar convergence of $\Delta\phi_{13}$ to approximately 0.55 in this example. Traces in bottom panels show anti-phase relationship of the red cell against the blue and green ones. Color coding of traces converging to red PM rhythmicity, (3-[1,2]), in panels A-C is implemented to align with this outcome.

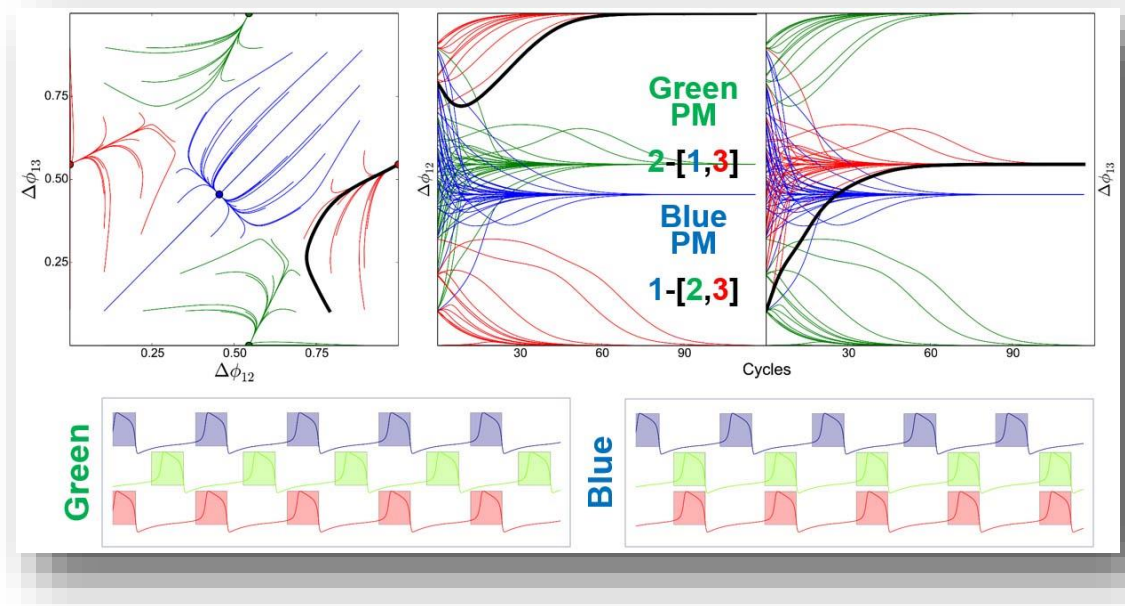


Figure A.2 Identification of remaining pacemakers using traces and phase lag

Detailed examination of convergence to remaining PM rhythms, near $(\Delta_{12}, \Delta_{13}) \approx (1/2, 1/2)$ and $(1/2, 0)$, with full phase-lag return map in (A). Convergence of both blue and green PM phase-lag Δ_{12} to approximately 0.45 and 0.55, respectively is observed in (B). Similar convergence of blue and green PM phase-lag Δ_{13} to approximately 0.45 and zero, respectively (C). Traces in bottom panels show anti-phase relationship blue and green PM activity, (2-[1,3]) and (1-[2,3]) respectively. Color coding of traces in panels A-C is implemented to align with all three PM outcomes observed.

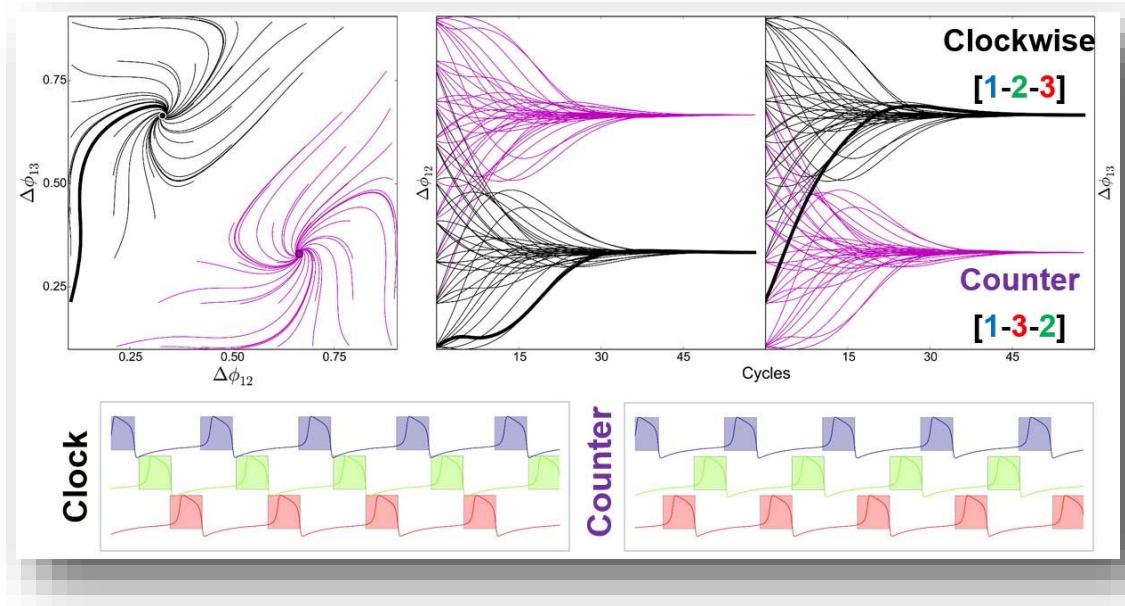


Figure A.3 Identification of traveling wave patterns using traces and phase lag
Detailed examination of convergence of TW rhythms, near $(\Delta_{12}, \Delta_{13}) \approx (1/3, 2/3)$ and $(2/3, 1/3)$, with full phase-lag return map in (A). Convergence of both black CTW and purple CCTW phase-lag Δ_{12} to approximately 0.33 and 0.66, respectively is observed in (B). Similar convergence of black CTW and purple CCTW phase-lag Δ_{13} to approximately 0.66 and 0.33, respectively (C). Traces in bottom panels show black clockwise, firing in (1-2-3) sequence, and purple counterclockwise, firing in (1-3-2) sequence, TW activity, respectively. Color coding of traces in panels A-C is implemented to align with both TW outcomes.

Appendix A.2: Sample Regime Identification in Release Bifurcation Diagrams

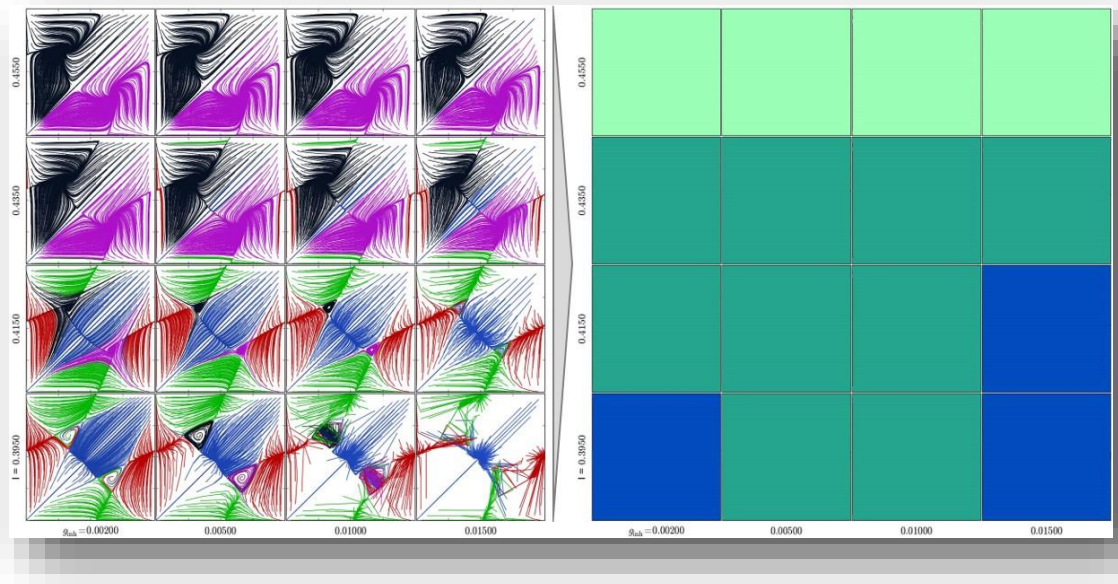


Figure A.4 Pattern identification in symmetric release networks

Example of classification of regime designation for phase-lag return maps within the release range of I_{app} for creation of bifurcation diagrams in the three-node symmetric motif. Poincaré return maps exhibiting only TW patterns, as seen in the top row of panels in the left-hand grid, are classified computationally as TW-only and coded with the light green color. Return maps exhibiting only PM patterns, as seen in the bottom left and right panels in the left-hand grid, are classified as PM-only and coded with the blue color. Return maps exhibiting both PM and TW patterns, as seen in the remaining panels in the left-hand grid, are classified as mixed PM/TW and coded with the dark green color. See Figure 2.5 for an extension of this logic for the full range of the bi-parametric (g_{ij}, I_{app}) -space explored for the symmetric motif, spanning I_{app} values from full release at $I_{app} = 0.39$ to full escape at $I_{app} = 0.6$.

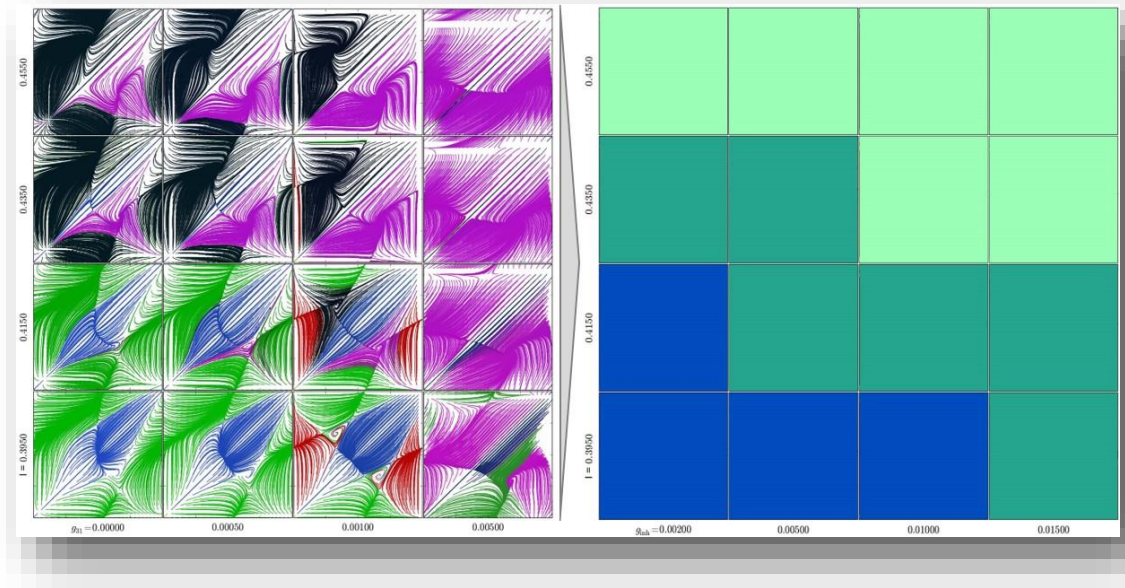


Figure A.5 Pattern identification in mono-biased release networks

Example of classification of regime designation for phase-lag return maps within the release range of I_{app} for creation of bifurcation diagrams in the three-node mono-biased motif. Poincaré return maps exhibiting only TW patterns, as seen in the top row of panels in the left-hand grid, are classified as TW-only and coded with the light green color. Return maps exhibiting only PM patterns, as seen in the bottom left panels in the left-hand grid, are classified as PM-only and coded with the blue color. Return maps exhibiting both PM and TW patterns, as seen in the remaining panels in the left-hand grid, are classified as mixed PM/TW and coded with the dark green color. See Figure 3.3 for an extension of this logic for the full range of the bi-parametric (g_{31}, I_{app}) -space, with $g_{ij} = 0.01$ otherwise, explored for the symmetric motif, spanning I_{app} values from full release at $I_{app} = 0.39$ to full escape at $I_{app} = 0.6$.

Appendix B: Supplementary Post-Inhibitory Rebound

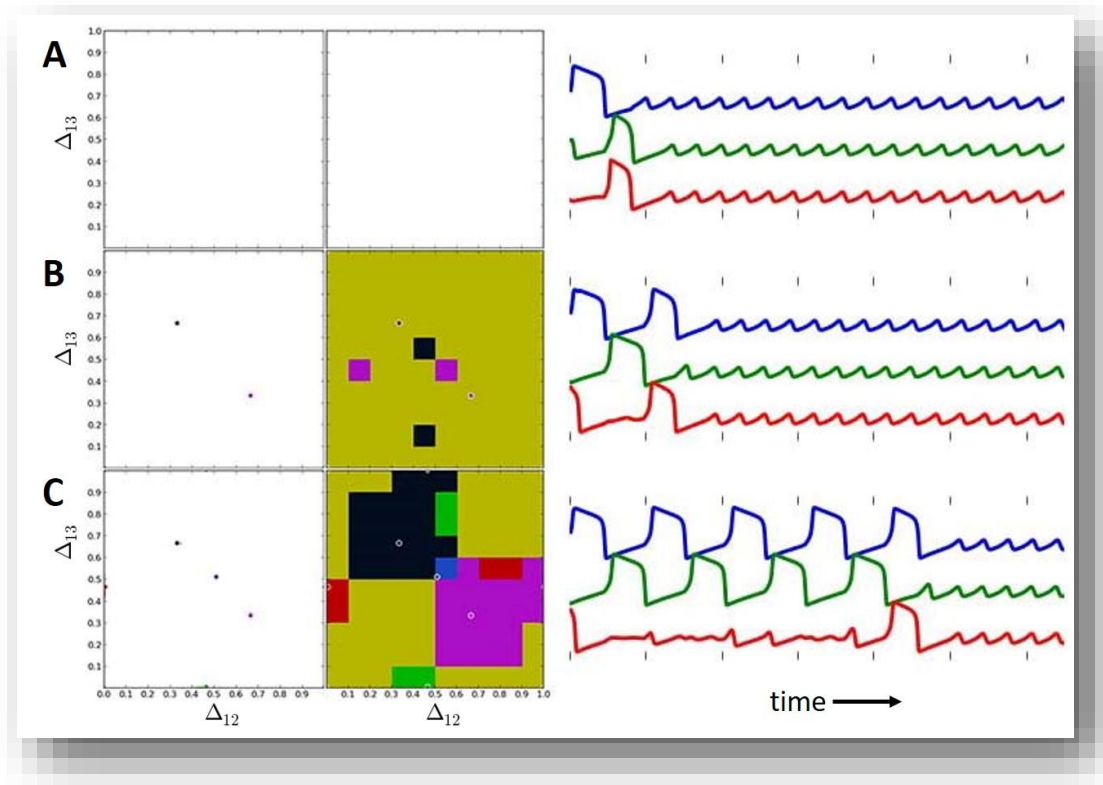


Figure A.6 PIR systems result in network silence for most conditions

Three sets showing the system with most or all initial condition space resulting in network silence. With increasing synaptic strength, small regions of persistent activity may emerge and grow transiently (traces for B and C). These fleeting periods of rhythmic behavior are described in Chapter 5, and recognized (tPM for transient PM activity that settles ultimately to quiescence). These periods also increase in length with increased coupling but may sometimes result in abnormal rhythmicity in which one cell may either remain quiescent, or rarely burst, relative to the others (C, and Figure 5.19).

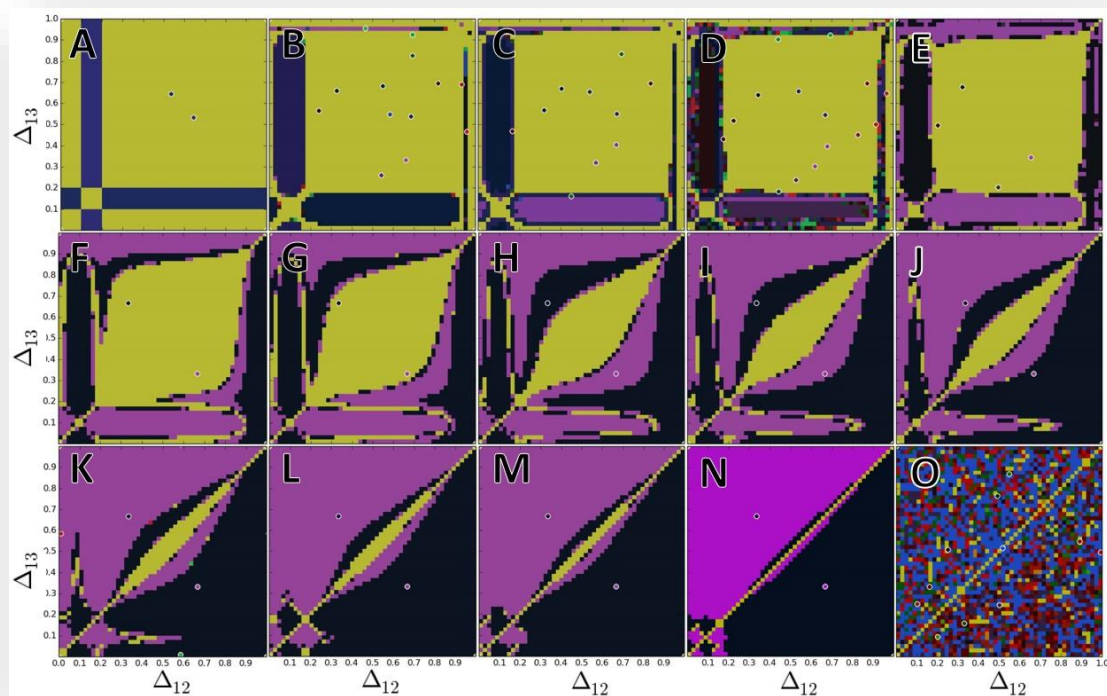


Figure A.7 Pattern transitions within the post-inhibitory rebound mechanism

Series of phase maps with synaptic strength slowly increasing in all connections. The series starts slightly too weakly connected to produce synaptic activity, gradually increasing to show the smooth emergence of both TW states and the growth of their basins of attraction until almost all of phase space is occupied by them. The last phase map shows the chaotic system that results if the synaptic strength is increased too much.

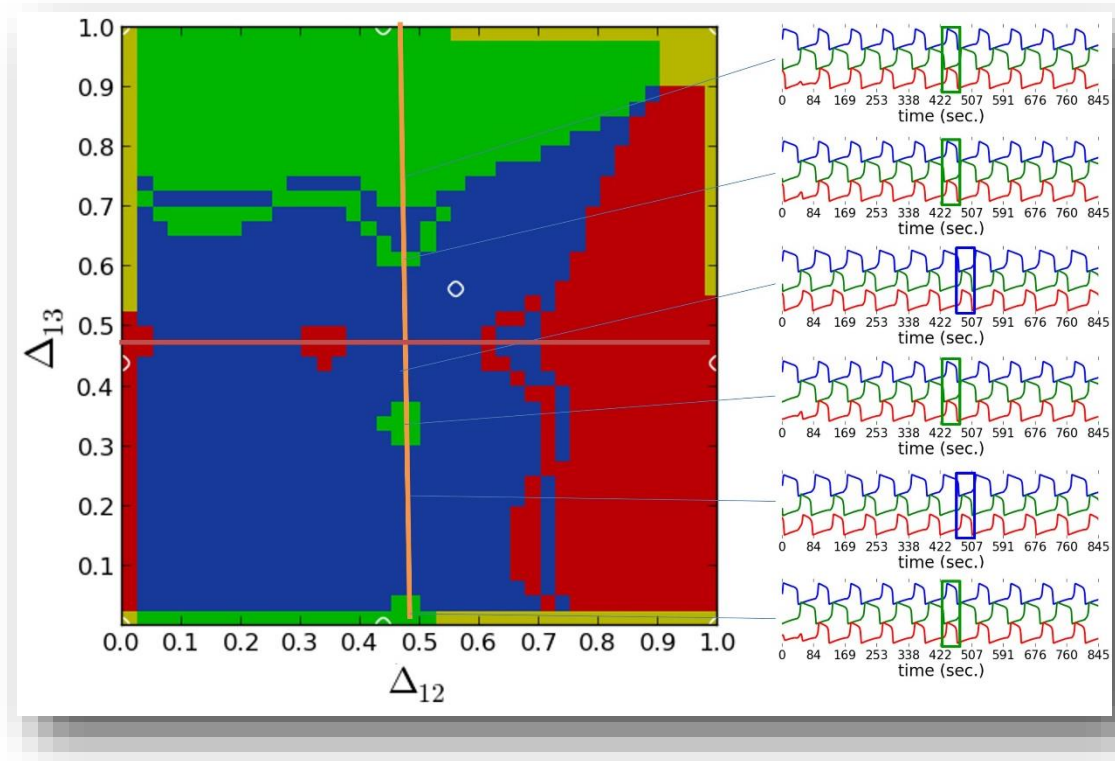


Figure A.8 Vertical traversal of PIR right walk case

For ICs beginning with cells 1 and 2 in anti-phase ($\Delta_{12} = 0.5$), beginning cell 3 at different relative positions can lead to distinctly different final rhythm outcomes. Traces on the right indicate that the system here will always converge to either green or blue PM behavior, emphasized with boxed examples of this rhythm. In general, this is directly a result of the system beginning in either of these two cases, with an interesting unexpected transition to green with the blue basin, or to blue within the green basin (shown as pockets of these colors within the larger basins of each).

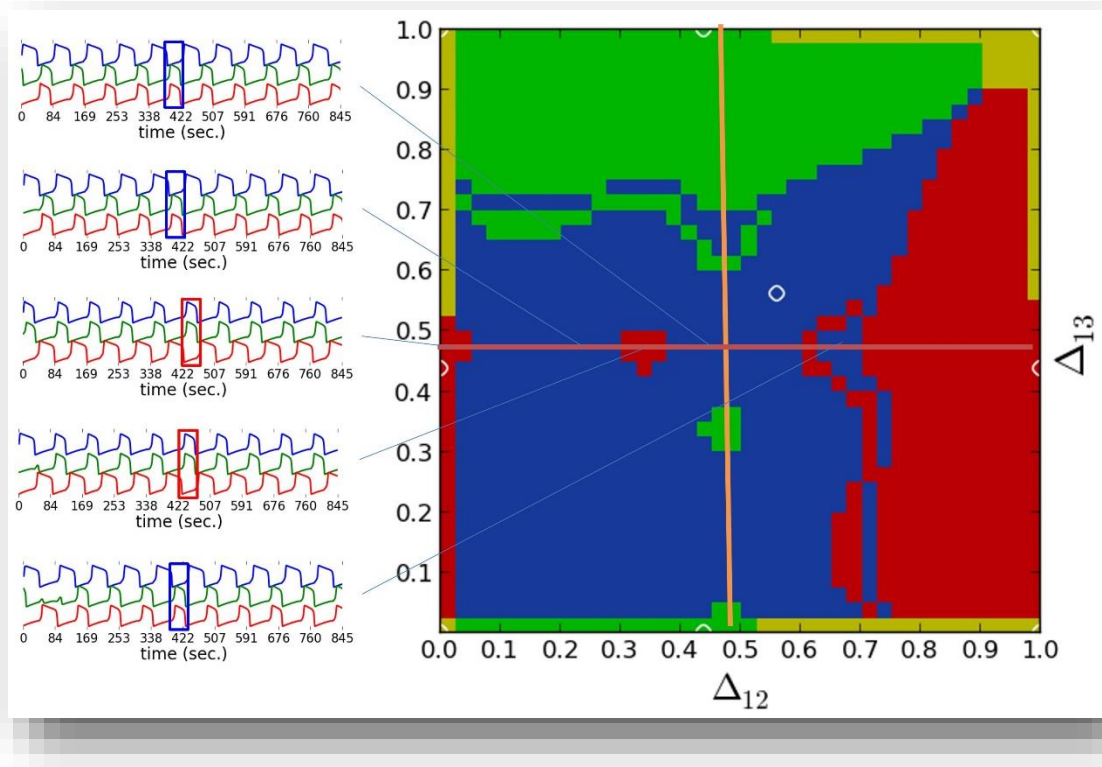


Figure A.9 Horizontal traversal of PIR right walk case

For ICs beginning with cells 1 and 3 in anti-phase ($\Delta_{13} = 0.5$), beginning cell 2 at different relative positions can lead to distinctly different final rhythm outcomes. Traces on the left indicate that the system here will always converge to either red or blue PM behavior, emphasized with boxed examples of this rhythm. In general, this is directly a result of the system beginning in either of these two cases, with an interesting unexpected transition to red with the blue basin, or to blue within the red basin (shown as pockets of these colors within the larger basins of each).

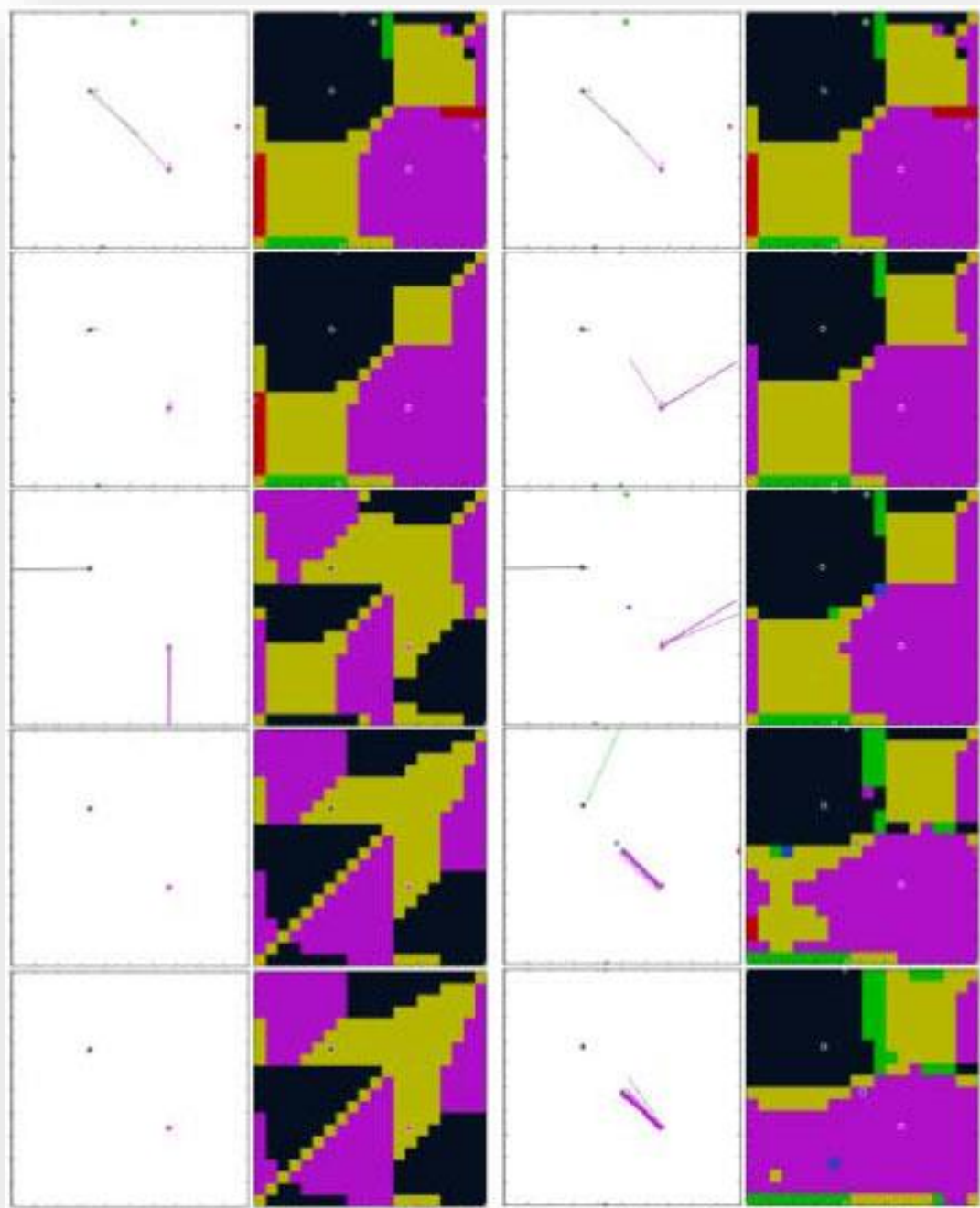


Figure A.10 Traveling wave dominance in fully oscillatory symmetric case PIR

Two sets showing the system with symmetric (left panels) or mono-biased (right panels) network connectivity with increasing coupling strength. Large regions of quiescent ICs are gradually acquired by increasing basins of attraction of the TWs in the symmetric case, while in the mono-biased system this is paired with regions of increased pacemaker behavior (green PM regions). Parameters: Symmetric with $g_{ij} = 0.07, 0.09, 0.12, 0.8, 1.5$; Mono-biased with $g_{ij} = 0.07$ except $g_{12} = 0.07, 0.09, 0.12, 0.4, 0.7$.



Figure A.11 Additional asymmetric motif results in PIR systems

Series of phase maps for asymmetric motifs with decreasing respective coupling strengths. At strong coupling strengths, distinct basins of rhythmic activity exist in all 4 motifs. With decreasing synaptic coupling, these basins diminish in size and become largely dominated by quiescent behavior. Strong coupling in all three systems favoring inhibition from cell 2, pairwise-biased, mono-biased, and KOM, all favor the red PM rhythm. The clockwise motif in this case behaves like release-escape systems in favoring CCTW rhythms at strong coupling, and CTW ones at weak. As in all PIR systems, regions of ICs always exist in which quiescent behavior remains at any coupling strength.

Appendix C: Supplementary Modular Networking

Appendix C.1: Doubly Electrically-Coupled Symmetric-Clock Hybrid

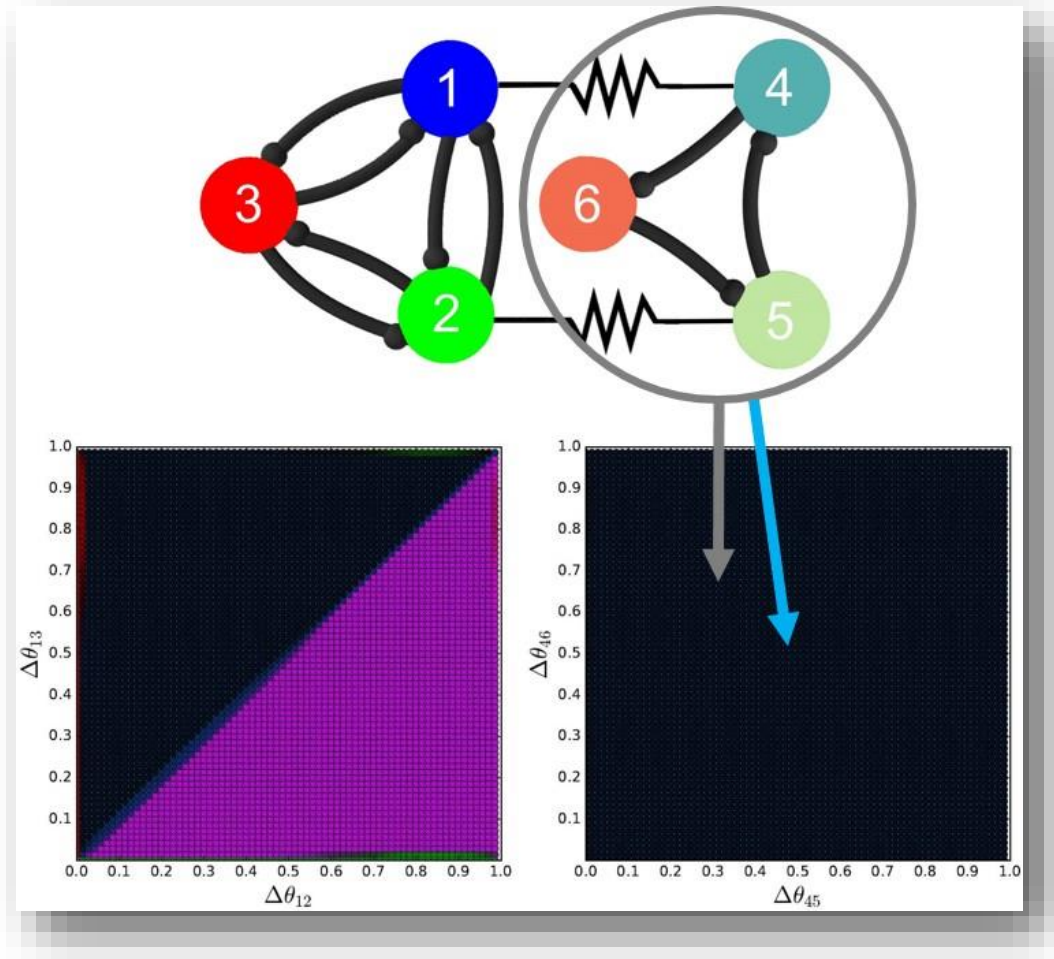


Figure A.12 Doubly-coupled electrically connected Symmetric-Clock hybrid system. Double electrical coupling of a symmetric network for which TW outcomes almost entirely dominate with a purely clockwise network for which only the black CTW pattern exists. Sample outputs for this network are shown in Figures A.13-16, spanning all $(\Delta_{12}, \Delta_{13})$ -space ICs while beginning [456] in either blue PM or black CTW phase-lag, near $(\Delta_{45}, \Delta_{46}) = (1/2, 1/2)$ and $(1/3, 2/3)$, respectively. Both begin with in-phase cells 1 and 4, $\Delta_{14} = 0$, followed by an anti-phase example for the CTW IC. Very strong coupling example for each followed last. Parameters: $I_{app} = 0.45$, $g_{ij} = g_{kl} = 0.008$.

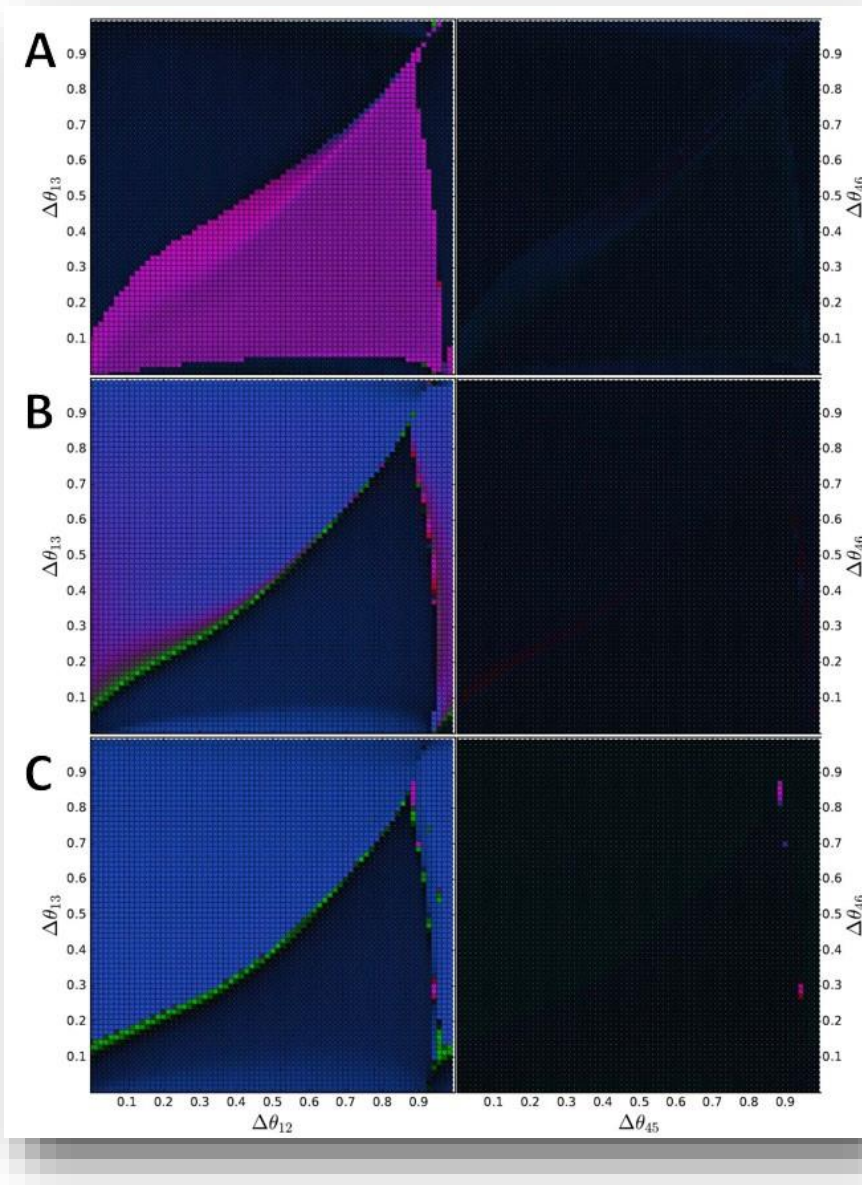


Figure A.13 Doubly-coupled electrically connected Sym-Clock, in-phase BPM

Connection of an almost entirely TW-dominated symmetric network with a purely clockwise network, with only black CTW patterns possible, via increasing electrical coupling of cells 1-to-4 and 2-to-5. Panels represent outcomes for both networks, spanning all $(\Delta_{12}, \Delta_{13})$ -space ICs while beginning [456] in blue PM phase-lag, near $(\Delta_{45}, \Delta_{46}) = (1/2, 1/2)$, with cells 1 and 4 in-phase at $\Delta_{14} = 0$. [123] converges again primarily to TW rhythms at weaker electrical coupling due to continued clockwise rhythmicity of [456], but with increasing presence of blue PM outcomes which grow to dominate at stronger coupling. [456] remains fixed as a black CTW at all coupling values. Parameters: $I_{app} = 0.45$, $g_{ij} = g_{kl} = 0.008$, $g_{elec} = 0.002, 0.005$, and 0.01 .

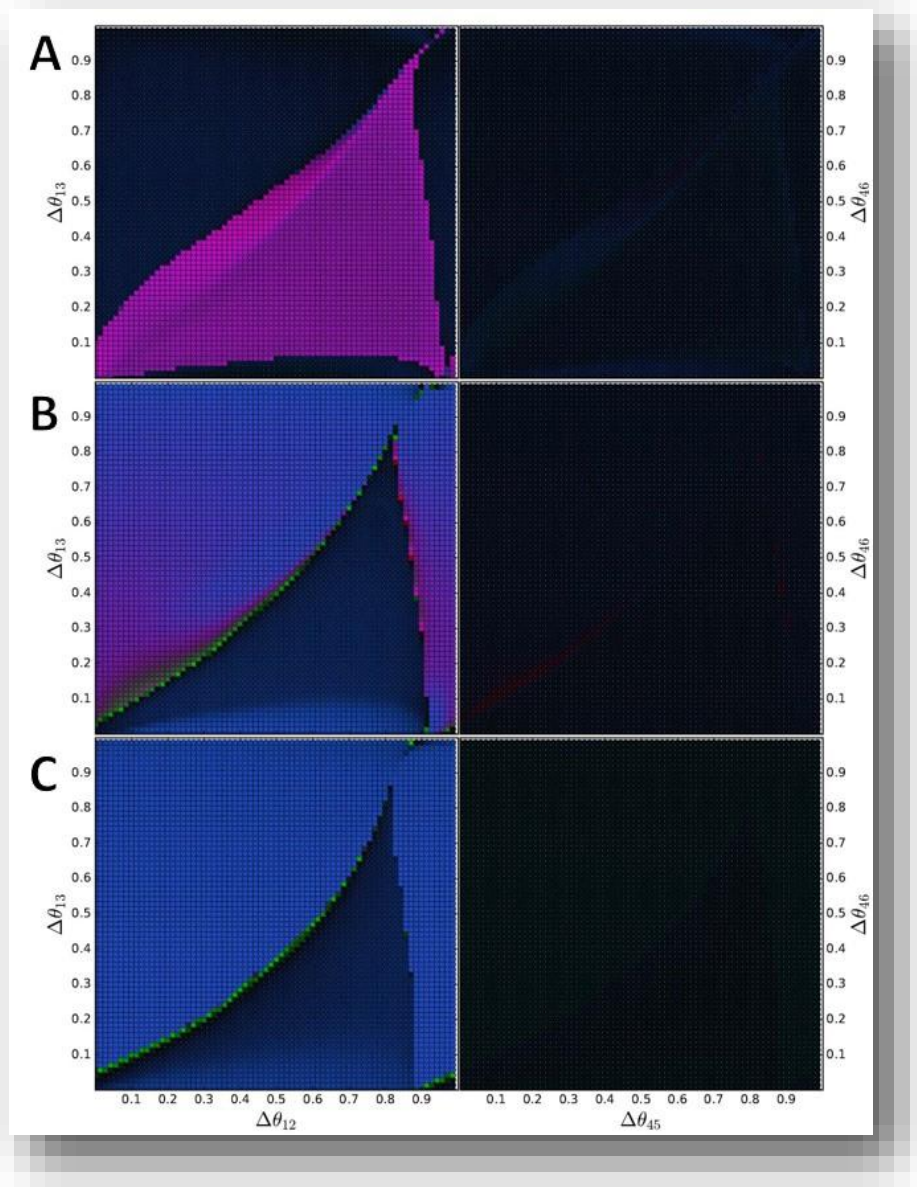


Figure A.14 Doubly-coupled electrically connected Sym-Clock, in-phase CTW

Connection of an almost entirely TW-dominated symmetric network with a purely clockwise network, with only black CTW patterns possible, via increasing electrical coupling of cells 1-to-4 and 2-to-5. Panels represent outcomes for both networks, spanning all $(\Delta_{12}, \Delta_{13})$ -space ICs while beginning [456] in black CTW phase-lag, near $(\Delta_{45}, \Delta_{46}) = (1/3, 2/3)$, cells 1 and 4 in-phase, with $\Delta_{14} = 0$. Entire system converges to nearly identical outcomes as in the in-phase blue PM example of Figure A.13, with the purely clockwise connectivity of [456] resulting in its immediate convergence to black CTW behavior in both cases. [123] again sees significant dominance of blue PM behavior with stronger coupling. Parameters: $I_{app} = 0.45$, $g_{ij} = g_{kl} = 0.008$, $g_{elec} = 0.002, 0.005$, and 0.01 .

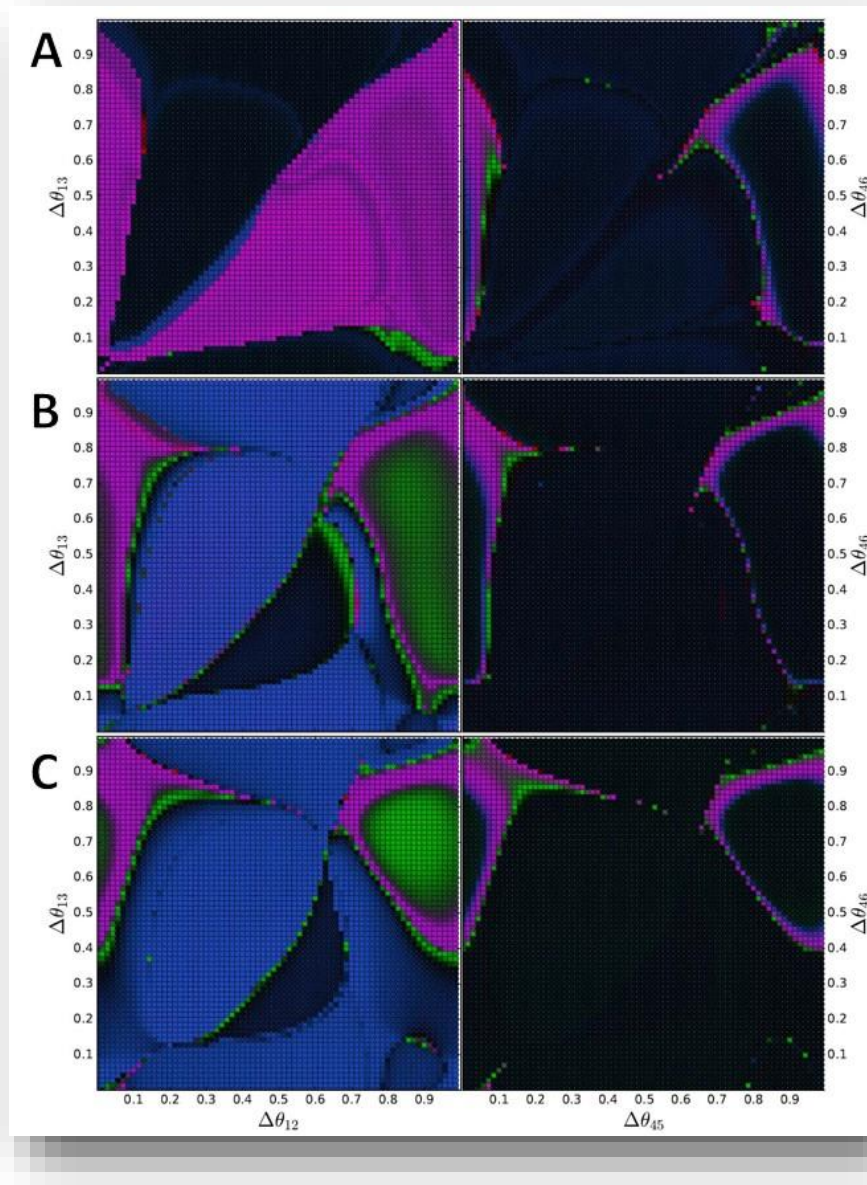


Figure A.15 Doubly-coupled electrically connected Sym-Clock, anti-phase CTW

Almost entirely TW-dominated symmetric network electrically coupled with a purely clockwise one, where only black CTW patterns exist, via connection of cells 1-to-4 and 2-to-5. Panels represent outcomes spanning all $(\Delta_{12}, \Delta_{13})$ -space ICs beginning [456] in black CTW phase-lag, near $(\Delta_{45}, \Delta_{46}) = (1/3, 2/3)$, in cells 1 and 4 anti-phase at $\Delta_{14} = 1/2$. [123] results mostly in TW rhythms at weaker coupling due to CTW dominance of [456], but with possible PM outcomes growing to dominate at stronger coupling with complex boundaries. [456] remains mostly black CTW, but now exhibits CCTW and very small regions of green PM activity for some $(\Delta_{12}, \Delta_{13})$ -ICs, decreasing in size with coupling. Parameters: $I_{app} = 0.45$, $g_{ij} = g_{kl} = 0.008$, $g_{elec} = 0.002$, 0.005, and 0.01.

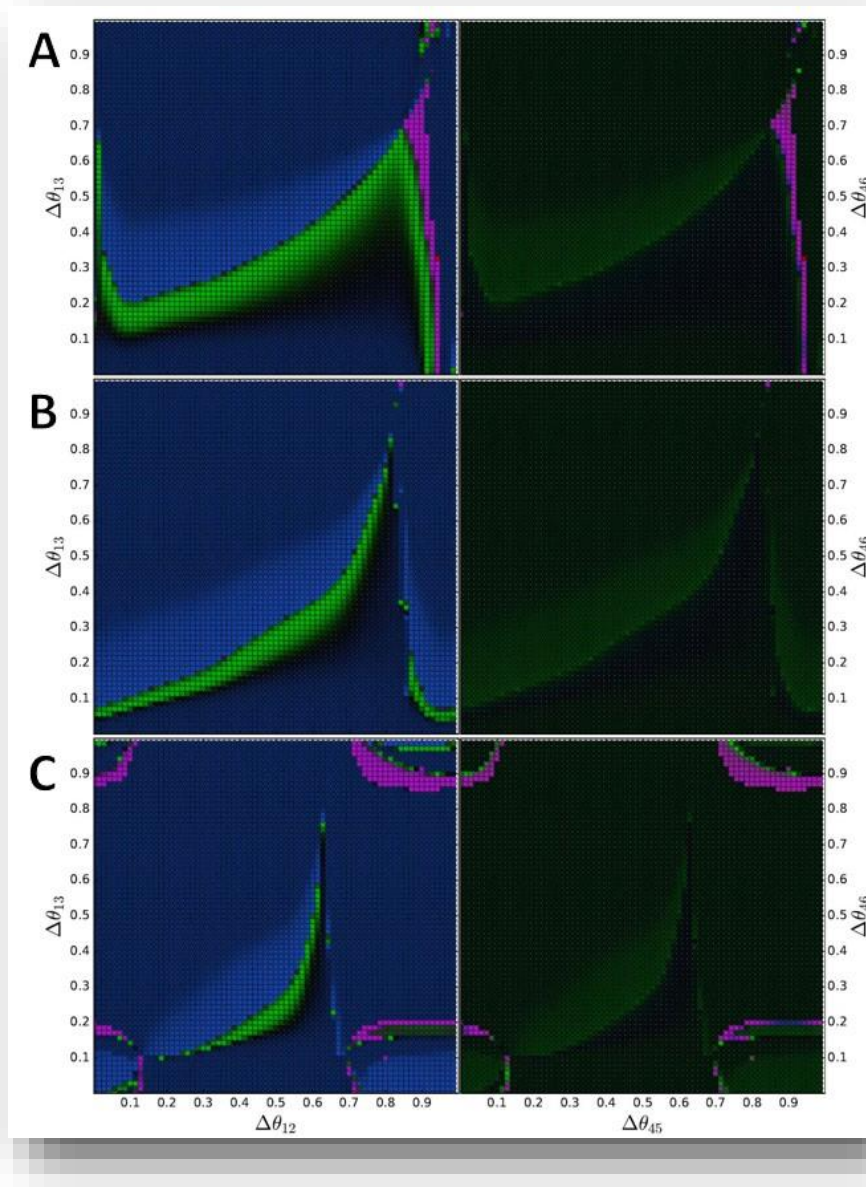


Figure A.16 Very strong double electrically-coupled symmetric-clock hybrid system
 Very strong double coupling of a symmetric motif producing primarily TW rhythms with a purely clockwise network with only CTW initially, extensions on Figures A.15-17. All $(\Delta_{12}, \Delta_{13})$ -space ICs are spanned for the [123]-motif. (A) When [456] begins in-phase BPM, $(\Delta_{14}, \Delta_{45}, \Delta_{46}) = (0, 0.5, 0.5)$, all blue PM behavior dominates in [123] with some green PM, and a narrow region in which CCTW outcomes occur in both networks. (B) When [456] begins in-phase CTW, $(\Delta_{14}, \Delta_{45}, \Delta_{46}) = (0, 0.33, 0.67)$, CCTW is lost entirely, with green PM behavior also diminishing in [123], black CTW dominating all [456]. (C) When [456] begins anti-phase in staggered CTW, $(\Delta_{14}, \Delta_{45}, \Delta_{46}) = (0.5, 0.17, 0.83)$, blue PM behavior dominates [123] and matching regions of CCTW rhythmicity are observed in both networks with a small zone of green PM ICs possible in [123]. Parameters: $I_{app} = 0.45$, $g_{ij} = g_{kl} = 0.008$, and $g_{elec} = 0.05$.

Appendix C.2: Triply Electrically-Coupled Symmetric-Clock Hybrid

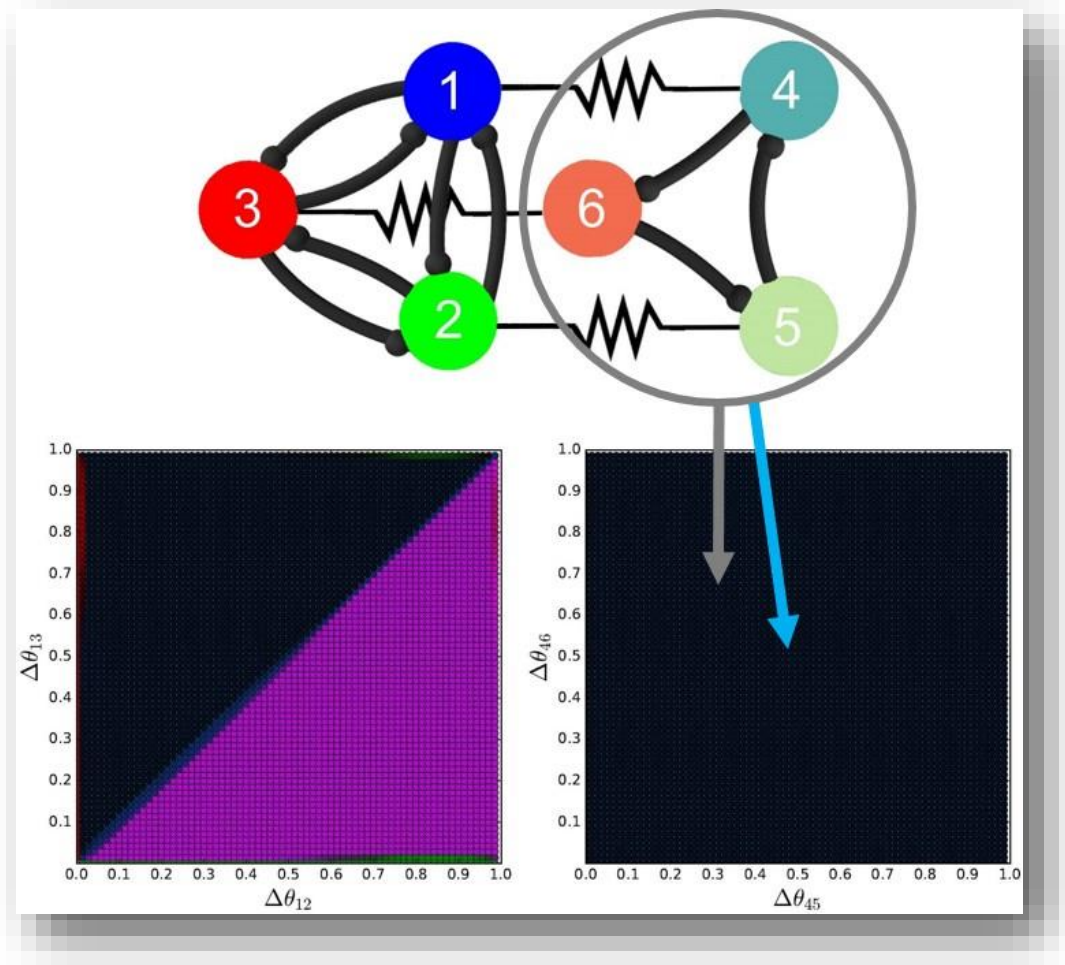


Figure A.17 Triply-coupled electrically connected Symmetric-Clock hybrid system
Triple electrical coupling of a symmetric network for which TW outcomes almost entirely dominate with a purely clockwise network for which only the black CTW pattern exists. Sample outputs for this network are shown in Figures A.20-23, spanning all $(\Delta_{12}, \Delta_{13})$ -space ICs while beginning [456] in either blue PM or black CTW phase-lag, near $(\Delta_{45}, \Delta_{46}) = (1/2, 1/2)$ and $(1/3, 2/3)$, respectively. Both begin with in-phase cells 1 and 4, $\Delta_{14} = 0$, followed by an anti-phase example for the CTW IC. Very strong coupling example for each followed last. Parameters: $I_{app} = 0.45$, $g_{ij} = g_{kl} = 0.008$.

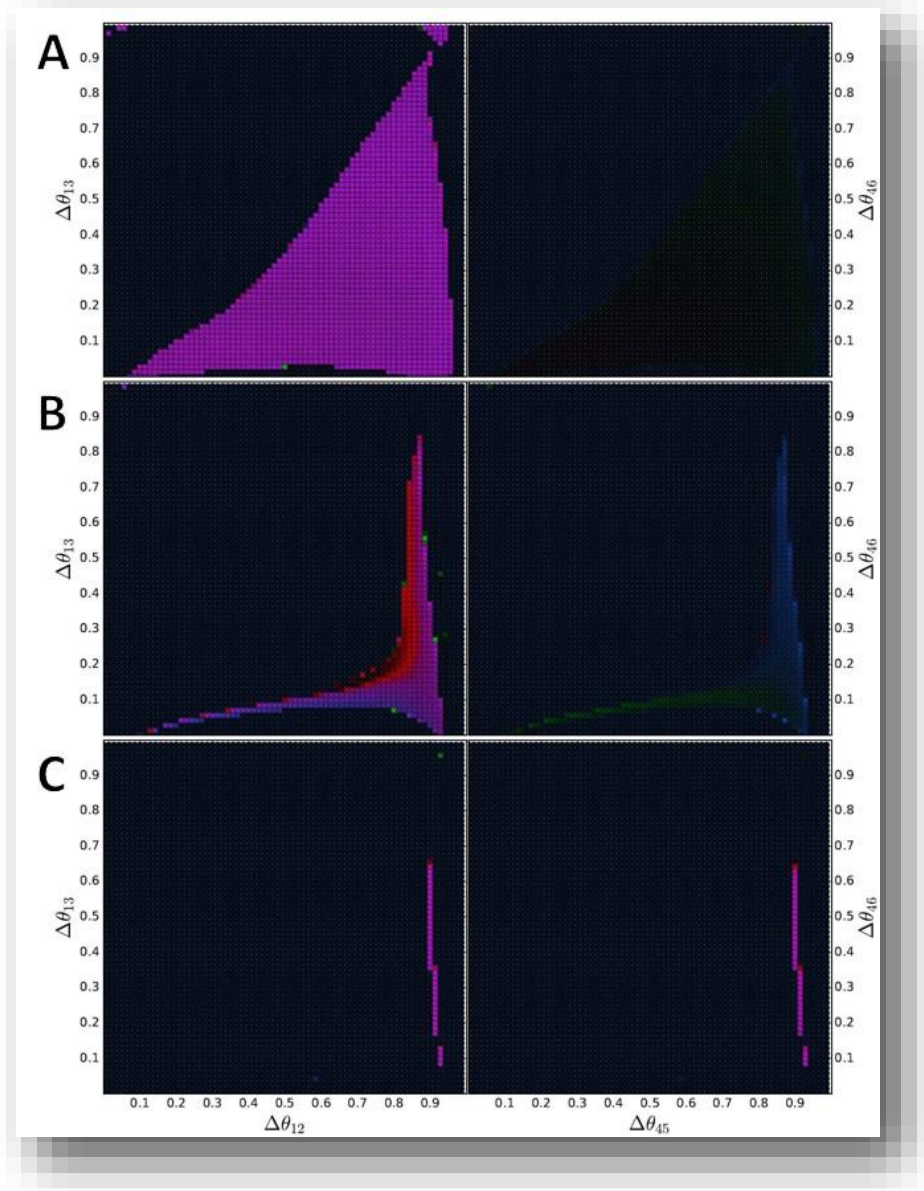


Figure A.18 Triply-coupled electrically connected Sym-Clock, in-phase BPM

Connection of an almost entirely TW-dominated symmetric network with a purely clockwise network, with only black CTW patterns possible, via increasing electrical coupling of cells 1-to-4, 2-to-5, and 3-to-6. Panels represent outcomes for both networks, spanning all $(\Delta_{12}, \Delta_{13})$ -space ICs while beginning [456] in blue PM phase-lag, near $(\Delta_{45}, \Delta_{46}) = (1/2, 1/2)$, with cells 1 and 4 in-phase at $\Delta_{14} = 0$. [123] converges primarily to TW rhythms at weaker electrical coupling due to continued clockwise rhythmicity of [456], but with a brief window of possible red PM outcomes at intermediate coupling for some ICs. [456] remains fixed as a black CTW at nearly all coupling values and ICs, with a very small region at stronger coupling in which CCTW rhythmicity occurs in both networks simultaneously. Parameters: $I_{app} = 0.45$, $g_{ij} = g_{kl} = 0.008$, $g_{elec} = 0.002, 0.005$, and 0.01 .

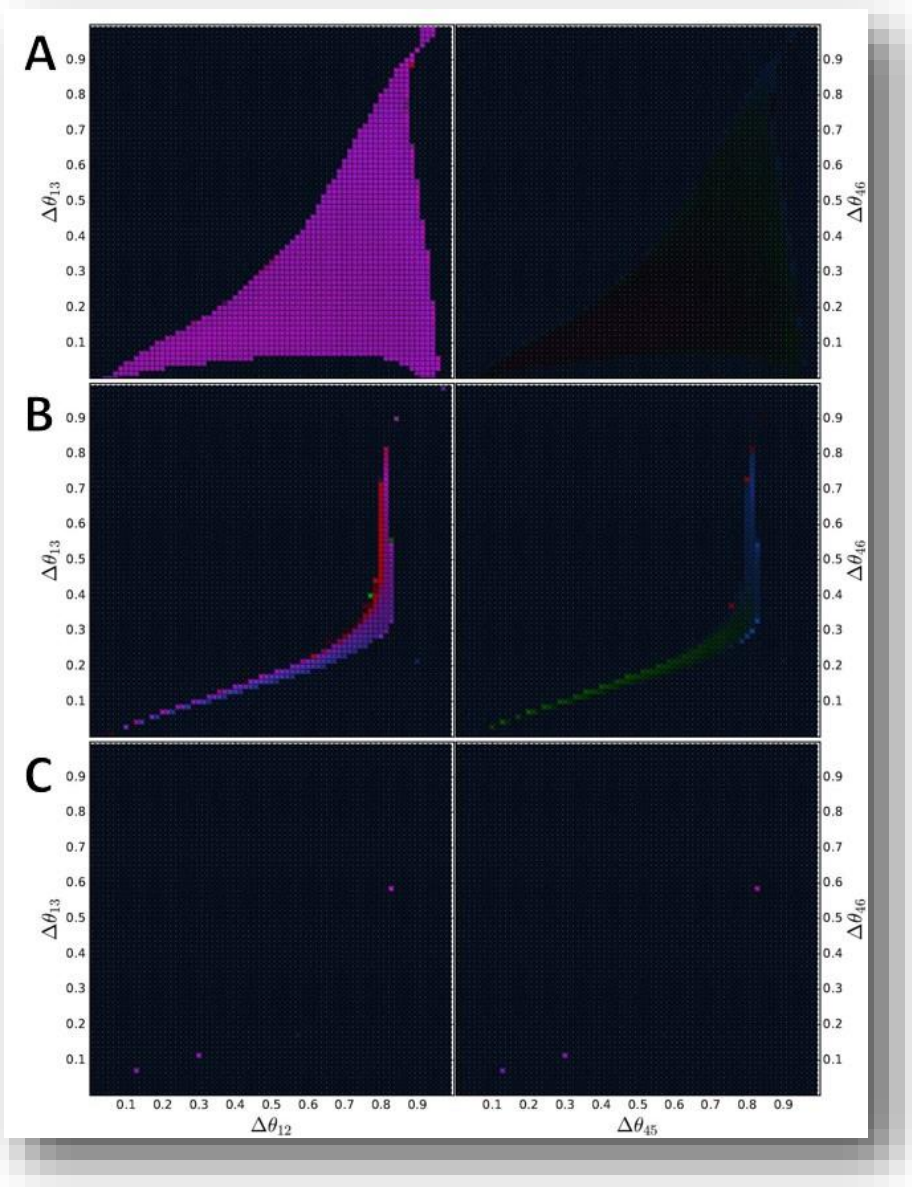


Figure A.19 Triply-coupled electrically connected Sym-Clock, in-phase CTW

Connection of an almost entirely TW-dominated symmetric network with a purely clockwise network, with only black CTW patterns possible, via increasing electrical coupling of cells 1-to-4, 2-to-5, and 3-to-6. Panels represent outcomes for both networks, spanning all $(\Delta_{12}, \Delta_{13})$ -space ICs while beginning [456] in black CTW phase-lag, near $(\Delta_{45}, \Delta_{46}) = (1/3, 2/3)$, cells 1 and 4 in-phase, with $\Delta_{14} = 0$. System converges to nearly identical outcome as in Figure A.18, with purely counterclockwise inhibition in [456] resulting in immediate convergence to CTW behavior in both cases, which drives outcomes in [123]. Simultaneous CCTW observed previously is no longer possible. Parameters: $I_{app} = 0.45$, $g_{ij} = g_{kl} = 0.008$, $g_{elec} = 0.002, 0.005, 0.01$.

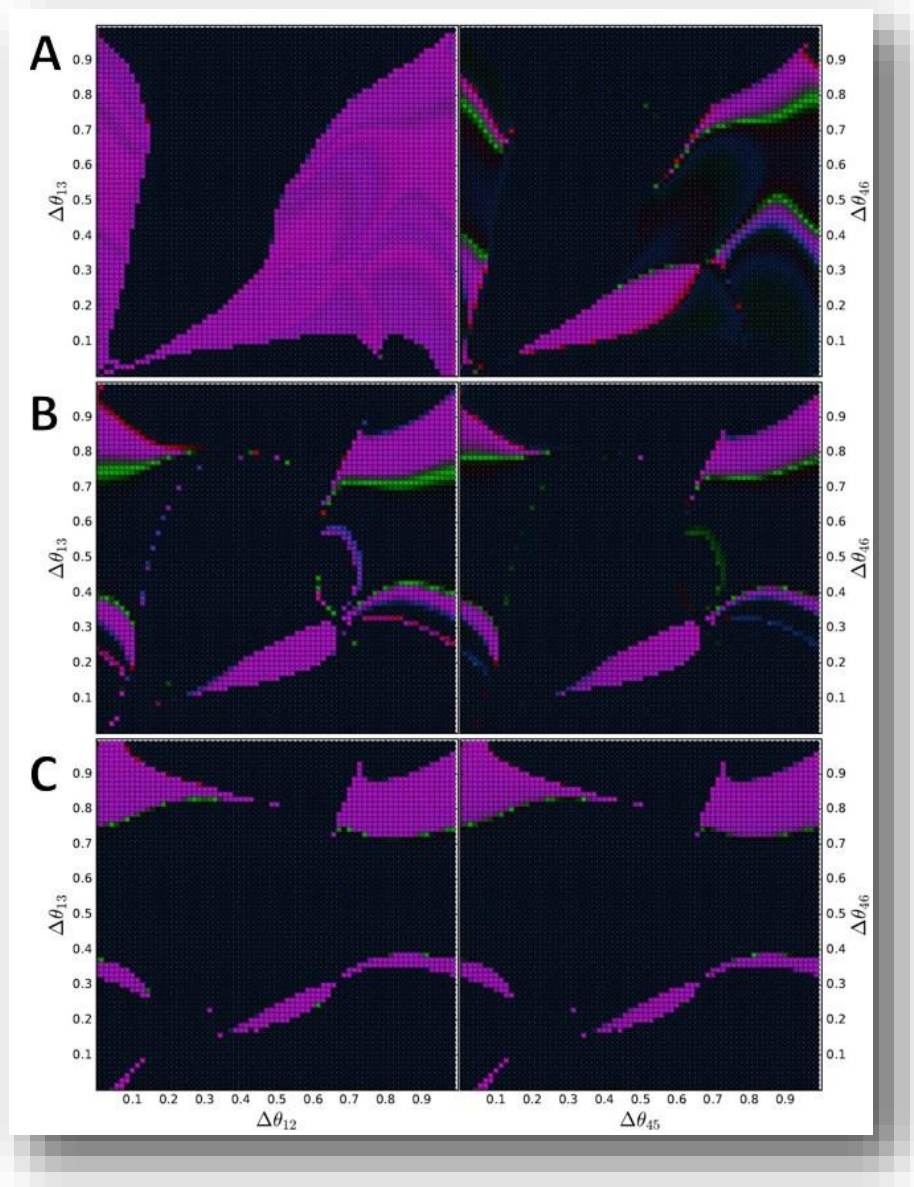


Figure A.20 Triply-coupled electrically connected Sym-Clock, anti-phase CTW.

Almost entirely TW-dominated symmetric network electrically coupled with a purely clockwise one, where only black CTW patterns exist, via connection of cells 1-to-4, 2-to-5, and 3-to-6. Panels represent outcomes spanning all $(\Delta_{12}, \Delta_{13})$ -space ICs beginning [456] in black CTW phase-lag, near $(\Delta_{45}, \Delta_{46}) = (1/3, 2/3)$, in cells 1 and 4 anti-phase at $\Delta_{14} = 1/2$. [123] results mostly in TW rhythms at weaker coupling due to CTW dominance of [456], but anti-phase initiation can drive both networks into CCTW rhythms. Small zones of possible green PM outcomes exist at lower coupling with complex boundaries. With stronger coupling, both networks are driven into full synchronicity and exhibit identical rhythm outcomes for all $(\Delta_{12}, \Delta_{13})$ -ICs. Parameters: $I_{app} = 0.45$, $g_{ij} = g_{kl} = 0.008$, $g_{elec} = 0.002, 0.005$, and 0.01 .

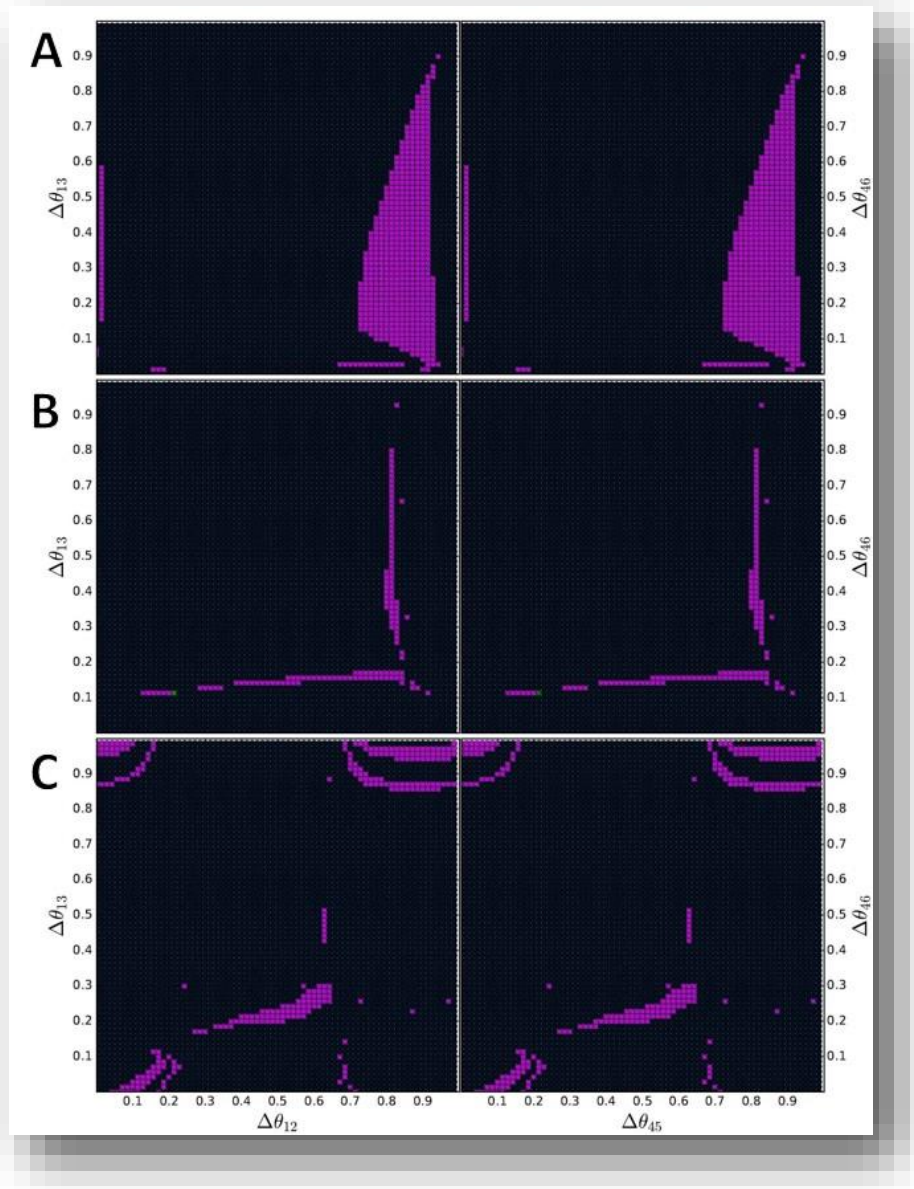


Figure A.21 Very strong triple electrically-coupled symmetric-clock hybrid system

Very strong coupling of a symmetric motif producing primarily TW rhythms with a purely clockwise network with only CTW initially, extensions on Figures A.20-22. All $(\Delta_{12}, \Delta_{13})$ -space ICs are spanned for the [123]-motif. Strong electrical coupling of all three nodes in each network leads to full synchronicity and both networks identical rhythm outcomes for all $(\Delta_{12}, \Delta_{13})$ -ICs. (A) When [456] begins in-phase BPM, $(\Delta_{14}, \Delta_{45}, \Delta_{46}) = (0, 0.5, 0.5)$, a larger zone of CCTW outcomes is possible. (B) When [456] begins in-phase CTW, $(\Delta_{14}, \Delta_{45}, \Delta_{46}) = (0, 0.33, 0.67)$, CCTW patterns diminish as full synchronicity beginning in CTW will typically remain there. (C) When [456] begins anti-phase in staggered CTW, $(\Delta_{14}, \Delta_{45}, \Delta_{46}) = (0.5, 0.17, 0.83)$, more complex boundaries between rhythm outcomes occur and it is possible for the system to stabilize to CCTW. Parameters: $I_{app} = 0.45$, $g_{ij} = g_{kl} = 0.008$, and $g_{elec} = 0.05$.